Magmatic Differentiation in Arc and Mid-Ocean Ridge Settings

Thesis by

Madeline Janine Lewis

In Partial Fulfillment of the Requirements for the degree of

Doctor of Philosophy

CALIFORNIA INSTITUTE OF TECHNOLOGY

Pasadena, California

2021

(Defended May 18, 2021)

Madeline Janine Lewis
ORCID: 0000-0001-7968-2822

ACKNOWLEDGEMENTS

This thesis is the result of many years of education and encouragement from advisors, peers, family, and colleagues, of which there are too many to individually name. I would like to specifically thank many of those who have helped me reach this point, and broadly acknowledge all others who have inspired and assisted me along the way.

I would firstly like to thank my PhD advisors Paul Asimow and Claire Bucholz for their endless support and constructive criticism that has helped me grow significantly as a researcher. I am also grateful for the collaboration and mentorship from members of my thesis advisory committee —Woody Fischer, George Rossman, and Ed Stolper— throughout my time at Caltech.

The work presented here would not be possible without the excellent analytical support from Nathan Dalleska, Chi Ma, and Yunbin Guan. I am also incredibly thankful to the support staff and residents of the Arms Building, and particularly Mark Garcia for his help with preparation for many class field trips and research fieldwork and for forgiving my return of mud-covered vehicles.

I am grateful to collaborators within and beyond Caltech, including Sarah McCart for much work put into characterization and analysis of sediment cores, to Dave Lund for spear-heading the sediment cores projects, to Oli Jagoutz for helpful conversation and manuscript comments, to Ayman Maurice for providing samples and interpretations of BIFs, and to Juliet Ryan-Davis for analyses for our semi-overlapping Sierra Nevada batholith projects. I would also like to thank the many field assistants who have helped me collect, and more importantly carry rocks over mountains: Joe Biasi, Juliet Ryan-Davis, Allyson Trussell, Emma Sosa, Matt Barickman, Sam Newall, and last but not least, my mom Liane Lewis.

Finally, I would like to thank my family and friends for their never-ending encouragement. The 2015-16 Pit, the residents of second floor Arms, and the Caltech dining and arts folks have all been wonderful in creating social and creative outlets. I cannot express how much the support from my parents has helped me to reach this point. Thank you for always letting me play in the dirt, taking me on my first trips to the Sierras, paying for my undergraduate education, and making many Sunday dinners during grad school. And lastly, I thank my husband Joe for your love and support, and for always being there for me when I need it most.

ABSTRACT

The compositional variation of igneous rocks and construction of Earth's crust is the result of magmatic differentiation —crystallization, melting, and assimilation mechanisms that cause the composition of magmas to change over time. This thesis investigates magma generation and evolution at both convergent and divergent plate boundaries. The resulting magmatic arcs and mid-ocean ridges create the vast majority of Earth's crust, though the details of crustal construction and the specific processes that generate the observed magmatic and volcanic products are complex. Accordingly, this work uses the geochemical signatures encoded in rocks and minerals to explain magmatic differentiation histories in multiple tectonic settings.

Here, I present five main studies that utilize field and textural observations, geochemical analyses, and computational modeling to investigate the compositional structure of the crust beneath magmatic arcs and mid-ocean ridges. In addition, this work explores the pyroclastic and sedimentary products dispersed by magmatically heated hydrothermal fluids in submarine environments. Chapters 2 and 3 investigate the crystallization histories of mafic intrusions in the eastern-central Sierra Nevada batholith paleo-continental arc, California. This work has implications for the compositional and temporal generation of both mafic and evolved magmas throughout the batholith and in other continental arcs. Chapters 4 and 5 explore records of submarine volcanic ash deposits associated with explosive mid-ocean ridge eruptions from the East Pacific Rise and Pacific-Antarctic Ridge, as well as the effects that sea level change has on melting of the mantle, eruption styles, and the compositional evolution of mid-ocean ridge magmas. Chapter 6 examines the mineral hosting of rare earth elements (REEs) in the Wadi Karim banded iron formation, and the implications of element mobility on interpretations based on REE abundances.

PUBLISHED CONTENT AND CONTRIBUTIONS

The chapters of this thesis, exempting the Introduction, were each prepared as individual manuscripts or portions of manuscripts (in the case of Chapter 4). The term "we" is used throughout this text in reference to the following co-authors:

CHAPTER 2: Lewis MJ, Bucholz CE, Jagoutz OE (*submitted to CMP, Jan 2021*) Evidence for Polybaric Fractional Crystallization in a Continental Arc: Hidden Lakes Mafic Complex, Sierra Nevada Batholith, California. (*in review for Contributions to Mineralogy and Petrology*)

> MJL participated in conception of this project, collected samples, completed field mapping, analyzed samples, completed fractionation modeling, interpreted results, and wrote most of the manuscript.

CHAPTER 4: *Adapted from:* Lund DC, Seeley EI, Asimow PD, **Lewis MJ**, McCart SE, Mudahy AA (2018) Anomalous Pacific-Antarctic Ridge Volcanism Precedes Glacial Termination 2. Geochemistry, Geophysics, Geosystems 19(8):2478-2491 https://doi.org/10.1029/2017GC007341

> Sections included here consist of only the portions of the project for which MJL completed the geochemical analyses, modeling, and drafting of the manuscript. All other analyses and interpretations from the project (completed by co-authors) are cited as Lund et al. (2018) in the text.

MANUSCRIPTS IN PREPARATION WITH CO-AUTHORS

CHAPTER 3: Lewis MJ, Ryan-Davis JR, Bucholz CE. Mafic Intrusions Reveal a Mantle Driver of Arc Episodicity and Crustal Thickening in the Sierra Nevada Batholith. (*in preparation for Geology*)

> MJL led the conception of the project, fieldwork, geochronology, bulk-rock analyses, and manuscript preparation.

CHAPTER 5: Lewis MJ, McCart SE, Asimow PD, Lund DC. Multiple Sills Tapped by Explosive Eruptions from the East Pacific Rise: Ties to Sea Level Variation. (*in preparation*)

> MJL completed sample preparation and analysis, interpreted results, completed fractionation modeling, and drafted the manuscript.

CHAPTER 6: Lewis MJ, Asimow PD, Fischer WW, Maurice AE. Hosting of REE in Accessory Minerals in the Wadi Karim BIF: Implications for the Preservation of Bulk-rock Trace Element Signatures in Iron Formation. (*in preparation for Precambrian Research*)

> MJL completed SEM maps and *in-situ* compositional analyses, completed REE budget calculations, interpreted results, and wrote much of the manuscript.

TABLE OF CONTENTS

LIST OF FIGURES

Chapter 6

LIST OF TABLES

SUPPLEMENTARY TABLES

Supplementary tables are included in the Supplementary Data File (.xlsx). Sheet names (CH#-S#) are given rather than page numbers.

CHAPTER 1

Introduction

1.1 Background

On the modern Earth and since the onset of plate tectonics, Earth's crust is dominantly and continuously produced at magmatic arcs and mid-ocean ridges. The global mid-ocean ridge system produces roughly 20 km^3, or a surface area of about 2.7 km^2, of new oceanic crust per year (Cogné and Humler 2006) due to decompression of the mantle caused by plate spreading (e.g., Gast 1968; Kay et al. 1970). Plate convergence is coupled to plate spreading, causing either subduction of oceanic crust into the mantle or orogenesis that eventually results in erosion of mountains into the oceanic basins. In both cases, crustal volumes equivalent to the newly generated oceanic crust are recycled into the mantle over long timescales at subduction zones, which in turn drives continental and oceanic arc magmatism. The average composition of continental crust is consistent with magmas generated in arc settings (Rudnick 1995), completing the cycle of crustal production. This discussion excludes intraplate magmatism in favor of focusing on the magmatic systems that are most compositionally representative of oceanic and continental crust. Thus, this thesis explores the processes that generate the largest volumes of crust throughout the majority of Earth history since the onset of modern plate tectonics.

Within arc and mid-ocean ridge settings, magmas undergo differentiation, a term for process that changes the composition of a magma through cooling, partial melting, or eruption. Fractional crystallization, or the separation of crystallizing minerals from a liquid that causes continuous evolution of the melt composition, was the first proposed (Bowen 1928) and most commonly invoked differentiation process. Additional differentiation mechanisms include assimilation of bulk crust or partial melts of preexisting crust, magma mixing and rejuvenation, and incomplete liquid-crystal separation. Distinguishing between the different differentiation mechanisms can be difficult, as multiple processes are likely to occur within the same magma

body. However, modeling of the evolving melt composition, also called a liquid line of descent (LLD), can aid in determining which processes dominantly act to generate a series of magmatic compositions derived from a common parent magma. Thus, the following chapters work to decipher the details of magmatic differentiation in multiple tectonic settings to aid in our understanding of the construction of Earth's crust.

1.2 Dissertation Summary

This thesis explores the processes of magma generation and compositional evolution in a continental arc and beneath mid-ocean ridges, as well as investigating the pyroclastic and sedimentary products dispersed by magmatically-heated hydrothermal fluids.

Chapters 2 and 3 present geochemical, geochronological, and modeling results from mafic intrusive complexes of the eastern central Sierra Nevada batholith (SNB), California. The SNB is a Triassic through Cretaceous paleo-continental arc that is exposed to dominantly upper crustal depths (100-400 MPa), with the exception of limited deeper exposures at the southern end of the batholith (up to 1 GPa) (Chapman et al. 2012; Klein and Jagoutz 2021). While the bulk of the batholith volume is made up of felsic plutons (mainly granodiorites, tonalities, and granites; i.e., granitoids), small (<25 km^2) gabbro through diorite intrusions are common throughout the SNB upper crust (Coleman et al. 1995; Frost 1987; Ratajeski et al. 2001; Sisson et al. 1996). This is in contrast to the generalized model of arc crust that is compositionally stratified, with a lower crust dominated by mafic cumulates and an upper crust constructed of granitoid plutons (e.g., Jagoutz 2014). The upper crustal mafic complexes present opportunities to study both lower and upper crustal processes, as the melts that form these intrusions must ascend through the arc crust. Studying these intrusions is beneficial in comparison to granitoids, as the mafic

rocks are more similar in composition to their mantle source, and thus have not undergone such extensive compositional evolution as to obscure previous differentiation stages.

The processes leading to the production of granitoids in continental arcs is debated, as extensive mafic cumulates are generally lacking from the upper crust, but experimental studies show that extensive lower crustal differentiation at high pressures (> 1 GPa) generates aluminum-enriched (peraluminous) melt compositions that are not commonly observed in arcs (Blatter et al. 2013). To investigate where differentiation occurs in continental arcs, Chapter 2 details a case study of the Hidden Lakes mafic complex (HLMC), an upper crustal mafic body in the central-eastern SNB. Field relationships support *in-situ* fractional crystallization of a norite through monzonite crystallization sequence at ~300 MPa, as supported by a modeled fractional crystallization LLD constructed by stepwise removal of cumulate compositions from an evolving melt. Mineral compositions from the HLMC show that the first melt to intrude into this complex was not a pure melt of the mantle, but rather experienced crystallization deep in the crust prior to its ascent. We therefore also model an initial stage of lower crustal differentiation (1 GPa) to generate the compositions observed within the HLMC. The fractionation model is thus polybaric, with two differentiation stages occurring at vastly different pressures. This model reproduces the range of compositions found within HLMC, and when extended to higher SiO_2 contents, also replicates the compositions of felsic plutons that comprise most of the SNB. Therefore, this work supports a two-stage differentiation origin for intermediate to evolved magmas in the SNB, with evidence for both lower crustal and upper crustal fractionation.

Throughout continental arcs, volumetric magma intrusion rates are temporally variable over millions of years. A pattern of episodic arc flare-ups, when up to 80% of final batholith volumes are intruded in ~10 to 15 Ma periods, amongst lulls with comparatively little magmatic

activity, is recognized in continental arcs worldwide (Ducea et al. 2015; Paterson et al. 2011). Though many hypotheses have been proposed for triggers of magmatic flare-ups (e.g., Ardila et al. 2019; Chapman et al. 2013; DeCelles et al. 2009; DeCelles and Graham 2015; Ducea 2001; Schwartz et al. 2017), the drivers of voluminous magma generation during these events remain unclear. In the SNB, 70 to 95% of the granitoid volume intruded during flare-ups in the Late Jurassic (160-145 Ma) and Late Cretaceous (100-85 Ma) (Ducea 2001). The relationship between mafic and felsic melts in the batholith is uncertain, and while several mafic intrusions in the central SNB have been dated to Late Cretaceous time (91-103 Ma) (Coleman et al. 2001; Ratajeski et al. 2001), the large majority are undated. Chapter 3 presents geochronology and geochemistry results from 17 mafic bodies in the central-eastern SNB, and identifies two main pulses of mafic magmatism (155-146 Ma and 99-89 Ma) coincident with the Late Jurassic and Late Cretaceous flare-ups. Mineral chemistry from these intrusions show that the parental melts of the complexes were not primitive mantle melts and therefore require a stage of lower crustal differentiation, very similar to the lower crustal stage of differentiation discussed in Chapter 2. Moreover, bulk-rock geochemistry and field observations show evidence for upper crustal fractionation, thereby corroborating the general regional validity of our polybaric fractionation model from the HLMC. Because the intrusion of mafic melts into the upper crust occurs dominantly during flare-ups in the SNB, our results strongly imply that arc flare-ups are driven by episodic pulses of enhanced mantle melting, rather than resulting from a crustal trigger.

In contrast to continental arcs, mid-ocean ridge (MOR) magma production is thought to be a relatively steady-state process controlled by decompression of the mantle at rates set by plate spreading. However, proxies for magmatic flux to MOR axes —hydrothermal fluxes and seafloor bathymetry— suggest temporal variability of magma flux consistent with timescales of

glacial-interglacial cycles (e.g., Costa et al. 2017; Crowley et al. 2015; Lund et al. 2016; Middleton et al. 2016; Tolstoy 2015). Correlations between glacial cycling and magmatism have been observed in high-latitude subaerial volcanic systems, with increased volcanic fluxes occurring during interglacial periods (Glazner et al. 1999; Huybers and Langmuir 2009). In mid-ocean ridge settings, glacial periods are thought to affect the mantle melting regime by causing rapid changes in sea level. This loading or unloading of the seafloor occurs at rates up to 50% of typical depressurization due to seafloor spreading, thus significantly modulating the melting regime (Huybers and Langmuir 2009; Lund and Asimow 2011). In Chapters 4 and 5, we investigate a new proxy for anomalous MOR magmatism: basaltic glass shards preserved in sediment cores retrieved from near MOR axes. Chapter 4 presents geochemistry and modeling results from glass shards found in a sediment core from site OC170-26-159, located off axis of the Pacific-Antarctic Ridge (PAR) (originally published in Lund et al. 2018). At the time of the shard producing eruptions (135-145 kyr) the core site was 7 km from the ridge axis, much farther than the 3 km that has been previously observed for submarine pyroclasts (Clague et al. 2009; Ferguson et al. 2017), and requiring an anomalously energetic series of eruptions for shard distribution. The glasses cluster into a single compositional group with MgO contents ranging from 5.8 to 6.5 wt.%, which is more evolved than typical mid-ocean ridge basalt (MORB). Modeling of a fractional crystallization LLD starting from a composition similar to axial MORB reproduces the glass shard compositions, indicating that the shards represent an evolved member of the axial magmatic system.

Chapter 5 investigates an ash layer in core Y71-07-53, taken from off axis of the East Pacific Rise at a site that was 8 to 9 km from the ridge axis during the eruption interval (343-342 kyr) (McCart 2020), and requiring even more energetic eruptions than the PAR glasses. These

glass shards fall into three compositional groups that represent two separate LLDs. Both LLDs are consistent with derivation from the axial magmatic system. The lowest MgO shards in this suite represent the most evolved MORB pyroclasts yet recorded (MgO= 5 wt.%). The two LLDs require different starting concentrations of K_2O, H_2O, and highly incompatible trace elements, which we attribute to assimilation of hydrothermally altered E-MORB crust into a nominally N-MORB sill. The maintenance of two independently differentiating LLDs indicates multiple separate magma storage chambers beneath the EPR axis, and sourcing from both chambers during the explosive eruption interval.

The ash layers at the PAR and EPR were deposited coincident with glacial terminations T2 and T4, respectively. Both eruption intervals occur ~50 kyr after rapid drops in sea level associated with the onset of glacial periods, an offset consistent with the time needed for melts to ascend to the axial magma chamber from depths where melting occurs in the mantle (Boulahanis et al. 2020; Langmuir and Forsyth 2007; Weatherley and Katz 2016). The evolved shard compositions suggest a period of low melt-flux to the ridge axis prior to eruption that allows for cooling and fractionation, followed by an anomalously high heat (and thus, melt) flux at the time of the eruptions to generate a hot water plume that dispersed the shards up to 9 km from their sources. We posit that prior to the sea level drops, relatively high, constant sea level led to a decline in melt generation at depth, followed by enhanced melting associated with sea level drop. Thus, the glass shard compositions and timing of large, explosive eruptions from the EPR and PAR support sea level forcing of melting beneath MORs.

Circulation of seawater within oceanic crust in close proximity to magmas, either in mid-ocean ridge or oceanic arc settings, leads to significant leaching of iron and other metals from the heated crust. In the Archean and Neoproterozoic, these hydrothermal fluids acted as major

sources of Fe and Si in the deposition of iron formations (IFs) in anoxic marine basins (e.g., Klein 2005). Additional Fe and Si (the main components of IFs) were sourced from seawater and detrital inputs. To determine the relative contribution of Fe and Si in IFs, previous studies primarily use bulk-rock IF rare earth element (REE) signatures (e.g., Abd El-Rahman et al. 2020; Basta et al. 2011; Frei and Polat 2007; Khan and Naqvi 1996), with the assumption that the current REE concentrations are representative of the IF source at the time of deposition. However, the dominant minerals that make up IF, Fe-oxides and chert, contain very low concentrations of REEs. In Chapter 6, we determine that the majority of the REE budget in the Wadi Karim banded IF is hosted in accessory minerals: 36 to 75% of the REEs are hosted in apatite, with an additional 10 to 13% hosted in calcite, though these minerals collectively make up <9% of the samples. Detailed micro-textural observations show that apatite and calcite are commonly present in veins and were likely mobile throughout the samples. This calls the validity of bulk-rock IF REE patterns as source proxies into question, as REEs may be introduced or lost from IFs during metamorphism and alteration.

1.3 Remaining Questions and Potential Future Directions

This research contributes to our understanding of how continental crust is constructed, feedback between climate cycling and mid-ocean ridge magmatism, and the preservation of chemical signatures of Earth's past. However, additional questions arise from the results presented in each chapter, which could be investigated in future studies.

The lower crustal crystallization model constructed in Chapter 2 relies on the assumption of a magmatic oxygen fugacity (fO_2) value for liquids generated by melting in the mantle beneath the SNB. Though arc melts are commonly found to be more oxidized than MORB, the origin of

this oxidation is debated (e.g., Bucholz and Kelemen 2019; Carmichael 1991). The fO_2 value that we use is based on mineral oxybarometry from the upper crustal samples, though the initial magmatic fO_2 may evolve with differentiation in the lower crust. To improve our fractionation model of the Hidden Lakes mafic complex (HLMC), and to be incorporated into Lewis et al. (2021), we will utilize the compositions of cumulate xenoliths originating from the SNB lower crust (1-3 GPa) (Lee et al. 2006) to model a lower crustal differentiation stage. As this is a cumulate subtraction model similar to our modeling of upper crustal differentiation within the HLMC (see Section 2.7.5, this thesis), the model will be independent of fO_2 and does not require the assertion of a specific crystallization pressure.

The geochronology of mafic intrusions presented in Chapter 3 shows that nearly all sampled mafic intrusions were emplaced in the upper crust during magmatic flare-ups, suggesting that melting of the mantle is enhanced during these periods. However, our results do not distinguish between different causes for variation in melt flux from the mantle, such as episodic fluxing of the mantle wedge, changes to the subduction angle or convergence rate, mantle upwelling, or a combination of these and other processes (Ardila et al. 2019; Decker et al. 2017; Schwartz et al. 2017). Comparison of magmatic compositions intruded during and between flare-ups could potentially highlight differences in the depth or extent of melting, or isotopic character of melts, which may point to particular melt sources or melting processes.

Chapters 4 and 5 identify only two cases of large explosive MOR eruptions that were likely caused by a series of changes to sea level that influenced melt supply to the ridge axis. The ash-bearing sediment cores needed to identify additional similar eruptions are rare, as they must be retrieved within roughly 40 km of the volcanic source (for fast-spreading ridges, and given a maximum ~10 km shard dispersal distance), where sediment is typically relatively thin. To

expand this investigation and to determine if the effects of sea level change on the axial magmatic system extend to more slowly spreading ridges, focused collection of sediment cores proximal to ridge axes may be required. In addition, reported megaplumes —the mechanism that we support for dispersal of ash to the core locations— have mainly been observed at MOR locations, though few have been reported from major seamounts and intraplate hot spot systems (Pegler and Ferguson 2020). Investigation of sediment cores located near these intraplate submarine volcanoes could determine whether sea level change modulates magma production in these magmatic systems as well. Further, it may be significant to determine how common such large shard-producing eruptions are preceding glacial terminations, and whether the magnitude of heat and CO_2 addition to the deep oceans associated with these eruptions is enough to trigger significant ice loss and ultimately end the glacial period.

Reconstruction of the REE budget of the Neoproterozoic Wadi Karim IF (WKB) in Chapter 6 shows that a significant portion of the bulk-rock REEs are hosted in accessory minerals, but this has not been investigated in detail in other IF deposits. IF occurrences span over 1.5 Ga of Earth history, with a range of metamorphic grades and phosphate contents preserved, so the importance of accessory mineral hosts to the REE budget and the preservation of depositional REE patterns is likely to vary between IFs. Therefore, it may be important to investigate IFs deposited during different time periods and depositional settings, such as the very low P_2O_5 Archean IFs and the much higher P_2O_5 (>2 wt.%) Rapitan-type Neoproterozoic IFs (Klein 2005). It is also possible that other accessory minerals, in addition to apatite and calcite, may host a significant portion of the REE budget in other IFs depending on their mineralogy, potentially affecting the preservation of REE patterns differently than in the WKB.

1.4 References Cited

Abd El-Rahman Y, Gutzmer J, Li X-H, Seifert T, Li C-F, Ling X-X, Li J (2020) Not all Neoproterozoic iron formations are glaciogenic: Sturtian-aged non-Rapitan exhalative iron formations from the Arabian–Nubian Shield. Mineralium Deposita 55(3):577-596

Ardila AMM, Paterson SR, Memeti V, Parada MA, Molina PG (2019) Mantle driven cretaceous flare-ups in Cordilleran arcs. Lithos 326:19-27

Basta FF, Maurice AE, Fontboté L, Favarger P-Y (2011) Petrology and geochemistry of the banded iron formation (BIF) of Wadi Karim and Um Anab, Eastern Desert, Egypt: implications for the origin of Neoproterozoic BIF. Precambrian Research 187(3-4):277-292

Blatter DL, Sisson TW, Hankins WB (2013) Crystallization of oxidized, moderately hydrous arc basalt at mid-to lower-crustal pressures: implications for andesite genesis. Contributions to Mineralogy and Petrology 166(3):861-886

Boulahanis B, Carbotte SM, Huybers PJ, Nedimović MR, Aghaei O, Canales JP, Langmuir CH (2020) Do sea level variations influence mid-ocean ridge magma supply? A test using crustal thickness and bathymetry data from the East Pacific Rise. Earth and Planetary Science Letters 535:116121

Bowen NL (1928) The Evolution of the Igneous Rocks. Princeton University Press 332

Bucholz CE, Kelemen PB (2019) Oxygen fugacity at the base of the Talkeetna arc, Alaska. Contributions to Mineralogy and Petrology 174(10):1-27

Carmichael IS (1991) The redox states of basic and silicic magmas: a reflection of their source regions? Contributions to Mineralogy and Petrology 106(2):129-141

Chapman AD, Saleeby JB, Eiler J (2013) Slab flattening trigger for isotopic disturbance and magmatic flare-up in the southernmost Sierra Nevada batholith, California. Geology 41(9):1007-1010

Chapman AD, Saleeby JB, Wood DJ, Piasecki A, Kidder S, Ducea MN, Farley KA (2012) Late Cretaceous gravitational collapse of the southern Sierra Nevada batholith, California. Geosphere 8(2):314-341

Clague DA, Paduan JB, Davis AS (2009) Widespread strombolian eruptions of mid-ocean ridge basalt. Journal of Volcanology and Geothermal Research 180(2-4):171-188

Cogné JP, Humler E (2006) Trends and rhythms in global seafloor generation rate. Geochemistry, Geophysics, Geosystems 7(3)

Coleman D, Glazner A, Miller J, Bradford K, Frost T, Joye J, Bachl C (1995) Exposure of a Late Cretaceous layered mafic-felsic magma system in the central Sierra Nevada Batholith, California. Contributions to Mineralogy and Petrology 120(2):129-136

Costa KM, McManus JF, Middleton JL, Langmuir CH, Huybers PJ, Winckler G, Mukhopadhyay S (2017) Hydrothermal deposition on the Juan de Fuca Ridge over multiple glacial–interglacial cycles. Earth and Planetary Science Letters 479:120-132

Crowley JW, Katz RF, Huybers P, Langmuir CH, Park S-H (2015) Glacial cycles drive variations in the production of oceanic crust. Science 347(6227):1237-1240

DeCelles PG, Ducea MN, Kapp P, Zandt G (2009) Cyclicity in Cordilleran orogenic systems. Nature Geoscience 2(4):251-257

DeCelles PG, Graham S (2015) Cyclical processes in the North American Cordilleran orogenic system. Geology 43(6):499-502

Decker M, Schwartz J, Stowell H, Klepeis K, Tulloch A, Kitajima K, Valley J, Kylander-Clark A (2017) Slab-triggered arc flare-up in the Cretaceous Median Batholith and the growth of lower arc crust, Fiordland, New Zealand. Journal of Petrology 58(6):1145-1171

Ducea MN (2001) The California arc: Thick granitic batholiths, eclogitic residues, lithospheric-scale thrusting, and magmatic flare-ups. GSA today 11(11):4-10

Ducea MN, Paterson SR, DeCelles PG (2015) High-volume magmatic events in subduction systems. Elements 11(2):99-104

Ferguson DJ, Li Y, Langmuir CH, Costa KM, McManus JF, Huybers P, Carbotte SM (2017) A 65 ky time series from sediment-hosted glasses reveals rapid transitions in ocean ridge magmas. Geology 45(6):491-494

Frei R, Polat A (2007) Source heterogeneity for the major components of~ 3.7 Ga Banded Iron Formations (Isua Greenstone Belt, Western Greenland): tracing the nature of interacting water masses in BIF formation. Earth and Planetary Science Letters 253(1-2):266-281

Frost TP (1987) Sample localities, radiometric ages, descriptions, and major-and trace-element abundances of Late Jurassic mafic plutonic rocks, eastern Sierra Nevada, California. Department of the Interior, US Geological Survey,

Gast PW (1968) Trace element fractionation and the origin of tholeiitic and alkaline magma types. Geochimica et Cosmochimica Acta 32(10):1057-1086

Glazner AF, Manley CR, Marron J, Rojstaczer S (1999) Fire or ice: Anticorrelation of volcanism and glaciation in California over the past 800,000 years. Geophysical Research Letters 26(12):1759-1762

Huybers P, Langmuir C (2009) Feedback between deglaciation, volcanism, and atmospheric CO2. Earth and Planetary Science Letters 286(3-4):479-491
Jagoutz O (2014) Arc crustal differentiation mechanisms. Earth and Planetary Science Letters 396:267-277

Kay R, Hubbard N, Gast P (1970) Chemical characteristics and origin of oceanic ridge volcanic rocks1. Journal of Geophysical Research 75(8):1585-1613

Khan R, Naqvi S (1996) Geology, geochemistry and genesis of BIF of Kushtagi schist belt, Archaean Dharwar Craton, India. Mineralium Deposita 31(1-2):123-133
Klein BZ, Jagoutz O (2021) Construction of a trans-crustal magma system: Building the Bear Valley Intrusive Suite, southern Sierra Nevada, California. Earth and Planetary Science Letters 553:116624

Klein C (2005) Some Precambrian banded iron-formations (BIFs) from around the world: Their age, geologic setting, mineralogy, metamorphism, geochemistry, and origins. American Mineralogist 90(10):1473-1499

Langmuir CH, Forsyth DW (2007) Mantle melting beneath mid-ocean ridges. Oceanography 20(1):78-89

Lee C-TA, Cheng X, Horodyskyj U (2006) The development and refinement of continental arcs by primary basaltic magmatism, garnet pyroxenite accumulation, basaltic recharge and delamination: insights from the Sierra Nevada, California. Contributions to Mineralogy and Petrology 151(2):222-242

Lund D, Asimow P, Farley K, Rooney T, Seeley E, Jackson E, Durham Z (2016) Enhanced East Pacific Rise hydrothermal activity during the last two glacial terminations. Science 351(6272):478-482

Lund DC, Asimow PD (2011) Does sea level influence mid-ocean ridge magmatism on Milankovitch timescales? Geochemistry, Geophysics, Geosystems 12(12)

Lund DC, Seeley EI, Asimow PD, Lewis MJ, McCart SE, Mudahy AA (2018) Anomalous Pacific-Antarctic Ridge Volcanism Precedes Glacial Termination 2. Geochemistry, Geophysics, Geosystems 19(8):2478-2491

McCart SE (2020) Assessing the Sea Level Hypothesis with Hydrothermal and Volcanic Ash Records from the East Pacific Rise and Pacific-Antarctic Ridge. Master's Thesis, University of Connecticut

Middleton JL, Langmuir CH, Mukhopadhyay S, McManus JF, Mitrovica JX (2016) Hydrothermal iron flux variability following rapid sea level changes. Geophysical Research Letters 43(8):3848-3856

Paterson SR, Okaya D, Memeti V, Economos R, Miller RB (2011) Magma addition and flux calculations of incrementally constructed magma chambers in continental margin arcs: Combined field, geochronologic, and thermal modeling studies. Geosphere 7(6):1439-1468

Pegler S, Ferguson D (2020) Rapid heat discharge during deep-sea eruptions generates megaplumes and disperses tephra.

Ratajeski K, Glazner AF, Miller BV (2001) Geology and geochemistry of mafic to felsic plutonic rocks in the Cretaceous intrusive suite of Yosemite Valley, California. Geological Society of America Bulletin 113(11):1486-1502

Rudnick RL (1995) Making continental crust. Nature 378(6557):571-578
Schwartz JJ, Klepeis KA, Sadorski JF, Stowell HH, Tulloch AJ, Coble MA (2017) The tempo of continental arc construction in the Mesozoic Median Batholith, Fiordland, New Zealand. Lithosphere 9(3):343-365

Schwartz JJ, Klepeis KA, Sadorski JF, Stowell HH, Tulloch AJ, Coble MA (2017) The tempo of continental arc construction in the Mesozoic Median Batholith, Fiordland, New Zealand. Lithosphere 9(3):343-365

Sisson T, Grove T, Coleman D (1996) Hornblende gabbro sill complex at Onion Valley, California, and a mixing origin for the Sierra Nevada batholith. Contributions to Mineralogy and Petrology 126(1-2):81-108

Tolstoy M (2015) Mid-ocean ridge eruptions as a climate valve. Geophysical Research Letters 42(5):1346-1351

Weatherley SM, Katz RF (2016) Melt transport rates in heterogeneous mantle beneath mid-ocean ridges. Geochimica et Cosmochimica Acta 172:39-54

CHAPTER 2

Evidence for Polybaric Fractional Crystallization in a Continental Arc: Hidden Lakes Mafic Complex, Sierra Nevada Batholith, California

2.1 ABSTRACT

Many studies investigate the voluminous granitoids found in the upper crust of continental arcs, but comparatively few focus on the origin of mafic bodies intruded to similar crustal levels. We present field and petrographic observations, geochronology, and geochemistry of the Hidden Lakes mafic complex in the central Sierra Nevada batholith. This complex comprises norites, gabbros, monzondiorites, and monzonites that document fractional crystallization of a hydrous (~3 wt.% H_2O) high-Al, non-primitive basalt within the upper crust (0.3 GPa) of a paleo-continental arc at c. 95-96 Ma. To quantitatively model the generation of the parental basalt and the observed lithologies, we construct a two-stage polybaric crystallization model using both thermodynamic and mass balance modeling based on bulk-rock data. First, a primitive, mantle-derived basalt fractionally crystallizes 33% (by mass) in the lower crust (1.1 GPa), generating dominantly pyroxenite cumulates. The remaining melt ascends to the upper crust where it fractionates further to produce the observed norites through monzonites within the Hidden Lakes mafic complex. Extension of this model to higher-silica melt compositions (>65 wt.% SiO_2) replicates observed granodiorite compositions in the batholith, suggesting that polybaric crystallization may be an important process for the generation of granitoid melts. The depth of differentiation in continental arcs is debated, as field observations indicate abundant lower crustal fractionation while experimental data suggests that high-pressure crystallization cannot produce the observed non-peraluminous granitoid compositions. Our model resolves this inconsistency, supporting fractionation in both the lower and upper crust and identifying a process for the evolution of continental arc melts.

2.2 INTRODUCTION

The generation of batholith-scale granodiorite intrusions in continental arc settings is an

unresolved problem, as differentiation mechanisms produce only small volumes of granitic melt (~10-20% of original melt mass) in comparison to much greater volumes of ultramafic and mafic cumulates or restites (Jagoutz and Klein 2018; Kay and Kay 1985; Soesoo 2000). However, lower crustal mafic and ultramafic cumulates are ubiquitous in magmatic arcs exhumed to 30-55 km depths (Debari and Sleep 1991; Greene et al. 2006; Guo et al. 2020; Jagoutz 2014; Otamendi et al. 2012; Walker et al. 2015) and may be brought to the surface as xenoliths in active volcanic arcs (Arai and Ishimaru 2008; Debari et al. 1987). Therefore, magmatic differentiation by lower crustal fractional crystallization of hydrous basalts is considered an important process in the formation of granodiorites and granites characteristic of the upper crust (Greene et al. 2006; Guo et al. 2020; Jagoutz 2014; Otamendi et al. 2012; Walker et al. 2015). Experimental studies (Müntener et al. 2001; Müntener and Ulmer 2018; Nandedkar et al. 2014; Sisson et al. 2005; Ulmer et al. 2018) and thermodynamic modeling (Annen et al. 2006; Jagoutz and Klein 2018) also support the hypothesis that deep (>0.7 GPa) differentiation of hydrous basalts can produce high-silica melts.

However, detailed experimental high-pressure crystallization studies suggest that differentiation in the deep crust cannot be solely responsible for the compositional stratification observed in arcs. Crystallization of hydrous primitive basalts in the lower crust (i.e. >0.7 GPa) produces peraluminous andesites, which are not observed in arc batholiths (Blatter et al. 2013; Cawthorn and Brown 1976; Cawthorn and O'Hara 1976; Müntener and Ulmer 2018; Nandedkar et al. 2014; Ulmer et al. 2018). Though the experimental basalts used in some of these studies are Al-enriched, their starting compositions are within the range of observed primitive arc basalts, as compiled by Schmidt and Jagoutz (2017). At lower crustal pressures or high water contents, suppression of plagioclase and abundant early clinopyroxene crystallization drives residual melts

towards peraluminous compositions (i.e., ASI > 1.1 where ASI = molar Al/(Ca-1.67×P+Na+K). In contrast, at lower pressures (<0.7 GPa) and/or lower water contents plagioclase will saturate in a basalt at higher temperatures, limiting the Al-enrichment in a crystallizing melt. The discrepancy between high-pressure experimental studies and the rock record implies that differentiation in arcs is not a simple story of high-pressure differentiation.

Thus, there are two observations that must be reconciled: (1) lower crustal arc sections dominated by ultramafic to mafic cumulates indicating the importance of deep crustal fractional crystallization and (2) experimental crystallization studies suggesting that although high-silica melts can be produced at these pressures, they will become peraluminous at relatively low SiO_2 contents (<60 wt.%), a feature not observed in arc batholiths. Two processes have been proposed to explain this apparent contradiction; (1) polybaric differentiation and (2) mixing between low-Mg basaltic and granitic melts (e.g., Sisson et al. 1996; 2005; Grove et al. 2003; Blatter et al. 2013; Müntener and Ulmer 2018). Both of these processes require the presence of an evolved (i.e., low-Mg) basalt produced through lower crustal differentiation of a more primitive, high MgO basalt. This low-Mg basalt can either ascend into the upper crust to differentiate further, producing non-peraluminous silicic melts, mix with granitic melts (formed through fractional crystallization or partial melting), or both, to produce granodioritic magmas.

To test whether these processes play an important role in the generation of arc batholiths, this paper focuses on an upper crustal mafic complex in a continental arc batholith. Although less common than voluminous silicic plutons, upper crustal mafic intrusions potentially preserve information on the nature and origin of low-Mg basalts in the formation of arc batholiths. In addition, investigation of mafic, rather than evolved, intrusions avoids complications of extensive fractionation and mixing that may obscure the effects of lower crustal processes. Here,

we undertake a case study of Hidden Lakes mafic complex (HLMC), an exposure of cumulate norite and gabbro through melt-like monzonite sequence in the upper crust of the Sierra Nevada batholith. We present detailed field mapping to document intrusive relationships and the range of mafic lithologies. We undertake U-Pb zircon geochronology in order to constrain the timing of crystallization of the HLMC relative to surrounding granodiorites and granites. Using bulk-rock and mineral chemistry data, as well as comparisons to experimental studies, we aim to constrain crystallization pressures, temperatures, H_2O content, and oxygen fugacity (fO_2) of the crystallizing magma. As field, petrographic, and geochemical data suggest a fractional crystallization origin for the HLMC, we construct a two-stage polybaric fractionational crystallization model to replicate the composition of the evolving melt. In light of our findings, we discuss the importance of evolved basalts in the formation of high-silica arc batholiths.

2.2.1 Geologic Setting

The HLMC is located in the eastern central Sierra Nevada batholith (SNB), the largely granodioritic intrusive product of the Sierra Nevada paleo-continental arc. From the Late Triassic through Late Cretaceous, magmatism related to subduction of the Farallon plate beneath North America produced felsic intrusions that now form the bulk of the batholith. Magmatism ceased by 80 Ma due to shallowing of the subduction angle (English et al. 2003; Kirsch et al 2016). Presently, most of the SNB is exposed to upper crustal depths (0.2 to 0.4 GPa), with the exception of the southernmost lower crustal section which extends to 1.0 GPa pressures (Ague and Brimhall 1988; Pickett and Saleeby 1993). The Late Jurassic (145-160 Ma) and late Cretaceous (85-100 Ma) periods in the SNB are characterized by enhanced magmatic activity, during which of 85% of the batholith volume was generated (DeCelles et al. 2009; Ducea et al.

2015; Kirsch et al. 2016).

Numerous mafic bodies throughout the SNB upper crust were noted during early studies of the batholith (Bateman and Eaton 1967; Frost 1987; Mayo 1941), but have been less comprehensively studied as compared to the felsic batholith due to their relatively small areal fraction of the exposed SNB. Early workers in the Sierra Nevada batholith described them as "basic forerunners" based on field relationships suggesting that they were emplaced prior to the volumetrically dominant granitoids (Bateman and Eaton 1967; Mayo 1941; Ross 1989). Subsequent geochronological studies on a few of the mafic bodies, however, demonstrated that they are coeval with the surrounding granitoids and therefore may play a critical role in the formation of the granitoid batholith (Coleman et al. 1995; Ratajeski et al. 2001). Several mafic bodies have been investigated in previous studies (Coleman et al. 1995; Frost 1987; Frost and Mahood 1987; Ratajeski et al. 2001; Sisson et al. 1996), all of which document the presence of hydrous, low-Mg basalts in the upper crust of the SNB.

2.3 FIELD RELATIONSHIPS

The Hidden Lakes mafic complex (HLMC) is exposed in the central SNB near Bishop, CA, and covers an area of 2.5 km^2. Our field mapping (Fig 1) refines the outer margins of the mafic complex where it is in contact with surrounding granodiorite plutons, as previously mapped by Bateman (1992), and displays the variation in rock types and the nature of contacts within the mafic complex. Amphibole- and biotite-bearing medium- to fine-grained gabbros are the dominant lithology throughout HLMC. Smaller bodies of coarse-grained and poikilitic (i.e., "spotted") gabbros are present throughout the medium to fine-grained gabbro. Norites and biotite-bearing anorthosites occur as small pods within the gabbro in the eastern section of

HLMC. In the northeastern section of HLMC, near its contact with the Round Valley Peak granodiorite, lithologies grade transitionally from gabbro to monzodiorite to monzonite toward the northern edge of the mafic complex. The interiors of rocks are minimally altered and lack macroscopic evidence for deformation, except for thin (< 5 mm) epidote veins that were avoided during sampling. The field occurrences and macroscopic characteristics of each rock type in the mapped area are described in detail below.

2.3.1 Norites

Norites are the most primitive lithology found in HLMC and are present as small, rounded pods (up to 3 m in diameter) within the gabbro unit in the eastern section of the complex (Fig 2a). Their volumetric abundance within the gabbro is difficult to ascertain due to exposure on steep cliff faces, however, they weather out and occur as large boulders in the scree fields to the west of the cliffs. Norite boulders are significantly less abundant in scree fields than gabbro boulders, so it is presumed that norite is less common than gabbro in the cliffs. Surface alteration in norite samples is recognizable as rusty olivine and pyroxenes, as well as actinolite present along grain boundaries.

2.3.2 Anorthosites

Anorthosite was observed only in boulders below gabbro-dominated cliffs in the southeastern section of HLMC (Fig1). The anorthosite is medium-fine grained (0.5-2 mm), isotropic, and texturally homogenous, containing 90 to 95% dark grey plagioclase and 5 to 10% biotite.

2.3.3 Gabbros

Amphibole-biotite gabbro is the volumetrically dominant rock type in HLMC and is present in most areas of the mafic complex, except for the northern margin characterized by more evolved lithologies (Fig 1). The gabbros contain abundant plagioclase and amphibole, along with common clinopyroxene and biotite, and minor orthopyroxene. Based on their macroscopic textures, the gabbros are divided into three main groups: (1) medium-fine grained gabbro, (2) coarse-grained gabbro, and (3) "spotted" gabbro (Fig 2b, 2c).

Medium-fine grained gabbro is the most common rock type in HLMC and contains dark gray plagioclase, amphibole, and pyroxene of roughly equal size (1-3 mm crystals) with evenly distributed finer grained biotite flakes (~1 mm).

The coarse-grained gabbro is present in elongate bodies within and interfingering with the medium-fine grained gabbro. These bodies are up to 250 m long and 100 m wide (Fig 1) and their long axes trend approximately north-south. The mineral assemblage in this textural type is identical to the medium-fine grained gabbros, with slightly less plagioclase. Plagioclase in this textural type is light gray in color, making the rocks appear lighter than the medium-fine grained gabbro despite higher proportions of dark-colored amphibole, biotite, and clinopyroxene.

The "spotted" gabbro is located in two elongate bodies, up to 400 m long and 150 m wide (Fig 1). This texture is characterized by 1-2 cm clots of poikilitic amphibole+biotite enclosing pyroxene and minor plagioclase, which give it a spotted surface appearance (Fig 2b). Roughly 35% of this lithology is composed of clots, which are enclosed in a matrix (1-3 mm grain size) that is very similar to the medium-fine grained gabbro.

Contacts between the different textural gabbroic units can be gradational over 1 to 5 m, or can exhibit mingling textures as shown in Figure 2c and 2d. The elongate intrusion geometry is

evident in the western and southern areas of HLMC, while the eastern section appears to be a single large intrusion composed mainly of medium-fine grained gabbro that grades into monzodiorite, as described in the following section.

2.3.4 Monzodiorites and Monzonites

In the northeastern section of HLMC, two bodies of monzodiorite and two elongate bodies of monzonite are in largely gradational contact with one another over >5 m. Dikes (4-10 cm wide) occur within rare sections of the contact where these lithologies are mutually intrusive and angular xenoliths of gabbro (5-20 cm) can be found in the monzodiorite (Fig 3a). In addition, mingling textures between the monzonite and monzodiorite, as well as dikes of monzonite intruding into monzodiorite, and vice versa, are present. Thus, these are synmagmatic lithologies that were mobilized shortly after crystallization of the northeastern section of gabbro.

The monzodiorites are medium-fine grained, dominated by plagioclase, and contain biotite, K-feldspar, amphibole, and interstitial quartz in order of decreasing abundance. Rare clinopyroxene is present in the cores of amphibole grains. The monzonites are typically medium to coarse grained, with plagioclase crystals and clusters of biotite crystals (both 4 to 6 mm) and smaller amphibole often associated with the biotite. K-feldspar is more common than in the monzodiorites, and quartz is typically minor (< 5%) and interstitial.

2.3.5 Diabase Bodies

Generally small, irregularly shaped bodies of diabase, as well as diabase dikes, are present within and near HLMC. Intrusions are fine grained (<1 mm) with slightly larger biotite flakes (5% modally, 1-2 mm) and rarely contain blocks of HLMC gabbro. Contacts between the

diabase and the mafic complex are sharp, in contrast with the generally gradational contacts between the coarser grained lithologies. Diabase dikes are <40 cm in width, fine-grained, and biotite-rich. Similar dikes are present in the adjacent Lake Edison granodiorite, though it is unclear if dikes that intrude granodiorite are the same generation as those that intrude the HLMC. Yet, the sharp contacts between diabase bodies and the gabbroic rocks suggest that the diabase is younger than much of HLMC.

2.3.6 Leucogranite Pods and Dikes

Late stage leucocratic rocks, while not abundant, are present within the study area and sharply crosscut contacts within HLMC. These lithologies are K-feldspar- and quartz-rich, occasionally containing minor biotite, and have widely variable grain sizes. Sub-meter scale aplite dikes are equally common within the mafic complex and in the surrounding granodiorite plutons, and therefore likely intruded in a late stage event unrelated to the evolution of the HLMC magmatic system.

2.3.7 Surrounding Felsic Plutons and Outer Contacts

Three felsic intrusions are in contact with HLMC around its perimeter: the granite of Chickenfoot Lake to the west and south, the Lake Edison granodiorite to the east, and the Round Valley Peak granodiorite (Krv) to the north (Fig 1).

The granite of Chickenfoot Lake (Jcf, 191.6 ± 1.0 Ma, this study) is medium-coarse grained, unfoliated, and comprises (in decreasing abundance) albite, quartz, amphibole, coarse orthoclase (1 cm), and minor biotite. K-feldspar crystals can reach 1.5 cm, while all other major minerals are < 1 cm. Diorite dikes originating from HLMC inrtude into Jcf. Where observed, the

contact between Jcf and HLMC is a 0.1 to 1 m wide gradational zone of dioritic composition that occasionally includes coarse orthoclase xenocrysts, which are not present in the adjacent gabbros and so presumably originated as crystals in Jcf (Fig 3b).

The Lake Edison granodiorite (Kle, 90.9 Ma; Lackey et al. 2008) is a medium-grained biotite-amphibole granodiorite with macroscopic (1-2 mm) titanite, consistent with previous descriptions of Kle (Bateman 1992). Kle intruded HLMC on its eastern side, though the majority of this contact is within the cliffs on the western flanks of Mount Morgan, and so was only observed at a single location. The contact is subvertical and sharp, with Kle truncating layering in HLMC.

The Round Valley Peak granodiorite (Krv, 88.8 Ma; Lackey et al. 2008) is a medium-fine grained equigranular granodiorite containing biotite and amphibole in roughly equal proportions. Small (< 5 cm) mafic enclaves are common in this unit and are elongated parallel to the contact between Krv and HLMC. Krv forms a complicated contact zone (which we call the Heterogeneous Intrusive Zone) where it intrudes the northeastern margin of HLMC, described below.

2.3.8 Heterogeneous Intrusive Zone

The east-west trending contact between Krv and HLMC is a 150 m wide contact zone, which we term the Heterogeneous Intrusive Zone (HIZ). This zone consists of 50 to 85% Krv granodiorite that has entrained angular to subangular blocks of gabbro, monzodiorite, and monzonite. Mafic blocks vary in size (5 cm-10 m) and angularity with the most angular blocks present on the southern margin of HIZ. Blocks become progressively more rounded and partially digested towards the north (Fig 3c). Mafic magmatic enclaves typical of Krv and rare

metsedimentary xenoliths are also found in the HIZ. Meter to sub-meter scale dikes of the Krv intrude the HLMC immediately south of the HIZ, and sometimes contain angular xenoliths of gabbros, monzodiorites, and monzonites from the HLMC (Fig 3d). Blocks within these dikes vary in terms of their modal mineralogy and do not always match the wall rock of the dike, indicating potentially significant magmatic transport of the HLMC-sourced blocks. Along the southern section of the HIZ, closest to HLMC, the matrix surrounding mafic blocks is a mingled granodiorite and quartz-monzonite (Fig 3e). The quartz-monzonite is medium-fine grained and therefore texturally similar to the Krv, in contrast to the coarser grained monzonites of the HLMC, but has a higher abundance of biotite (up to 20%) than Krv. The quartz-monzonite appears to be a portion of the Krv felsic melt that digested small amounts of mafic material during intrusion of the Krv, resulting in a hybridized lithology.

2.4 PETROGRAPHY

Descriptions of 28 representative samples in thin section are given below, with at least three sections from each rock type. Modal percent of major minerals were estimated by eye (Table 1) and grain size ranges include all observations of a particular phase in each lithology.

2.4.1 Norites

The norites consist of orthopyroxene (15-75%), plagioclase (15-40%), amphibole (0-20%), biotite (5-15%), clinopyroxene (1-5%) and olivine (<1%), along with minor Fe-Ti oxides and accessory apatite and zircon. Norite samples exhibit ad- and mesocumulate textures with rounded orthopyroxene grains that range in size from 50 to 600 μm (Fig 4a). All samples contain interstitial plagioclase and few contain euhedral plagioclase crystals ranging from 0.2 to 3 mm,

which are infrequently seriticized. Amphibole is not present in all samples but was observed in 6 out of 7 thin sections. It occurs as either large oikocrysts (1 cm) enveloping orthopyroxene and plagioclase ± olivine (Fig 4b), or as overgrowths on orthopyroxenes and clinopyroxenes (Fig 4c). Amphibole-rimmed pyroxenes are present in all norites containing amphibole, while amphibole oikocrysts are found in only two samples. Late crystallizing biotite (0.4-2 mm) fills interstitial spaces and surrounds rounded orthopyroxenes. Olivine was observed in two samples, and crystals (0.2-1 mm) are only present as inclusions in amphibole oikocrysts, which also contain inclusions of orthopyroxene (Fig 4b). Minor Fe- and Fe-Ti-oxides are included in orthopyroxene and plagioclase. The inferred crystallization sequence of major minerals is: olivine → orthopyroxene + Fe- and Fe-Ti-oxides ± clinopyroxene → plagioclase ± amphibole → plagioclase + biotite.

2.4.2 Gabbros

The relative proportions of mineral phases in the medium-fine grained gabbros are variable, with the following ranges: plagioclase 65 to 75%, amphibole 5 to 20%, clinopyroxene 5 to 15%, biotite 5 to 10%, and orthopyroxene ~5%. The coarse-grained gabbros contain plagioclase (45-70%), amphibole (25-50%), clinopyroxene (5-20%), and biotite (5-10%). The spotted gabbros consist of 35% amphibole clots surrounded by a matrix of the medium-fine grained gabbro.

Gabbros with both cumulative and non-cumulative textures are present in HLMC. Coarse-grained and spotted gabbro samples, as well as some of the medium-fine grained gabbros, preserve textural evidence for accumulation of plagioclase and clinopyroxene. These meso- to adcumulate samples are dominated by equant, nearly euhedral plagioclase (0.5-4 mm)

and rounded clinopyroxene (0.5-3 mm) crystals. Orthopyroxene is far less prevalent than clinopyroxene but has similar morphology, and both pyroxenes commonly contain exsolution lamellae and have thin rims (10-30 μm) of very fine-grained actinolitic amphibole. Amphibole is present as a primary magmatic phase, secondary magmatic rims nucleated on pyroxenes, and as psuedomorphs after pyroxene. These are distinguished by color and texture, as magmatic amphiboles have a brown to honey color and few micro-inclusions, while secondary magmatic rims and pseudomorphic amphiboles are green. The pseudomorphs contain numerous small plagioclase and quartz inclusions (<10 μm) that give the crystals a cloudy appearance (Fig 4d and 4e). Biotite is a late crystallizing interstitial phase and very irregularly shaped, containing inclusions of clinopyroxene, plagioclase, and Fe-Ti-oxides.

A subset of the medium-fine grained gabbros contain clinopyroxene (50-300 μm) enclosed within an interlocking framework of subhedral to anhedral randomly oriented feldspars. These samples contain only ~5% amphibole and 5-10% biotite, which is a much lower proportion of these minerals than in other HLMC gabbros (Fig 4f).

The crystallization sequence observed in the gabbros is very similar to that of the norites, but with minimal orthopyroxene crystallization and lacking olivine, as follows: Fe-Ti oxides → clinopyroxene ± orthopyroxene → plagioclase + amphibole → plagioclase + biotite. Exsolution of pyroxene end members and the recrystallization of pyroxenes to pseudomorphic amphibole occurs with slow cooling after initial crystallization.

2.4.3 Monzodiorites and Monzonites

The monzodiorites and monzonites of HLMC are distinguished from the gabbros by a decreased abundance of pyroxene, though many monzodiorites contain pseudomorphs of

pyroxene altered to amphibole. These pseudomorphs occasionally have ortho- and clinopyroxene cores. The monzodiorites consist of 60 to 70% plagioclase, 15 to 20% biotite, 10 to 15% K-feldspar, 5 to 15% amphibole, <2% quartz, and minor ortho- and clinopyroxene (0- 2%). In the monzodiorites, plagioclase crystals are subhedral to anhedral and up to 5 mm in length. K-feldspars (1-3 mm) are irregularly shaped with concave outward rounded edges, associated with minor interstitial quartz. All three occurrences of amphibole are common (primary magmatic, secondary magmatic, and pseudomorphic), but in contrast to the gabbros, any may appear green in this lithology. Primary magmatic amphiboles are green or brown in plain polarized light, do not contain abundant micro-inclusions, have regular cleavage planes, and are approximately the same grain size as the feldspars. Secondary magmatic amphiboles are varying shades of green, and either exist as masses of many small (50-100 μm) subhedral crystals or as rims on pyroxenes and pseudomorphic amphiboles. Pseudomorphs are green cloudy crystals containing abundant micro-inclusions, as in the gabbros. Amphibole, biotite, and Fe-Ti-oxides are often found together in 1-3 mm clots, which appear to have originated around a pyroxene grain that has been converted to amphibole (Fig 4g). Crystallization occurred in the following sequence: Fe-Ti-oxides ± clinopyroxene (later converted to amphibole) → amphibole + plagioclase → plagioclase + amphibole + biotite → plagioclase + K-feldspar → K-feldspar + quartz.

The monzonites contain 40 to 60% plagioclase, 20 to 35% K-feldspar, 10 to 20% biotite, 0 to 5% amphibole, and minor quartz (<5%). Euhedral to subhedral primary magmatic amphibole grains (0.3-1.5 mm) lie between generally coarse anhedral plagioclase and K-feldspars (Fig 4h). Rare ortho- and clinopyroxene cores are present in < 5% of amphiboles. Irregularly shaped flakes of biotite (0.5- 2 mm) are packed between plagioclase crystals and can be included in K-feldspars. Quartz (up to 0.5 mm) occurs interstitially. Monzonite crystallization

continues from the monzodiorite crystallization sequence: Fe-Ti-oxides + amphibole → plagioclase + amphibole + biotite → plagioclase + K-feldspar → K-feldspar + quartz.

2.5 ANALYTICAL METHODS

2.5.1 Zircon U-Pb Geochronology and Trace Elements

Samples were selected for potential analyses of zircon based on bulk-rock Zr concentrations >120 ppm (see XRF methods below). Samples were crushed and sieved to 105-250 μm. After washing, the magnetic fraction was removed using a Frantz magnetic separator. Heavy minerals were separated from the non-magnetic fraction using LST heavy liquid, and single zircon grains were hand-picked under a binocular microscope, mounted in epoxy, and polished for analysis. Zircon was separated from six mafic samples and one granite. Each grain was imaged for cathodoluminescence response on the Zeiss 1550 VP scanning electron microscope at Caltech. Grains typically do not contain partially resorbed cores. Rare apatite inclusions were identified and avoided during ablation.

Zircons from 6 samples were analyzed using laser-ablation split-stream inductively coupled mass spectrometry (LA-ICPMS) at the University of California, Santa Barbara to collect U and Pb isotopic ratios and trace element concentrations, following the methods of Kylander-Clark et al. (2013). Grains were ablated using a Photon Machines Analyte 193 nm excimer laser operating with a 30 μm spot diameter, 4 Hz frequency, 3.5 J/cm^2 fluence, and 100 shots per analysis. U and Pb isotopes were measured on a Nu Instruments Plasma HR-ES multicollector ICPMS, and trace elements (Ti, Y, Nb, REE, and Hf) were simultaneously measured on an Agilent 7700x quadrupole ICPMS. To correct for down-hole fractionation and instrumental drift, zircon standards 91500 and GL-1 were used as the primary and secondary standards,

respectively, and analyzed after every 8 unknown spots. Isotope ratios, individual grain ages, analytical uncertainties, and drift corrections were calculated using the Iolite data reduction software.

U-Pb isotopic data of zircon from one granitic sample (Jcf, sample SNB-18-2) were measured via LA-ICPMS at the Arizona Laserchron Center following the methods of Pullen et al. (2018). Analyses were collected using a Photon Machines 193 nm G2 laser coupled to a Thermo Scientific Element2 HR single collector ICPMS. Laser conditions were a 30 μm spot diameter, 7 Hz frequency, 7 J/cm^2 fluence, and 380 shots per analysis. Primary standards FC and SL were placed between every 5 unknown analyses and used to correct for instrument drift and down-hole fractionation. A secondary standard R33 was interspersed between every 20 to 30 analyses. AgeCalc (Gehrels et al. 2008) was used to reduce the data.

In both analytical facilities, laser spots were placed near grain rims and analyses with concordance ($[^{206}Pb/^{238}U]_{age}/[^{207}Pb/^{235}U]_{age}$) < 95% were discarded, resulting in 25-50 acceptable analyses per sample. Crystallization ages were calculated in IsoplotR (Vermeesch 2018) as an error-weighted mean of individual spot ages for each sample, and reported uncertainties are 2 sigma of acceptable single-grain ages in each sample.

2.5.2 Bulk-rock Major and Trace Element Analyses

58 samples were analyzed for bulk-rock compositions. Samples for bulk-rock analysis were sawed to remove any potentially altered surfaces or veining. To ensure homogeneity, ~0.5-1 kg of rock was crushed for each sample depending on the grain size and powdered in an agate ball mill. 33 samples were analyzed for major and trace element analysis via XRF and ICPMS at the Peter Hooper Geoanalytical Lab at Washington State University following methods in

Johnson, et al. (1999) and further detailed on the WSU GeoAnalytical Lab website (environment.wsu.edu/facilities/geoanalytical-lab/technical-notes/icp-ms-method).

The remaining 25 samples were analyzed at Caltech. Powders were dried overnight at 110 °C, then heated to 1050 °C for one hour to determine loss on ignition (LOI). Glass beads were prepared using a 10:1 mass ratio of Li-borate flux to sample powder and fused at 1200 °C. Major elements (Si, Ti, Al, Fe, Mn, Mg, Ca, Na, K, P) in the glass beads were analyzed using a Panalytical Zetium wavelength-dispersive X-ray fluorescence (XRF) spectrometer following methods in Bucholz and Spencer, (2019). A comprehensive suite of trace elements (Cr, Ni, Rb, Sr, Y, Zr, Ba, Nb, Cs, all REEs, Hf, Ta, Pb, Th, U) was then measured via solution ICPMS. Chips (25±1 mg) of shattered glass beads used in XRF analyses were weighed into polypropylene tubes and digested in 2 mL of a 3:1 mixture of concentrated nitric and hydrofluoric acids in a heating block at 99 °C for 8 hours. The resulting solutions were diluted to a 30 mL final volume with 2% nitric acid. Calibration standard solutions made from Li-borate beads using USGS standard powders and a blank flux bead were prepared under the same method. Sample and calibration standard solutions were analyzed on an Agilent 8800 triple quadrupole ICPMS at Caltech. An internal standard solution consisting of Ga, In, Re, Rh, and Bi, as well as a quality control solution made from a mixture of the sample solutions, was used to monitor and correct for time- and mass-dependent analytical drift. Calibration curves were constructed in the MassHunter software and used to calculate elemental concentrations in the samples. Calibration standards were the USGS powders AGV-2, GSP-2, BCR-2, and RGM-2, and composition values used were taken from the GeoREM database preferred values (Jochum et al. 2005).

2.5.3 Mineral Chemistry

Major element compositions of olivine, ortho- and clinopyroxene, amphibole, biotite, feldspars, and Fe-Ti oxides from 22 samples were analyzed using the JEOL JXA-8200 electron probe micro-analyzer (EPMA) at Caltech. For common minerals, between 10 and 25 points per phase per sample were analyzed to ensure collection of a representative suite of compositions. If mineral abundance was low in a particular sample, fewer points may have been analyzed (3 to 9 points). Analysis point locations were selected to measure both cores and rims of potentially zoned crystals (at least 3 points per grain where size allowed). Operation conditions were a 25 nA beam current, a 15 kV acceleration voltage, and a focused beam diameter (<1 μm). Standards used were synthetic forsterite, fayalite, Mn-olivine, anorthite, F-phlogopite, TiO_2, and Cr_2O_3, and natural standards Amelia albite, Asbestos microcline, Durango apatite, and sodalite. On-peak counting times for each element were 20 s. We use a mean atomic number (MAN) background correction and CITZAF matrix correction program (Armstrong 1995) for data reduction. Detection limits were <0.008 wt% for Si, Al, Mg, K, Cl, and P, and 0.01-0.02 wt% for Ti, Fe, Ca, Na, Cr, and F.

2.6 RESULTS

Zircon U-Pb isotopic measurements, bulk-rock major and trace element concentrations, and mineral chemistry data are included along with sample GPS locations in the Supplementary Data file.

2.6.1 Geochronology

All six dated samples from HLMC (locations shown in Fig 1) are late Cretaceous in age, regardless of rock type. Weighted mean crystallization ages and 2σ errors for monzondiorite samples are 95.1 ± 1.0 Ma for SNB-16-6, 95.6 ± 0.8 Ma for SNB-16-9, and 96.5 ± 0.8 Ma for SNB-14-34. HL-17-2, an anorthosite, has an age of 95.7 ± 0.7 Ma. The monzonite ages are 96.3 ± 0.8 Ma for SNB-16-12 and 90.5 ± 0.8 Ma for SNB-14-40. These ages allow for up to 6 Ma of magmatic activity in HLMC and constrain crystallization ages of the more mafic parts of the HLMC at 5 and 7 million years older than the Lake Edison granodiorite (90.9 Ma; Lackey et al. 2008) and Round Valley Peak granodiorite (88.8 Ma; Lackey et al. 2008), respectively. HLMC is significantly younger than the granite of Chickenfoot Lake (at 191.6 ± 1.0 Ma, this study). These ages are consistent with field relationships, in which HLMC lithologies are observed intruding into Jcf and intruded by Kle and Krv. Sample SNB-14-40, a monzonite from the northern edge of the mafic complex near the contact with Krv, has a crystallization age ~5 Ma younger than the other five mafic samples (90.5 ± 0.8 Ma). This may represent a late stage melt associated with differentiation of HLMC magmas that was remobilized by intrusion of Kle, as their ages overlap within uncertainty. We presume that the gabbros and norites crystallized within the range of monzodiorte ages (95.1- 96.5 Ma), though neither of these lithologies were directly dated due to the rarity of zircon.

2.6.2 Bulk-rock Major Element Chemistry

Major element compositions from HLMC display a trend of magmatic evolution that straddles the boundary between a monzonitic series and granodioritic series (Bas et al. 1986; Middlemost 1994). For simplicity, we retain the lithology names norite, gabbro, monzodiorite

and monzonite as classified based on mineralogy in previous sections, even if all samples of one lithology do not fit precisely within a single chemically defined field (Fig 5a). SiO_2 contents from the full suite of HLMC samples range from 43.6 to 62.0 weight percent (wt.%) and molar magnesium numbers (Mg# = 100*Mg/(Mg+Fe), calculated using total Fe) range from 73.1 to 35.7 (Fig 5d). All samples from HLMC are metaluminous (ASI < 1.1, where ASI= Al/ [Ca-1.67×P+ Na+ K]).

The norites represent the most primitive cumulates to crystallize from an HLMC melt, based on their high Mg#s (73.1-64.6). The norites contain 49.8 to 53.6% SiO_2, 10.2 to 20.0 wt.% MgO, and 9.8 to 14.8 wt.% FeO. Relatively constant SiO_2 content with decreasing MgO and FeO reflects increasing abundance of plagioclase relative to orthopyroxene with progressive fractionation. Likewise, co-variation in CaO (3.0-7.7 wt.%, Fig 5c) and Al_2O_3 (4.9-12.9 wt.%) is controlled by the proportion of plagioclase relative to clinopyroxene, orthopyroxene, and olivine. To highlight the differences in mineral abundances, we separate the norites into two groups: high-Ca plagioclase-rich norites (CaO>7 wt.%) and low-Ca plagioclase-poor norites (CaO < 6 wt.%), as shown in Figure 5b. In general, the more differentiated norite samples (high-Ca group) have slightly lower SiO_2 contents, significantly lower MgO and FeO contents, and elevated TiO_2, CaO, Al_2O_3, K_2O, Na_2O as compared to the less differentiated low-Ca group. ASI varies from 0.57 to 0.72 in the norites but does not clearly correlate with SiO_2.

The sequence of gabbros through monzonites follows a trend of increasing SiO_2, K_2O, and Na_2O contents with decreasing MgO, FeO, CaO, Al_2O_3, and TiO_2 contents (Fig 5). ASI gradually increases from 0.70 to 0.96 from the gabbros to the monzonites, in accordance with a decrease in the modal abundance of calcic amphiboles relative to Al-bearing phases. Gabbros are the most voluminous rock type in HLMC and fall into two groups based on major-element

concentrations: 1) low-SiO_2 gabbros, with 43.9 to 46.8 wt.% SiO_2 and 2) high-SiO_2 gabbros, with 49.2 to 52.5 wt.% SiO_2. The low-Si gabbros have higher proportions of Fe-Ti oxides and pseudomorphic amphiboles relative to clinopyroxenes in the high-SiO_2 gabbros. High-SiO_2 gabbros also contain greater modal abundance of plagioclase. Al_2O_3 contents are significantly higher in the gabbros (17.3-23.4 wt.%) than the norites due to greater abundance of plagioclase and lower abundance of orthopyroxene. Al_2O_3 concentration peaks at 23.4 wt.% and 52.2 wt.% SiO_2, then gradually decreases with increasing silica content through the monzodiorites and monzonites. P_2O_5 content is controlled by apatite fractionation, which is low in the norites, increases in the gabbros, peaks at 0.55 wt.% in the monzodiorites, and decreases in the monzonites.

Two samples from cross-cutting diabase dikes and pods are shown to have very different Mg#s (64.1 and 42.6) despite similar SiO_2 content (47.0 and 49.2 wt.%). The lower Mg# sample has considerably higher alkali (Fig 5a) and P_2O_5 (0.84 wt.%) concentrations than other HLMC samples with similar silica contents (~0.25-0.4 wt.%), so this sample is unlikely to be co-genetic with HLMC. The higher Mg# diabase is similar in composition to the least primitive norites or highest Mg# gabbros, and therefore may be related to the HLMC system.

2.6.3 Bulk-rock Trace Element Chemistry

All norite samples have low Sr concentrations (89-407 ppm) that increase with increasing modal abundance of plagioclase (Fig 5e). Higher Sr contents (705-1030 ppm) in the gabbros are reflective of higher plagioclase abundance. Sr contents in the monzodiorites (659-921 ppm) and monzonites (604-934 ppm) overlap with and extend to slightly lower values compared to the gabbros. Sr/Nd and Al/Si ratios, and Eu anomalies are positively correlated and indicate the

extent of plagioclase accumulation. Primitive mantle normalized Eu anomalies ($Eu/Eu^* = [Eu]_N / sqrt([Sm]_N \times [Gd]_N)$) are < 1 in the norites (0.45-0.78) and 0.72 to 1.46 in all other HLMC lithologies.

The norites have relatively high Ni and Cr contents (97-504 ppm and 123-551 ppm, respectively, Fig 5f), which reflect the abundance of orthopyroxene in these samples, as well as the presence of minor olivine and clinopyroxene. Ni and Cr contents are low in the low-SiO_2 gabbro group (3-24 ppm Ni, 2-21 ppm Cr), then increase slightly in the high-SiO_2 gabbros to 29 and 121 ppm, respectively and remain relatively constant in the monzodiorites and monzonites.

On primitive-mantle normalized spider diagrams (Fig 6), all samples display strong Nb and Ta depletions and Pb enrichment consistent with a subduction-related origin for the HLMC parental melts (Miller et al. 1994; Stolz et al. 1996). Most of the gabbros, particularly the low-SiO_2 gabbros, exhibit Ti enrichments as controlled by crystallization of Fe-Ti-oxides, biotite, and titanite. Significant titanium depletions are observed in the norties, as these lack titanite. Besides the norites, all lithologies display Sr enrichment, reflecting accumulation of plagioclase in higher abundances than olivine and pyroxenes. Some norites are considerably enriched in LIL elements, particularly Cs and Rb (up to 34 and 50 ppm, respectively), likely due to biotite crystallization. In the more evolved rocks and in two norites (Fig 7a, b, f-i), relative enrichments or depletions in Zr and Hf are controlled by zircon saturation, with the higher concentrations suggesting that zircon is present.

Rare earth elements (REEs) and other incompatible element concentrations (Ba, Th, Nb, Pb, Hf, Ta, U, Rb, Zr) are positively correlated with SiO_2. HREE elements are depleted relative to LREE elements in all rock types, and La/Yb ratios increase with increasing silica content, though there is significant overlap between rock types.

2.6.4 Mineral Chemistry

Olivine

Olivine is rare in HLMC and present only in two low-Ca norite samples, SNB-14-62 and SNB-14-52. The most primitive (highest Mg#) olivine analyses are found as chadacrysts within in large amphibole oikocrysts. Olivine chadycrysts have Mg#s ranging from 79.6 to 81.3, while non-chadacrystic olivine grains have Mg#s ranging from 79.0 to 79.8. Olivines have 0.28 to 0.35 wt.% MnO, which is negatively correlated with Mg# (Fig 7a).

Orthopyroxene

Orthopyroxene is abundant in the norites, occasionally present in the gabbros, and rare in the monzodiorites and monzonites where it is found only in amphibole cores. The Mg# of orthopyroxenes decreases from the norites (65.3-80.1) to the gabbros (50.5-64.9). In the monzodiorites and monzonites, compositions significantly overlap with those in the gabbros (Mg# = 48.5-59.4), suggesting that these lithologies experience an early interval of orthopyroxene crystallization followed by amphibole crystallization.

Orthopyroxene Cr_2O_3 contents generally decrease with decreasing Mg# and vary from 0.01 to 0.11 wt.% in the norites and are below detection limit to 0.03 wt.% in the gabbros, monzodiorites, and monzonites. Similarly, Al_2O_3 is positively correlated with Mg#, ranging from 0.35 to 2.1 wt.% in the norites and 0.29 to 1.1 wt.% in all other orthopyroxene-bearing lithologies. MnO increases with decreasing Mg# and varies between 0.30 and 0.55 wt.% in the norites, and 0.59 and 1.1 wt.% in the gabbros and monzodiorites. The monzonites have slightly higher orthopyroxene MnO concentrations of 0.95 to 1.2 wt.%.

Clinopyroxene

Clinopyroxene is a minor phase in the norites (<5% modal abundance), more common in the gabbros (5-15% modal abundance), and occasionally present in the cores of amphiboles in the monzodiorites and monzonites. Both orthopyroxene and clinopyroxene are found in amphibole cores in 3 out of 4 pyroxene-bearing monzodiorite and monzonite samples. In one monzonite, clinopyroxene cores present while orthopyroxene cores are absent. In the norites, clinopyroxene Mg#s range from 73.4 to 79.5 and decrease from individual grain cores to rims. Analogous to the orthopyroxenes, clinopyroxene compositions in the gabbros, monzondiorites, and monzonites are very similar to one another. In particular, the clinopyroxenes from the cumulate gabbros and the liquid-like monzondiorites overlap significantly in Mg#, which may indicate that these clinopyroxenes in HLMC may have crystallized from a basalt similar to the gabbros. Clinopyroxene Mg#s vary from 61.0 to 73.0 in the gabbros, 61.3 to 75.1 in the monzodiorites, and 60.2 to 67.9 in the monzonites. In all three of these rock types, the Mg# of clinopyroxene commonly decreases from grain cores to rims. Few exceptions (3 of 31 crystals) show slight core to rim increases in Mg# and concurrent increase in Al_2O_3 consistent with Tschermak's exchange.

Clinopyroxene Cr_2O_3 contents are roughly correlated with Mg#, ranging from 0.03 to 0.11 wt.% in the low-Ca norites, 0.02 to 0.03 wt.% in the high-Ca norites, and commonly below detection limit (~0.015 wt. %) in all other rock types, with a maximum of 0.04 wt.%. Clinopyroxene MnO content increases consistently with decreasing Mg# (from 0.18 to 0.56 wt. %). Al_2O_3 content is variable between 0.47 and 2.8 wt.%, commonly decreasing (~75% of grains) and occasionally increasing (~25% of grains) from crystal cores to rims. Al_2O_3 in clinopyroxene cores increases from the norites (0.56-1.28 wt.%) and peaks at 1.79 wt.% in the

liquid-like gabbros, then decreases through the gabbros, monzodiorites, and monzonites to 1.09 wt.%. This peak corresponds to the maximum in bulk-rock Al_2O_3 concentration.

Amphibole

Amphibole is present in all rock types in HLMC and may be a primary magmatic phase, secondary magmatic overgrowth on pyroxene crystals, pseudomorphic replacement of pyroxene due to reaction with an evolving melt, or actinolitic metamorphic alteration. There is no distinct compositional difference between the magmatic occurrences, however pseudomorphic amphiboles contain abundant plagioclase micro-inclusions. Magmatic amphibole compositions are dominated by magnesiohornblende based on the classification of Leake et al. (1997). Analyses with <0.75 formula units of Al (calculated on a 23-oxygen basis) are considered metamorphic alteration products and not further discussed. Nearly all amphibole in the high-SiO_2 gabbros (cumulate and liquid-like) is actinolite, while all other rock types contain magmatic amphibole.

There are two compositional populations of amphiboles in the low-Ca norites, which are distinguishable by their aluminum contents and both fall under the classification of magnesiohornblende (Fig 7c). Mg#s of both groups are comparable, with the high-Al population ranging from 71.4 to 77.1 and the lower-Al population ranging from 71.6 to 78.8. The high-Al population (9.6-12.8 wt.% Al_2O_3) is characterized by primary magmatic oikocrysts that surround olivine grains and is only present in samples SNB-14-52 and SNB-14-62 (*c.f.*, Fig 4b). This population is also high in TiO_2 (2.9-3.6 wt.%) and Na_2O (1.7-2.3 wt.%) compared to other amphiboles in the norites with similar Mg#s (0.2-1.3 wt.% TiO_2 and 0.6-1.1 wt.% Na_2O). The lower-Al population (4.5-5.9 wt.% Al_2O_3,) appears to also be of primary magmatic origin based

on the euhedral to subhedral crystal shapes, but likely crystallized later in the fractionation sequence. These two populations are not observed in the same samples and so may indicate variations in crystallizing melt water contents, with a slightly elevated water content allowing for earlier crystallization of the oikocrysts in some pods. All amphiboles in the high-Ca norites are similar in composition with Mg#s ranging from 66.8 to 71.3 and Al_2O_3 varying between 4.8 and 6.3 wt.%. Amphibole Mg#s in the gabbros and monzodiorites are negatively correlated with Al_2O_3 in a series of parallel trends, which each represent within-sample compositional variation reflecting sub-solidus Tschermak exchange. Similarly, TiO_2 and Na_2O are negatively correlated with Mg# within individual samples. Amphibole MnO content increases with decreasing Mg# and is relatively constant within each rock type, ranging from 0.09 to 0.31 wt.% in the norites, 0.21 to 0.34 wt.% in the gabbros, 0.28 to 0.59 wt.% in the monzodiorites, and 0.48 to 0.62 wt.% in the monzonites. CaO content is negatively correlated with Mg#, though there is considerable overlap between rock types.

Biotite

Biotite is present in all rock types and appears late in the crystallization sequence. The Mg# of biotite in the low-Ca norites ranges from 53.7 to 75.8, with a compositional gap between 58.7 and 63.0. The high-Mg# biotite group extends to higher TiO_2 (2.4-5.2 wt.%) and F (0.42-0.81 wt.%) than the low-Mg# group (1.7-4.1 and 0.32-0.43 wt.%, respectively). There is no clear textural difference between the low- and high-Mg# biotite, though individual samples only contain biotite from one compositional group. Biotite Mg# decreases to the high-Ca norites (51.8-59.8) and gabbros (47.0-61.1). The range of biotite Mg#s in the monzondiorites (44.5-58.0) overlaps with that of the gabbros and the monzonites (47.1-51.5).

MnO contents systematically increase with decreasing Mg#, from 0.02 to 0.18 wt.% in the norites to a maximum of 0.43 wt.% in the monzonites. Al_2O_3 content of biotite in the norites is variable (11.9-14 wt.%), and not clearly correlated with Mg#, but increases with decreasing Mg# in the gabbros through monzonites (12.1-16.2 wt.%). Na_2O contents reach 0.18 wt.% in high-Mg# biotite in the norites, and is <0.11 wt.% in other lithologies, and often below detection limit. Fluorine decreases with decreasing Mg#, following established Fe-F avoidance trends (Fig 7c) (Icenhower and London 1997; Mason 1992). Biotite F content ranges from 0.32 to 0.91 wt.% in the norites, and in other rock types biotite contains between 0.19 and 0.54 wt.% F.

Feldspars

Plagioclase feldspar is dominantly interstitial in the norites, though occasional euhedral crystals are present, and is a common fractionating phase in all other HLMC rock types. The anorthite content (An) of interstitial plagioclase in norites is highly variable, ranging from An_{29} to An_{72}, while euhedral plagioclase has approximately An_{82}. Euhedral to subhedral plagioclase in the gabbros can have distinct core and rim compositions with An_{76} to An_{92} cores and An_{40} to An_{62} rims. In crystals without a core-rim compositional difference, the composition is comparable to the aforementioned rims. Distinct cores and rims are present in <5% of plagioclase crystals in the monzodiorite plagioclase and absent from the monzonites. Plagioclase is An_{27} to An_{58} in rims and ~An_{77} in cores in the monzodiorites, and An_{31} to An_{54} in the monzonites.

Alkali feldspar is found as interstitial patches in the norites and is rare in the gabbros, but becomes increasingly common in the monzodiorites and monzonites. Anorthite content for all alkali feldspars is <3.5, and commonly <1. Orthoclase (Or) and albite (Ab) content is similar for all rock types, with variation between $Or_{72}Ab_{18}$ and $Or_{98}Ab_2$.

Zircon

Zircon grains from HLMC have Ti concentrations ranging from 2.4 to 24.4 ppm in the monzonites, 4.3 to 30.6 ppm in the anorthosites, and 5.0 to 26.9 ppm in the monzodiorites. Zircon is rare in the gabbros and norites and was therefore not separated for analysis. Hf concentration is negatively correlated with Ti concentration within each sample, ranging from 8610 to 17100 ppm, with 2470 to 7670 ppm of intra-sample variation.

REE concentrations of melts in equilibrium with the zircons were calculated using the methods of Chapman et al. (2016). Primitive mantle normalized REE (plus Nb and Y) patterns of calculated melts are nearly parallel to the corresponding whole-rock patterns, except for consistent Dy depletions that may be artifacts of the calculation (Fig 8). In cumulate samples, calculated melt compositions are similar to the whole rock concentrations in the LREE, and slightly higher or lower in the HREE. The samples with liquid-like bulk compositions typically have higher REE concentrations than the cumulative samples, but the compositions of zircons and calculated melts are very similar to the cumulate samples. REE concentrations in the liquid-like samples are up to three times higher than in the calculated melts, thus, another REE-bearing mineral must coexist in these samples, such as apatite. Though pyroxene can be a significant REE host, modal abundance is low (<1%) in these lithologies. Calculated melts have Eu anomalies <1 (0.70-0.81) that are slightly lower or equal within error (2 sigma of all analyses within a sample) than in the corresponding whole rock composition, implying that zircon saturation occurred after some plagioclase fractionation.

2.7 DISCUSSION

2.7.1 Crystallization Conditions

Out best estimates for crystallization pressures, temperatures, fO_2, and H_2O content of HLMC lithologies are summarized in Table 2 and described below.

Pressure

We perform Al-in-hornblende mineral barometry calculations using amphibole analyses from monzonites, as this is the only HLMC lithology that contains the requisite phase assemblage for these calculations (Mutch et al. 2016). Additionally, these samples exhibit a lesser degree of Tschermak exchange than the gabbros and monzodiorites, a process which could result in inaccurately low calculated pressures. Using high-Al, low-Mg# amphibole analyses (i.e., those inferred to have experienced the least Tschermak exchange) we calculate pressures of 0.29-0.34 GPa with a mean of 0.32 GPa, equating to 10.2 km depth.

Our results are in agreement with previous studies and show that HLMC crystallized in the upper crust of the SNB. The central SNB exposes dominantly upper crustal intrusions that crystallized between 0.1-0.4 GPa. Previous studies place the location of HLMC at pressures of 0.2 to 0.3 GPa (Ague and Brimhall 1988; Chapman et al. 2012), and 0.30 to 0.35 GPa (Nadin et al. 2008), or 7.6 to 13.2 km depth.

Temperature

We use a variety of mineral thermometers to constrain crystallization temperatures across the range of lithologies. In the norites, ortho- and clinopyroxene pairs are out of Fe-Mg equilibrium, with partition coefficients ($[Fe/Mg]_{cpx}/[Fe/Mg]_{opx}$) of 0.65-0.86 as opposed to the equilibrium value of 1.09 ± 0.14 (Putirka 2008). This is not surprising due to the presence of pervasive exsolution lamellae for samples with coexisting ortho- and clinopyroxene. Thus, two-

pyroxene equilibrium temperatures of 760 to 950 °C (Köhler and Brey 1990; Putirka 2008) likely represent cooling, rather than primary crystallization temperatures. In norites with little to no clinopyroxene and no discernable exsolution, the Ca-in-orthopyroxene thermometer of Köhler and Brey (1990) yields crystallization temperatures of 900 to 1170 °C.

Thermometry based on coexisting plagioclase and amphibole (Blundy and Holland 1990) defines a wide range of crystallization temperatures within HLMC depending on the rock type. We identify suitable pairs as plagioclase and amphibole crystals in contact, using the most proximal pair of analyses in corresponding grains. Subsolidus Tschermak exchange is pervasive in the gabbros and monzodiorites (Fig 7c), resulting in removal of Al and Si from amphiboles. This results in increased temperature estimates for the same plagioclase composition, thus, our reported temperatures may be overestimates if Tschermak exchange has affected an analysis site. In the norites, crystallization temperatures of amphibole oikocrysts and associated plagioclase are 865 to 950 °C, while estimates from non-oikocrystic amphibole in the same samples are 700-765 °C. This temperature offset combined with compositional differences (high Al_2O_3 and TiO_2 in the oikocrysts) indicates two periods of amphibole fractionation in the norites, with the oikocrysts forming earlier at higher temperatures, and all other amphiboles forming after a period of cooling and fractionation. The gabbros have two ranges of calculated temperatures that correlate with textural occurrences of amphibole. Primary and secondary magmatic amphibole temperatures are indistinguishable from one another and range from 740 to 815 °C. The pseudomorphic grains (formed via a magmatic reaction of pyroxene to amphibole) return much higher estimates of 1040 to 1120 °C. While the pseudomorphic amphibole compositions are similar to the primary and secondary magmatic amphiboles, plagioclase in contact with pseudomorphic amphibole is highly anorthitic ($\sim An_{80-85}$) compared to the other plagioclase rims

in the gabbros (~An_{40-50}). High An content results in increased temperature estimates, and may be a due to incorporation of excess Ca produced by the reaction of melt + clinopyroxene → melt + amphibole. Amphibole-plagioclase pairs in the monzodiorites and monzonites yield temperatures of 815 to 870 °C and 800 to 850 °C, respectively.

Our upper temperature estimate for the norites based on Ca-in-orthopyroxene (1170 °C) is similar to experiments by Hamada and Fuji (2008), which produce an olivine + orthopyroxene + plagioclase assemblage from a high MgO basalt starting at 1160 °C, 0.4 GPa, 1.6-2.7 wt.% H_2O, and one log unit above the Ni-NiO buffer (ΔNNO+1). Clinopyroxene appears in the experimental assemblage at 1130 °C, and the assemblage of orthopyroxene + clinopyroxene + plagioclase + Fe-oxides continues to 1100°C and the termination of the experiment. The assemblage orthopyroxene + clinopyroxene + plagioclase + amphibole first crystallizes at 990 °C, 0.2 GPa, NNO, and 4.5 wt.% H_2O in experiments by Grove et al. (2003). Based on these two studies, the onset of gabbro fractionation, characterized by common clinopyroxene and minimal orthopyroxene, likely occurred between 1100 and 990 °C.

Water Content and Oxygen Fugacity

Early crystallization of amphibole, and to a lesser extent biotite, in the HLMC fractionation sequence requires a hydrous parental melt. Experiments by Blatter et al. (2013) using an arc basalt starting material similar to HLMC melt-like gabbro compositions first crystallize amphibole + orthopyroxene + clinopyroxene + plagioclase from a primitive high-Al arc basalt at 0.4 GPa, 1000 °C, and 4 wt% H_2O. However, orthopyroxene and clinopyroxene are present in roughly equal proportions and olivine is not present. Orthopyroxene is part of the fractionating assemblage (magnetite + orthopyroxene + clinopyroxene + plagioclase) of mid-

ocean ridge dacites during 0.2 GPa crystallization experiments under oxidizing conditions (NNO +1 to +2.1) with H_2O contents between 0.8 and 2 wt.% (Erdmann and Koepke 2016). At higher water contents (>2 wt.%) in these experiments, the assemblage lacks orthopyroxene. The dominance of orthopyroxene over clinopyroxene in the first crystallized HLMC cumulates indicates a reduced H_2O content compared to Blatter et al. (2013), but the early crystallization of amphibole suggests H_2O contents higher than in experiments conducted by Erdmann and Koepke (2016) (H_2O > 2 wt.%). Experimental evidence thus constrains the H_2O content of the HLMC parental melt between 2 and 4 wt.%.

We apply the plagioclase-liquid hygrometer of Waters and Lange (2015) to plagioclase cores in the liquid-like gabbros to estimate melt H_2O content. We use plagioclase core compositions because they represent the earliest crystalized compositions that are most likely to be in equilibrium with the bulk-rock "melt" composition. Using 990 to 1100 °C as the temperature range for the onset of gabbro crystallization in HLMC based on experimental studies (Grove et al. 2003; Hamada and Fujii 2008), we estimate initial H_2O contents of 2.9 to 3.5 wt.% in the liquid like gabbros, which is within the 2 to 4 wt.% range predicted by experimental studies.

Oxygen fugacities (fO_2) play a significant role in the Fe-Mg partitioning into ferromagnesian minerals during crystallization. Oxygen fugacities elevated above that for mid-ocean ridge basalts (near the fayalite-magnetite-quartz buffer) are expected, as arc magmas are commonly characterized by fO_2 at NNO or higher (Brounce et al. 2014; Kelley and Cottrell 2009; Rowe et al. 2009; Sisson et al. 2005). In the HLMC norites, amphibole oikocrysts containing olivine imply that these phases coexist in the magma. Crystallization experiments of Krawczynski et al. (2012) limit the stability of this assemblage between ΔNNO +1 and ΔNNO

+3 at 0.3 GPa at the calculated crystallization temperature of these amphiboles (~950 °C). Applying the oxybarometer of Loucks et al. (2020), which utilizes the concentrations of U, Ti, and Ce in zircon grains, we find a range of fO_2 values from ΔNNO -1.6 to 1.3 in the dated grains from monzodiorite and monzonite samples, with an average fO_2 of ΔNNO -0.5. Using biotite and bulk-rock compositions and MELTS thermodynamic modeling to calculate fO_2 as presented in Bucholz et al. (2018) for melt-like monzonite SNB-16-9, we find that the HLMC melts are oxidized to between NNO and ΔNNO +0.6 (± 1 log unit). We estimate ΔNNO +1 as the approximate fO_2 of the HLMC parental melt, as this is within error of both the calculated and experimentally constrained values.

2.7.2 A Cogenetic Fractionation Sequence

Field and Petrographic Evidence

The western limb of HLMC is composed of mainly medium-fine grained gabbro with elongate, N-S trending texturally distinct gabbro bodies (coarse-grained and spotted gabbros, Fig 1). All coarse-grained and spotted gabbros, as well as some of the medium-fine grained gabbros, exhibit ortho- to mesocumulate textures. The contacts between individual gabbro bodies and the medium-fine grained gabbro are gradational over 1 to 5 cm, exhibiting mingling textures and inclusions of gabbros with contrasting textures (Fig 2c, d; Fig 3a). These characteristics suggest that the gabbros of the western limb accumulated from multiple pulses of magma that supplied compositionally similar melts within a relatively short period of time, such that previously intruded gabbroic magma (which ultimately crystallized into the medium-fine grained gabbro) was still partially molten to allow for mingled and gradational contacts. Due to their close temporal association, these pulses of magma likely originated from the same source, and are

therefore part of a cogenetic sequence. Textural variation between the bodies was likely caused by local thermal conditions and minor compositional zonation. The presence of both liquid-like and cumulate gabbros in the western limb suggest that the parental melts to the gabbros continued to fractionate *in-situ*, but because mingling is common between melt pulses, cumulate layering is not well preserved.

The southeastern section of HLMC consists of a single large medium-fine grained gabbro body containing norite and anorthosite cumulate pods, as well as a lens of coarse-grained gabbro, but is overall more texturally homogenous than the western section. The presence of well-defined cumulate textures in these rocks indicates that separation of crystals and liquid occurred within the mafic complex. The contacts between gabbros, monzodiorite, and monzonite in the northern and northeastern section of HLMC (Fig 1) are largely gradational over 5 to 10 m, and there is no distinct contact between the medium-fine grained gabbros of the western limb and this lithology in the eastern section. This suggests that eastern HLMC and the western medium-fined grained gabbros were emplaced as a single large intrusion that differentiated *in-situ* to create the norite and gabbro cumulates and melt was extracted from the gabbros to produce the more evolved monzodiorites and monzonites. However, these lithologies are locally mutually intrusive as evidenced by diffuse dikes (10-20 cm wide) and segregations of monzodiorite within the gabbros. This suggests that these are all synmagmatic lithologies and that the magmas were mobile after compositional segregation. The gabbros were likely significantly more crystal rich than the monzodiorites and monzonites during this period, but not fully solidified because monzodiorite-gabbro intrusion boundaries are not sharp. This is consistent with petrographic observations suggesting that most of the gabbros are meso- and adcumulates, with the exception of three liquid-like gabbro samples.

The presence of both cumulate and liquid-like gabbros, monzodiorites, and monzonites suggests that the gabbroic HLMC parental intrusions fractionated *in-situ*. Multiple intrusions into the medium-fine grained gabbro are preserved as gabbros with contrasting textures, and the bodies that represent separate intrusions all have basaltic parental melts of similar composition. The gradational boundaries between the gabbros and monzonitic lithologies, as well as evolved pods within the gabbros, indicate that the evolved lithologies were generated by extraction of melt from the gabbroic cumulates. While some melts may have been extracted to shallower levels in the crust, the liquid-like compositions present in HLMC represent melts generated by fractionation within HLMC.

Evidence for mixing between HLMC and felsic melts at the level of emplacement is minimal and confined to the outer margins of the complex, and so is unlikely to have caused the compositional variation within the mafic body. Locally, the 90.5 to 96.5 Ma HLMC parental melts intruded into the much older granite of Chickenfoot Lake (Jcf, 191.6 Ma), which would have been fully crystallized prior to the mafic intrusions. Any volume of Jcf-derived felsic melt would need to be produced by heat from HLMC intrusions. This effect is visible along the HLMC-Jcf contact, where a dioritic gradational zone (Fig 3b) indicates short-distance mixing between a HLMC parental melt and granitic melt produced by partial melting of Jcf. However, this hybridized lithology does not extend more than 1 m from the granite-gabbro contact. The contact between Kle and HLMC is sharp and indicates little to no mixing or assimilation. Because Krv is younger than HLMC, and HLMC-sourced blocks in the brecciated contact between these units are angular with sharp contacts, HLMC was likely solidified by the time of Krv intrusion and therefore could not mix. Field evidence precludes substantial magma mixing

origin for the compositional diversity within HLMC and supports *in-situ* fractional crystallization.

Geochemical Evidence

The HLMC compositional trends suggest that the various rock types are related to one another by fractional crystallization. Bulk-rock analyses preserve a continuous and wide range of SiO_2 contents from 43.6 to 61.5 wt.% (Fig 5). Bulk-rock Mg# decreases from 73.1 to 35.8, though a compositional gap exists between the norites and gabbros (Mg#= 57.8 to 64.6). This may result from sampling bias, as we focused on collecting the most primitive norites, or from Mg removal via recrystallization of clinopyroxene to amphibole (Oliver 1951; Piispanen and Alapieti 1977), which is pervasive in the low-SiO_2 gabbros. Al_2O_3, TiO_2, CaO, MgO, and FeO contents are variable over approximately constant SiO_2 content in the norites, then smoothly decrease from the gabbros to monzodiorites to monzonites. Similar trends are present in K_2O and Na_2O, but their concentrations increase with increasing SiO_2 content. These compositional relationships are consistent with a fractional crystallization liquid line of descent (LLD) and associated cumulates in arc settings (Müntener and Ulmer 2018).

In general, trace element concentrations gradually increase with increasing SiO_2 content, indicating enrichment of these incompatible elements in the liquid with progressive fractionation. Exceptions to this are Ni and Cr, which are compatible in olivine and pyroxene and so are rapidly removed from the melt during norite crystallization, and thus negatively correlated with SiO_2. HREE elements are depleted relative to LREE elements in all rock types (Fig 6), and this depletion, indicated by La/Yb ratio, increases with increasing silica content. Though there is

significant overlap in the degree of HREE depletion between rock types, this pattern nevertheless supports a fractional crystallization origin for the HLMC lithologies.

Mineral compositions are also consistent with a cogenetic fractionation sequence. Very similar trends are seen in ortho- and clinopyroxene, in which MnO and Mg# are negatively correlated and higher Mg#s correspond to lithologies crystallized earlier in the fractionation sequence. Cr_2O_3 and Al_2O_3 in orthopyroxene (Fig 7b) continuously decrease with decreasing Mg# and with increasing bulk-rock SiO_2 content, indicating depletion of these components in the melt with olivine + pyroxene and plagioclase fractionation. Euhedral plagioclase crystals in the norites have very similar An content to the plagioclase cores in the gabbros and monzodiorites, suggesting that these cores crystalized from a melt similar to the norite parental melt and were progressively rimmed by lower-Ca plagioclase as the remaining melt evolved. In biotite, the observed decreasing F (Fig 7d) and TiO_2 content with decreasing Mg# correspond to increasing FeO content in the biotite and decreasing crystallization temperature, respectively.

Thus, both the mineral compositions and modal mineralogy of the rocks indicate derivation by fractional crystallization from a common parental melt defined by a lithological progression of norites → gabbros → monzodiorites → monzonites and a mineral crystallization sequence of olivine + amphibole(high-Al)→ orthopyroxene + Fe-Ti oxides → clinopyroxene → plagioclase + amphibole(low-Al) → biotite → K-feldspar → quartz.

2.7.3 Composition of the HLMC Parental Melt

We define the HLMC parental melt as a representative, initial basaltic melt composition that intruded into the upper crust at the location of HLMC and fractionated to produce the range of observed lithologies. Based on our inferred fractionation sequence, olivine is the first phase to

crystallize from the parental melt and is our best indicator of its composition. The most primitive olivine in HLMC has a Mg# of 81.3. We calculate the Mg# of the parental melt coexisting with this olivine to be 51, using the olivine-melt distribution coefficient of 0.303 (Beattie 1993) and assuming an fO_2 of NNO+1 and thus Fe^{3+}/Fe^{T} ratio of 0.2 (Kress and Carmichael 1991).

Primitive lavas erupted at continental arcs are thought to be representative of sub-arc mantle melts, and span a Mg# range of 67 to 73 based on a global compilation by Schmidt and Jagoutz (2017). The Mg# of the HLMC parental melt (51) is significantly lower than these values and therefore does not represent a (non-modified) partial melt of the mantle, but rather one that has experienced prior differentiation at deeper crustal levels. The major and trace element concentrations (Cr, Ni, Rb, Sr, Y, Zr, Nb, Ba, REEs, Hf, Ta, Pb, Th, U) of the HLMC parental melt are determined via alphaMELTS as discussed below, and the melt composition is given in Table 3. Though a basaltic dike exists in HLMC that appears to be a potential parental melt composition based on major element concentrations (SNB-14-39), this sample is enriched in incompatible trace elements (particularly Nb, Rb, La, Ce, Lu, Ta, and Th) relative to the liquid-like gabbros and some liquid-like monzodiorites. Thus, we infer that this dike is not a parental melt and prefer the calculated parental melt composition.

2.7.4 Evidence for Lower Crustal Crystallization-Differentiation

Although the SNB is dominated by felsic plutons that crystallized at shallow pressures (generally <0.5 GPa; Nadin et al., 2016), direct evidence for deep crustal processes is present as ultramafic to mafic Cretaceous xenoliths in Miocene to Pliocene basalts in the central SNB, soured from 1 to 3 GPa (Dodge et al. 1986; Dodge et al. 1988; Domenick et al. 1983; Ducea and Saleeby 1998; Ducea and Saleeby 1996; Lee et al. 2006; Lee et al. 2001; Lockwood and

Bateman 1976; Mukhopadhyay 1991; Mukhopadhyay and Manton 1994; Peselnick et al. 1977). In addition, southern exposures of the batholith in the Tehachapi Mountains range from 0.7 to 1.0 GPa (Klein and Jagoutz 2021; Lackey et al. 2005; Pickett and Saleeby 1993; Ross 1985; Ross 1989; Saleeby et al. 2008; Sams and Saleeby 1988). Orthopyroxene compositions from lower crustal garnet-websterite and pyroxenite cumulate xenoliths range from Mg# ~80 to 90 (Fig 7b; Dodge et al. 1986; Lee et al. 2006). Using the orthopyroxene-melt distribution coefficient of 0.284 (Beattie 1993) and assuming an fO_2 of NNO+1 (as above), the orthopyroxene crystallized from melts ranging from a primitive mantle melt (Mg# = 69) to a fractionated basalt (Mg# = 48). These cumulates therefore record lower crustal differentiation and the generation of low-Mg basalts that are consistent with the HLMC parental melt composition. Additionally, the most primitive HLMC norite orthopyroxene compositions overlap with the least primitive compositions in the xenoliths (Mg# ~80), indicating that both cumulates crystallized from similarly fractionated melts.

Likewise, a lower crustal section of the southern SNB is exposed in the Tehachapi Mountains, and exposes depths of up to 30 km (1.0 GPa) (Ague and Brimhall 1988; Pickett and Saleeby 1993). Within the Tehachapi Complex, the Bear Valley Intrusive suite (0.4-1.0 GPa) consists of tonalite, norites, and hornblende gabbros (Klein and Jagoutz 2021). The mineralogical similarities between the gabbroic cumulate rock types of the Bear Valley Intrusive Suite and the HLMC mafic cumulates, particularly the prevalence of amphibole and orthopyroxene, suggest that the melts that intruded into the upper crust are compositionally similar to those that crystallized in the SNB mid-lower crust. Additionally, the most primitive bulk rock analysis of gabbroid cumulates from the Bear Valley Intrusive Suite (Mg#=73.4; Klein and Jagoutz 2021) is similar to the most primitive HLMC norite (Mg#=73.1), suggesting that the

parental melts to both intrusions were similarly evolved basalts. Thus the parental melts to both the Bear Valley Intrusive Suite and the HLMC may be generated by the same process, namely through deeper crustal differentiation as recorded by the ultramafic xenoliths.

In our case study of HLMC, differentiation of a primitive basalt is required prior to the intrusion of the evolved (low-Mg) parental basalt in the upper crust. We favor lower crustal fractional crystallization over partial melting of underplated basalts as thermal modeling studies demonstrate that this latter process is more likely to produce more silicic rather than basaltic compositions (Annen et al., 2006; Jagoutz and Klein, 2018). Remaining possibilities for generating an evolved basaltic melt include assimilation of felsic crust by a primitive basalt or direct fractionation from a primitive basalt in the lower, mid- or upper crust. Assimilation of crustal material is highly unlikely to produce the HLMC parental melt composition from a mantle melt because assimilation of enough crustal melt to decrease the basalt Mg# from ~70 to 51 would significantly increase the melt SiO_2 content. Mid- and upper crustal fractionation of large volumes of primitive basalt is improbable because ultramafic cumulates are rarely observed at these depths in the SNB. We therefore infer that the initial stage of fractional crystallization occurred in the lower crust within the range of cumulate-dominated lithologies, as observed in accreted arc sections.

2.7.5 Polybaric Fractionation Model

Field relationships and geochemistry indicate that the HLMC rocks may be related by a fractional crystallization liquid line of descent (LLD), and their trace element signatures indicate that parental melts could have been sourced from a sub-arc mantle melt. However, as discussed above, this melt was fractionated relative to a primitive mantle melt. Thus, fractionation must

have occurred prior to the intrusion of the HLMC parental melts at their current level in the crust (~0.3 GPa) where further differentiation occurred. In agreement with studies of polybaric fractionation in arcs (Almeev et al. 2013; Hamada et al. 2014; Melekhova et al. 2015), we construct a two-stage fractionation model to test our fractional crystallization hypothesis. Stage 1 models fractional crystallization of a primitive mantle melt in the lower arc crust using alphaMELTS, and Stage 2 is a mass balance model in which measured cumulate compositions from HLMC are progressively removed from an evolving modeled liquid composition. It is conceivable that multiple episodes of fractionation could have occurred prior to Stage 2 at different levels in the crust below 0.32 GPa. However, we choose the simplest approach and assume only one stage of lower crustal crystallization.

Stage 1: Lower Crustal Fractionation Model Description

The initial phase of deep crustal crystallization of a sub-arc mantle-derived melt is modeled using alphaMELTS (Asimow and Ghiorso 1998; Ghiorso and Sack 1995; Smith and Asimow 2005). The starting major and trace element composition was varied within the range of primitive basalts from the Andes, Cascades, Central American, Mexican, and New Zealand continental arcs (Schmidt and Jagoutz 2017) and input into alphaMELTS as an isobaric, purely fractional crystallization calculation. In Table 3, we present the starting composition that produces a fractionated melt in equilibrium with the most primitive cumulates in HLMC at the end of the Stage 1 fractionation and most successfully reproduces the liquid-like compositions when input into the Stage 2 model. A crystallization pressure of 1.1 GPa, or ~35 km depth, was used to replicate the lower crust of the Sierra Nevada arc. This pressure represents a transition between garnet-bearing cumulates and lower crustal intrusions as predicted by seismic studies

(Fliedner et al. 2000; Jones and Phinney 1998; Ruppert et al. 1998), and may act as a permeability barrier where ascending melts are likely to stall (Kelemen and Aharonov 1998; Klein and Jagoutz 2021).

Following our best estimates for oxygen fugacity, we performed models at NNO+1. Initial water contents were assumed to be 2 wt.% H_2O, which is within the range of primitive (Mg# = 65-74) melt inclusion concentrations from basalts in the Mexican, Cascade, and Kamchatkan arcs (1.0-5.2 wt.% H_2O; Cervantes and Wallace 2003; Portnyagin et al. 2007; Sisson and Layne 1993) and reproduces the H_2O content (2.9-3.5 wt.%) of the HLMC gabbros after completion of the crystallization model.

The MELTS model begins with a primitive arc basalt composition that crystallizes orthopyroxene in the lower crust at 1380°C, followed by clinopyroxene at 1305°C. Fractionation continues until the evolving melt reaches a Mg# of 51 at 1250°C and 50.7% SiO_2 after 33% crystallization of the initial melt mass. The fractionating assemblage is primarily ortho- and clinopyroxene. We terminate the lower crustal fractionation model here because this melt is in Fe-Mg equilibrium with the most primitive olivine in HLMC. We assume that the melt intrudes into the upper crust at this stage of differentiation. We continue to model fractionation of the remaining melt at 1.1 GPa to compare this fractionation trend to the upper crustal LLD (Fig 10), but this is not included in our polybaric crystallization model.

Stage 2: Upper Crustal Fractionation Model Description

We use a mass balance approach to model the LLD of the HLMC parental melt as it fractionally crystallizes in the upper crust. In this method, we progressively subtract bulk cumulate compositions from a melt composition, following the methods of Jagoutz (2010).

Average cumulate compositions are calculated for 6 representative lithologies (Table 4) following the fractionation sequence discussed above. The starting liquid composition is the HLMC parental melt as generated by our lower crustal fractionation model (Table 3). We do not use alphaMELTS to model this stage for two reasons: 1) amphibole is a common fractionating phase in the HLMC and alphaMELTS currently lacks an amphibole model that accurately reproduces observed phase assemblages from experimental and natural studies, and 2) the fractionating assemblage and cumulate compositions can be constrained from field and geochemical observations.

Classification of Cumulate and Liquid-Like Samples

The LLD modeling method described above requires that cumulate samples be distinguished from samples that are representative of melt compositions. Petrographic textures are the primary means of classification, however not all samples were observed in thin section and some evolved samples may not exhibit clear cumulate textures, so a secondary compositional classification is applied.

All norites are classified as cumulates based on two lines of evidence; (1) cumulate textures were identified in all norite thin sections (both low- and high-Ca groups) and (2) all of the norite bulk-rock Mg#s are higher than the parental melt Mg#. Gabbro textures are variable from meso- or orthocumulates, to randomly oriented masses of interlocking crystals (Fig 4f). The latter is suggestive of rapidly crystallized melt-like lithologies. In addition, we use Al/Si and Sr/Nd ratios as tracers of plagioclase accumulation (Bucholz et al. 2014; Jagoutz 2010) and define cumulate gabbros as those with Al/Si > 0.21 and cumulate monzodiorites and monzonites as those with Sr/Nd > 30 (Fig 9a). These values place samples with textural observations into the

correct categories and allows us to classify samples for which we do not have petrographic constraints.

When compared to the macroscopic rock textures as shown in Figure 2, all liquid-like gabbros are medium-fine grained gabbros, and all coarse-grained and spotted gabbros are cumulates, but some medium-fine grained gabbros are also classified as cumulates based on our compositional criteria. Eu anomalies are variable within rock types, and either similar between liquids and cumulates of the same rock type (e.g., liquid-like monzodiorites and cumulate monzodiorites), or slightly elevated in the cumulate group. Eu anomalies are < 1 in the norites (0.45- 0.69), reflecting minimal plagioclase accumulation and incompatibility of Eu^{2+} in olivine and orthopyroxene (Fig 9b).

Proportions of Cumulates Crystallized

Fractionation of a primitive arc basalt during Stage 1 fractionation (1.0 GPa) produces 33% by mass of pyroxenites, and the resulting liquid composition is input into the Stage 2 model. In accordance with our inferred fractionation sequence, low-Ca norites are the first cumulates to crystallize in Stage 2 (2% crystallization by melt mass), followed by high-Ca norite fractionation (9.3%). Clino- and orthopyroxenes are consistently exsolved in the gabbros, therefore we infer that the Mg# of the melt was between that of the low-SiO_2 (Mg#= 46) and liquid-like gabbros (Mg#= 49) at the onset of gabbro crystallization. Gabbro is assumed to crystallize until the liquid-like monzonite compositions are replicated at 63 wt.% SiO_2 (71.5% crystallization by mass). Fractionation of cumulate monzodiorites continues from 63 wt.% SiO_2 and Mg# 44.7 to 70 wt.% SiO_2 and Mg# 40 (7.3% by mass). Cumulate monzonites then fractionate until SiO_2 reaches 78 wt.% (2.8% by mass), near the maximum for granites in the SNB.

2.7.6 Model Results

Our polybaric fractionation model reproduces the range of major and trace element compositions of the HLMC, and when extended to higher SiO_2 contents is capable of replicating the compositional trends defined by the SNB felsic plutons (63-78 wt.% SiO_2, Fig 10). In Stage 1, differentiated basalts are produced by 33% fractionation by mass of a primitive arc basalt at the base of the crust (1.1 GPa). The resulting melt composition is the HLMC parental basalt, which has an H_2O content of 3.1 wt.% consistent with our estimates from plagioclase hygrometry in the liquid-like gabbros. This lower crustal fractionation interval corresponds to cooling of the melt from 1380 to 1250°C and is dominated by crystallization of orthopyroxene followed by clinopyroxene. This assemblage is corroborated by experimental pyroxenites produced at 1.2 GPa (Müntener et al. 2001) and with xenoliths from the Sierra Nevada lower crust which have estimated crystallization depths of 35-40 km (1.1-1.3 GPa, Ducea and Saleeby 1996). During this crystallization stage, the Mg# of the melt drops from 69 to 51 over a slight decrease in SiO_2 content from 51 to 50.1 wt.% due to fractionation of ortho- and clinopyroxene. Because the melt is not hydrous enough to crystallize amphibole at this stage, the bulk cumulates have an SiO_2 content of 52.6 wt.% and cause a slight decrease, rather than an increase, in melt SiO_2 content with progressive fractionation. CaO content in the melt increases from 11 to 12.2 wt.% during orthopyroxene-only crystallization, then decreases to 10.4 wt.% after clinopyroxene saturation. No significant Al-bearing phases saturate at this stage, and the fractionating assemblage contains only 2.3 to 5.6 wt.% Al_2O_3. Al_2O_3 increases from 12.7 to 17.4 wt.% while CaO decreases due to clinopyroxene crystallization, causing ASI to increase from 0.55 to 0.72 (Fig 10b).

The derivative basalt produced at the end of Stage 1 is assumed to subsequently ascend, intrude into the upper crust, and further differentiate. Geochemical trends in the upper crustal LLD are controlled by the fractionating cumulate compositions. The removal of norite cumulates drives an initial decrease in the melt Mg# from 57 to 41 at relatively constant SiO_2 (Fig 10). CaO, Al_2O_3, Na_2O, and Sr content increase in the melt during this interval due to the paucity of accumulated feldspar in the norites. Ni and Cr content sharply decrease from 35 to 8 ppm and 50 to 18 ppm, respectively, while incompatible trace elements increase slightly.

Following the onset of low-SiO_2 gabbro crystallization, MgO, CaO, FeO, and TiO_2 smoothly decrease through the remaining LLD, while K_2O, ASI, and incompatible trace elements consistently increase. Fractionation of the low-SiO_2 gabbros causes a significant increase in the melt SiO_2 content from 49.9 to 56 wt.%. The low SiO_2 (43.9-46.8 wt.%) and high FeO and TiO_2 (9.6-13.6 and 1.2-1.6 wt.%, respectively) content of the low-SiO_2 gabbros is due to abundant amphibole and Fe-Ti oxides. As such, fractionation of these cumulates drives the SiO_2 enrichment and FeO and TiO_2 decrease in the melt. The liquid also decreases in MgO and CaO content over this fractionation interval. In contrast to norite fractionation, plagioclase is now a major fractionating phase and the Al_2O_3 content of the melt increases only slightly during low-SiO_2 gabbro fractionation, from 18.2 to 18.5 wt.%. Na_2O and P_2O_5 increase due to crystallization of high-Ca plagioclase ($\sim An_{80}$) and a lack of apatite in the low-SiO_2 gabbros. Because Sr is compatible in plagioclase, Sr content continuously decreases after a maximum at 720 ppm at the end of norite fractionation.

High-SiO_2 gabbro fractionation continues the trend of increasing SiO_2 content (56-63 wt.%) with a limited decrease in Mg# (47.6 to 45). Plagioclase is abundant in these cumulates and has lower An content ($\sim An_{50}$) than in the low-SiO_2 gabbros, causing Al_2O_3 to decrease and

the rate of Na_2O increase to shallow. P_2O_5 content begins to decrease rapidly after a maximum at 0.35 wt.% due to apatite saturation. Al_2O_3, Na_2O, and P_2O_5 content continue to decrease for the remainder for the LLD. When gabbro fractionation ceases, the model has reproduced the most fractionated liquid-like monzonite in HLMC with 16.2% of the mass of HLMC parental melt remaining, or 10.9% for the primitive arc basalt.

Fractionation of monzordiorite cumulates from the remaining melt continues the increasing trends in SiO_2 (63-71 wt.%), K_2O (3.0-4.5 wt.%), and Na_2O (3.5-3.7 wt.%). Incompatible trace element concentrations also increase, while Ni, Cr, and Sr contents consistently decrease. The melt Mg# decreases from 45 to 40, along with decreasing MgO, TiO_2, and FeO primarily due to amphibole and biotite crystallization, and decreasing CaO and Al_2O_3 which are depleted by plagioclase and amphibole fractionation. This crystallization interval replicates a representative SNB granodiorite composition (67.5 wt.% SiO_2, Table 3) with 9% of the parental melt and 6% of the primitive melt masses remaining. Monzonite fractionation continues the monzodiorite fractionation trends, causing the evolving melt composition to increase from 71 to 78 wt.% SiO_2. Mg# notably decreases from 40 to nearly 0 as MgO is consumed by fractionating amphibole and biotite. At this point, the remaining granitic melt mass is 5% of the HLMC parental melt and 3.3% of the primitive arc basalt.

To determine if the HLMC evolved rocks and SNB granodiorites could be produced by continued lower crustal fractionation, we extend the alphaMELTS model to lower temperatures and Mg#s<51 (gray dotted line, Fig 10). Though the starting composition we use is within the low range of ASI and Al_2O_3 values found in primitive arc basalts (Schmidt and Jagoutz 2017), our model of lower crustal fractionation always produces peraluminous andesite liquids (e.g., SiO_2 >57 wt.%). In our model and in the Blatter et al. (2013) experiments, plagioclase does not

become a significant fractionating phase at 0.9-1.1 GPa until 33 to 30% of the initial melt mass is remaining. Initially, Al removal from the melt is caused by minor incorporation into ortho- and clinopyroxene, which contain 2.8 to 5.6 wt.% Al_2O_3. Spinel is the first aluminous phase to fractionate, crystallizing after 53% fractionation by mass in our model. However, the drastic increase in ASI (0.55 to 1.1) caused by pyroxene fractionation produces a peraluminous melt before spinel saturation. Though our model does not produce garnet within the lower crustal fractionation interval, garnet-pyroxenite xenoliths from the SNB lower crust have been found in addition to websterites (Dodge et al. 1986; Dodge et al. 1988; Mukhopadhyay 1991; Mukhopadhyay and Manton 1994; Lee et al. 2006; Lee et al. 2001). However, the garnet pyroxenites have low ASI values (0.26-0.54) and SiO_2 values similar to a primitive arc basalt (48.3-49.6 wt.%, Lee at al. 2006) which would drive an increase in ASI and only slight increase, if any, in SiO_2. If the crystallizing cumulates were garnet-pyroxenites rather than websterites, lower crustal fractionation would still produce peraluminous andesites. Thus, the HLMC compositions and non-peraluminous evolved arc melts are inconsistent with extensive lower crustal fractionation.

2.7.7 Comparison to Other Upper Crustal Mafic Bodies in the SNB

Numerous mafic bodies are preserved in the SNB upper crust and several have been investigated for geochronology and geochemistry (Coleman et al 1995; Frost 1987; Frost and Mahood 1987; Holland et al. 2013; Ratajeski et al. 2001; Sisson et al. 1996). The Onion Valley (92.1 ± 0.3 Ma), Armstrong Canyon (91.5 ± 0.1 Ma), and Lake Sabrina (91.1 ± 0.3 Ma) mafic complexes in the eastern Sierra Nevada (Coleman et al. 1995) are broadly coeval with HLMC (90.5-96.5 Ma). Mafic magmatism in all four localities was contemporaneous with voluminous

late Cretaceous felsic intrusions throughout the Sierra Nevada arc (Ducea 2001), demonstrating that mafic and felsic magmatism was coeval and possibly cogenetic.

Geochemical data from the lower crustal Bear Valley Intrusive Suite (Klein and Jagoutz 2021) and 10 upper crustal SNB mafic complexes in addition to HLMC are presented in Figure 12. All localities are in the eastern SNB from Frost (1987) and Sisson et al. (1996) except for the Yosemite samples of Ratajeski et al. (2001) and the Ash Mountain complex of Holland et al. (2013). Amphibole-gabbros (± olivine) and amphibole-bearing diorites are common throughout the mafic complexes, indicative of crystallization from hydrous parental melts. In particular, the parental melt to the Onion Valley complex is estimated to have 6 wt.% H_2O (Sisson et al. 1996). The most primitive cumulates in the Onion Valley complex are olivine-hornblendites and the intrusion is generally pyroxene-poor. This is in contrast to the orthopyroxene-dominated norites of HLMC, which indicate crystallization from a less hydrous parental melt (estimated 3.1 wt.% H_2O). In both cases, elevated water contents likely facilitate the ascent of the low-Mg, high-Al basalts into the upper crust due to their decreased density and viscosity (Sisson et al. 1996).

Layered cumulates and internal compositional ranges from gabbro to diorite within each body (Frost 1987; Sisson et al. 1996) suggest that *in-situ* upper crustal fractionation is common in the mafic complexes. Olivines from the Onion Valley complex have a maximum Mg# of 81.7 (in equilibrium with melt Mg# = 52), and sheeted sills interpreted as representative of melt compositions have Mg#s ranging from 41 to 54.5 (Sisson et al. 1996). The most primitive sill and the olivine-melt estimates are slightly more primitive, but still comparable to the HLMC parental melt (Mg# = 51), suggesting that the parental melts to these two bodies were fractionated to a similar degree in the lower crust prior to ascent. Analyses of mineral chemistry only exist for the Onion Valley and Hidden Lakes mafic complexes, rendering it is difficult to

calculate the Mg# of parental melts for the other complexes. However, maximum bulk-rock Mg#s in each complex range from 53 to 76.5, and therefore did not fractionate from a primitive basalt (Mg# of cumulates > 80). Thus lower crustal differentiation is required to generate low-Mg basalts in order to produce these upper crustal mafic intrusions. Derivation of the upper crustal mafic complexes from evolved basalts and the presence of upper crustal cumulate lithologies demonstrate that polybaric fractionation is a common process in generating the range of compositions in SNB mafic complexes.

All mafic complex samples have ASI values less than 1, indicating that the basalts that escape the lower crust are generally not peraluminous. Samples with high ASI relative to their SiO_2 content (ASI = ~0.8-0.97, SiO_2= 40.7-50.3 wt.%) are likely cumulates, and thus reflect plagioclase accumulation rather than parental melts with initially high ASI values. Lower crustal fractionation of a primitive arc basalt creates peraluminous melts at 51 wt.% SiO_2 (our model) to 56 wt.% SiO_2 (Blatter et al. 2013) by ~55% crystallization. Thus, melts that generate the mafic complexes must escape the lower crust (>0.7 GPa) before evolving to andesitic compositions. Because some lithologies found in these complexes have SiO_2 > 56 wt.%, upper crustal differentiation must occur to create these compositions after extraction from the lower crust.

Though mineral compositional data is limited to two complexes, those that do exist define a narrow range of parental melt compositions (Mg# = 51-54.5). The range of bulk-rock cumulate compositions from other complexes are similar in Mg# to the Onion Valley and Hidden Lakes mafic complexes, suggesting that all upper crustal mafic complexes may be derived from melts that are fractionated to a similar degree in the lower crust. Additionally, the SiO_2 content of parental melts cannot exceed 56 wt.% without becoming peraluminous during fractional crystallization at >0.7 GPa. Therefore, we suggest that there may be a narrow window of

rheologic properties that allow these hydrous basalts to ascend. For example, the hydrous, but still relatively low-SiO_2 nature of these basalts reduces their viscosity and decreases their density, enhancing their ability to ascend via diking (Sisson et al. 1996).

2.7.8 Production of Sierra Nevada Batholith Granitoids

Our polybaric fractionation model results support the hypothesis that the HLMC is an example of upper crustal fractional crystallization of a low-Mg basalt in a continental arc and that lower crustal fractionation is required to produce the HLMC parental basalt. We show that arc-like granodiorite and granite compositions can be generated by this two-stage crystallization process and thus polybaric crystallization can contribute to the generation of non-peraluminous granitoids in the SNB. However, volumes of mafic (noritic to gabbroic) cumulates at upper crustal depths (0.1-0.4 GPa) are relatively small. We posit that the fractionation of a low-MgO basalt deeper than the exposures of much of the SNB, yet above the level of plagioclase saturation (<1 GPa), could generate evolved non-peraluminous melts. This is supported by gabbro and gabbronorite lithologies with a maximum Mg# identical to the HLMC (Mg#= 73) in the ~0.8-1 GPa section of the Bear Valley Intrusive Suite (Klein and Jagoutz 2021). Because these did not crystallize from a primitive mantle melt, an initial stage of fractionation is required below ~1 GPa, analogous to Stage 1 in our model for the HLMC. Throughout the batholith, Stage 2 fractionation may occur below exposures of the bulk of the SNB (>0.4 GPa) to produce granodioritic melts consistent with SNB compositions, which proceed to intrude into the upper crust. This reconciles the discrepancy between experimental and observational data, in which experiments indicate that melts produced by lower crustal fractionation rapidly become peraluminous (Blatter et al. 2013; Cawthorn and Brown 1976; Cawthorn and O'Hara 1976;

Müntener and Ulmer 2018; Nandedkar et al. 2014; Ulmer et al. 2018), yet lower crustal ultramafic cumulates are ubiquitous in arc crustal cross sections (Debari and Sleep 1991; Greene et al. 2006; Guo et al. 2020; Jagoutz 2014; Otamendi et al. 2012; Walker et al. 2015). HLMC has captured a local example of upper crustal differentiation, indicating that granodiorite compositions consistent with the SNB can be produced by a polybaric fractionation processes with a range of possible depths for fractionation of a low-MgO basalt.

The volumes of intermediate to evolved (>60 wt.% SiO_2) melt produced by fractional crystallization will be small compared to the volumes of cumulates, so polybaric crystallization may not be the only mechanism for the generation of arc granodioites. Previously proposed mixing models for the SNB (e.g., Reid et al. 1983; Frost and Mahood 1987; Sisson et al. 1996), require both a high-SiO_2 melt, and an evolved basalt similar to the HLMC parental melt. These models also resolve the problem of peraluminous melt compositions generated by lower crustal fractionation, because the homogenized products between non-peraluminous, low-Mg basalts and mildly peraluminous (i.e, ASI<1.1) granitic melts are consistent with batholith granitoid compositions (Blatter et al. 2013). Our modeling identifies a potential low-Mg basaltic end member composition (the HLMC parental melt) produced by lower crustal fractionation. We show that evolved basalts must be generated in the lower crust, and are thus available to participate in both mixing and polybaric crystallization proceses that contribute to the production of batholith-scale volumes of granodiorite.

2.8 CONCLUSIONS

The Late Cretaceous Hidden Lakes mafic complex is a preserved example of intrusion of melt into the upper crust of the Sierra Nevada batholith contemporaneously with more

voluminous felsic magmas. Bulk-compositions of lithologies ranging from olivine-norites to monzonites are consistent with fractional crystallization from a moderately hydrous basalt (3.1 wt% H_2O) at ~0.3 GPa, and oxidizing conditions (ΔNNO +1 to +3). The parental melt to the HLMC is a low-Mg basalt produced through differentiation in the lower crust prior to intruding into the upper crust.

We model this polybaric fractional crystallization process in two-stages, using alphaMELTS to calculate the composition of an evolving primitive arc basalt at 1.1 GPa in the lower crust (Stage 1) and constructing a mass balance model for upper crustal fractionation based on measured cumulate and liquid-like sample compositions (Stage 2). Our model indicates 33% mass fractionation in the lower crust, followed by extraction to upper crustal pressures and subsequent fractionation to form all HLMC cumulates and melt compositions. Polybaric fractionation of mantle-derived basalt to produce granodiorite resolves the disagreement between the prevalence of lower crustal cumulates in arcs and experimental data that suggest lower crustal fractionation will produce peraluminous melts inconsistent with arc batholith compositions.

The HLMC contains rock types that are lithologically and compositionally similar to those other upper crustal mafic complexes of the SNB, suggesting that these intrusions crystallized from hydrous, fractionated basalts of comparable compositions. Consequently, their composition may be governed by unifying rheologic characteristics that facilitate their ascent from the lower crust such as reduced density and viscosity.

2.9 Acknowledgements

We thank Joe Biasi, Allyson Trussel, and Ben Klein for their assistance in the field over the years, and thank Chi Ma for help with microprobe analyses and Nathan Dalleska for ICPMS support. We are grateful to Andrew Kylander-Clark and the UCSB Petrochronology lab, as well as Sarah George, Martin Pepper, and others at the Arizona Laserchron Center, for their assistance with zircon LA-ICPMS. The geochronology analyses were supported by a GSA AGeS2 award to M.Lewis.

2.10 References Cited

Ague JJ, Brimhall GH (1988) Magmatic arc asymmetry and distribution of anomalous plutonic belts in the batholiths of California: Effects of assimilation, crustal thickness, and depth of crystallization. Geological Society of America Bulletin 100(6):912-927

Almeev RR, Ariskin AA, Kimura J-I, Barmina GS (2013) The role of polybaric crystallization in genesis of andesitic magmas: phase equilibria simulations of the Bezymianny volcanic subseries. Journal of Volcanology and Geothermal Research 263:182-192

Annen C, Blundy J, Sparks R (2006) The genesis of intermediate and silicic magmas in deep crustal hot zones. Journal of Petrology 47(3):505-539

Arai S, Ishimaru S (2008) Insights into petrological characteristics of the lithosphere of mantle wedge beneath arcs through peridotite xenoliths: a review. Journal of Petrology 49(4):665-695

Armstrong JT (1995) Citzaf-a package of correction programs for the quantitative Electron Microbeam X-Ray-Analysis of thick polished materials, thin-films, and particles. Microbeam Analysis 4(3):177-200

Asimow PD, Ghiorso MS (1998) Algorithmic modifications extending MELTS to calculate subsolidus phase relations. American Mineralogist 83(9-10):1127-1132

Bas ML, Maitre RL, Streckeisen A, Zanettin B, Rocks ISotSoI (1986) A chemical classification of volcanic rocks based on the total alkali-silica diagram. Journal of petrology 27(3):745-750

Bateman PC (1992) Pre-Tertiary bedrock geologic map of the Mariposa 1° by 2° quadrangle, Sierra Nevada, California; Nevada. The Survey,

Bateman PC, Eaton JP (1967) Sierra Nevada Batholith: The batholith was generated within a synclinorium. Science 158(3807):1407-1417

Beattie P (1993) Olivine-melt and orthopyroxene-melt equilibria. Contributions to Mineralogy and Petrology 115(1):103-111

Blatter DL, Sisson TW, Hankins WB (2013) Crystallization of oxidized, moderately hydrous arc basalt at mid-to lower-crustal pressures: implications for andesite genesis. Contributions to Mineralogy and Petrology 166(3):861-886

Blundy JD, Holland TJ (1990) Calcic amphibole equilibria and a new amphibole-plagioclase geothermometer. Contributions to mineralogy and petrology 104(2):208-224

Brounce M, Kelley K, Cottrell E (2014) Variations in Fe3+/∑ Fe of Mariana Arc basalts and mantle wedge f O2. Journal of Petrology 55(12):2513-2536

Bucholz CE, Jagoutz O, Schmidt MW, Sambuu O (2014) Fractional crystallization of high-K arc magmas: biotite-versus amphibole-dominated fractionation series in the Dariv Igneous Complex, Western Mongolia. Contributions to Mineralogy and Petrology 168(5):1072

Bucholz CE, Spencer CJ (2019) Strongly Peraluminous Granites across the Archean–Proterozoic Transition. Journal of Petrology 60(7):1299-1348

Bucholz CE, Stolper EM, Eiler JM, Breaks FW (2018) A comparison of oxygen fugacities of strongly peraluminous granites across the Archean–Proterozoic boundary. Journal of Petrology 59(11):2123-2156

Cawthorn RG, Brown PA (1976) A model for the formation and crystallization of corundum-normative calc-alkaline magmas through amphibole fractionation. The Journal of Geology 84(4):467-476

Cawthorn RG, O'Hara MJ (1976) Amphibole fractionation in calc-alkaline magma genesis. American Journal of Science 276(3):309-329

Cervantes P, Wallace PJ (2003) Role of H2O in subduction-zone magmatism: new insights from melt inclusions in high-Mg basalts from central Mexico. Geology 31(3):235-238

Chapman AD, Saleeby JB, Wood DJ, Piasecki A, Kidder S, Ducea MN, Farley KA (2012) Late Cretaceous gravitational collapse of the southern Sierra Nevada batholith, California. Geosphere 8(2):314-341

Chapman JB, Gehrels GE, Ducea MN, Giesler N, Pullen A (2016) A new method for estimating parent rock trace element concentrations from zircon. Chemical Geology 439:59-70

Coleman D, Glazner A, Miller J, Bradford K, Frost T, Joye J, Bachl C (1995) Exposure of a Late Cretaceous layered mafic-felsic magma system in the central Sierra Nevada Batholith, California. Contributions to Mineralogy and Petrology 120(2):129-136

Debari S, Kay SM, Kay R (1987) Ultramafic xenoliths from Adagdak volcano, Adak, Aleutian Islands, Alaska: deformed igneous cumulates from the Moho of an island arc. The Journal of Geology 95(3):329-341

Debari SM, Sleep NH (1991) High-Mg, low-Al bulk composition of the Talkeetna island arc, Alaska: Implications for primary magmas and the nature of arc crust. Geological Society of America Bulletin 103(1):37-47

DeCelles PG, Ducea MN, Kapp P, Zandt G (2009) Cyclicity in Cordilleran orogenic systems. Nature Geoscience 2(4):251-257

Dodge F, Calk L, Kistler R (1986) Lower crustal xenoliths, Chinese Peak lava flow, central Sierra Nevada. Journal of Petrology 27(6):1277-1304

Dodge F, Lockwood J, Calk L (1988) Fragments of the mantle and crust from beneath the Sierra Nevada batholith: Xenoliths in a volcanic pipe near Big Creek, California. Geological Society of America Bulletin 100(6):938-947

Domenick MA, Kistler RW, Dodge F, Tatsumoto M (1983) Nd and Sr isotopic study of crustal and mantle inclusions from the Sierra Nevada and implications for batholith petrogenesis. Geological Society of America Bulletin 94(6):713-719

Ducea M, Saleeby J (1998) A case for delamination of the deep batholithic crust beneath the Sierra Nevada, California. International Geology Review 40(1):78-93

Ducea MN (2001) The California arc: Thick granitic batholiths, eclogitic residues, lithospheric-scale thrusting, and magmatic flare-ups. GSA today 11(11):4-10

Ducea MN, Paterson SR, DeCelles PG (2015) High-volume magmatic events in subduction systems. Elements 11(2):99-104

Ducea MN, Saleeby JB (1996) Buoyancy sources for a large, unrooted mountain range, the Sierra Nevada, California: Evidence from xenolith thermobarometry. Journal of Geophysical Research: Solid Earth 101(B4):8229-8244

English JM, Johnston ST, Wang K (2003). Thermal modelling of the Laramide orogeny: testing the flat-slab subduction hypothesis. Earth and Planetary Science Letters *214*(3-4):619-632

Erdmann M, Koepke J (2016) Silica-rich lavas in the oceanic crust: experimental evidence for fractional crystallization under low water activity. Contributions to Mineralogy and Petrology 171(10):83

Fliedner MM, Klemperer SL, Christensen NI (2000) Three-dimensional seismic model of the Sierra Nevada arc, California, and its implications for crustal and upper mantle composition. Journal of Geophysical Research: Solid Earth 105(B5):10899-10921

Frost TP (1987) Sample localities, radiometric ages, descriptions, and major-and trace-element abundances of Late Jurassic mafic plutonic rocks, eastern Sierra Nevada, California. Department of the Interior, US Geological Survey,

Frost TP, Mahood GA (1987) Field, chemical, and physical constraints on mafic-felsic magma interaction in the Lamarck Granodiorite, Sierra Nevada, California. Geological Society of America Bulletin 99(2):272-291

Gehrels GE, Valencia VA, Ruiz J (2008) Enhanced precision, accuracy, efficiency, and spatial resolution of U-Pb ages by laser ablation–multicollector–inductively coupled plasma–mass spectrometry. Geochemistry, Geophysics, Geosystems 9(3)

Ghiorso MS, Sack RO (1995) Chemical mass transfer in magmatic processes IV. A revised and internally consistent thermodynamic model for the interpolation and extrapolation of liquid-solid equilibria in magmatic systems at elevated temperatures and pressures. Contributions to Mineralogy and Petrology 119(2-3):197-212

Greene AR, DeBari SM, Kelemen PB, Blusztajn J, Clift PD (2006) A detailed geochemical study of island arc crust: the Talkeetna arc section, south–central Alaska. Journal of Petrology 47(6):1051-1093

Grove TL, Elkins-Tanton LT, Parman SW, Chatterjee N, Müntener O, Gaetani GA (2003) Fractional crystallization and mantle-melting controls on calc-alkaline differentiation trends. Contributions to Mineralogy and Petrology 145(5):515-533

Guo L, Jagoutz O, Shinevar WJ, Zhang HF (2020) Formation and composition of the Late Cretaceous Gangdese arc lower crust in southern Tibet. Contributions to Mineralogy and Petrology 175:58

Hamada M, Fujii T (2008) Experimental constraints on the effects of pressure and H 2 O on the fractional crystallization of high-Mg island arc basalt. Contributions to Mineralogy and Petrology 155(6):767-790

Hamada M, Okayama Y, Kaneko T, Yasuda A, Fujii T (2014) Polybaric crystallization differentiation of H 2 O-saturated island arc low-K tholeiite magmas: a case study of the Izu-Oshima volcano in the Izu arc. Earth, Planets and Space 66(1):1-10

Holland JE, Surpless B, Smith DR, Loewy SL, Lackey JS (2013) Intrusive history and petrogenesis of the Ash Mountain Complex, Sierra Nevada batholith, California (USA). Geosphere 9(4):691-717

Icenhower JP, London D (1997) Partitioning of fluorine and chlorine between biotite and granitic melt: experimental calibration at 200 MPa H 2 O. Contributions to Mineralogy and Petrology 127(1-2):17-29

Jagoutz O (2014) Arc crustal differentiation mechanisms. Earth and Planetary Science Letters 396:267-277

Jagoutz O, Klein B (2018) On the importance of crystallization-differentiation for the generation of SiO2-rich melts and the compositional build-up of arc (and continental) crust. American Journal of Science 318(1):29-63

Jagoutz OE (2010) Construction of the granitoid crust of an island arc. Part II: a quantitative petrogenetic model. Contributions to Mineralogy and Petrology 160(3):359-381

Jochum KP, Nohl U, Herwig K, Lammel E, Stoll B, Hofmann AW (2005) GeoReM: a new geochemical database for reference materials and isotopic standards. Geostandards and Geoanalytical Research 29(3):333-338

Johnson D, Hooper P, Conrey R (1999) XRF analysis of rocks and minerals for major and trace elements on a single low dilution Li-tetraborate fused bead. In: Advances in X-ray Analysis, v, 41, p 843–867 Le Bas, MJ, vol. Citeseer,

Jones CH, Phinney RA (1998) Seismic structure of the lithosphere from teleseismic converted arrivals observed at small arrays in the southern Sierra Nevada and vicinity, California. Journal of Geophysical Research: Solid Earth 103(B5):10065-10090

Kay SM, Kay R (1985) Role of crystal cumulates and the oceanic crust in the formation of the lower crust of the Aleutian arc. Geology 13(7):461-464

Kelemen, PB, Aharanov, E (1998) Periodic formation of magma fractures and generation of layered gabbros in the lower crust beneath oceanic spreading ridges. Geophysical Monograph-America Geophysical Union 106:267-290

Kelley KA, Cottrell E (2009) Water and the oxidation state of subduction zone magmas. Science 325(5940):605-607

Kirsch M, Paterson SR, Wobbe F, Ardila AMM, Clausen BL, Alasino PH (2016). Temporal histories of Cordilleran continental arcs: Testing models for magmatic episodicity. American Mineralogist, 101(10): 2133-2154.

Klein BZ, Jagoutz OE (2021) Construction of a trans-crustal magma system: Building the Bear Valley Intrusive Suite, southern Sierra Nevada, California. Earth and Planetary Science Letters, 553:116624

Köhler T, Brey G (1990) Calcium exchange between olivine and clinopyroxene calibrated as a geothermobarometer for natural peridotites from 2 to 60 kb with applications. Geochimica et Cosmochimica Acta 54(9):2375-2388

Krawczynski MJ, Grove TL, Behrens H (2012) Amphibole stability in primitive arc magmas: effects of temperature, H 2 O content, and oxygen fugacity. Contributions to Mineralogy and Petrology 164(2):317-339

Kress VC, Carmichael IS (1991) The compressibility of silicate liquids containing Fe2O3 and the effect of composition, temperature, oxygen fugacity and pressure on their redox states. Contributions to Mineralogy and Petrology 108(1-2):82-92

Kylander-Clark AR, Hacker BR, Cottle JM (2013) Laser-ablation split-stream ICP petrochronology. Chemical Geology 345:99-112

Lackey JS, Valley JW, Saleeby JB (2005) Supracrustal input to magmas in the deep crust of Sierra Nevada batholith: Evidence from high-δ18O zircon. Earth and Planetary Science Letters 235(1-2):315-330

Lackey, JS, Valley, JW, Chen, JH, Stockli, DF (2008). Dynamic magma systems, crustal recycling, and alteration in the central Sierra Nevada batholith: The oxygen isotope record. Journal of Petrology, 49(7):1397-1426

Leake BE, Woolley AR, Arps CE, Birch WD, Gilbert MC, Grice JD, Hawthorne FC, Kato A, Kisch HJ, Krivovichev VG (1997) Nomenclature of amphiboles; report of the subcommittee on amphiboles of the International Mineralogical Association, Commission on New Minerals and Mineral Names. The Canadian Mineralogist 35(1):219-246

Lee, C-TA, Bachmann, O (2014). How important is the role of crystal fractionation in making intermediate magmas? Insights from Zr and P systematics. Earth and Planetary Science Letters, 393:266-274

Lee C-TA, Cheng X, Horodyskyj U (2006) The development and refinement of continental arcs by primary basaltic magmatism, garnet pyroxenite accumulation, basaltic recharge and delamination: insights from the Sierra Nevada, California. Contributions to Mineralogy and Petrology 151(2):222-242

Lee C-T, Rudnick RL, Brimhall Jr GH (2001) Deep lithospheric dynamics beneath the Sierra Nevada during the Mesozoic and Cenozoic as inferred from xenolith petrology. Geochemistry, Geophysics, Geosystems 2(12)

Lockwood J, Bateman P (1976) Geologic map of the Shaver Lake 15-minute quadrangle, central Sierra Nevada, California: US Geological Survey. Geologic Quadrangle Map GQ-1271, scale 1(62,500)

Mason RA (1992) Models of order and iron-fluorine avoidance in biotite. The Canadian Mineralogist 30(2):343-354

Mayo EB (1941) Deformation in the interval Mt. Lyell-Mt. Whitney, California. Bulletin of the Geological Society of America 52(7):1001-1084

Melekhova E, Blundy J, Robertson R, Humphreys MC (2015) Experimental evidence for polybaric differentiation of primitive arc basalt beneath St. Vincent, Lesser Antilles. Journal of Petrology 56(1):161-192

Middlemost EA (1994) Naming materials in the magma/igneous rock system. Earth-Science Reviews 37(3-4):215-224

Miller DM, Goldstein SL, Langmuir CH (1994) Cerium/lead and lead isotope ratios in arc magmas and the enrichment of lead in the continents. Nature 368(6471):514-520

Mukhopadhyay B (1991) Garnet breakdown in some deep seated garnetiferous xenoliths from the central Sierra Nevada: petrologic and tectonic implications. Lithos 27(1):59-78

Mukhopadhyay B, Manton W (1994) Upper-mantle fragments from beneath the Sierra Nevada Batholith: partial fusion, fractional crystallization, and metasomatism in a subduction related ancient lithosphere. Journal of Petrology 35(5):1417-1450

Müntener O, Kelemen PB, Grove TL (2001) The role of H2O during crystallization of primitive arc magmas under uppermost mantle conditions and genesis of igneous pyroxenites: an experimental study. Contributions to Mineralogy and Petrology 141(6):643-658

Müntener O, Ulmer P (2018) Arc crust formation and differentiation constrained by experimental petrology. American Journal of Science 318(1):64-89

Mutch E, Blundy J, Tattitch B, Cooper F, Brooker R (2016) An experimental study of amphibole stability in low-pressure granitic magmas and a revised Al-in-hornblende geobarometer. Contributions to Mineralogy and Petrology 171(10):85

Nadin, ES, Saleeby, JB, Wong, M.(2016) Thermal evolution of the Sierra Nevada batholith, California, and implications for strain localization. Geosphere, 12(2):377-399

Nadin ES, Saleeby JB, Wright J, Shervais J (2008) Disruption of regional primary structure of the Sierra Nevada batholith by the Kern Canyon fault system, California. Special Papers-Geological Society of America 438:429

Nandedkar RH, Ulmer P, Müntener O (2014) Fractional crystallization of primitive, hydrous arc magmas: an experimental study at 0.7 GPa. Contributions to Mineralogy and Petrology 167(6):1015

Oliver TA (1951) The effect of uralitization upon the chemical composition of the Sudbury norite. American Mineralogist: Journal of Earth and Planetary Materials 36(5-6):421-429

Otamendi JE, Ducea MN, Bergantz GW (2012) Geological, petrological and geochemical evidence for progressive construction of an arc crustal section, Sierra de Valle Fertil, Famatinian Arc, Argentina. Journal of Petrology 53(4):761-800

Peselnick L, Lockwood JP, Stewart R (1977) Anisotropic elastic velocities of some upper mantle xenoliths underlying the Sierra Nevada batholith. Journal of Geophysical Research 82(14):2005-2010

Pickett DA, Saleeby JB (1993) Thermobarometric constraints on the depth of exposure and conditions of plutonism and metamorphism at deep levels of the Sierra Nevada batholith, Tehachapi Mountains, California. Journal of Geophysical Research: Solid Earth 98(B1):609-629

Piispanen R, Alapieti T (1977) Uralitization-an example from Kuusamo, Finland. Bulletin of the Geological Society of Finland 49(2):39-46

Portnyagin M, Hoernle K, Plechov P, Mironov N, Khubunaya S (2007) Constraints on mantle melting and composition and nature of slab components in volcanic arcs from volatiles (H2O, S,

Cl, F) and trace elements in melt inclusions from the Kamchatka Arc. Earth and Planetary Science Letters 255(1-2):53-69

Pullen A, Ibáñez-Mejia M, Gehrels GE, Giesler D, Pecha M (2018) Optimization of a laser ablation-single collector-inductively coupled plasma-mass spectrometer (Thermo Element 2) for accurate, precise, and efficient zircon U-Th-Pb geochronology. Geochemistry, Geophysics, Geosystems 19(10):3689-3705

Putirka KD (2008) Thermometers and barometers for volcanic systems. Reviews in mineralogy and geochemistry 69(1):61-120

Ratajeski K, Glazner AF, Miller BV (2001) Geology and geochemistry of mafic to felsic plutonic rocks in the Cretaceous intrusive suite of Yosemite Valley, California. Geological Society of America Bulletin 113(11):1486-1502

Reid Jr JB, Evans OC, Fates DG (1983) Magma mixing in granitic rocks of the central Sierra Nevada, California. Earth and Planetary Science Letters 66:243-261

Ross DC (1985) Mafic: gneissic complex (batholithic root?) in the southernmost Sierra Nevada, California. Geology 13(4):288-291

Ross DC (1989) The metamorphic and plutonic rocks of the southernmost Sierra Nevada, California, and their tectonic framework. In, vol.,

Rowe MC, Kent AJ, Nielsen RL (2009) Subduction influence on oxygen fugacity and trace and volatile elements in basalts across the Cascade Volcanic Arc. Journal of Petrology 50(1):61-91

Ruppert S, Fliedner MM, Zandt G (1998) Thin crust and active upper mantle beneath the southern Sierra Nevada in the western United States. Tectonophysics 286(1-4):237-252

Saleeby J, Ducea MN, Busby C, Nadin E, Wetmore PH, Wright J, Shervais J (2008) Chronology of pluton emplacement and regional deformation in the southern Sierra Nevada batholith, California. Special Papers- Geological Society of America 438:397

Sams DB, Saleeby JB (1988) Geology and petrotectonic significance of crystalline rocks of the southernmost Sierra Nevada, California.

Schmidt MW, Jagoutz O (2017) The global systematics of primitive arc melts. Geochemistry, Geophysics, Geosystems 18(8):2817-2854

Sisson T, Grove T, Coleman D (1996) Hornblende gabbro sill complex at Onion Valley, California, and a mixing origin for the Sierra Nevada batholith. Contributions to Mineralogy and Petrology 126(1-2):81-108

Sisson T, Layne G (1993) H2O in basalt and basaltic andesite glass inclusions from four subduction-related volcanoes. Earth and Planetary Science Letters 117(3-4):619-635

Sisson T, Ratajeski K, Hankins W, Glazner AF (2005) Voluminous granitic magmas from common basaltic sources. Contributions to Mineralogy and Petrology 148(6):635-661
Soesoo A (2000) Fractional crystallization of mantle-derived melts as a mechanism for some I-type granite petrogenesis: an example from Lachlan Fold Belt, Australia. Journal of the geological Society 157(1):135-149

Smith PM, Asimow PD (2005) Adiabat_1ph: A new public front-end to the MELTS, pMELTS, and pHMELTS models. Geochemistry, Geophysics, Geosystems 6(2)

Stolz A, Jochum K, Spettel B, Hofmann A (1996) Fluid-and melt-related enrichment in the subarc mantle: evidence from Nb/Ta variations in island-arc basalts. Geology 24(7):587-590

Sun, S. S., & McDonough, W. F. (1989). Chemical and isotopic systematics of oceanic basalts: implications for mantle composition and processes. Geological Society, London, Special Publications, 42(1), 313-345

Ulmer P, Kaegi R, Müntener O (2018) Experimentally derived intermediate to silica-rich arc magmas by fractional and equilibrium crystallization at 1· 0 GPa: an evaluation of phase relationships, compositions, liquid lines of descent and oxygen fugacity. Journal of Petrology 59(1):11-58

Vermeesch P (2018) IsoplotR: A free and open toolbox for geochronology. Geoscience Frontiers 9(5):1479-1493

Walker BA, Bergantz GW, Otamendi JE, Ducea MN, Cristofolini EA (2015) A MASH zone revealed: the mafic complex of the Sierra Valle Fértil. Journal of Petrology 56(9):1863-1896

Waters LE, Lange RA (2015) An updated calibration of the plagioclase-liquid hygrometer-thermometer applicable to basalts through rhyolites. American Mineralogist 100(10):2172-2184

2.11 FIGURES AND CAPTIONS

Figure 1

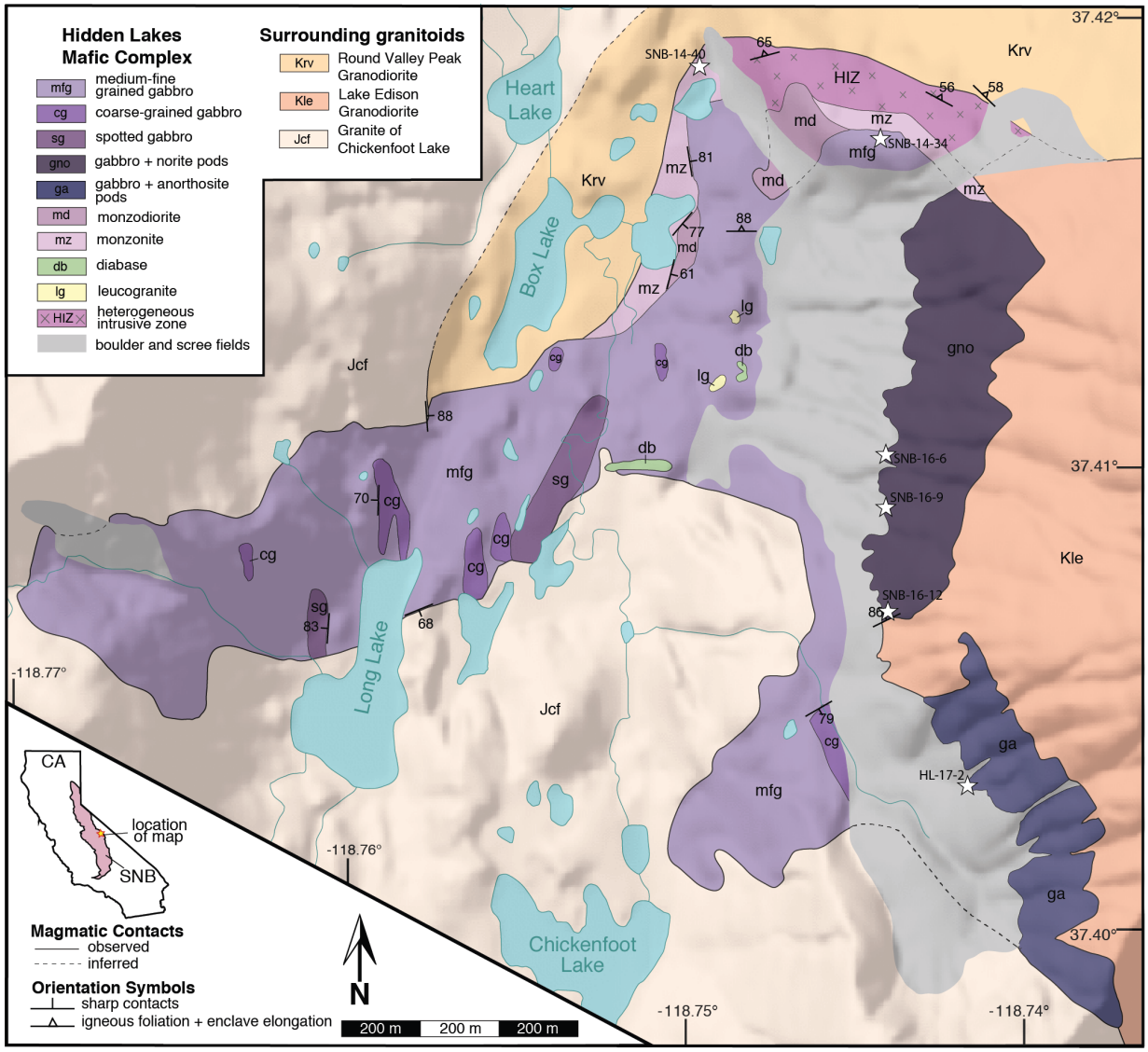

Figure 1 Geologic map of the Hidden Lakes mafic complex study area and surrounding granite and granodiorite plutons, located in the central Eastern Sierra Nevada Mountains. Star symbols mark the locations of samples used for geochronology, and sample numbers are shown adjacent to the symbols. See Supplementary Material for all sample GPS locations. Contacts within HLMC and those that define the boundary of the mafic complex are based on our own field mapping. Some contacts may be gradational over several meters, as described in the text, but are indicated by sharp contacts here. Locations of contacts between the felsic plutons (Kle, Krv, and Jcf) are based on Bateman (1992).

Figure 2

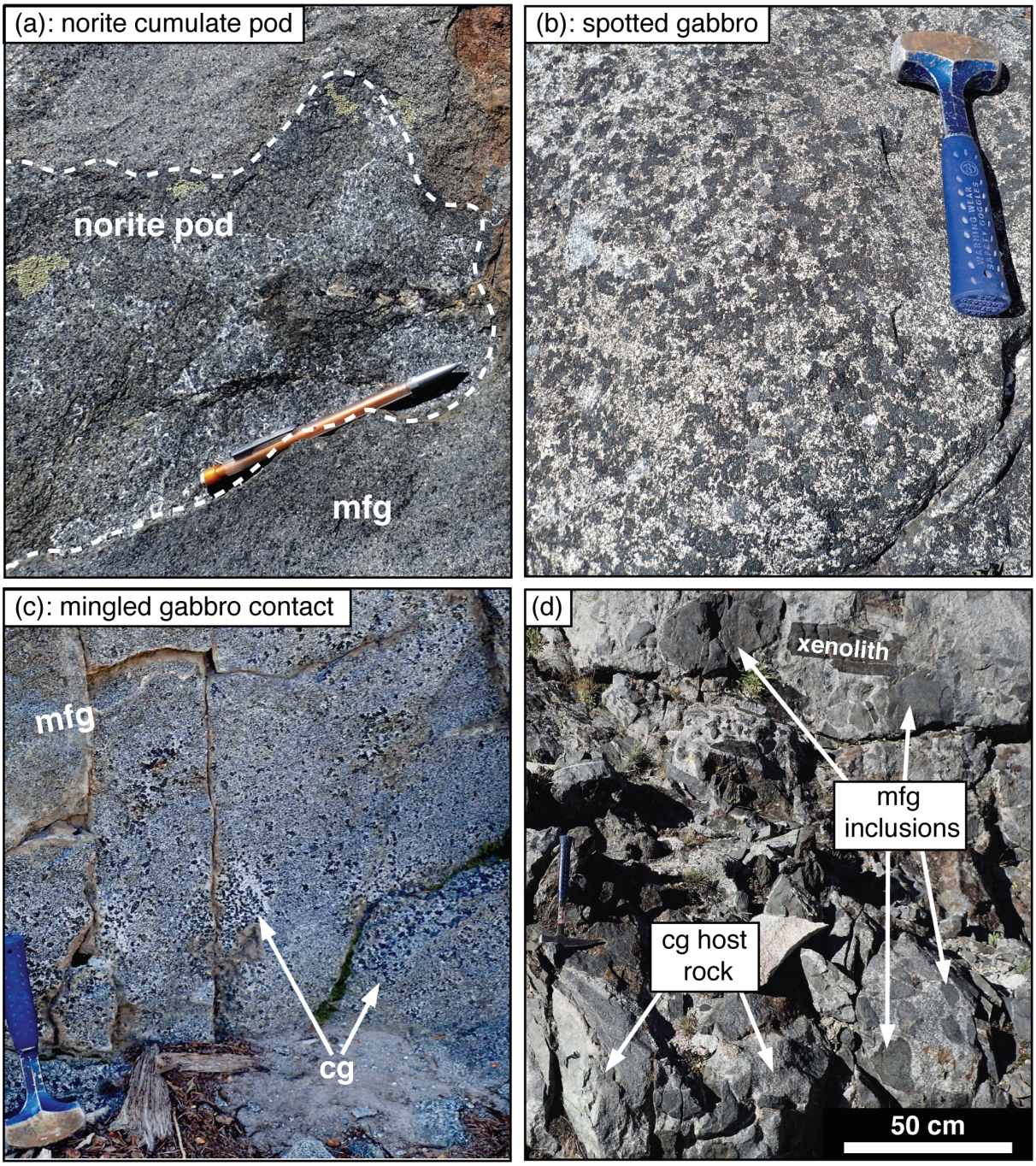
(a): norite cumulate pod
norite pod
mfg
(b): spotted gabbro
(c): mingled gabbro contact
mfg
cg
(d)
xenolith
mfg inclusions
cg host rock
50 cm

Figure 2 Photos of gabbros and norite in the field. See Figure 1 legend for unit abbreviations. **a** A pod of norite with light colored interstitial plagioclase, surrounded by medium-fine grained gabbro. Pencil is 15 cm. **b** Amphibole oikocrysts in the spotted gabbro unit. **c** Contact zone between intrusions of fine-grained gabbro (homogeneous gray) and coarse-grained gabbro (speckled). Small clumps of amphibole crystals or single amphibole crystals are disaggregated into the medium-fine grained gabbro. In b and c, the hammer is 28 cm long. **d** Inclusions of medium-fine grained gabbro (dark gray) and a metasedimentary xenolith (rare in HLMC) contained within a coarse-grained gabbro intrusion. Note the 50 cm scale bar.

Figure 3

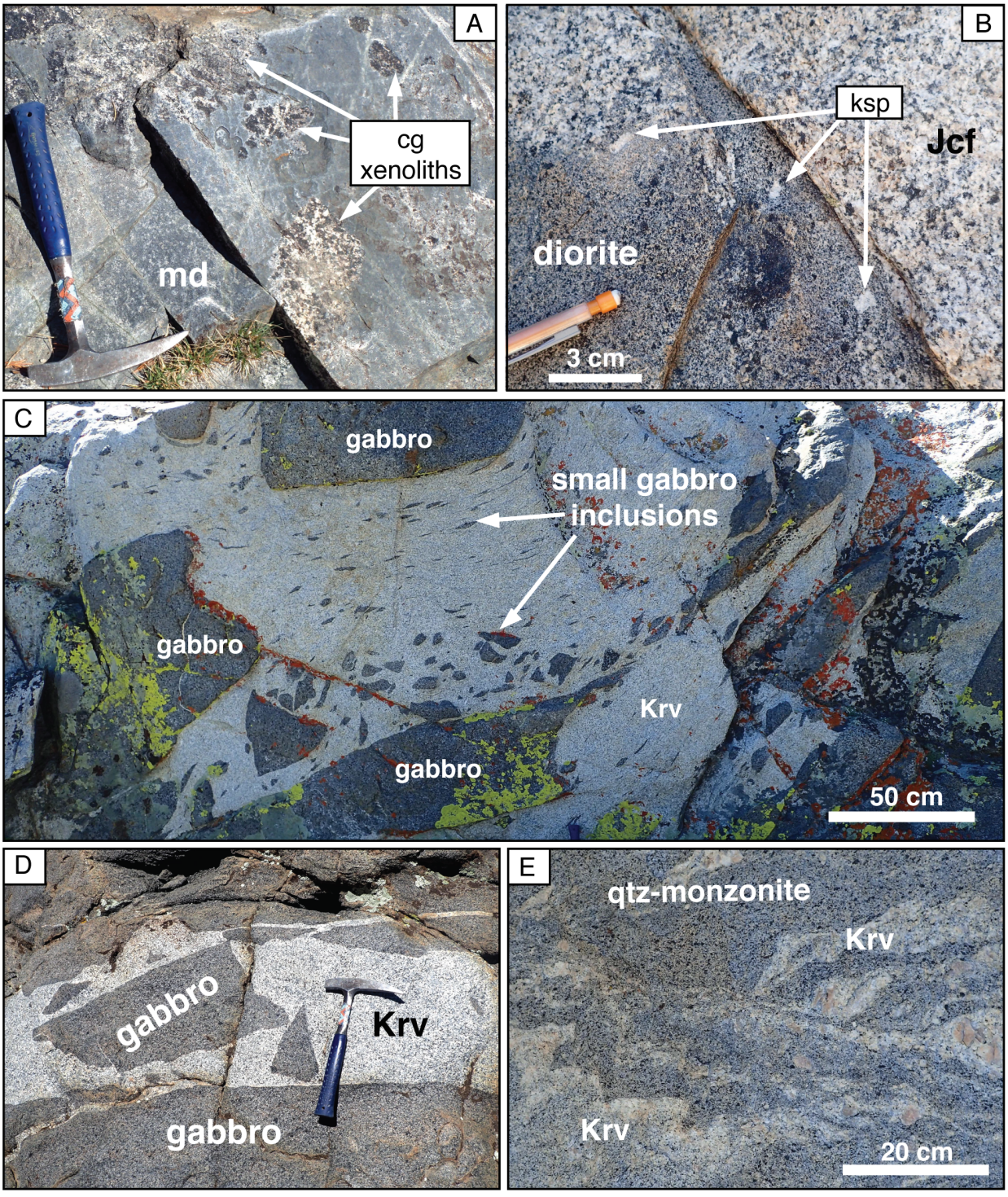
A
cg
xenoliths
md
B
ksp
Jcf
diorite
3 cm
C
gabbro
small gabbro
inclusions
gabbro
Krv
gabbro
50 cm
D
gabbro
Krv
gabbro
E
qtz-monzonite
Krv
Krv
20 cm

Figure 3 Examples of contact relationships in the study area. Unit abbreviations are as in Figure 1. **a** Angular xenoliths of gabbro contained within a finer grained monzodiorite. **b** Contact zone between the granite of Chickenfoot Lake (Jcf) and HLMC gabbro, which is hybridized to a diorite near its margins. Coarse K-feldspars (ksp) from Jcf are engulfed in the diorite. **c** Representative outcrop from the heterogeneous intrusive zone (HIZ). Gabbroic blocks sourced from HLMC are hosted in the Round Valley Peak granodiorite (Krv) up to 150 m from HLMC. **d** Dike of Krv cutting through HLMC gabbro and containing gabbroic blocks. **e** Krv mingled with a quartz monzonite in the HIZ, which is a result of mixing between Krv and HLMC mafic material. Hammers in a and c are 33 cm long. Note scale bars in b, c, and e.

Figure 4

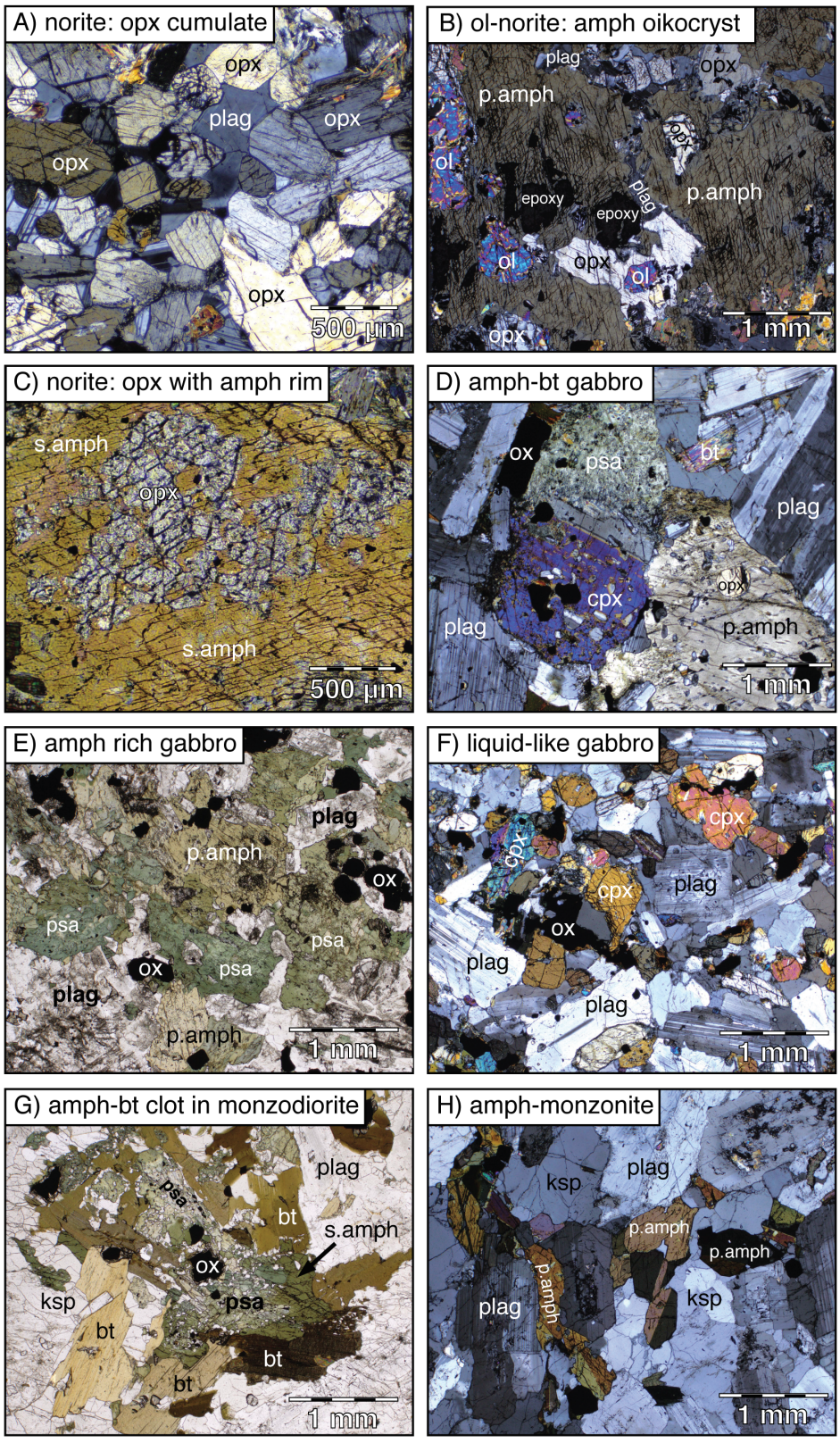
A) norite: opx cumulate
opx
plag
opx
opx
opx
opx
500 µm
B) ol-norite: amph oikocryst
plag
opx
p.amph
opx
ol
epoxy
plag
epoxy
p.amph
ol
opx
ol
opx
1 mm
C) norite: opx with amph rim
s.amph
opx
s.amph
500 µm
D) amph-bt gabbro
ox
psa
bt
plag
cpx
opx
plag
p.amph
1 mm
E) amph rich gabbro
plag
p.amph
ox
psa
psa
ox
psa
plag
p.amph
1 mm
F) liquid-like gabbro
cpx
opx
cpx
plag
ox
plag
plag
1 mm
G) amph-bt clot in monzodiorite
plag
psa
bt
s.amph
ox
ksp
psa
bt
bt
bt
1 mm
H) amph-monzonite
ksp
plag
p.amph
p.amph
p.amph
plag
ksp
1 mm

Figure 4 Photomicrographs of various rock types and textures. a-d, f, and h were taken in cross-polarized light. e and g were taken in plain-polarized light. Mineral abbreviations: p.amph = primary magmatic amphibole, s.amph = secondary magmatic amphibole (rims on pyroxenes), psa = pseudomorphic amphibole (pyroxene replacement), bt = biotite, cpx = clinopyroxene, opx = orthopyroxene, ksp = K-feldspar, plag = plagioclase, ox = Fe-Ti-oxide, ol = olivine. **a** Opx-rich norite adcumulate with interstitial plagioclase , SNB-14-59. **b** Poikolitic amphibole-bearing norite with olivine and orthopyroxene chadacrysts within coarse amphibole crystal, SNB-14-62. **c** Orthopyroxene surrounded by rim of secondary magmatic amphibole in a norite, SNB-14-48. **d** Coarse-grained gabbro containing clinopyroxene, amphibole, biotite, plagioclase, and Fe-Ti-oxides. The upper half of the clinopyroxene crystal has been converted to green amphibole, SNB-16-02. **e** Amphibole-rich medium-finegrained gabbro with both primary magmatic amphibole (honey colored), pseudomorphic amphibole (green), plagioclase, and Fe-Ti-oxides, SNB-18-3. **f** Medium-fine grained gabbro with clinopyroxene, plagioclase, and Fe-Ti-oxides, representative of a non-cumulate texture, SNB-14-54. **g** Monzodiorite with an amphibole-biotite clot, containing both secondary magmatic amphibole and pseudomorphic amphibole. The pseudomorphs were originally pyroxene with a secondary magmatic amphibole rim, SNB-16-18. **h** Representative monzonite with primary magmatic amphibole, plagioclase, and K-feldspar.

Figure 5

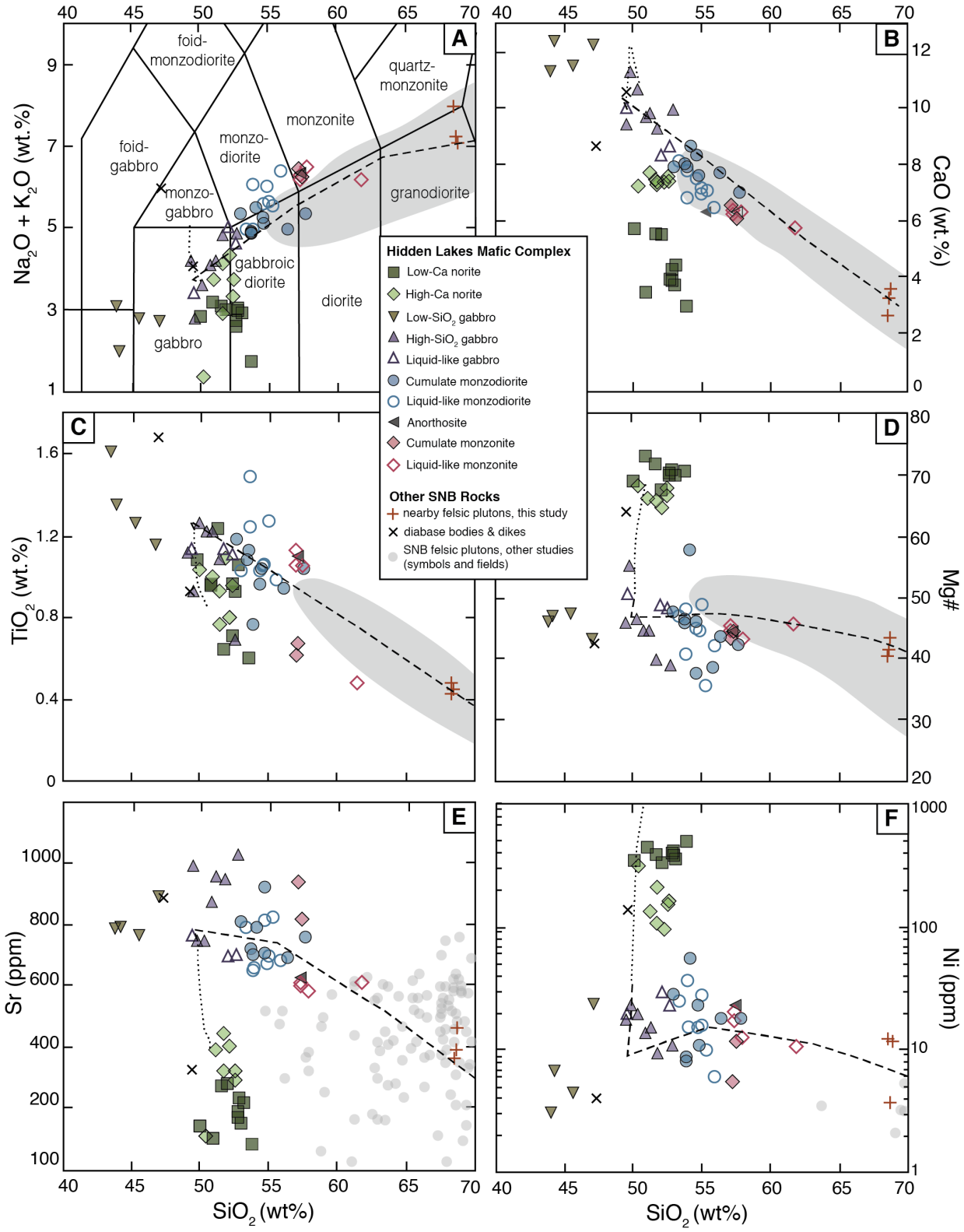
A
B
C
D
E
F
foid-monzodiorite
quartz-monzonite
monzonite
foid-gabbro
monzo-diorite
monzo-gabbro
granodiorite
gabbroic diorite
diorite
gabbro
Na2O + K2O (wt.%)
CaO (wt.%)
TiO2 (wt.%)
Mg#
Sr (ppm)
Ni (ppm)
SiO2 (wt%)
SiO2 (wt%)
Hidden Lakes Mafic Complex
Low-Ca norite
High-Ca norite
Low-SiO2 gabbro
High-SiO2 gabbro
Liquid-like gabbro
Cumulate monzodiorite
Liquid-like monzodiorite
Anorthosite
Cumulate monzonite
Liquid-like monzonite
Other SNB Rocks
nearby felsic plutons, this study
diabase bodies & dikes
SNB felsic plutons, other studies (symbols and fields)

Figure 5 Bulk-rock major element, trace element, and Mg# vs SiO_2 diagrams for all analyzed HLMC samples. Filled symbols represent samples with cumulate signatures and open symbols represent liquid-like bulk compositions, as defined by criteria discussed in the text. Plus signs indicate felsic plutons surrounding the HLMC, analyzed in this study. Black dotted and dashed lines show the results of our LLD model. Dotted lines indicate lower crustal fractionation (modeled in alphaMELTS) and dashed lines trace the upper crustal LLD (mass balance model). The SNB fields in a-d represent over 800 samples. In the trace element plots (e,f), SNB compositions are plotted as single points rather than fields, because there are far fewer published analyses available. Note that Ni (panel f) is plotted on a log scale. Gray fields and circles define the compositions present in the bulk of the SNB (from the GEOROC database, http://georoc.mpch-mainz.gwdg.de/georoc/).

Figure 6

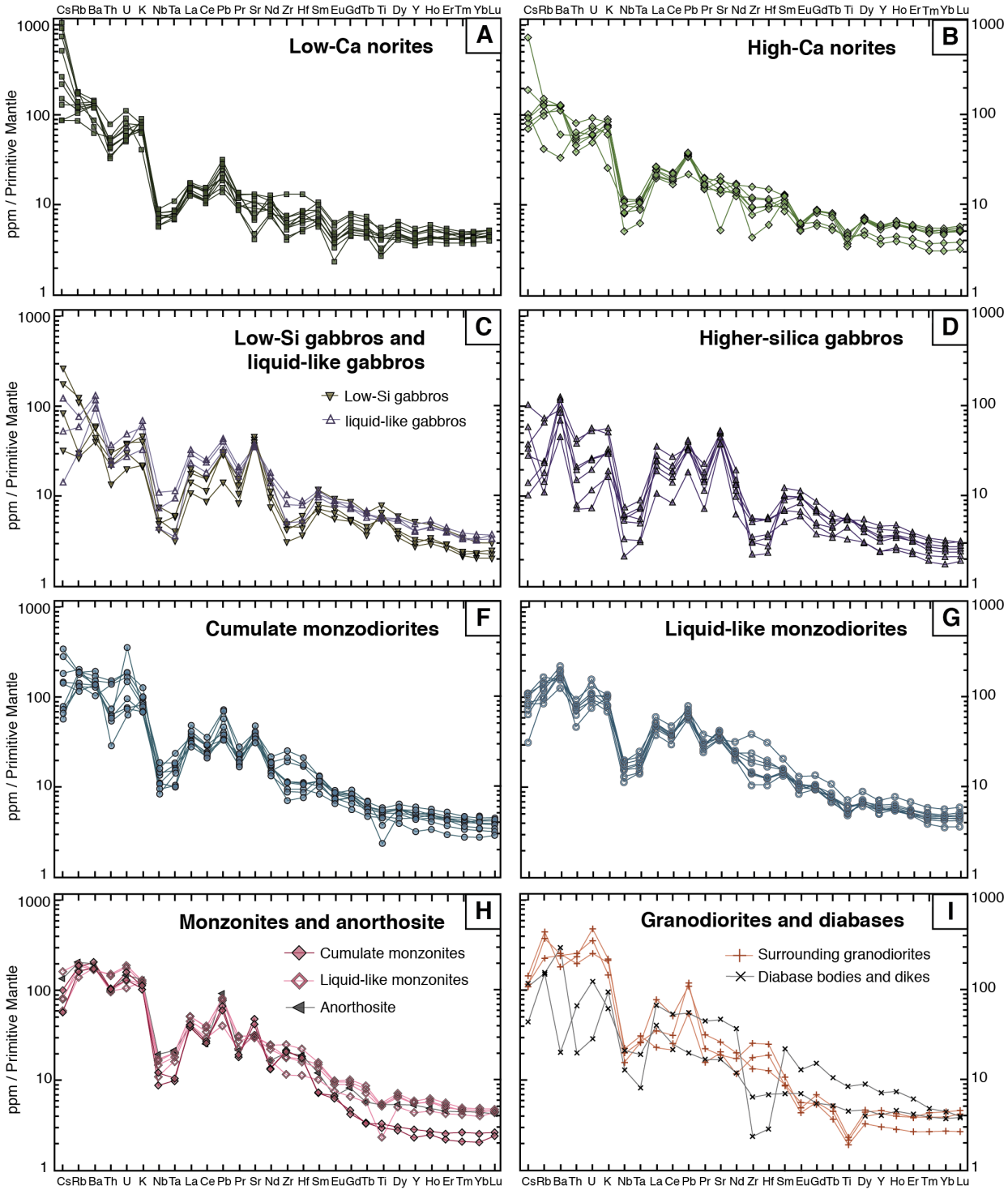
Cs Rb Ba Th U K Nb Ta La Ce Pb Pr Sr Nd Zr Hf Sm Eu Gd Tb Ti Dy Y Ho Er Tm Yb Lu
ppm / Primitive Mantle
1000
100
10
1
A
Low-Ca norites
B
High-Ca norites
C
Low-Si gabbros and liquid-like gabbros
Low-Si gabbros
liquid-like gabbros
D
Higher-silica gabbros
F
Cumulate monzodiorites
G
Liquid-like monzodiorites
H
Monzonites and anorthosite
Cumulate monzonites
Liquid-like monzonites
Anorthosite
I
Granodiorites and diabases
Surrounding granodiorites
Diabase bodies and dikes

Figure 6 Bulk-rock trace element compositions for each sample, normalized to the primitive mantle (Sun and McDonough 1989) and separated by lithology. Open symbols represent liquid-like compositions and filled symbols represent cumulates. **a** low-Ca norites, **b** high-Ca norites, **c** liquid-like gabbros (purple triangles) and low-SiO_2 gabbros (brown triangles), **d** high-SiO_2 gabbros, **e** cumulate monzodiorites, **f** liquid-like monzodiorites, **g** liquid-like monzonites (pink open diamonds), cumulate monzonites (pink filled diamonds), and anorthosites (gray triangles), and **h** granodiorites (orange plus signs) and diabases (black X's).

Figure 7

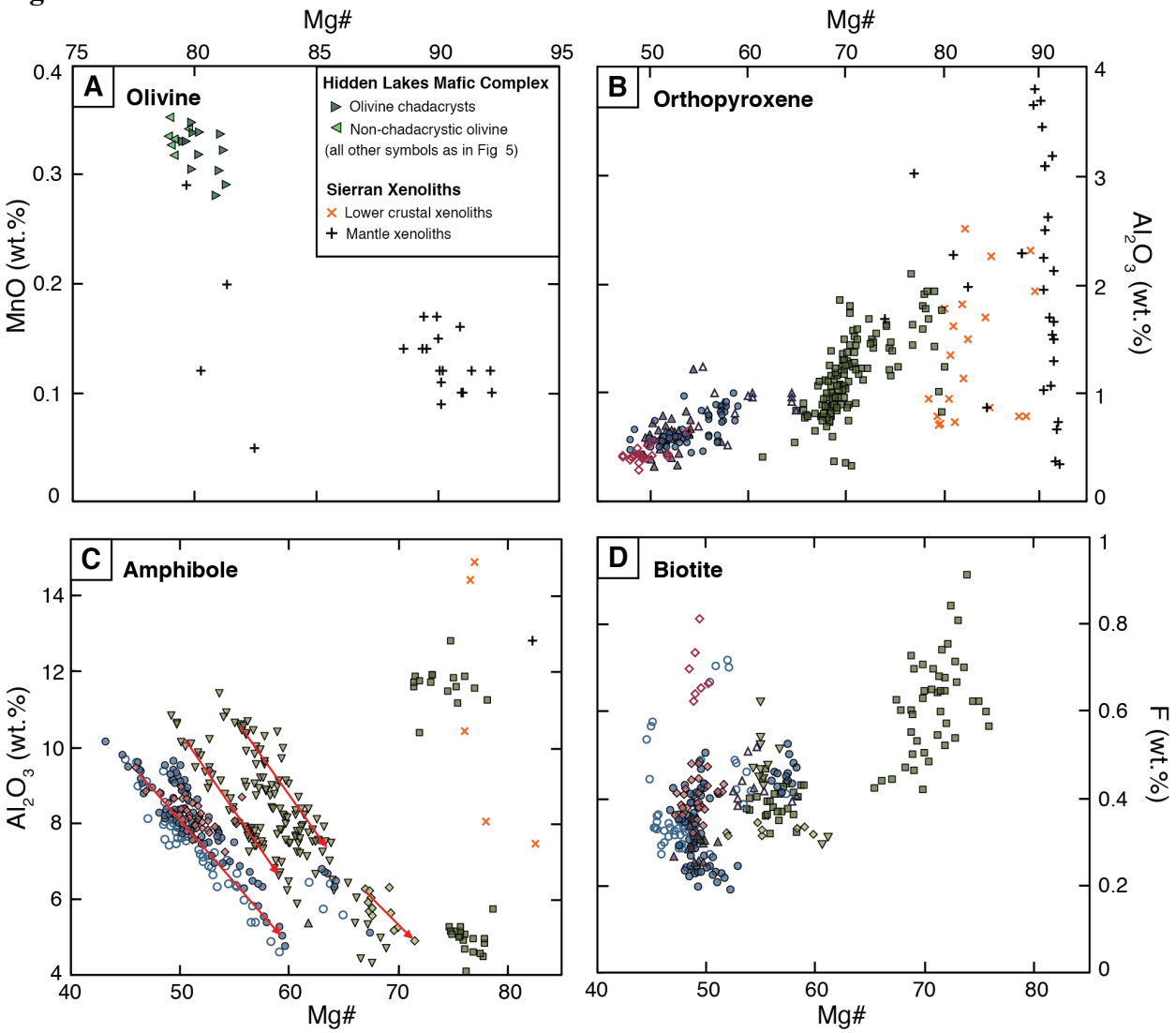

Figure 7 Selected mineral chemistry collected via EPMA. Each symbol represents one analysis. Symbols are the same as in Figure 5 unless otherwise noted, and the rock type indicated by the symbol is the rock type in which the mineral was analyzed. **a** MnO of olivine in HLMC low-Ca norites, **b** Al_2O_3 in orthopyroxene, **c** Al_2O_3 in primary magmatic, secondary magmatic overgrowths, and pseudomorphic amphibole, and **d** F in biotite. Red arrows in c indicate trends caused by subsolidus Tschermak's exchange. HLMC compositions are compared to mantle and lower crustal xenoliths hosted in Neogene volcanic rocks in the Sierra Nevada (Dodge et al. 1986; Dodge et al. 1988; Mukhopadhyay and Manton 1994; Lee et al. 2001; and Lee et al. 2006). No biotite analyses from the xenoliths have been reported.

Figure 8

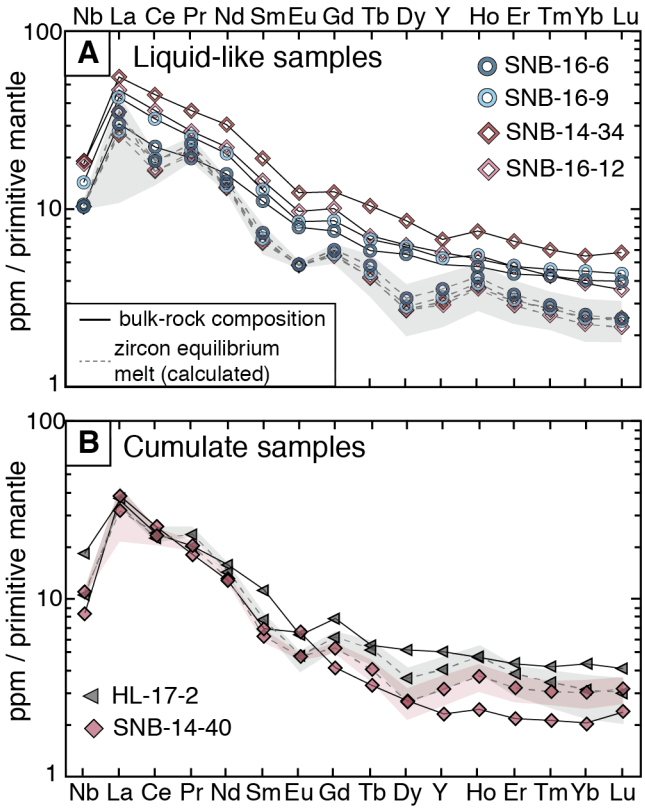

Figure 8 Primitive mantle normalized (Sun and McDonough 1989) REEs, Y, and Nb content of melts in equilibrium with zircons, in comparison to the corresponding bulk-rock compositions. Zircon parent magma compositions are calculated based on Chapman et al. (2016). Panel **a** shows samples with liquid-like bulk compositions and **b** shows samples of cumulate character. Solid black likes indicate bulk-rock compositions and dashed gray lines indicate calculated zircon parental melts. Shaded areas are error envelopes for the calculated melt compositions, given as 1 sigma standard deviation of melts calculated from all zircon analyses from a particular sample. All four zircon parental melts in **a** have very similar compositions, thus the errors are presented collectively. In **b**, the pink and gray shaded areas correspond to the cumulate monzonite SNB-14-40 and the anorthosite cumulate HL-17-2, respectively.

Figure 9

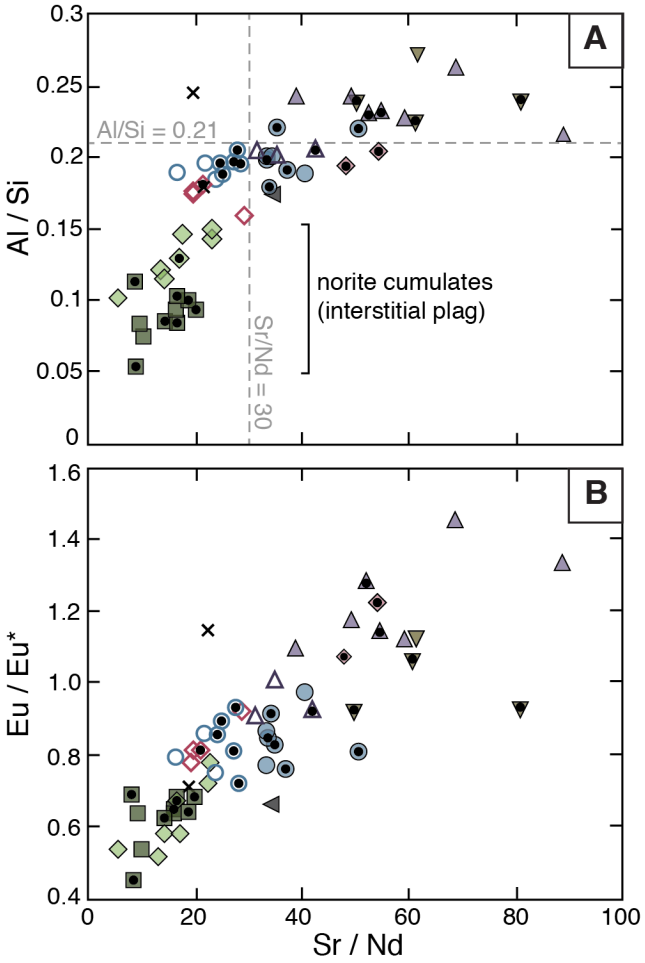

Figure 9 Bulk-rock major and trace element ratios used to distinguish cumulate and liquid-like samples. Sr/Nd ratio is compared to **a** Al/Si and **b** Eu anomaly, Eu/Eu* (primitive mantle normalized). All ratios indicate the accumulation of plagioclase, which has not significantly occurred in the norites. Symbols represent different rock types and are the same as in Figure 5. Filled symbols are cumulates and open symbols have liquid-like bulk compositions. The addition of a black circle inside of the symbol indicates petrographic observation of the sample texture.

Figure 10

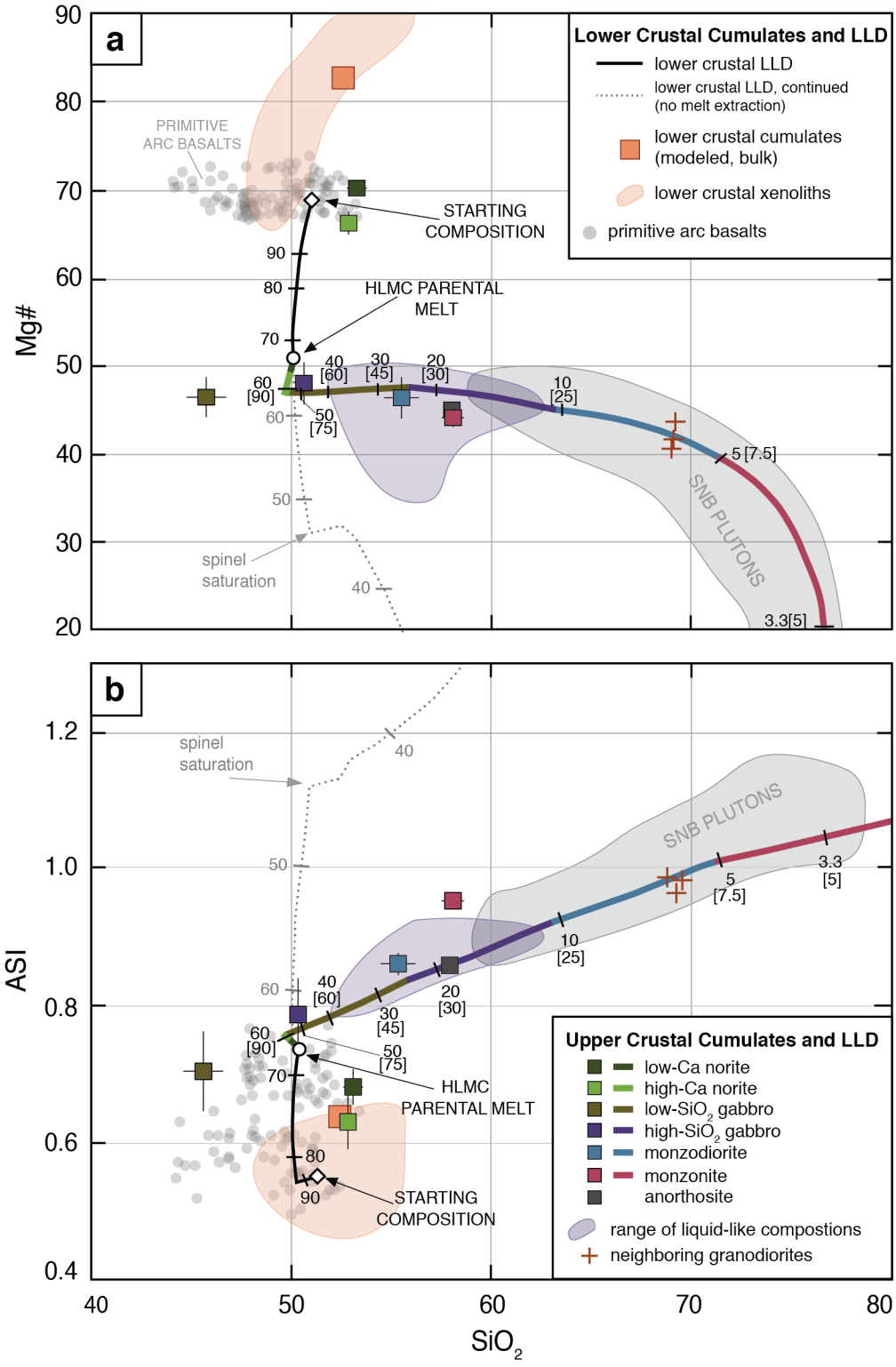
a
b
Lower Crustal Cumulates and LLD
lower crustal LLD
lower crustal LLD, continued (no melt extraction)
lower crustal cumulates (modeled, bulk)
lower crustal xenoliths
primitive arc basalts
PRIMITIVE ARC BASALTS
STARTING COMPOSITION
HLMC PARENTAL MELT
spinel saturation
SNB PLUTONS
Mg#
ASI
SiO2
Upper Crustal Cumulates and LLD
low-Ca norite
high-Ca norite
low-SiO2 gabbro
high-SiO2 gabbro
monzodiorite
monzonite
anorthosite
range of liquid-like compostions
neighboring granodiorites

Figure 10 Summary of LLD modeling, showing **a** Mg# and **b** ASI, relative to wt.% SiO_2. Mg# is calculated as Mg/(Mg+Fe) and ASI as Al/(Ca-1.67×P+Na+K). Colored squares are the average composition of the cumulate groups, full compositions given in Table 4. Error bars are 2σ of all bulk-rock compositions in a particular cumulate group. The diamond symbol indicates the primitive arc basalt composition used as the starting composition for Stage 1 fractionation. The circle symbols is the HLMC parental melt produced by Stage 1 fractionation and used as the staring composition for the Stage 2 model (compositions given in Table 3). The thick black line follows the Stage 1 LLD of a primitive arc basalt crystallizing at 1.1 GPa, modeled using alphaMELTS (Asimow and Ghiorso 1998; Ghiorso and Sack 1995). The dotted gray line is the LLD that would have been produced had the primitive arc basalt continued to fractionate in the lower crust instead of ascending after reaching an Mg# of 51. The thick colored line shows the trajectory of the Stage 2 upper crustal LLD calculated by incremental subtraction of cumulates. The colors of cumulate composition symbols (squares) match the line color when that cumulate is crystallizing. Ticks on the LLDs are spaced to show 10% fractionation by mass of the primitive arc basalt and the percent of crystallized mass is labeled at each tick. Numbers in brackets are the % fractionation by mass of the HLMC parental melt during Stage 2. The purple field shows the range of HLMC liquid-like gabbros, monzodiorites, and monzonites. Legends within a and b apply to both panels.

Figure 11

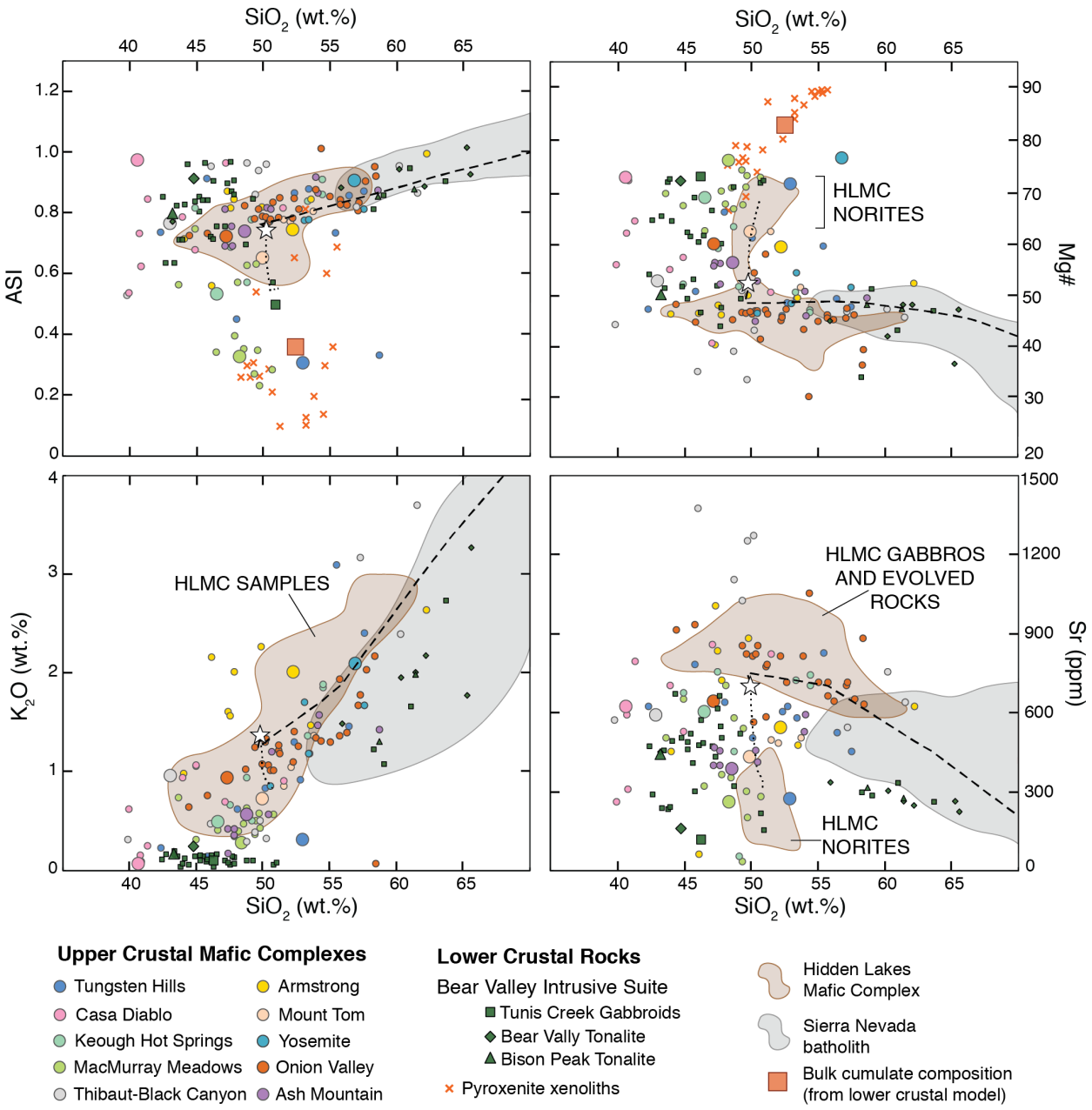
SiO2 (wt.%)
ASI
Mg#
HLMC NORITES
K2O (wt.%)
HLMC SAMPLES
Sr (ppm)
HLMC GABBROS AND EVOLVED ROCKS
HLMC NORITES
Upper Crustal Mafic Complexes
Tungsten Hills
Armstrong
Casa Diablo
Mount Tom
Keough Hot Springs
Yosemite
MacMurray Meadows
Onion Valley
Thibaut-Black Canyon
Ash Mountain
Lower Crustal Rocks
Bear Valley Intrusive Suite
Tunis Creek Gabbroids
Bear Vally Tonalite
Bison Peak Tonalite
Pyroxenite xenoliths
Hidden Lakes Mafic Complex
Sierra Nevada batholith
Bulk cumulate composition (from lower crustal model)

Figure 11 Bulk-rock compositions from other mafic complexes in the SNB upper crust (Frost 1987; Frost and Mahood 1987; Holland, et al. 2013; Ratajeski, et al. 2001; Sisson, et al. 1996), the lower crustal Bear Valley Intrusive Suite (Klein and Jagoutz 2021), and lower crustal xenoliths (Dodge et al. 1986; Dodge et al. 1988; Lee et al. 2006). Showing **a** ASI, **b** Mg#, **c** K_2O, and **d** Sr, relative to SiO_2. Larger symbols indicate the most primitive (highest Mg#) sample from each complex and the star denotes the HLMC parental melt composition used in our LLD model and given in Table 3. Note that the Sr content of the most primitive Yosemite sample was not determined. The brown fields encompass all HLMC samples, including both cumulate and liquid-like compositions. The dotted line represents our modeled lower crustal LLD and the dashed line is the upper crustal LLD. Xenolith K_2O and Sr contents are commonly below detection limit or not measured, and thus excluded. Gray fields are felsic compositions from the SNB upper crust, attained from the GEOROC database (http://georoc.mpch-mainz.gwdg.de/georoc/).

2.12 Tables

Table 1: Summary of Modal Mineralogies

	norite	gabbro (coarse-grained)	gabbro (medium-fine grained)	monzodiorite	monzonite	anorthosite
olivine	0-<1[a]	–	–	–	–	–
orthopyroxene	15-75	–	~5	–	0-<1	–
clinopyroxene	1-5	5-20	5-15	0-2	0-<1	–
plagioclase	15-40	45-70	65-75	60-70	40-60	90-95
amphibole	0-20	25-50	5-20	5-15	0-5	–
biotite	5-15	5-10	5-10	15-20	10-20	5-10
K-feldspar	0-<1	<1	<1	10-15	20-35	–
quartz	–	–	–	0-2	0-5	–

[a] all modal mineralogies are given in percent

Table 2: Calculated Crystallization Conditions

	Method	norites	gabbros	monzodiorites	monzonites
Temperature (°C)	Ca-in-opx[a]	900- 1170	930- 1100	970- 1030	850- 1010
	plag-amph pairs[b]	865- 950 (oikocrysts) 700- 765 (non-oikocrystic)	740- 815 (magmatic amph) 1040-1120 (pseudomorphic amph)	815- 870	800- 850
Pressure (GPa)	Al-in-amph[c]	[0.32][f]	[0.32]	[0.32]	0.32
H_2O (wt.%)	plag hygrometry[d]		2.9- 3.5		6-7
fO_2 (ΔNNO, ±1 log unit)	biotite[e]				0-0.6

[a] Method of Köhler and Brey (1990)
[b] Method of Blundy and Holland (1990)
[c] Method of Mutch et al. (2016)
[d] Method of Waters and Lange (2015)
[e] Method of Bucholz et al. (2018)
[f] Values in brackets indicate those that were not calculated from that particular rock type due to mineral assemblage constraints, but are assumed to be constant throughout the fractionation sequence (e.g. pressure and fO_2)

Table 3: Primitive and Calculated Melt Compositions

	Primitive arc basalt[a]	HLMC parental melt[b]	Arc-like granodiorite[c]
SiO_2[d]	50.00	48.82	67.49
TiO_2	0.84	1.20	0.44
Al_2O_3	12.46	16.86	15.87
FeO(T)	9.57	10.33	3.43
MnO	0.12	0.19	0.26
MgO	11.86	6.06	1.36
CaO	10.77	9.72	3.63
Na_2O	1.48	2.33	3.43
K_2O	0.77	1.20	3.95
P_2O_5	0.13	0.20	0.14
H_2O	2.00	3.10	–
Total	100.00	100.00	100.00
Mg#	68.83	51.12	41.48
ASI	0.55	0.75	0.97
Cr	235	50	13
Ni	1300	36	5
Rb	38.0	57.0	153.0
Sr	430	700	387
Y	13.5	19.0	32.3
Zr	58	90	411
Nb	3.7	5.8	20.0
Ba	385	590	1917
La	9.8	15.4	49.0
Ce	21.5	32.0	101.0
Pr	2.9	4.5	13.0
Nd	12.5	19.0	55.0
Sm	3.00	4.30	8.60
Eu	0.80	1.30	2.10
Gd	3.00	4.20	7.90
Tb	0.47	0.61	1.26
Dy	2.90	3.80	7.60
Ho	0.56	0.74	1.67
Er	1.45	1.90	4.00
Tm	0.20	0.27	0.47
Yb	1.30	1.68	3.40
Lu	0.19	0.24	0.50
Hf	1.70	2.50	9.90
Ta	0.21	0.35	1.53
Pb	4.2	6.6	22.2
Th	2.2	3.6	15.2
U	0.72	1.17	4.75

[a] Within range of primitive continental arc lavas (Schmidt and Jagoutz, 2017)
[b] Produced by Stage 1 model, input into Stage 2 model
[c] Produced by Stage 2 fractionation, SiO_2 content of average SNB
[d] Major element oxides given in wt.%, trace element concentrations given in ppm

Table 4: Cumulate Compositions used in Upper Crustal LLD Model

	Low-Ca norite		High-Ca norite		Low-SiO_2 gabbro		High-SiO_2 gabbro		Monzodiorite		Monzonite	
	N=10[a]	2σ	N=7	2σ	N=4	2σ	N=7	2σ	N=8	2σ	N=2	2σ
SiO_2	53.19	2.05	52.90	1.12	46.29	2.63	50.15	1.49	55.46	3.27	57.72	1.04
TiO_2	0.94	0.48	0.97	0.25	1.45	0.40	1.25	0.24	1.04	0.26	1.09	0.26
Al_2O_3	8.00	3.53	11.61	3.11	18.31	3.95	19.24	2.19	18.79	2.29	17.42	1.31
FeO(T)	12.98	2.16	11.00	1.80	12.67	4.00	9.35	1.47	7.42	2.42	7.38	0.17
MnO	0.24	0.09	0.21	0.08	0.16	0.05	0.24	0.26	0.13	0.13	0.18	0.37
MgO	17.33	3.05	12.24	3.21	6.21	2.60	4.96	2.58	3.61	1.69	3.35	0.27
CaO	4.47	2.27	7.64	0.31	12.07	1.03	10.22	1.50	8.06	0.97	6.40	0.61
Na_2O	0.98	0.42	1.55	0.95	1.93	0.62	3.39	1.01	3.35	0.53	3.59	0.03
K_2O	1.84	0.76	1.82	1.12	0.75	0.56	0.72	0.66	1.83	0.60	2.53	0.24
P_2O_5	0.04	0.02	0.07	0.14	0.14	0.23	0.47	0.40	0.31	0.09	0.34	0.03
Total	100.00	–	100.00	–	100.00	–	100.00	–	100.00	–	100.00	–
Mg#	70.42	1.69	66.48	2.59	46.66	3.62	48.62	10.04	46.45	11.45	44.74	1.87
ASI	0.68	0.08	0.63	0.11	0.71	0.12	0.79	0.13	0.86	0.05	0.88	0.00
Cr	459	142	221	182	7.0	16.6	43	89	32	27	8.1	0.1
Ni	401	106	170	154	4.8	19.3	18.1	9.3	16.6	30.7	8.7	8.9
Rb	86.3	43.7	74.1	46.5	50.1	58.5	12.0	23.4	90.0	35.3	97.9	17.0
Sr	186	125	327	218	783	114	848	213	764	154	877	164
Y	19.7	4.9	24.0	7.8	16.5	9.1	16.5	7.0	21.2	6.8	11.4	3.3
Zr	74	58	116	84	45	17	40	29	149	138	221	2
Nb	5.2	1.4	6.7	3.2	4.0	1.9	3.2	2.0	8.7	4.6	7.0	3.0
Ba	812	406	734	559	297	105	569	394	872	322	1200	231
La	10.5	2.5	16.5	3.9	9.2	5.2	14.5	10.7	22.4	7.7	25.3	2.0
Ce	22.9	6.3	36.0	7.5	20.1	11.0	28.9	21.5	42.6	16.1	44.1	3.0
Pr	3.1	1.0	4.9	1.1	3.0	1.6	3.8	2.7	5.4	1.8	4.8	0.3
Nd	13.4	4.9	20.5	4.7	13.7	7.6	16.5	11.6	21.4	6.8	17.2	0.3
Sm	3.50	1.4	5.11	1.45	3.61	1.85	3.79	2.12	4.86	1.33	3.04	0.03
Eu	0.73	0.40	1.00	0.15	1.14	0.50	1.39	0.68	1.28	0.27	1.04	0.13
Gd	3.55	1.45	4.84	1.45	3.67	1.89	3.71	1.98	4.43	1.14	2.55	0.29
Tb	0.60	0.21	0.80	0.25	0.50	0.25	0.52	0.20	0.61	0.15	0.35	0.00
Dy	3.78	1.16	4.78	1.56	3.22	1.53	3.24	1.08	3.78	1.12	2.08	0.23
Ho	0.78	0.21	0.96	0.34	0.59	0.26	0.62	0.21	0.75	0.22	0.41	0.05
Er	2.18	0.49	2.57	0.92	1.51	0.63	1.63	0.48	1.97	0.60	1.11	0.26
Tm	0.33	0.06	0.38	0.14	0.23	0.11	0.23	0.07	0.29	0.10	0.17	0.04
Yb	2.17	0.39	2.35	0.89	1.32	0.60	1.43	0.43	1.86	0.61	1.11	0.36
Lu	0.35	0.06	0.37	0.14	0.18	0.06	0.21	0.05	0.27	0.07	0.18	0.03
Hf	2.34	1.37	3.32	1.76	1.48	0.58	1.16	0.82	3.77	2.82	5.10	0.05
Ta	0.33	0.10	0.41	0.15	0.18	0.11	0.19	0.18	0.58	0.37	0.40	0.04
Pb	4.1	2.1	6.6	2.3	4.3	2.7	5.4	2.5	8.2	5.3	10.6	1.8
Th	4.2	2.2	5.0	2.4	2.0	1.1	1.2	0.6	6.0	6.1	7.9	0.2
U	1.5	0.8	1.4	0.6	0.7	0.3	0.4	2.7	2.2	3.6	2.7	0.8

[a] N= the number of samples averaged to establish a representative cumulate composition
[b] Major element oxides given in wt.%, trace element concentrations given in ppm

2.13 Supplementary Figures

Supplementary Figure 1

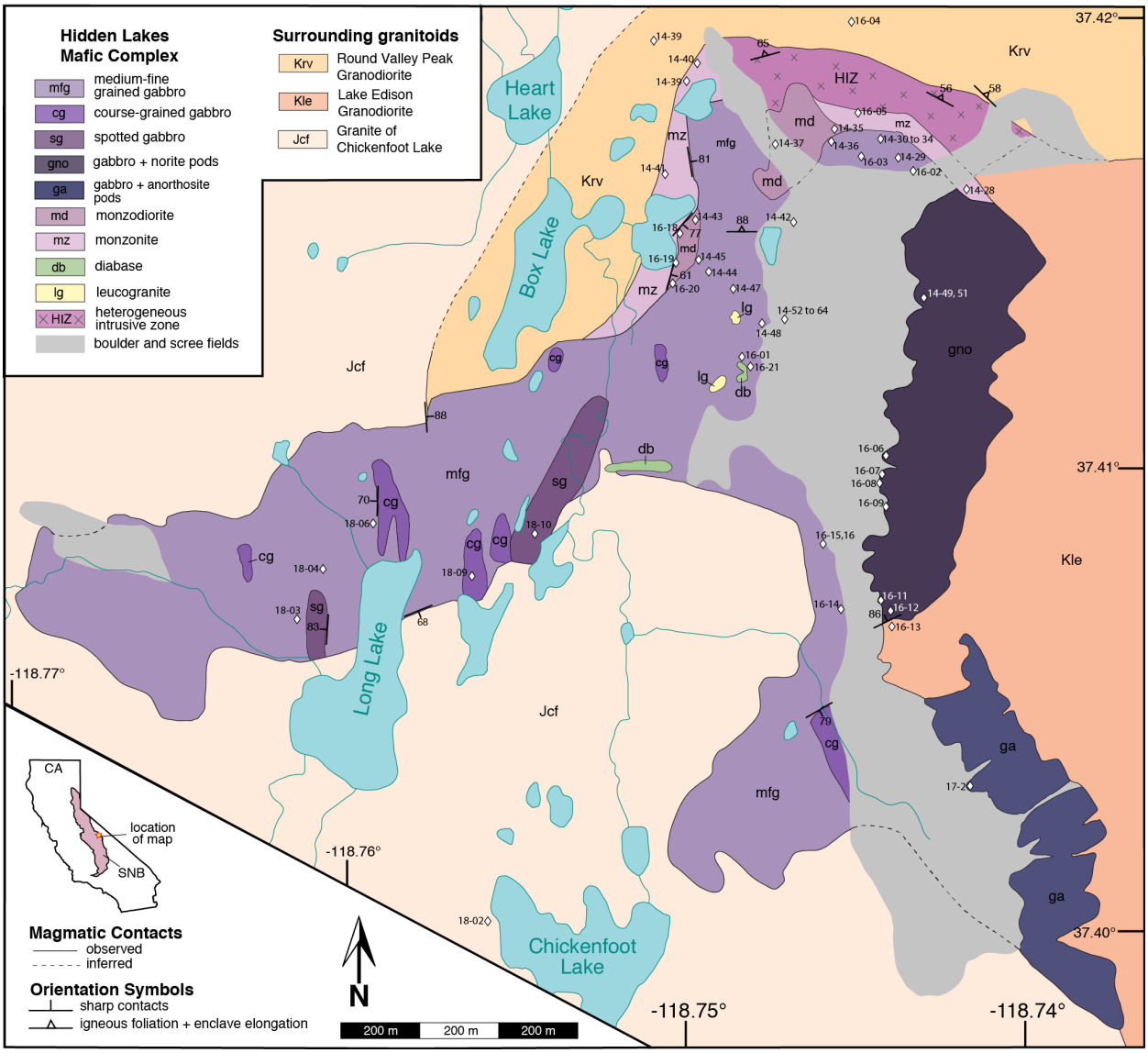

Supplementary Figure 1 Geologic map of HLMC with sample locations. All geology, symbols, and colors are as in Fig 1. GPS locations of samples can be found in the Supplementary Data File. Diamonds represent sample locations. Sample names have been shortened to contain only the final 3-4 digits listed in the Supplementary Data file, for clarity.

APPENDIX TO CHAPTER 2

Development of a Solution ICP-MS Protocol for High Precision Bulk-rock Trace Element Analysis in Li-borate Glasses

2.14 INTRODUCTION

Chapter 2 briefly describes a method for analyzing trace element concentrations in rock samples using solution inductively coupled plasma mass spectrometry (ICPMS). We developed the analytical protocol for this method in the Environmental Analysis Center at Caltech, which has since been utilized for many samples by users from multiple labs. Details of the method procedure are as follows.

We developed a method to analyze an extensive suite of trace elements (Fig A1, Table A1) that are present in low abundances in most rock samples (on orders 0.1-1000 ppm), but that are useful for interrogating petrologic problems. These elements are typically near or below the limits of quantification for X-ray fluorescence spectrometry (XRF) analysis. Thus, we utilize a solution ICPMS method to more precisely analyze these elements. Our method utilizes chips of Li-borate glass beads that are first prepared for major-element XRF analysis, and are generally not subsequently needed. However, it is possible to re-fuse XRF beads after removing a chip for the ICPMS method if a bead needs to be re-analyzed by XRF. Many solution ICPMS methods for trace element analysis in rocks make use of rock powders. Powders contain fragments of highly refractory phases (e.g. zircon, chromite, etc) that are difficult to fully digest completely, yet are rich in many of the analyzed trace elements. These procedures typically require multiple digestion, heating, and drying steps, and may involve transferring the sample between multiple containers. The glass beads are much more easily dissolved, as the original mineral phases are dissolved into the Li-borate flux and homogenized at high temperature. Thus, we are able to complete full digestion within one heating step and in one container, reducing both the time and

labor required for digestion, as well as the potential for cross contamination that is introduced when transferring solutions between containers.

2.15 Digestion Procedure

Glass beads are fused using Li-borate flux and dehydrated rock powder in a 10:1 ratio, as intended for XRF analyses (e.g. methods of Bucholz and Spencer 2019). Notably, an agate ball mill is used for powdering rock samples, which avoids trace element contamination associated with tungsten carbide crushing vessels (W, Nb, Ta). After XRF analysis to measure major element and some trace element contents, glass beads are shattered in a plastic bag and 25 ± 1 mg chips of glass are weighed into 50 mL polypropylene RackLock DigiTubes and capped. Exact chip weights (accuracy to 0.1 mg) are recorded for correction after analysis. Tubes are ideally stored upright to prevent bead chips from sticking to the walls of the tube or inside of the cap, but this issue can be resolved with the use of an anti-static gun and gently tapping the side of the tube before opening.

The digestion steps were completed in the Caltech Environmental Analysis Center. In a fume hood approved for use with concentrated nitric and hydrofluoric acids, we loaded tubes into an acrylic rack designed for use with a 24-sample heating block. Tubes were then uncapped and 2 mL of a 3:1 mixture of concentrated nitric acid (70%) and hydrofluoric acid (50%) was pipetted into each tube. All tubes were then capped and the acrylic rack was transferred to the heating block. We heated the tubes for 8 hours at 99°C to ensure full dissolution of the bead chips, then allowed the tubes to cool to room temperature in the heating block for at least 3 hours. Occasionally flakes of plastic from the tube would dislodge into the solution, but these did not appear to affect the analyses as the flakes sink to the bottom of the tube where they do not

interfere with the ICPMS autosampler. The acrylic rack and tubes were then removed from the heating block, and tubes were gently tapped before opening to cause any condensed droplets on the cap to fall into the tube. 28 mL of 2% nitric acid was then dispensed into each tube to bring the final volume up to 30 mL. If the final volume was slightly below 30 mL after this step, either due to vapor escape during the heating process or a bubble in the line while dispensing the 2% nitric acid, we used a dropper to bring the final volume up to 30 mL. As there is a slight possibility that some concentrated acid could be transferred to the outside of the tubes at this stage, tubes are left in the fume hood overnight to ensure that any remaining concentrated acids have evaporated. At this stage, the tubes can be handled with nitrile gloves (rather than rubber gloves) and are ready for analysis. We do not re-use the polypropylene tubes because they become brittle after the heating step.

2.16 ICPMS Procedure

We use an Agilent 8800 triple quadrupole ICPMS running in helium collision mode (He flow rate 4.3 mL/min) for the trace element analyses. Operation of the instrument and data processing are both accomplished using the Agilent MassHunter software.

Standard, Blank, and Quality Control Solutions

Calibration standards were prepared from Li-borate beads made using USGS standard powders of high silica (RGM-1, rhyolite), moderate silica (AGV-2, andesite) and low silica (BHVO-2, basalt) lithologies. These tubes are run as calibration standards once at the beginning of each batch and interspersed as unknown samples throughout the batch. This standardization procedure has since been improved by using a mixture of high purity solutions of the analyzed

elements. To create a range of standard solution concentrations, five different dilutions of the element mixture solution are added to a flux blank (see below), which is used to replicate the Li-borate concentrations of the sample solutions. USGS standard bead solutions are still analyzed as samples throughout the runs for monitoring the agreement between measured and accepted concentrations.

Flux blank solutions are prepared for each bottle of Li-borate flux by digesting a 25 mg bead chip from a glass bead fused with no rock powder. Blanks are run with the calibration standards at the beginning of the batch.

We also prepare a quality control solution (QC) from a mixture of samples in the batch, so that the QC is representative of the compositions being analyzed in that particular batch. This solution is run multiple times at the start of the batch to stabilize the recorded elemental count rates, and run between every 5-10 samples following. The consistency of these measurements is used to monitor and correct for drift in the instrument.

Virtual Internal Standard

We use an on-line virtual internal standard solution (VIS) consisting of known concentrations of elements that are typically not geologically relevant to monitor and correct for time- and mass-dependent drift in the ICPMS measurements. The solution consists of 5 ppm Be and 100 ppb each of Rh, In, Re, and Bi in a 2% nitric acid solution, to span the range of masses in the analyzed trace element suite. This solution is introduced continuously into the nebulizer on a separate line from the sample, such that the VIS is analyzed during all samples, standards, and blanks. We do not calculate a measured concentration of these elements, but rather monitor the count rate to assess ionizing and counting efficiency at different masses over time. Because these

elements are introduced, their concentrations in the sample cannot be measured, though these specific elements were selected because they are not commonly used for geological studies.

Batch Set-Up and Run

During the instrument warm-up stages, we input a Ca solution in order to coat the sampling and skimmer cones in an easily removed material before introducing the Li-borate solutions. Alone, the Li-borate solutions deposit a hard crust on the cones that is very difficult to remove and can clog the apertures. The Ca coating does not prevent this Li-borate crust from forming, but makes it easier to remove between analytical batches. Thus, both cones are inspected and cleaned often between batches.

The sample and VIS solutions are introduced into the ICPMS by separate Tygon tubing, at 5 and 0.3 mL/min flow rates, respectively, with an uptake time of 24 s per sample. We use three stages of 5% nitric acid rinses between each standard and unknown analysis to ensure that the previous solution has been fully flushed from the system. Dwell times for each analyte range from 0.03 to 0.8 s (Table A1) and 100 sweeps through all analytes results in a total run time of approximately 6.2 minutes per tube, including rinses. Each analysis uses approximately 2 mL of solution, which should be accounted for when preparing enough QC solution for the full batch.

The analytical batch begins with 10 analyses of the QC solution to ensure that analytical counts stabilize. This is followed by analysis of the standards and blank(s). If multiple bottles of flux were used to make the beads in the batch, flux blanks made from each bottle of flux are included. The remainder of the run is organized into “blocks”, which each begin with an analysis of the QC, followed by 5 to 10 unknowns. The run ends with a final analysis of the QC. The run length is limited by the capacity of the autosampler, which can hold a total of 84 50 mL tubes

and must include all standards, blanks, the QC, and samples. However, shorter runs (~40 samples or less) typically return better results as there is less time for instrument drift.

2.17 Data Processing

MassHunter

Counts per second (CPS) values are recorded continuously into the Agilent MassHunter program during the run, allowing us to monitor the QC solution for consistency. We then use the GeoREM database preferred values (Jochum, et al. 2005) for generating calibration curves based on the CPS and accepted concentrations of the standards. Accepted concentrations are adjusted based on the relative bead chip weights of the standards. Linear calibrations using the four standards and at least one flux blank are deemed acceptable if the linear R-value is >0.9, and points may be removed from the calibration for individual elements if they are anomalous. If multiple flux blanks are needed for a single batch, the calibration curves and sample concentrations are calculated separately for each flux blank. A correction is applied for differences in the bead chip weights using the Total Dilution function. In addition, the MassHunter VIS correction is applied, which uses variation in the counts of elements in the VIS solution to interpolate mass dependent variation in instrument sensitivity over time.

Drift Correction

After exporting the concentration data from MassHunter, we perform an external drift adjustment based on variability in the measured QC concentration. A hypothetical example of this calculation is illustrated in Figure A2. This is beneficial, because though the VIS correction accounts for some mass-dependent drift, Cheatham et al. (1993) find that mass- and time-

dependent drift in ICPMS analyses are non-linear, and thus not easily predicted by internal standard corrections. We do not perform this adjustment if the QC values are beyond 10% of the average from the initial two QCs (those that bracket the standards) and instead re-run the samples in the associated blocks.

This method assumes that drift for each element is roughly linear within each block (5-10 samples), though the amount of drift is likely different for each mass. We first fit a line to each sequential pair of QC analyses and rotationally transform this line to horizontal, while applying the same transformation to the samples in the block between the two QCs (Fig A2b). The horizontal segments for each block, including the both samples and QCs, are then translated up or down such that all QCs match the average value of the two QCs measured immediately before and immediately after the standards (Fig A2c). We use the standard-bracketing QC analyses to determine the "correct" QC value for each run, as there will presumably have been minimal instrumental drift between the analysis of these two QCs and the standards. This calculation is performed separately for each analyzed mass.

2.18 Results

Detection limits for elements in this protocol are approximately 0.0001 to 0.5 ppm (in the rock samples) for elements that are not reliably analyzed on the XRF (Table A1), equivalent to 0.008 ppt to 0.4 ppb in the analyzed solutions. Analytical uncertainties calculated as 1σ of 100 sweeps through the element of interest are typically between 1 and 5% of the concentration values. Few difficult to analyze elements have uncertainties of roughly 10 to 15% due to mass interference with common polyatomic species (^{45}Sc, overlaps with $^{29}Si^{16}O^{+}$) or very low concentrations (Mo, Cs, Tl).

Analyses of USGS Standards

This method reproduces the accepted concentrations of USGS standards, prepared as Li-borate beads and digested as samples, typically within 10%. Figure A3 shows a comparison between some measurements of USGS standards, analyzed as unknowns, and their corresponding accepted concentrations. Outliers are mostly first row transition zone elements, which are commonly difficult to measure with ICPMS due to mass overlaps with some common polyatomic ions. The use of He collision mode on the ICPMS improves this problem. We recommend using the XRF values for these elements if their concentrations are sufficiently high.

2.19 References Cited in Appendix

Bucholz CE, Spencer CJ (2019) Strongly Peraluminous Granites across the Archean–Proterozoic Transition. Journal of Petrology 60(7):1299-1348

Cheatham MM, Sangrey WF, White WM (1993) Sources of error in external calibration ICP-MS analysis of geological samples and an improved non-linear drift correction procedure. Spectrochimica Acta Part B: Atomic Spectroscopy 48(3):487-506

Jochum KP, Nohl U, Herwig K, Lammel E, Stoll B, Hofmann AW (2005) GeoReM: a new geochemical database for reference materials and isotopic standards. Geostandards and Geoanalytical Research 29(3):333-338

2.20 Appendix Tables

Table A1: Summary of Analyzed Masses

Element	Mass Number	Integration Time (s)	LOD (ppm)[a]
Li	7	0.1	-
Be	9	0.1	-
B	11	0.1	-
Al	27	0.1	478
Ca	44	0.1	2349
Sc	45	0.1	0.25
Ti	47	0.1	554
V	51	0.1	0.048
Cr	52	0.1	0.11
Mn	55	0.1	0.73
Fe	56	0.1	1.74
Co	59	0.1	0.022
Ni	60	0.03	0.50
Cu	63	0.03	0.016
Zn	66	0.03	0.85
Ga	71	0.4	0.077
Rb	85	0.4	0.22
Sr	88	0.1	0.56
Y	89	0.4	0.030
Zr	90	0.4	0.19
Nb	93	0.4	0.011
Mo	95	0.4	0.28
Rh	103	0.1	-
In	113	0.1	-
Cs	133	0.4	0.0062
Ba	137	0.1	0.58
La	139	0.4	0.0015
Ce	140	0.4	0.0052
Pr	141	0.4	0.0011
Nd	146	0.4	0.023
Sm	147	0.4	0.016
Eu	153	0.8	0.00053
Gd	157	0.4	0.0030
Tb	159	0.4	0.00010
Dy	163	0.4	0.0059
Ho	165	0.4	0.000089
Er	166	0.4	0.0013
Tm	169	0.8	0.000044
Yb	172	0.4	0.0013
Lu	175	0.4	0.000039
Hf	178	0.4	0.0015
Ta	181	0.4	0.00014
W	182	0.4	0.0016
Re	185	0.1	-
Tl	205	0.8	0.00041
Pb	208	0.1	0.0077
Bi	209	0.1	-
Th	232	0.4	0.00040
U	238	0.4	0.00021

a Limit of detection (LOD, ppm in the rock) is calculated as (3.3×1σ of the flux blank)/slope of the calibration curve, and averaged over multiple batches. LOD is not calculated for masses that we do not quantify (Li, B, and VIS elements).

2.21 Appendix Figures

Appendix Figure A1

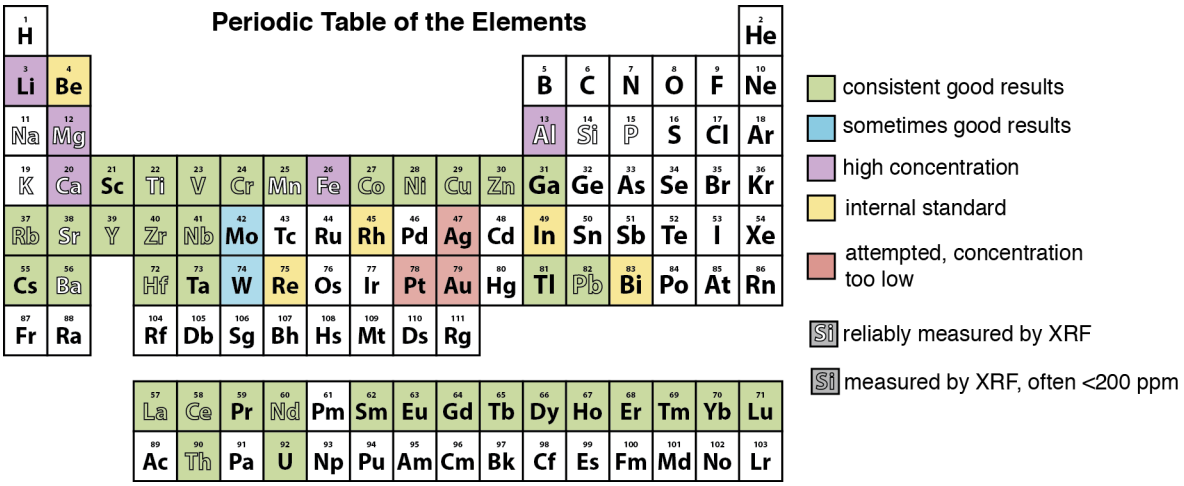

Figure A1 All of the color-highlighted elements have been analyzed with variable success. All green colored elements are routinely measured with consistent results, and the blue elements occasionally return good results if their abundances are high enough in a particular sample. Purple elements are run for completeness and comparison to XRF major element data, but have very high abundances that are not ideal for ICPMS analysis. Li and B are monitored to ensure that equivalent amounts of digested Li-borate glass are included in each solution, but are not quantitatively measured. For most elements, solution ICPMS is a more accurate technique for measurement of elemental concentrations below 200 ppm, in comparison to XRF. The few elements that are commonly within the concentration range to produce reliable results from both XRF and ICPMS analysis (Mn, Sr, Ba, sometimes Ti) are useful for comparison between the two techniques.

Appendix Figure A2

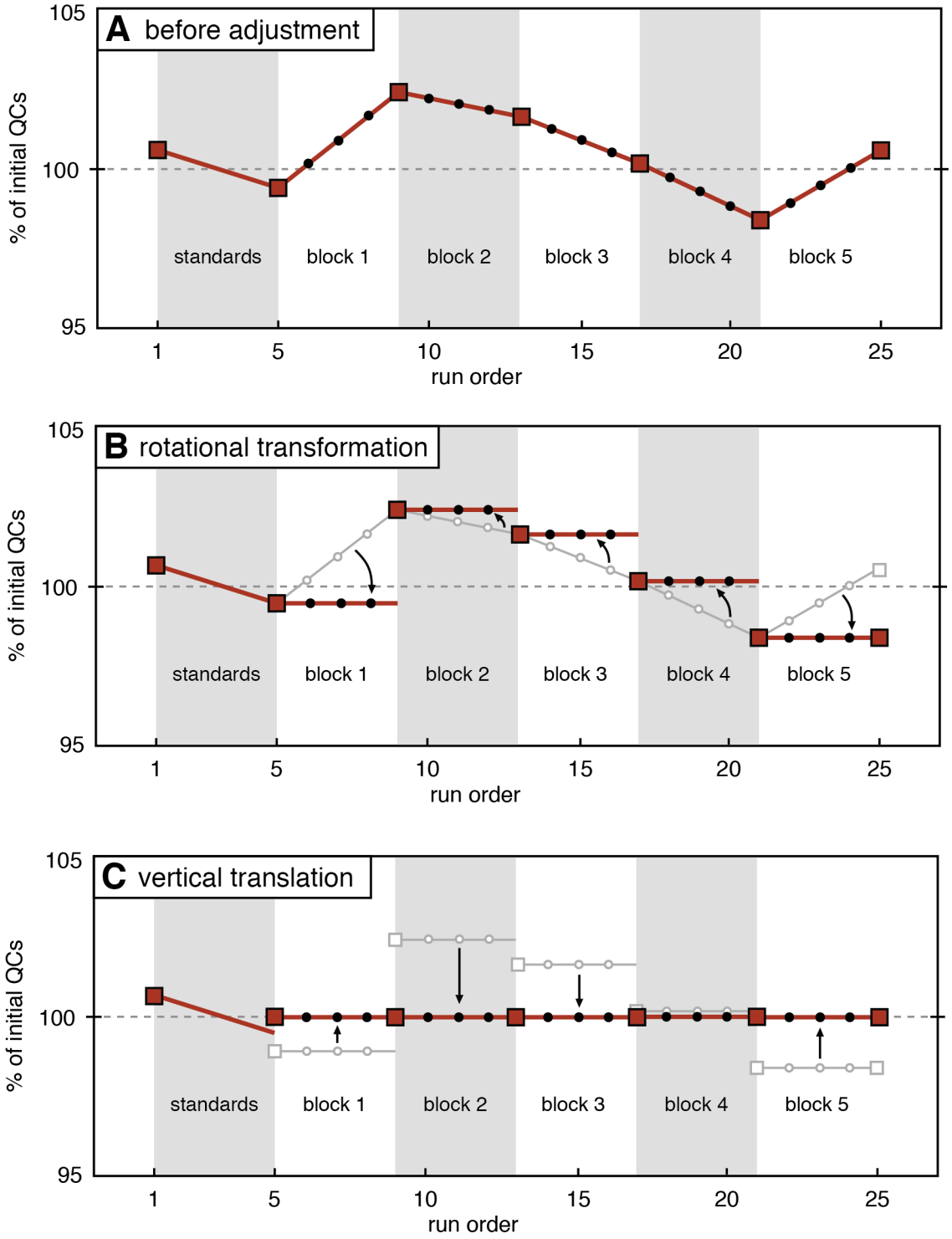

Figure A2 Hypothetical example of the QC-based drift adjustment for one element. Red squares are the QC analyses and black circles are the samples in each block, between the QCs. Grayed-out solid lines, circles, and squares indicate the location of points in the previous panel. **a** The initial QC monitoring results reported as a percent of the average of the QCs run immediately before and after the standards. **b** The line segments between each block are rotated to horizontal, and the same transformation is applied to the sample values. Note that only three samples are shown in each block for simplicity, though blocks in actual batches will contain 5 to 10 samples. **c** The line segments, including both QCs and samples, are translated up or down such that all QC values match the average of the first two QCs.

Appendix Figure A3

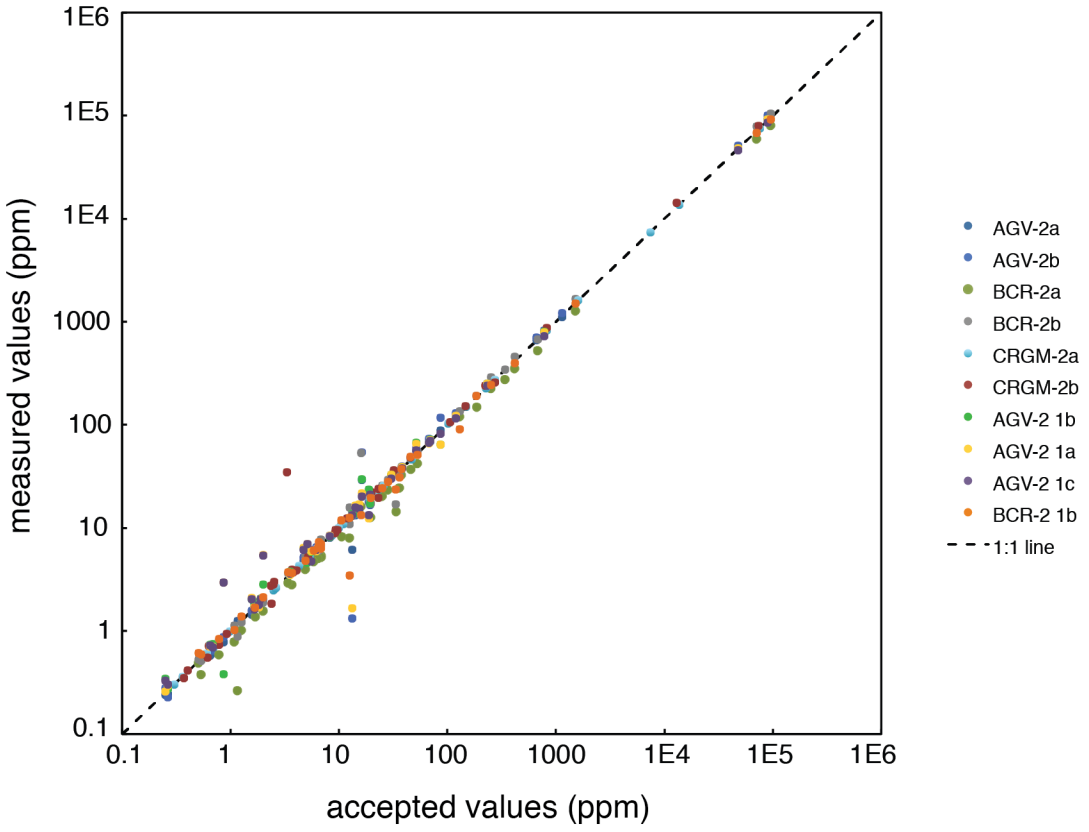

Figure A3 Comparison of accepted standard concentrations (from GeoREM database, Jochum et al. 2005) to measured concentrations. The dashed line is a one-to-one line.

CHAPTER 3

Mafic Intrusions Reveal a Mantle Driver of Arc Episodicity and Crustal Thickening in the Sierra Nevada Batholith

3.1 Abstract

Cyclical magmatic intrusion rates are recognized in continental arcs worldwide with up to 80% of intrusive volumes (based on current areal exposure) forming during flare-up periods, and comparatively little magmatic activity during lulls. Proposed driving mechanisms for variation in temporally variable magma production rates can be separated into mantle- and crustal-driven processes. This study investigates the role of mantle melts in driving flare-ups though investigation of mafic intrusions in the upper crust of the Sierra Nevada batholith. Two main pulses of mafic magmatism occurred from 155 to 146 Ma, and from 99 to 89 Ma, concurrent with the Late Jurassic and Late Cretaceous flare-ups in the Sierra Nevada arc. These mafic complexes are the products of mantle-derived basalts that first differentiated in the lower crust prior to ascent and crystallization in the upper crust. Sr/Y ratios in melt-like (i.e. non-cumulate) mafic samples suggest crustal thickening from ~30 km in the Early Jurassic to ~44 km in the Late Cretaceous. Contemporaneous intrusion of mafic melts along with voluminous granitoid plutons during flare-ups strongly supports mantle melting driving periods of enhanced arc magmatism.

3.2 Introduction

Magmatism in continental arcs is widely documented as an episodic process, with arcs undergoing periods of high magmatic flux termed flare-ups, separated by lull stages when comparatively minor volumes of magma are intruded (e.g., Ducea et al. 2015; Paterson et al. 2011). However, the factors driving the variable magma generation and intrusion rates over time are debated. Hypotheses for triggers of arc flare-ups can be separated into mechanisms within the crust of the upper plate or external processes that enhance mantle melting. Crustal-driven

mechanisms include melting of relaminated subducted sediments (Chapman et al. 2013) and melting the base of continental crust that has been overthickened by underthrusting (DeCelles et al. 2009; DeCelles and Graham 2015; Ducea 2001; Yang et al. 2020). External mantle-driven processes involving changes to the subduction rate and slab angle, episodic fluxing of the mantle by slab fluids, or slab melting and mantle upwelling associated with delamination of lower crustal cumulates have been proposed (Ardila et al. 2019; Decker et al. 2017; Schwartz et al. 2017; Zhou et al. 2020). Fundamental differences in melt generation by these end member mechanisms have implications for the dominant processes of magma generation in arcs and growth of the continental crust (Rudnick 1995).

The Sierra Nevada batholith (SNB), located in eastern California, is one of the most widely studied paleo-continental arcs worldwide (e.g., Bateman 1992a). Magmatism driven by subduction of the Farallon plate beneath the North American continent was active between ~220 to 80 Ma (Lackey et al. 2008), with 70 to 95% of the total SNB volume generated during two 15 Myr flare-up periods. Estimates based on areal exposures of dated plutons indicate that roughly 10 to 15% of the total batholith was emplaced in the Late Jurassic (160-145 Ma) and 70 to 80% in the Late Cretaceous (100-85 Ma) (Ducea 2001).

The SNB is dominated by plutons of granodiorite, tonalite, and granite (hereafter referred to collectively as granitoids), which have been investigated extensively by previous petrologic, structural, and geochronologic studies. Comparatively small (<25 km^2) diorite and gabbro intrusions throughout upper crust of the SNB (Fig 1) have received relatively minor consideration despite their abundance. Initial studies suggest that these mafic bodies represent early melts intruded prior to the Jurassic flare-up (Bateman 1965; Mayo 1941). However, geochronology studies identify mainly Late Cretaceous mafic intrusions (91-103 Ma, Coleman et

al. 1995; Ratajeski et al. 2001) in addition to limited Jurassic gabbros (150 Ma, Ratschbacher et al. 2018), which represent hydrous basaltic melts that ascended into the upper crust. In addition, similar mafic lithologies within deep crustal sections of the SNB (~0.8-1 GPa) are also Cretaceous (Klein and Jagoutz 2021). As these mafic compositions throughout the arc crustal column cannot be generated by partial melting of the crust, they represent crystallization products of evolved mantle-derived melts and provide a window into both mantle and crustal processes within the arc system.

We present geochronology, bulk-rock geochemistry, and mineral chemistry from mafic complexes spanning 100 Myr from the Early Jurassic to Late Cretaceous in the central-eastern SNB to investigate the role of mantle-derived melts in driving arc tempos. Investigation of these lithologies illuminates both temporal trends within the batholith and differentiation mechanisms that lead to the construction of continental arc crust.

3.3 Field and Analytical Methods

The sample suite includes 101 mafic samples from 17 gabbro-diorite intrusions, and 8 additional granitoids from previously un-dated plutons in the eastern SNB (Fig 1). It is common for lithologies to vary within single complexes, from norite and gabbro cumulates, to more evolved amphibole-gabbros and amphibole- and biotite-rich diorites. Exceptions are the diorite-only bodies of Lake Sabrina and Shannon Canyon, and the Casa Diablo body composed entirely of cumulative gabbro and more primitive (olivine + pyroxene-bearing) cumulates. Internal contacts between lithologies within the mafic complexes are often gradational or display mingling textures, indicating coeval intrusion.

In sampling, we selected the most primitive observed cumulates, potentially melt-like samples (fine-grained rocks, dikes, or pillows), evolved samples likely to contain zircon, and samples representative of the most common rock types in each mafic body. We collected U-Pb analyses and trace element contents in zircon from 13 mafic and 9 granitoid samples using LA-ICPMS methods. Bulk-rock compositional analyses were completed for all samples via XRF and *in-situ* major element analyses of olivine, clinopyroxene, and orthopyroxene were collected from 28 mafic samples. Analytical details are included in the Appendix to this chapter.

3.4 Chronology of Mafic Intrusions

Geochronology results from 13 previously undated mafic bodies, as well as 4 previously dated complexes (Coleman et al. 1995; Lewis et al. 2021) reveal two main pulses of mafic magmatism in the SNB from 155 to 146 Ma (n=6) and 99 to 89 Ma (n=9). Two older bodies intruded at 172 and 191 Ma (Fig 2). These pulses are coincident with the late-Jurassic and late-Cretaceous intrusive flare-ups in the SNB, indicating a close connection between the production of mantle melts and voluminous felsic plutons. These intrusions are temporally offset from peaks in volcanic production from the arc (Attia et al. 2020), and thus are unlikely to feed subvolcanic reservoirs (Fig 2). Additionally, the mafic pulses coincide with regional dike intrusion events at 94-90 Ma and 148 Ma (Coleman et al. 2000), suggesting that an extensional regime may mitigate rheologic barriers to ascent of mafic melts into the upper crust.

Each mafic complex is in contact with granitoids of similar age, except for the small Casa Diablo intrusion (98.9±1.1 Ma) within the quartz monzonite of Wheeler Crest (210 Ma) (Lackey, et al. 2008). Notably, the two pre-flare-up Jurassic complexes of Pine Creek (190.8±3.9 Ma) and Shannon Canyon (171.9±2.4 Ma) are coeval, respectively, with the granite of

Chickenfoot Lake (191.8±4.2 Ma; Lewis et al. 2021) on the north side of the Pine Canyon body, and a lobe mapped as the quartz monzonite of Tungsten Hills in Shannon Canyon (171.5±2.7 Ma). Additionally, mingling is observed between the Lake Sabrina diorite (91.1±0.2 Ma) and the Lamarck granodiorite (91.9±0.6 Ma), as well as between the Armstrong Canyon complex (91.5±0.2 Ma) and the adjacent granite of Goodale Mountain (92.6±1.2 Ma)(Coleman et al. 1995). Concomitant mafic and felsic magmatic activity in adjacent locations further supports a link between the generation of these contrasting melt compositions in the SNB.

3.5 Melt Compositions and Differentiation Histories

Bulk-rock compositions in the mafic sample suite range from 39.1 to 64.3 wt.% SiO_2 and have magnesium numbers (Mg#=Mg/[Mg+Fe^T]) of 38 to 73.6 (Fig 3a). Lithologies of cumulate origin are present in nearly all of the complexes, indicating fractionation after intrusion into the upper crust. Further, SiO_2 contents within each complex vary by at least 10 wt.%, indicating upper crustal fractionation internal to each body, with the exception of several small cumulate-dominated complexes with more limited SiO_2 contents (CD, CM). Though extending to lower SiO_2 contents, the field of mafic compositions overlaps with the least evolved granitoid plutons in the SNB (Fig 3b, Fig A2), supporting a common production mechanism for the plutons and mafic complexes and potential relationship by magmatic differentiation.

We use olivine and clinopyroxene from cumulate samples to calculate the Mg# of the melts in equilibrium with these minerals (see Appendix). Using the most primitive (i.e. highest Mg#) minerals from each body, we find that the parental melts had Mg#s ranging from 35 to 60 (Fig 3b). The Jurassic and Cretaceous parental melts are offset in Mg#, with slightly more primitive intrusions in the Cretaceous pulse (Mg#=43-60) than in the Jurassic (Mg#=35-50).

Though these are minimum estimates, as it is not guaranteed that we sampled the most primitive sample in each body, we believe that Mg# 60 is a maximum, as this comes from the Onion Valley complex which has been studied in great detail (Sisson et al. 1996). Therefore, the mafic melts that intruded into the upper crust are not consistent with primitive mantle melts (Mg#~70), and must have fractionated at a deeper crustal level to produce lower MgO basalt compositions that then ascended and crystallized to form the upper crustal mafic bodies. As this fractionation interval would generate ultramafic cumulates that are not observed in the exposed SNB cross section, we posit that this initial stage of crystallization occurs at >1 GPa, below the deepest SNB exposures. In addition, clinopyroxene from low-MgO pyroxenite cumulate xenoliths from the SNB lower crust (2-3 GPa, Lee et al. 2006) is in equilibrium with melt compositions in the same Mg# range as the parental melts to the Cretaceous mafic bodies, and partially overlapping with with the slightly more evolved Jurassic parental melt compositions (Fig 3a). Thus, the melts parental to the suite of mafic bodies experienced initially lower and subsequently upper crustal differentiation, as supported by two previous detailed studies of SNB mafic plutonic bodies (Lewis et al. 2021; Sisson et al. 1996) and other studies of polybaric fractionation in arcs worldwide (Almeev, et al. 2013; Hamada, et al. 2014; Melekhova, et al. 2015).

3.6 Crustal Thickness Over Time

During arc flare-ups, enormous volumes of dominantly felsic magma are intruded over relatively short periods of 10 to 15 Ma, leading to crustal growth and thickening via upper crustal batholith construction and/or underthrusting in the foreland (DeCelles et al. 2009). Our analyses of liquid-like mafic samples and coupled geochronology allow for determination of the crustal thickness through time in the SNB. Bulk-rock Sr/Y ratios (Fig A3) record both garnet and

plagioclase fractionation, such that higher Sr/Y values are consistent with greater garnet fractionation and depth of differentiation, and can be used as a quasi-barometer (Profeta et al. 2015). As we have determined that the melts parental to the mafic complexes all require deeper crustal differentiation, it is probable that this initial fractionation depth is recorded in their bulk-rock Sr/Y ratios. For these calculations, we use only samples that display non-cumulative textures, and we take low Al/Si and Sr/Nd ratios to indicate minimal accumulation of plagioclase (Fig A4). To minimize the effects of upper crustal fractionation on Sr/Y ratios, we use samples with Mg#s within the range of the calculated parental melts, however, as we cannot completely rule out upper crustal fractionation, the calculated crustal thicknesses are minimum estimates. Mafic liquid-like compositions are more likely to record only the first lower crustal stage of fractionation compared to more felsic upper crustal intrusions, which record a combination of both lower and upper crustal differentiation.

Using the model of Profeta et al. (2015), we calculate an average crustal thickness of 33 to 38 km in the Jurassic flare-up and 40 to 48 km during the Cretaceous flare-up (Fig 4a), with shallower crustal thicknesses recorded by the two early- to mid-Jurassic complexes (29-32 km). Sr/Y ratios recorded by mafic liquids record a narrower range of crustal thickness than we calculate for contemporaneous granitoids, supporting our assertion that mafic melt-representative samples are ideal for crustal thickness calculation using bulk-rock Sr/Y. The maximum thicknesses calculated from granitoids increases at a rate consistent with the mafic liquid-like samples, corroborating the crustal thickness values. Based on the overall minimum recorded thickness of 29 km (190 Ma) and average thickness during the late-Cretaceous (44 km), the average crustal thickening rate between 190 and 85 Ma is 0.15 km/Ma. However, the thickening

rate may be episodic and correlated with flare-ups, resulting in a short-term growth rate potentially closer to 0.8 km/Ma between 100 and 90 Ma.

Our thickness calculations are in agreement with crustal shortening reconstructions (Cao et al. 2016) that predict an 80 km thick crust with 30 km root in the late-Cretaceous SNB, as mafic melts are likely to fractionate at the boundary between the felsic crust and deep crustal cumulates (Jagoutz 2014). In addition, garnet-bearing xenoliths representative of deep crustal SNB cumulates originated at a minimum of 45 km depth (Lee et al. 2001), consistent with our estimates for late-Cretaceous crustal thickness. Furthermore, garnet strongly fractionates MREEs from HREEs, and thus higher Dy/Yb ratios in extracted melts indicate greater fractionation depths. We present trace element analyses in zircon from dated diorites, gabbros, and granitoids (Fig 4b), which show a modest increase in average zircon Dy/Yb over time, supporting the record of crustal thickening in the SNB.

3.7 Mantle-triggered Flare-ups

The intrusion of mafic melts to the upper-crust during flare-up peaks demonstrates that voluminous felsic melt production is coeval with, and potentially triggered by, enhanced mantle melt flux. Migration of mantle melts to the base of the crust at an elevated rate provides both juvenile basalts that can differentiate to form felsic crust, as well as heat to drive melting of preexisting crust (e.g., Annen et al. 2006). In addition to the influx of mafic melts into the deep arc magmatic system, an increased crustal geothermal gradient facilitates the escape of mafic melts from the lower crust and intrusion at shallow depths. As the observed complexes contain abundant amphibole and biotite, they originate from hydrous melts, which are they are less dense than surrounding solidified granitoids and therefore able to ascend when unrestricted by

permeability barriers. For example, the parental melts to the Onion Valley Complex (Mg#=60, 4-6 wt.% H_2O) have densities of 2.45 to 2.55 g/cm^3, which would be buoyant in the surrounding granitoid crust (2.60-2.69 g/cm^3) (Sisson et al. 1996). The parental melt to the Hidden Lakes mafic complex, though more fractionated and less hydrous (Mg#=51, 3.1 wt.% H_2O) (Lewis et al. 2021), has a density of 2.51 g/cm^3, within the range of the Onion Valley melts and significantly less dense than the felsic Sierran plutons. Therefore, during periods when significant volumes of mafic melts are generated in the mantle, they should be capable of ascending after sufficient fractionation. Thus, the lack of mafic melts in the upper crust during the Early Cretaceous lull, and the infrequent mafic intrusions prior to the Jurassic flare-up, indicates that smaller volumes of mantle-derived melts are generated during magmatic lull periods than during flare-ups in the SNB, as these melts are less represented at upper crustal levels.

This mantle trigger hypothesis resolves seemingly contradictory observations in Cordilleran batholiths of decreased ε_{Nd} and elevated $\delta^{18}O$ values during flare-ups, both indicative of increased crustal recycling (Ducea and Barton 2007; Kirsch et al. 2016), and concurrent positive ε_{Hf} excursions consistent with elevated mantle input (Attia et al. 2020). This does not preclude the incorporation of melts sourced from relaminated schists or the base of a thick crust, however, Yang et al. (2020) find that melting at the base of overthickened crust does not generate the observed volumes of felsic melts without exceptionally high heat flux from the mantle. Thus, both the heat and magmatic volumes provided by mantle-derived melts are required to trigger the Jurassic and Cretaceous flare-ups in the SNB. Because evidence of the Late Cretaceous flare-up is found throughout the North American Cordillera, affecting the Coast Mountains and Peninsular Ranges batholiths (Gehrels et al. 2009; Premo et al. 2014) in addition

to the SNB, the processes affecting mantle melt generation must be laterally extensive. Though our results do not distinguish between different potential causes of episodic mantle flux, processes such as changes to the subduction angle or rate, or large-scale delamination and slab breakoff events may be capable of generating widespread enhancements in mantle melt generation to drive arc flare-ups.

3.8 Acknowledgements

We are grateful to many field assistants over the years: Joe Biasi, Allyson Trussell, Matt Barickman, Emma Sosa, Sam Newall, Barbara Ratschbacher, and Liane Lewis. We thank the Arizona Laserchron Center, and namely Sarah George and Martin Pepper for assistance with LA-ICPMS analyses. The geochronology work was funded by an AGeS2 (Awards for Geochronology Student Research) award to MJL, under National Science Foundation Grant Nos. EAR-1759200 and EAR-1759353.

3.9 References Cited

Almeev RR, Ariskin AA, Kimura J-I, Barmina GS (2013) The role of polybaric crystallization in genesis of andesitic magmas: phase equilibria simulations of the Bezymianny volcanic subseries. Journal of Volcanology and Geothermal Research 263:182-192

Annen C, Blundy J, Sparks R (2006) The genesis of intermediate and silicic magmas in deep crustal hot zones. Journal of Petrology 47(3):505-539

Ardila AMM, Paterson SR, Memeti V, Parada MA, Molina PG (2019) Mantle driven cretaceous flare-ups in Cordilleran arcs. Lithos 326:19-27

Attia S, Cottle JM, Paterson SR (2020) Erupted zircon record of continental crust formation during mantle driven arc flare-ups. Geology 48(5):446-451

Bateman PC (1965) Geology and tungsten mineralization of the Bishop district, California. In, vol. US Geological Survey Professional Paper 470,

Bateman PC (1992a) Plutonism in the central part of the Sierra Nevada batholith, California. US Government Printing Office,

Bateman PC (1992b) Pre-Tertiary bedrock geologic map of the Mariposa 1° by 2° quadrangle, Sierra Nevada, California; Nevada. The Survey,

Cao W, Paterson S, Saleeby J, Zalunardo S (2016) Bulk arc strain, crustal thickening, magma emplacement, and mass balances in the Mesozoic Sierra Nevada arc. Journal of Structural Geology 84:14-30

Chapman AD, Saleeby JB, Eiler J (2013) Slab flattening trigger for isotopic disturbance and magmatic flare-up in the southernmost Sierra Nevada batholith, California. Geology 41(9):1007-1010

Chen JH, Moore JG (1979) Late Jurassic Independence dike swarm in eastern California. Geology 7(3):129-133

Coleman D, Glazner A, Miller J, Bradford K, Frost T, Joye J, Bachl C (1995) Exposure of a Late Cretaceous layered mafic-felsic magma system in the central Sierra Nevada Batholith, California. Contributions to Mineralogy and Petrology 120(2):129-136

DeCelles PG, Ducea MN, Kapp P, Zandt G (2009) Cyclicity in Cordilleran orogenic systems. Nature Geoscience 2(4):251-257

DeCelles PG, Graham S (2015) Cyclical processes in the North American Cordilleran orogenic system. Geology 43(6):499-502

Decker M, Schwartz J, Stowell H, Klepeis K, Tulloch A, Kitajima K, Valley J, Kylander-Clark A (2017) Slab-triggered arc flare-up in the Cretaceous Median Batholith and the growth of lower arc crust, Fiordland, New Zealand. Journal of Petrology 58(6):1145-1171

Ducea MN (2001) The California arc: Thick granitic batholiths, eclogitic residues, lithospheric-scale thrusting, and magmatic flare-ups. GSA today 11(11):4-10

Ducea MN, Barton MD (2007) Igniting flare-up events in Cordilleran arcs. Geology 35(11):1047-1050

Ducea MN, Paterson SR, DeCelles PG (2015) High-volume magmatic events in subduction systems. Elements 11(2):99-104

Frost TP (1987) Sample localities, radiometric ages, descriptions, and major-and trace-element abundances of Late Jurassic mafic plutonic rocks, eastern Sierra Nevada, California. Department of the Interior, US Geological Survey

Gehrels G, Rusmore M, Woodsworth G, Crawford M, Andronicos C, Hollister L, Patchett J, Ducea M, Butler R, Klepeis K (2009) U-Th-Pb geochronology of the Coast Mountains batholith in north-coastal British Columbia: Constraints on age and tectonic evolution. Geological Society of America Bulletin 121(9-10):1341-1361

Hamada M, Okayama Y, Kaneko T, Yasuda A, Fujii T (2014) Polybaric crystallization differentiation of H 2 O-saturated island arc low-K tholeiite magmas: a case study of the Izu-Oshima volcano in the Izu arc. Earth, Planets and Space 66(1):1-10

Jagoutz O (2014) Arc crustal differentiation mechanisms. Earth and Planetary Science Letters 396:267-277

Kirsch M, Paterson SR, Wobbe F, Ardila AMM, Clausen BL, Alasino PH (2016) Temporal histories of Cordilleran continental arcs: Testing models for magmatic episodicity. American Mineralogist 101(10):2133-2154

Klein BZ, Jagoutz O (2021) Construction of a trans-crustal magma system: Building the Bear Valley Intrusive Suite, southern Sierra Nevada, California. Earth and Planetary Science Letters 553:116624

Lackey JS, Valley JW, Chen JH, Stockli DF (2008) Dynamic magma systems, crustal recycling, and alteration in the central Sierra Nevada batholith: The oxygen isotope record. Journal of Petrology 49(7):1397-1426

Lee CT, Rudnick RL, Brimhall Jr GH (2001) Deep lithospheric dynamics beneath the Sierra Nevada during the Mesozoic and Cenozoic as inferred from xenolith petrology. Geochemistry, Geophysics, Geosystems 2(12)

Lewis MJ, Bucholz CE, Jagoutz OE (2021, *in review*) Evidence for polybaric fractional crystallization in a continental arc: Hidden Lakes mafic complex, Sierra Nevada batholith, California. Contributions to Mineralogy and Petrology

Mahan KH, Bartley JM, Coleman DS, Glazner AF, Carl BS (2003) Sheeted intrusion of the synkinematic McDoogle pluton, Sierra Nevada, California. Geological Society of America Bulletin 115(12):1570-1582

Mayo EB (1941) Deformation in the interval Mt. Lyell-Mt. Whitney, California. Bulletin of the Geological Society of America 52(7):1001-1084

Melekhova E, Blundy J, Robertson R, Humphreys MC (2015) Experimental evidence for polybaric differentiation of primitive arc basalt beneath St. Vincent, Lesser Antilles. Journal of Petrology 56(1):161-192

Moore JG (1963) Geology of the mount Pinchot quadrangle, southern Sierra Nevada, California. US Government Printing Office,

Paterson SR, Okaya D, Memeti V, Economos R, Miller RB (2011) Magma addition and flux calculations of incrementally constructed magma chambers in continental margin arcs: Combined field, geochronologic, and thermal modeling studies. Geosphere 7(6):1439-1468

Premo WR, Morton DM, Wooden JL, Fanning CM, Miller F (2014) U-Pb zircon geochronology of plutonism in the northern Peninsular Ranges batholith, southern California: Implications for the Late Cretaceous tectonic evolution of southern California. Peninsular Ranges Batholith, Baja California and Southern California: Geological Society of America Memoir 211:145-180

Profeta L, Ducea MN, Chapman JB, Paterson SR, Gonzales SMH, Kirsch M, Petrescu L, DeCelles PG (2015) Quantifying crustal thickness over time in magmatic arcs. Scientific reports 5(1):1-7

Ratajeski K, Glazner AF, Miller BV (2001) Geology and geochemistry of mafic to felsic plutonic rocks in the Cretaceous intrusive suite of Yosemite Valley, California. Geological Society of America Bulletin 113(11):1486-1502

Ratschbacher BC, Keller CB, Schoene B, Paterson SR, Anderson JL, Okaya D, Putirka K, Lippoldt R (2018) A new workflow to assess emplacement duration and melt residence time of compositionally diverse magmas emplaced in a sub-volcanic reservoir. Journal of Petrology 59(9):1787-1809

Rudnick RL (1995) Making continental crust. Nature 378(6557):571-578

Schwartz JJ, Klepeis KA, Sadorski JF, Stowell HH, Tulloch AJ, Coble MA (2017) The tempo of continental arc construction in the Mesozoic Median Batholith, Fiordland, New Zealand. Lithosphere 9(3):343-365

Sisson T, Grove T, Coleman D (1996) Hornblende gabbro sill complex at Onion Valley, California, and a mixing origin for the Sierra Nevada batholith. Contributions to Mineralogy and Petrology 126(1-2):81-108

Stern T (1981) Isotopic U-Pb ages of zircon from the granitoids of the central Sierra Nevada, California.

Wenner JM, Coleman DS (2004) Magma mixing and cretaceous crustal growth: Geology and geochemistry of granites in the central Sierra Nevada Batholith, California. International Geology Review 46(10):880-903

Yang J, Cao W, Gordon SM, Chu X (2020) Does Underthrusting Crust Feed Magmatic Flare-Ups in Continental Arcs? Geochemistry, Geophysics, Geosystems 21(11):e2020GC009152

Zhou H, Zhang D, Wei J, Wang D, Santosh M, Shi W, Chen J, Zhao X (2020) Petrogenesis of Late Triassic mafic enclaves and host granodiorite in the Eastern Kunlun Orogenic Belt, China: Implications for the reworking of juvenile crust by delamination-induced asthenosphere upwelling. Gondwana Research 84:52-70

3.10 Figures and captions

Figure 1

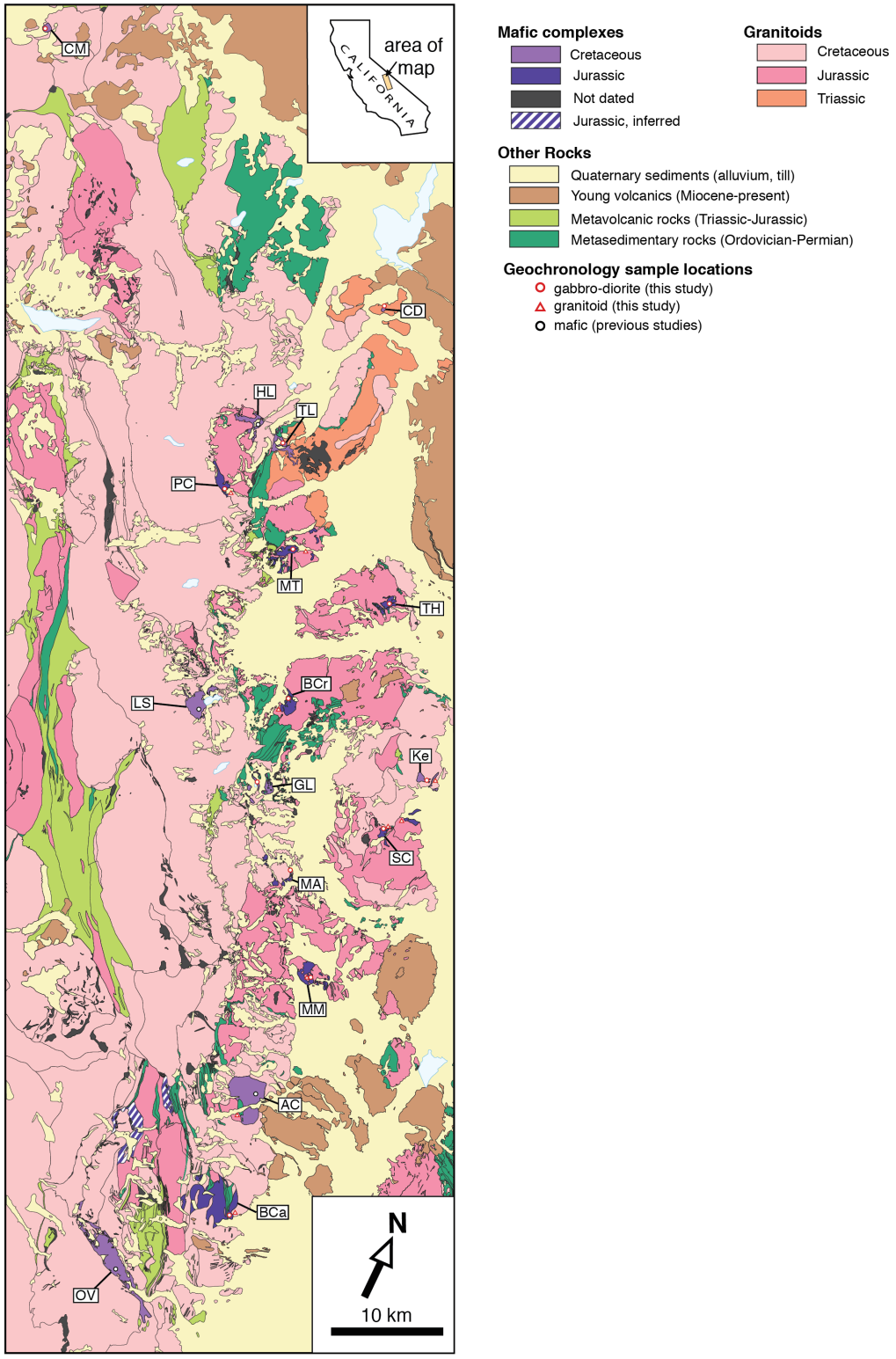

Figure 1 Simplified geologic map of the central-eastern SNB. Contacts are from Bateman (1992b), Elder and Reichert (2010), and Moore (1963). Abbreviations for mafic bodies are as follows: CM-Cargyle Meadows, CD-Casa Diablo, HL-Hidden Lakes, TL-Tamarack Lakes, PC-Pine Creek, MT-Mount Tom, TH-Tungsten Hills, LS-Lake Sabrina, BCr-Bishop Creek, Ke-Keough, GL-Green Lake, SC-Shannon Canyon, MA-Mount Alice, MM-McMurray Meadows, AC-Armstrong Canyon, BCa-Black Canyon, and OV-Onion Valley. The OV, LS, and AC mafic complexes were previously dated by Coleman et al. (1995), and HL was dated by Lewis et al. (2021). Granitoid ages are from Coleman et al. (1995), Lackey et al. (2008), Mahan et al. (2003), Stern (1981), and Wenner and Coleman (2004). Several undated mafic complexes are inferred to be Jurassic, as they are pervasively intruded by dikes of the Jurassic Independence dike swarm (148 Ma) (Chen and Moore 1979).

Figure 2

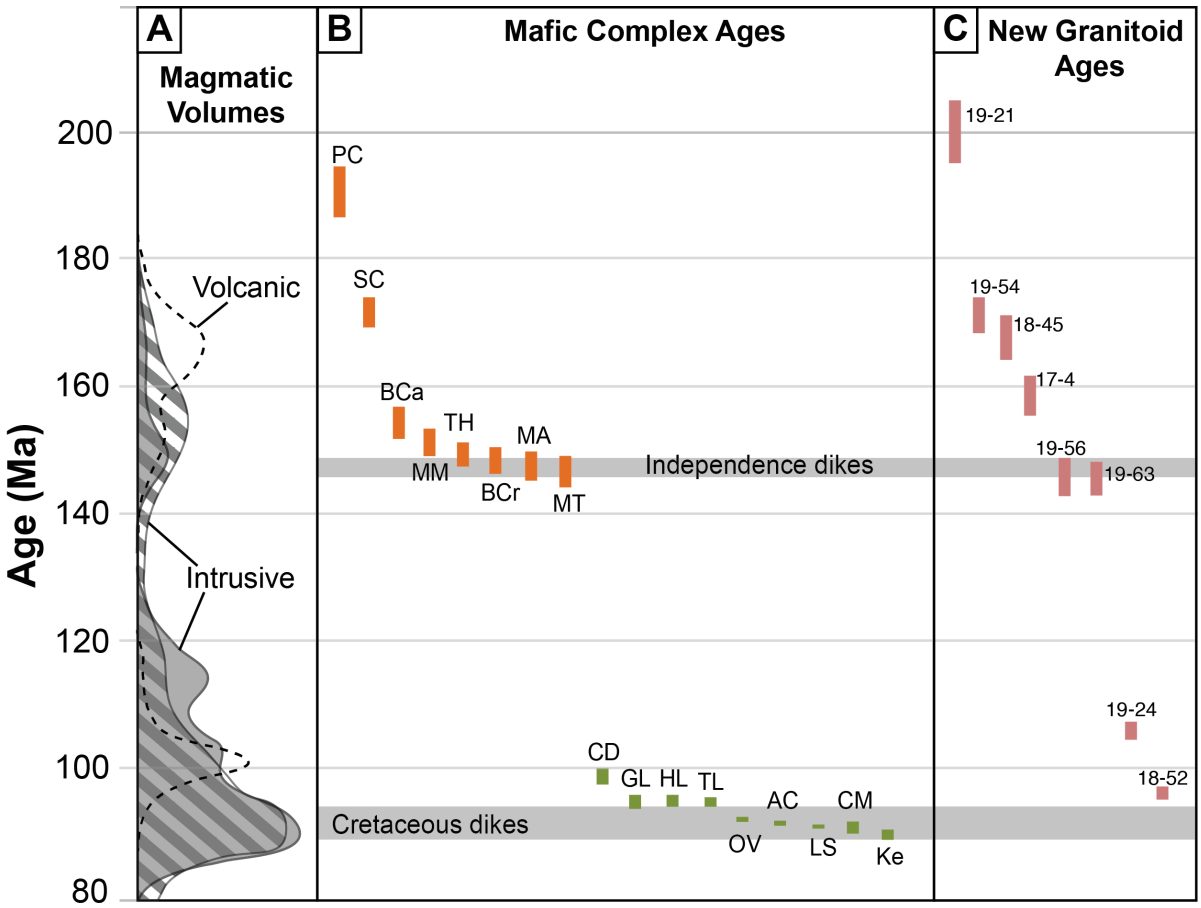

Figure 2 Summary of geochronology of mafic intrusions in the eastern SNB. **a** Relative areal exposure over time in the SNB, commonly interpreted to be correlated with volumetric magmatic flux. The filled gray area and dashed curve are the intrusive and volcanic abundances respectively, from Attia et al. (2020), and the striped area shows the intrusive record from Ducea (2001). **b** 13 new mafic geochronology analyses from this study, one age from Lewis et al. (2021) (HL), and three ages from Coleman et al. (1995) (OV, AC, LS). Abbreviations for mafic complexes are as in Figure 1. **c** New granitoid analyses from this study. Sample names are shortened for simplicity, and correspond to the digits following "SNB-" in Appendix Table 1.

Figure 3

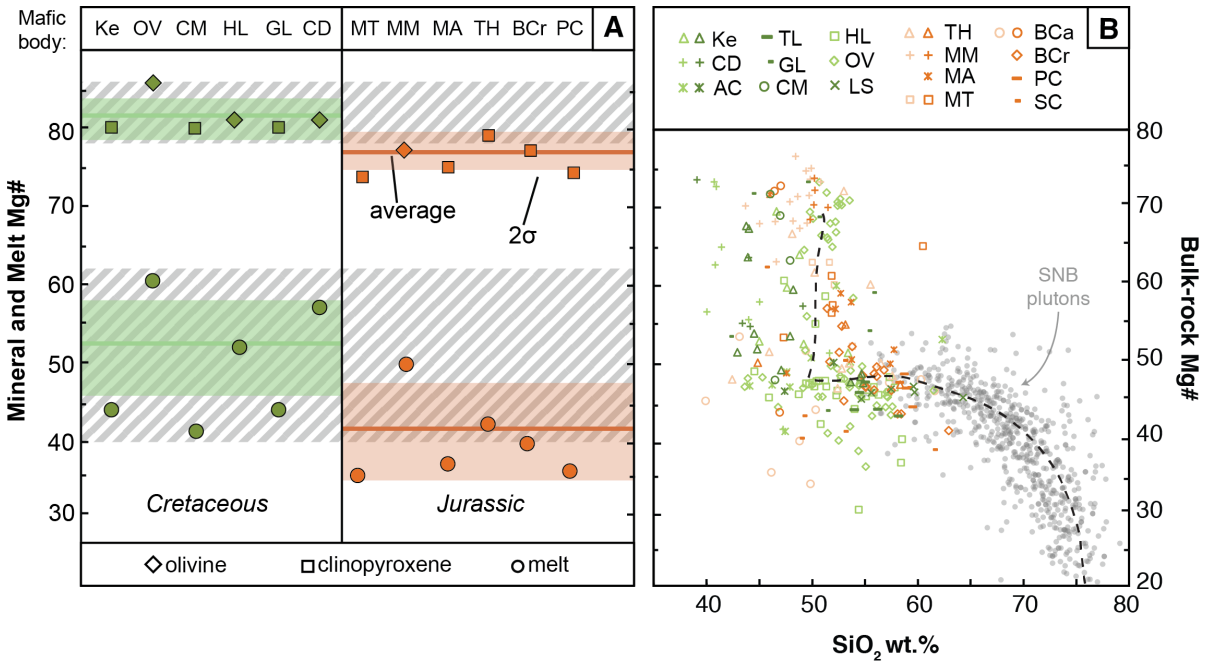

Figure 3 Magnesium numbers (Mg#= Mg/[Mg+Fe^T]) for **a** olivine, clinopyroxene, and calculated melt compositions and **b** bulk-rock analyses. **a** Mg#s of the most primitive olivine or clinopyroxene cores from each complex, and calculated parental melt compositions (see Appendix for calculation methods). Striped areas denote the range of Mg#s for clinopyroxenes and calculated equilibrium melts from low-MgO garnet-pyroxenite cumulate xenoliths originating from the SNB lower crust (Lee et al. 2006). **b** All bulk-rock samples, as well as samples from HL (Lewis et al. 2021), OV (Sisson, et al. 1996), and additional analyses from Frost (1987). Jurassic samples are shown in orange and Cretaceous samples are in green, and samples new to this study are shown in darker shades. The black dashed line is a representative fractionation trend for SNB mafic melts (Lewis et al. 2021). SNB plutonic compositions are from the GEOROC database (http://georoc.mpch-mainz.gwdg.de/georoc/), and filtered for totals between 98 and 102 wt.%.

Figure 4

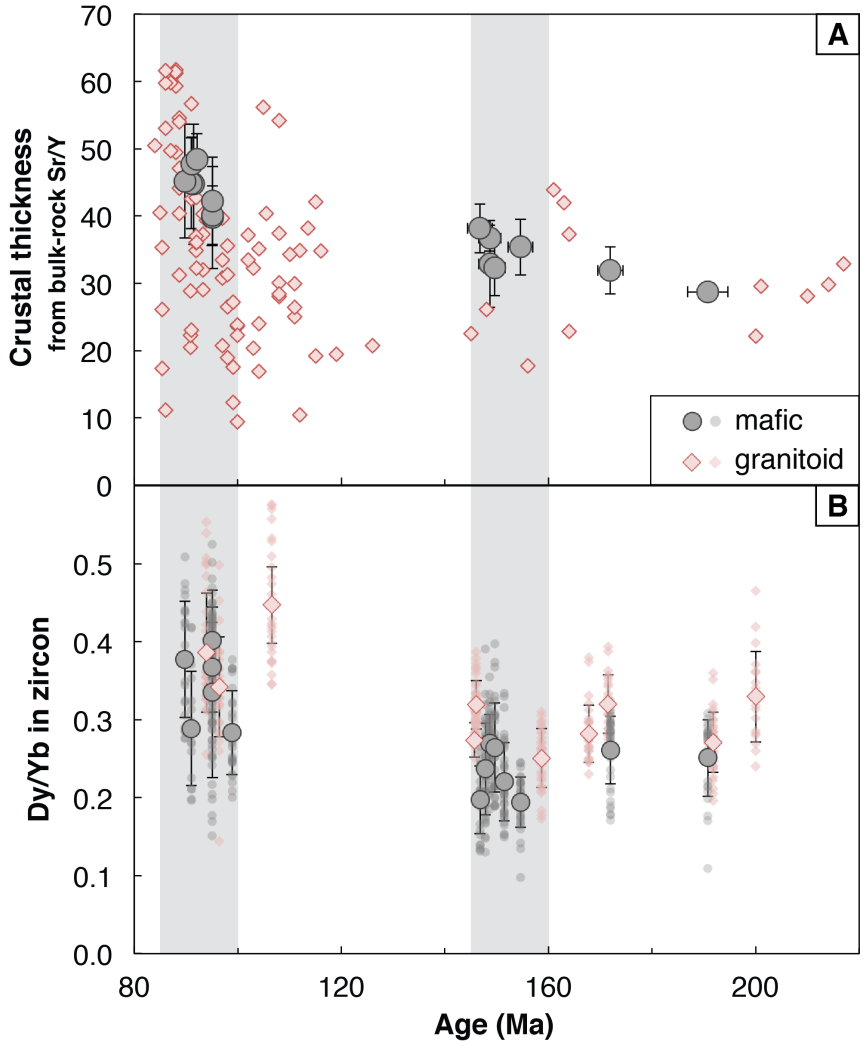

Figure 4 Proxies for crustal thickness in the SNB over time. **a** crustal thickness calculated from bulk-rock Sr/Y ratios (Profeta et al. 2015). Symbols for mafic complexes (gray circles) indicate the average crustal thickness calculated from liquid-like mafic samples from each body, and granitoid points represent bulk-rock compositions of individual samples from Lackey et al. (2008). **b** Dy/Yb in zircon from mafic bodies and granitoid samples in this study. Solid symbols are averages of all zircon analyses from a single sample, with 1σ error bars. Light colored symbols are individual grain analyses. Shaded vertical bars indicate the late Jurassic and late Cretaceous flare-up intervals in the SNB.

APPENXID TO CHAPTER 3

3.11 ANALYTICAL METHODS

3.11.1 Zircon analyses: U-Pb geochronology and trace element concentrations

We separated zircon from 21 total samples, including 13 gabbros and diorites and 8 granitoids, mounting between 25 and 52 grains per sample. Zircon grains were polished and imaged for cathodoluminescence response on the Zeiss 1550 VP scanning electron microscope at Caltech. U-Pb isotopic data and concurrent analysis of trace elements in zircon were measured via LA-ICPMS at the Arizona Laserchron Center following the methods of Pullen et al. (2018) and Chapman et al. (2016), with additional analytical details as given on the Arizona Laserchron Center website (https://sites.google.com/laserchron.org/arizonalaserchroncenter/home). Zircon were analyzed using a Photon Machines 193 nm G2 excimer laser attached to a Thermo Scientific Element2 HR single collector ICPMS. Laser conditions were a 30 μm spot diameter, 7 Hz frequency, 7 J/cm^2 fluence, and 380 shots per analysis. Masses analyzed were ^{27}Al, ^{29}Si, ^{31}P, ^{45}Sc, ^{49}Ti, ^{89}Y, ^{93}Nb, ^{139}La, ^{140}Ce, ^{141}Pr, ^{146}Nd, ^{152}Sm, ^{153}Eu, ^{157}Gd, ^{159}Tb, ^{164}Dy, ^{165}Ho, ^{166}Er, ^{169}Tm, ^{174}Yb, ^{175}Lu, ^{177}Hf, ^{181}Ta, ^{202}Hg, ^{204}(Hg+Pb), ^{206}Pb, ^{207}Pb, ^{208}Pb, ^{232}Th, and ^{235}U. Analytical dwell times for each mass range from 0.001 to 0.3 s. Laser spots were placed near grain rims to extract a crystallization age and avoid potential resorbed cores. Primary standards FC and SL were placed between every 5 unknown analyses and used to correct for drift in the ICPMS and down-hole fractionation. A secondary standard R33 was measured between every 20 to 30 analyses.

Data were reduced using the Excel-based reduction programs TREEcalc and AgeCalc (Gehrels et al. 2008). Analyses with concordance ($[^{206}Pb/^{238}U]_{age}/[^{207}Pb/^{235}U]_{age}$) < 95% were discarded, resulting in 5 to 41 acceptable analyses per sample. Crystallization ages were calculated in IsoplotR (Vermeesch 2018) as an error-weighted mean of individual spot ages for

each sample, and reported uncertainties are 2 sigma of acceptable single-grain ages in each sample. Weighted mean age plots for each new dated sample are show in Appendix Figure A1, a summary of new sample geochronology is given in Supplementary Table S1, and U-Pb isotopic measurements and trace element abundances for each zircon grain are given in Supplementary Table S2.

3.11.2 Bulk-rock analyses

97 samples were analyzed for bulk-rock compositions via X-ray fluorescence spectrometry (XRF). Samples for bulk-rock analysis were sawed to remove any potentially altered areas and sanded to remove any sawing residue. To ensure homogeneity, ~0.5-1 kg of each sample rock was crushed and ~25 mL of crushed rock was powdered in an agate ball mill. Powders were dried overnight at 110 °C, then heated to 1050 °C for one hour to determine loss on ignition (LOI). Glass beads were prepared using a 10:1 mass ratio of Li-borate flux to sample powder and fused at 1200 °C. Major elements and a suite of trace elements (Si, Ti, Al, Fe, Mn, Mg, Ca, Na, K, P, Rb, Ba, Sr, Nb, Zr, Hf, Y, Zn, Cu, Ni, Co, Cr, V, La, Ce, Nd, Pb, Th) in the glass beads were analyzed using a Panalytical Zetium wavelength-dispersive X-ray fluorescence (XRF) spectrometer following the methods of Bucholz and Spencer (2019). Bulk-rock compositions and GPS locations of each sample are given in Supplementary Table S3.

3.11.3 In-situ mineral analyses

Major element compositions of olivine, clinopyroxene, and orthopyroxene were analyzed in 28 samples using the JEOL JXA-8200 electron probe micro-analyzer (EPMA) at Caltech. At least three points per grain were positioned to analyze both grain cores and rims to assess zoning,

and five grains per sample were analyzed (where mineral abundances allow) to ensure collection of representative mineral compositions. Analyzed elements were Si, Ti, Al, Cr, Fe, Mn, Mg, Ca, Na, K, and Ni. Detection limits were <0.006 wt.% for Si, Al, Mg, Ca, and K, <0.02 wt.% for Ti, Fe, Na, Cr, and Mn, and ~0.025 wt.% for Ni. Operation conditions for the EPMA were a 25 nA beam current, a 15 kV acceleration voltage, and a focused beam diameter (<1 μm). For standardization, we use synthetic forsterite, fayalite, Mn-olivine, anorthite, TiO_2, NiO, and Cr_2O_3, and natural standards Amelia albite and Asbestos microcline. We use a mean atomic number (MAN) background correction and CITZAF matrix correction program (Armstrong 1995) for data reduction.

3.11.4 Calculation of parental melt compositions

We define "parental melt" as the most primitive (i.e. highest Mg#, where Mg#=Mg/[Mg+Fe^T]) melt to intrude into each mafic complex at the level of emplacement. Based on the prevalence of clino- and orthopyroxene-dominated cumulates in many of the sampled mafic complexes, it is likely that this melt differentiated within the upper crust to produce cumulates and more evolved liquids. Thus, we cannot directly sample and analyze the parental melt composition with certainty. Instead, we use the compositions of the most primitive minerals found in cumulates in each mafic complex to calculate the Mg# of a melt in equilibrium with these phases. We use the following experimentally determined Fe^{2+}/Mg mineral-melt distribution coefficients for this calculation: 0.303 for olivine and 0.284 for orthopyroxene (Beattie 1993), and 0.23 for clinopyroxene (Sisson et al. 1993). For simplicity, we assume all Fe in the mineral phases is Fe^{2+}. We utilize a ferric iron to total iron ratio of 0.18 in the melts, consistent with an oxygen fugacity (fO_2) at the nickel-nickel oxide buffer, which is common for continental arc

magmas and in agreement with fO_2 estimates from the Hidden Lakes mafic complex (Lewis et al. 2021). For bodies containing a combination of olivine, clinopyroxene, and/or orthopyroxene, we take the highest Mg# calculated melt to be the parental melt composition. Figure 3a shows only olivine and clinopyroxene analyses because clinopyroxene typically returns a melt Mg# 2 to 20% higher than melts calculated based on orthopyroxene, except for in the Hidden Lakes mafic complex where orthopyroxene is more primitive than clinopyroxene. Mineral compositions from the most primitive grains in each body, as well as the calculated parental melt Mg#s, are included in Supplementary Table S4.

These reported parental melt Mg#s are minimum estimates, as we have not sampled or analyzed every mineral within each complex. However, two complexes have been studied in great detail, the Onion Valley complex (Sisson et al. 1996) and the Hidden Lakes complex (Lewis et al. 2021), and we are confident that the highest Mg# mineral analyzed from these localities is representative of the parental melt. As the calculated parental melts in many of the other bodies are in a similar range to these, it is likely that we have calculated reasonable parental melt compositions for most of the intrusions. In the Shannon Canyon, Lake Sabrina, Tamarack Lakes, Armstrong Canyon, and Black Canyon complexes, we did not observe olivine or pyroxenes, and so cannot calculate a parental melt composition based on well established partition coefficients.

3.12 FIELD DESCRIPTIONS

3.12.1 Contacts

Contacts are largely obscured by talus or till in the low elevation complexes and glacial valleys, but were closely observed at the Lake Sabrina, Hidden Lakes, Onion Valley, Pine Creek, and Tamarack Lakes complexes. Margins between mafic intrusions and surrounding granitoids of similar age are often mingled, as in the Lake Sabrina diorite (91.1 Ma) and the Lamarck granodiorite (91.9 Ma), and the Armstrong Canyon complex (92.1 Ma) and the granite of Goodale Mountain (91.5 Ma) (Coleman, et al. 1995). Contacts between younger mafic complexes and older granitoids are commonly gradational over 10s of cm, as in the Hidden Lakes gabbros (95.1 Ma, Lewis et al. 2021) and the granite of Chickenfoot Lake (191.8 Ma, CH2) and Tamarack Lakes body and the Tungsten Hills quartz monzonite (Fig A5a, 210 Ma) (Lackey, et al. 2008). In the Hidden Lakes, Onion Valley, and Shannon Canyon complexes, diabase dikes extend from the mafic body into the surrounding granitoids. Where granitoids intrude mafic complexes that are significantly older, the contacts are sharp (Fig A5b) or the mafic complex may be brecciated by intrusion of younger granitoids, as in the Hidden Lakes mafic complex (95.1 Ma) and Round Valley Peak granodiorite (88.8 Ma, Lackey et al. 2008), and the Mount Alice complex (147.8±2.2 Ma) and the Leucogranite of Rawson Creek (95 Ma; Wenner and Coleman 2004).

3.12.2 Descriptions of Mafic Bodies

The locations and mapped areas of the suite of mafic complexes are shown in Figure 1. This mapping is based off of USGS maps (Bateman 1992; Moore 1963) and efforts of the US Forest Service (Elder and Reichert 2010). Intrusions in the eastern SNB are exposed to upper

crustal levels of 100 to 300 MPa pressures (Ague and Brimhall 1988; Chapman et al. 2012) equivalent to depths of ~3 to 9 km.

Cargyle Meadows

The Cargyle Meadows mafic body is a small (0.17 km^2), previously unmapped amphibole-rich diorite through gabbro body that crystallized at 91±0.9 Ma. The outcrops dominantly consist of coarse-grained amphibole-dominated gabbro containing amphibole oikocrysts up to 1.5 cm and rare, yet notable euhedral pyrite crystals up to 4 mm. Clinopyroxene is found in the cores of some amphiboles. Plagioclase is interstitial in the gabbros, and dominates the rock volume in amphibole-biotite diorites. The complex is surrounded by the 90 Ma Mount Givens granodiorite (Lackey et al. 2008), and may contact the ~168 Ma granodiorite of King Creek (Wesley et al. 2019) beneath Quaternary talus to the south.

Casa Diablo

This small mafic body is located near the town of Aspen Springs, CA, with a mapped area of 0.19 km^2. Its small, rounded geometry suggests a stock-like intrusion into the quartz monzonite of Wheeler Crest (210 Ma, Lackey et al. 2008). With an age of 98.9±1.1 Ma, this is the oldest mafic intrusion we dated in the Cretaceous pulse. The body is poorly exposed, however low outcrops show a medium-grained amphibole-gabbro, and coarse-grained olivine-gabbro containing blebs of olivine-websterite cumulates. Because all samples from this locality appear to be cumulates based on texture or chemistry, we do not calculate a crustal thickness based on any samples from Casa Diablo.

Hidden Lakes

The 95-96 Ma Hidden Lakes mafic complex (2.5 km^2), located within Little Lakes Valley, intrudes the 191.8±4.2 Ma granite of Chickenfoot Lake (Lewis et al. 2021), and is intruded by the Lake Edison granodiorite (90.9 Ma) and Round Valley Peak granodiorite (88.8 Ma) (Lackey et al. 2008). The body consists of mainly a medium-fine grained amphibole-biotite gabbro, though course-grained and spotted gabbros exist in lenses up to 200 m wide. The eastern section of the complex displays a gradational transition from south to north of norite and gabbro cumulates, to monzodiorites, to monzonites near the northern contact with the Round Valley Peak granodiorite. Lewis et al. (2021) (Chapter 1, this thesis) describes this body in more detail and presents a fractionation model for the complex.

Tamarack Lakes

The mafic body at Tamarack Lakes (95.1±0.8 Ma, 2.3 km^2) intrudes into the quartz monzonite of Wheeler Crest (210 Ma), and is separated from the Hidden Lakes mafic complex by a 1.5 km wide intrusion of the Lake Edison granodiorite (90.9 Ma, Lackey et al. 2008). Based on mapped geometries and coeval ages, it is possible that the Tamarack and Hidden Lakes bodies were once a single intrusion that was split apart by subsequent Cretaceous intrusions. The lowest exposure of the Tamarack Lakes body is ~500 ft higher than the observed portions of the Hidden Lakes mafic complex, and thus if these two bodies were part of the same system, Tamarack Lakes represents a slightly shallower level. This body consists of mainly equigranular medium-grained amphibole-gabbro, which contains several ~100 m pods of diorite. The diorites can be either fine-grained and plagioclase dominated with small amphibole grains, or a coarse-grained network of acicular amphibole with interstitial plagioclase.

Pine Creek

The Pine Creek body (190.8±3.9 Ma,1.8 km^2) is made up of medium-grained amphibole-biotite gabbro through diorite with variable amounts of plagioclase. The mafic rocks are pervasively intruded by aplite dikes. This complex is in contact with the coeval with the granite of Chickenfoot Lake (191.8±4.2 Ma, Lewis et al. 2021) on its northern side, and is intruded by the Lake Edison granodiorite and Mono Creek granite (87 Ma, Lackey et al. 2008).

Mount Tom

The Mount Tom complex consists of one main body (1.8 km^2) on the eastern flank of Mount Tom, surrounded by many smaller bodies that collectively cover ~ 1 km^2. We sampled only the main body of this complex (146.8±2.4 Ma), which intrudes into the Tungsten Hills quartz monzonite (200±4.6 Ma) and the metasedimentary Permian-Pennsylvanian Pine Creek pendant. The Mount Tom complex contains medium-grained equigranular amphibole-biotite gabbros and diorites, occasionally with very large biotite oikocrysts (up to 2 cm). Irregular pods of amphibole-norite cumulates 1-2 m in diameter are found within the gabbros (Fig A5h). Many of the gabbros also contain lense-shaped plagioclase-amphibole segregations, which we interpret as accumulations of late stage melts.

Tungsten Hills

The Tungsten Hills mafic body covers 1.3 km^2 on the eastern side of the Tungsten Hills near Bishop, CA. The 149.6±2 Ma intrusion was emplaced into the 200 Ma Tungsten Hills quartz monzonite. The most common rock type is a coarse-grained amphibole-biotite gabbro,

with variably developed cm-scale layering. Few outcrops of plagioclase-rich amphibole-diorite are found near the southern margin of the body. Many metasedimentary xenoliths are present, some up to 50 m in size. Garnet-bearing skarns are common along contacts between gabbros and metasedimentary rocks, though we avoided these areas when sampling.

Lake Sabrina

The mafic body at Lake Sabrina (91.1±0.2 Ma, Coleman et al. 1995) is entirely a diorite to quartz-diorite intrusion, with few associated basaltic dikes. The diorites cover an area of 4.3 km^2 and are generally medium-fine grained and contain both biotite and amphibole. Some diorite samples contain macroscopic titanite, up to 3 mm. This intrusion appears co-magmatic with the neighboring Lamarck granodiorite (91.9±0.6 Ma, Coleman et al. 1995), as enclaves of the Lake Sabrina diorite are observed separating into and mingling with the Lamarck granodiorite along the eastern margin of the diorite body.

Bishop Creek

The mafic complex at Bishop Creek (148.6±2 Ma) is located on the eastern side of the South Fork Bishop Creek Canyon. The dominant rock type is a biotite and clinopyroxene rich fine-grained gabbro (~2 mm grain size), which occasionally grades into coarser grained, porphyritic amphibole-gabbro (5-10 mm grain size). The northern margin of the complex is occupied by biotite-rich diorite. The mafic magmas intruded into the Tungsten Hills quartz monzonite, which is dated to 200 Ma near the north side of the Bishop Creek mafic complex (Lackey et al. 2008). However, we date the granitoid to the south of the mafic rocks, which is also mapped as the Tungsten Hills quartz monzonite, as crystallizing at 167.8±3.3 Ma. This is

likely a previously unrecognized granitoid body on the southern side of the complex, which had previously been lumped in with the Tungsten Hills quartz monzonite. Thin, elongate slivers of metasedimentary rock are common within the complex, likely sourced from the nearby Bishop Creek pendant on the west side of the same valley. Multiple mining claims within the complex exploit diopside, epidote, and garnet-bearing skarns that develop along contacts between metasedimentary rocks and mafic magmas.

Green Lake

The mafic complex at Green Lake consists of multiple hills and outcrops of amphibole-dominated diorites and gabbros, separated by extensive talus, which are potentially connected beneath the cover. We sampled from the two largest mapped mafic exposures, which sum to an area of ~1.1 km^2. Two main rock types are present: 1) a porphyritic amphibole gabbro with coarse (1 cm) amphibole crystals surrounded by a matrix of fine grained clinopyroxene and plagioclase (similar to Fig A5e, though this photo is from MM), and 2) a medium-grained amphibole-biotite gabbro that grades to diorite with increasing plagioclase content. We also observe a clinopyroxenite and gabbro xenoliths within the diorite (Fig A5g), suggesting that ultramafic cumulates are associated with this intrusion, but are not necessarily exposed. Co-magmatic fine-grained diabase intrusions are found with pillow-like morphologies in the medium-grained gabbros and diorites (Fig A5d), likely preserving melt compositions. The 95.1±0.9 Ma Green Lake mafic complex intrudes into the southern, now disaggregated section of the Bishop Creek metasedimentary pendant, and thus contains large xenolithic blocks and garnet-bearing skarns. The mafic rocks are intruded by the Lamarck granodiorite (91.9±0.6 Ma, Coleman et al. 1995) on the south side of the complex.

Keough

The three bodies that make up the Keough complex, located just west of Keough Hot Springs and cover an area of 0.85 km^2, intruded into the Leucogranite of Rawson Creek (96.4±8 Ma) at 89.8±0.7 Ma. Lithologies are biotite-amphibole gabbros through diorites, with two internal bodies (~150-200 m) of coarse-grained amphibole-rich cumulates with occasional clinopyroxene contained within amphibole cores. Metasedimentary xenolith blocks up to 100 m in length are entrained within the gabbro, however the origin of the blocks is unknown as the complex is not in contact with metasedimentary rocks at the level of exposure.

Shannon Canyon

Of the six mapped mafic bodies in the Shannon Canyon complex (summing to 2.1 km^2), we observed and sampled the four lowest elevation bodies (Fig 1, sampled bodies shown in purple, un-sampled shown in gray). The lithologies are dominantly amphibole-diorite, with patches of foliated biotite-rich diorite (~50 m wide) and pods of diabase with amphibole and biotite phenocrysts in a fine-grained plagioclase-dominated matrix. The Shannon Canyon complex (171.9±2.4 Ma) intruded contemporaneous, and possibly co-magmatic, with a granitoid mapped as the Tungsten Hills quartz monzonite, which we date as 171.5±2.7 Ma at this location, though contacts are not well exposed to discern the intrusive relationships. The north side of the complex was then intruded by a granite mapped as “rocks similar to the Cathedral Peak alaskite” (Bateman et al. 1965), which we date as 146.1±3 Ma.

Mount Alice

The Mount Alice mafic complex (147.8±2.2 Ma) is a series of small bodies exposed in both the south and north forks for Big Pine Creek Canyon with a collective area of ~1 km^2. The complex was likely originally fewer larger intrusions, which are now dissected by intrusion of the Leucogranite of Rawson Creek, locally dated to 95 Ma by Wenner and Coleman (2004). The mafic intrusions are in contact with the older Tinemahah granodiorite (164 Ma, Lackey et al. 2008) on the south side of the complex. Angular fragments of fine-grained biotite-bearing diabase and biotite-diroite, typically 5 to 10 cm in size, are common within the surrounding Leucogranite of Rawson Creek, suggesting that portions of the Mount Alice complex were brecciated by younger granitic intrusions. The complex contains two common lithologies: a fine-grained amphibole-gabbro, and a biotite-amphibole diorite. Enclaves of the gabbro can be found within the diorite. In addition, coarse-grained amphibole-rich cumulates can be found in the exposures on the east side of Mount Alice. Leucogranite dikes and pods intrude the gabbro body at First Lake and mingle with the mafic lithologies, locally forming amphibole-diorites (<5 m wide areas). Additionally, rounded elongate pipes of the leucogranite, ~10 to 30 cm wide intrude into the gabbros along the margins of the leucogranite pods (Fig A5c).

MacMurray Meadows

The MacMurray Meadows complex intruded at 151.4±2.1 Ma and was later fully surrounded by the granodiorite of MacMurray Meadows (145.7±2.5 Ma). The complex is dismembered into six main bodies, with many small surrounding mafic blocks engulfed by the granodiorite. The overall exposure of mafic rocks is roughly 2.4 km^2. The largest body surrounds four pod-like intrusions of granodiorite. This large body is mainly composed of porphyritic

amphibole gabbro, with amphibole crystals up to 1 cm (~30-40% modally), which can contain inclusions of clinopyroxene, olivine, and spinel. This gabbro is layered with norite cumulates (Fig A5f) of a similar texture, though the amphibole crystals are more common (up to 75% modally) and surrounded by a fine-grained orthopyroxene+ clinopyroxene+ plagioclase matrix (Fig A5e). Near the margins with the granodiorite, including the granodiorite pods, the gabbros grade to porphyritic amphibole diorite. The second largest and lowest elevation mafic exposure is cut by multiple aplite dikes, and is mainly composed of the porphyritic diorite lithology. All of our samples from this body are coarse-grained, and are clearly cumulates based on textures, mineralogy, and geochemistry. Thus, we do not calculate a crustal thickness from this locality.

Armstrong Canyon

We observe medium-grained amphibole- and biotite-bearing diorite and quartz-diorite within the mafic complex at Armstrong Canyon (9.7 km^2), also referred to as the Aberdeen Complex. Frost (1987) reports amphibole gabbro and layered biotite-amphibole gabbro at higher elevations in the complex. Coleman et al. (1995) date this complex at 91.5±0.2 Ma, as well as the coeval granite of Goodale Mountain (92.6±1.2 Ma). Mingling between the Armstrong diorites and granite of Goodale Mountain is observed along the western margin of the complex (Coleman et al. 1995). The mafic body intrudes the Mule Lake pluton on its southwestern side, which we date to 158.7±3.1 Ma, as well as a Permian metasedimentary pendant.

Black Canyon

The Black Canyon mafic body (154.6 Ma, 9.5 km^2) intruded into the Mule Lake pluton (158.7±3.1 Ma) and Permian metasedimentary rocks. It was then intruded by the Spook pluton

(106.6±1.1 Ma) on its northern side, McDoogle pluton (94 Ma) (Mahan et al. 2003) on the west side, and the undated McGann pluton to the south which is inferred to be younger than the McDoogle pluton based on intrusive relationships (Moore 1963). The northern portion of the complex is extensively cut by dikes, likely of the Independence dike swarm (148 Ma) (Chen and Moore 1979; Coleman et al. 2000), but the southern portion is not intruded by dikes while other nearby Jurassic plutons are pervasively intruded (such as the Tinemahah granodiorite at Woods Lake, the Independence dike type locality). Thus it is possible that the southern portion of the complex is slightly younger than the north side. We observe mainly foliated, biotite-rich diorites (Fig A5b) containing schlieren, and a small section of medium-grained amphibole gabbro. Frost (1987) reports mainly biotite gabbros from this body, as well as a pod of anorthosite in the high elevation western section of the body, which we did not reach.

Onion Valley

The mafic complex of Onion Valley (92.1±0.3 Ma; Coleman et al. 1995) is the largest mafic intrusion in the eastern SNB (~25 km^2), as well as the most primitive (parental melt Mg#=60). The body consists predominantly of layered gabbros overlain by sheeted sills of basaltic through dioritic composition, with smaller stocks of olivine-hornblendite that host olivine with Mg# = 86. Detailed field description, compositional analyses, and crystallization modeling was completed by (Sisson et al. 1996). The gabbros and sills intrude the Bullfrog pluton (103 Ma) to the south and the Dragon pluton to the north (103 Ma)(Lackey et al. 2008).

3.13. References Cited in Appendix

Ague JJ, Brimhall GH (1988) Magmatic arc asymmetry and distribution of anomalous plutonic belts in the batholiths of California: Effects of assimilation, crustal thickness, and depth of crystallization. Geological Society of America Bulletin 100(6):912-927

Armstrong JT (1995) Citzaf-a package of correction programs for the quantitative Electron Microbeam X-Ray-Analysis of thick polished materials, thin-films, and particles. Microbeam Analysis 4(3):177-200

Bateman P, Carmar M, Clark L, Jackson E, Parker R (1965) Geologic map of the Big Pine 15-minute quadrangle, California. US Geol Surv Prof Pap 470

Bateman PC (1992) Pre-Tertiary bedrock geologic map of the Mariposa 1° by 2° quadrangle, Sierra Nevada, California; Nevada. The Survey,

Beattie P (1993) Olivine-melt and orthopyroxene-melt equilibria. Contributions to Mineralogy and Petrology 115(1):103-111

Bucholz CE, Spencer CJ (2019) Strongly Peraluminous Granites across the Archean–Proterozoic Transition. Journal of Petrology 60(7):1299-1348

Chapman AD, Saleeby JB, Wood DJ, Piasecki A, Kidder S, Ducea MN, Farley KA (2012) Late Cretaceous gravitational collapse of the southern Sierra Nevada batholith, California. Geosphere 8(2):314-341

Chapman JB, Gehrels GE, Ducea MN, Giesler N, Pullen A (2016) A new method for estimating parent rock trace element concentrations from zircon. Chemical Geology 439:59-70

Chen JH, Moore JG (1979) Late Jurassic Independence dike swarm in eastern California. Geology 7(3):129-133

Coleman D, Glazner A, Miller J, Bradford K, Frost T, Joye J, Bachl C (1995) Exposure of a Late Cretaceous layered mafic-felsic magma system in the central Sierra Nevada Batholith, California. Contributions to Mineralogy and Petrology 120(2):129-136
Coleman DS, Carl BS, Glazner AF, Bartley JM (2000) Cretaceous dikes within the Jurassic Independence dike swarm in eastern California. Geological Society of America Bulletin 112(3):504-511

Elder D, Reichert M (2010) Region-wide GIS bedrock compilation mapping–an ArcSDE geodatabase Version 2.0: digital dataset–agency internal publication. USDA Forest Service, Pacific Southwest Region 5, Vallejo, California

Frost TP (1987) Sample localities, radiometric ages, descriptions, and major-and trace-element abundances of Late Jurassic mafic plutonic rocks, eastern Sierra Nevada, California. Department of the Interior, US Geological Survey,

Gehrels GE, Valencia VA, Ruiz J (2008) Enhanced precision, accuracy, efficiency, and spatial resolution of U-Pb ages by laser ablation–multicollector–inductively coupled plasma–mass spectrometry. Geochemistry, Geophysics, Geosystems 9(3)

Lackey JS, Valley JW, Chen JH, Stockli DF (2008) Dynamic magma systems, crustal recycling, and alteration in the central Sierra Nevada batholith: The oxygen isotope record. Journal of Petrology 49(7):1397-1426

Mahan KH, Bartley JM, Coleman DS, Glazner AF, Carl BS (2003) Sheeted intrusion of the synkinematic McDoogle pluton, Sierra Nevada, California. Geological Society of America Bulletin 115(12):1570-1582

Moore JG (1963) Geology of the mount Pinchot quadrangle, southern Sierra Nevada, California. US Government Printing Office,

Pullen A, Ibáñez-Mejia M, Gehrels GE, Giesler D, Pecha M (2018) Optimization of a laser ablation single collector inductively-coupled plasma mass spectrometer (Thermo Element 2) for accurate, precise, and efficient zircon U-Th-Pb geochronology. Geochemistry, Geophysics, Geosystems 19(10):3689-3705

Sisson T, Grove T, Coleman D (1996) Hornblende gabbro sill complex at Onion Valley, California, and a mixing origin for the Sierra Nevada batholith. Contributions to Mineralogy and Petrology 126(1-2):81-108

Vermeesch P (2018) IsoplotR: A free and open toolbox for geochronology. Geoscience Frontiers 9(5):1479-1493

Wenner JM, Coleman DS (2004) Magma mixing and cretaceous crustal growth: Geology and geochemistry of granites in the central Sierra Nevada Batholith, California. International Geology Review 46(10):880-903

Wesley A, Paterson SR, Attia S, Ardill KE (2019) Jurassic structural evolution of the King Creek area, southern Ritter Range, Sierra Nevada, CA. In: AGU Fall Meeting Abstracts, vol 2019. pp T23F-0448

3.14 Appendix Figures and captions

Appendix Figure A1

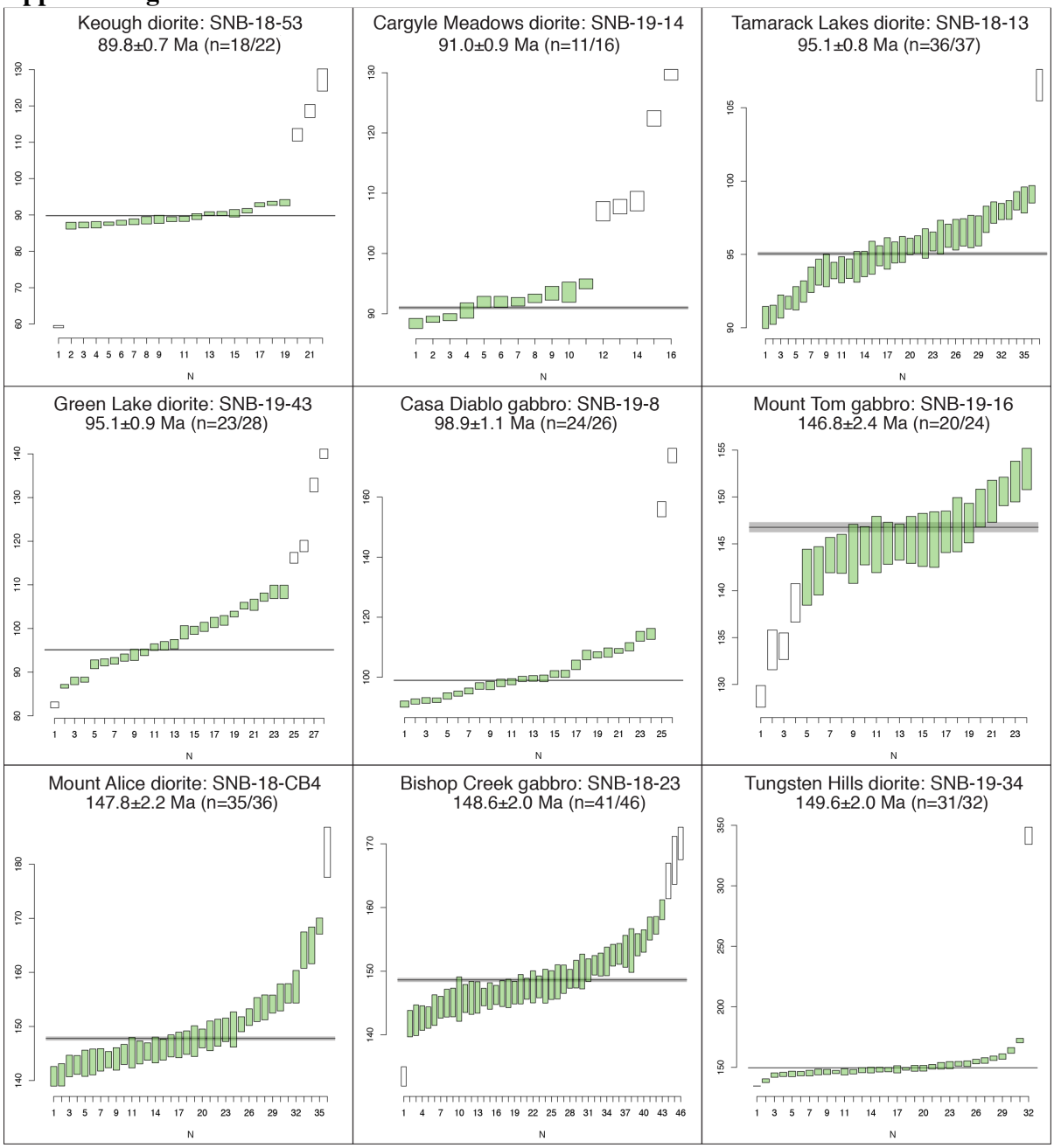

Appendix Figure A1 (cont.)

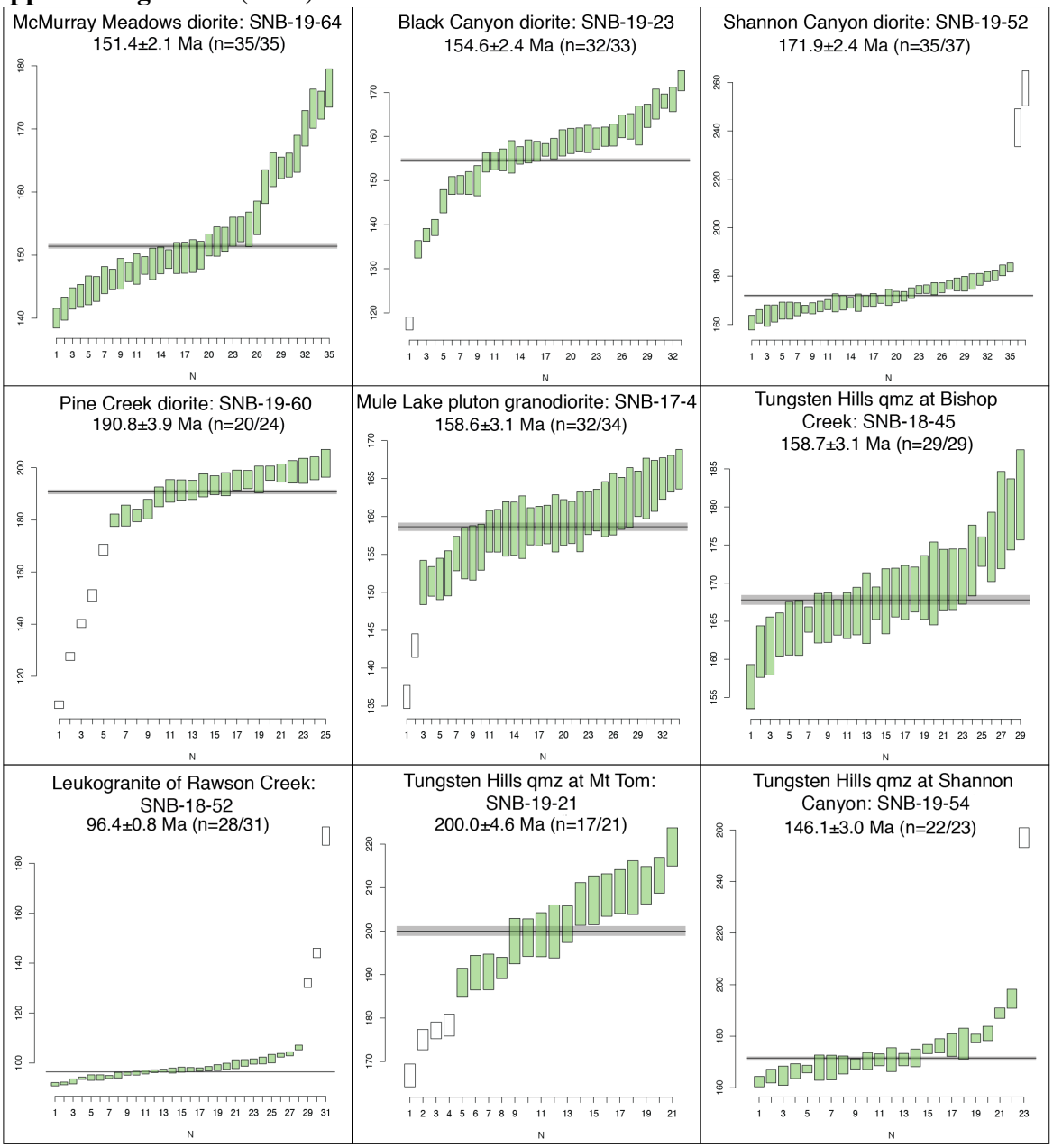

Appendix Figure A1 (cont.)

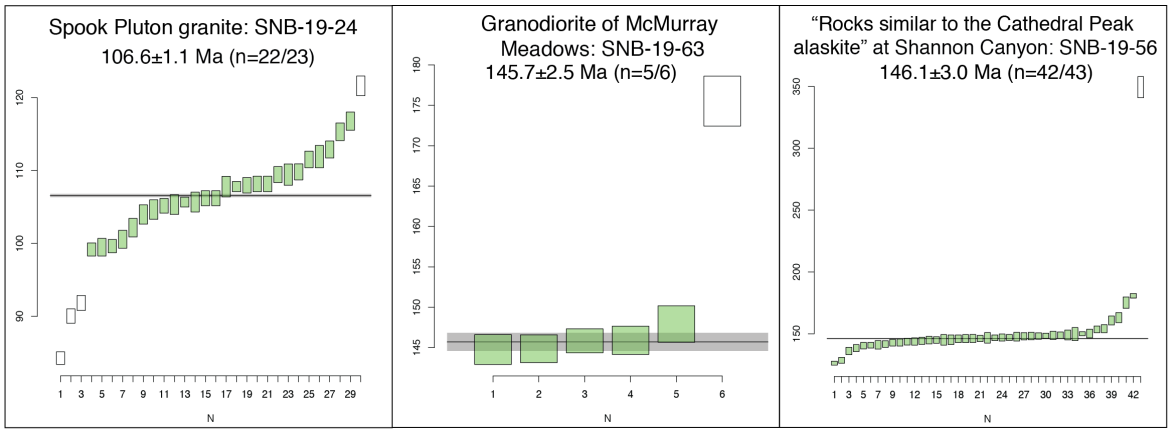

Figure Al Weighted mean age plots for all new U-Pb zircon geochronology samples. Green bars are good analyses that are included in the age calculation. White bars are considered outliers or inherited grains and excluded. Discordant grains are not shown on these plots. The horizontal black line is the sample age, gray bar is 1 standard error, and the error given with the age at the top of each panel is 2σ of the acceptable zircon analyses.

Appendix Figure A2

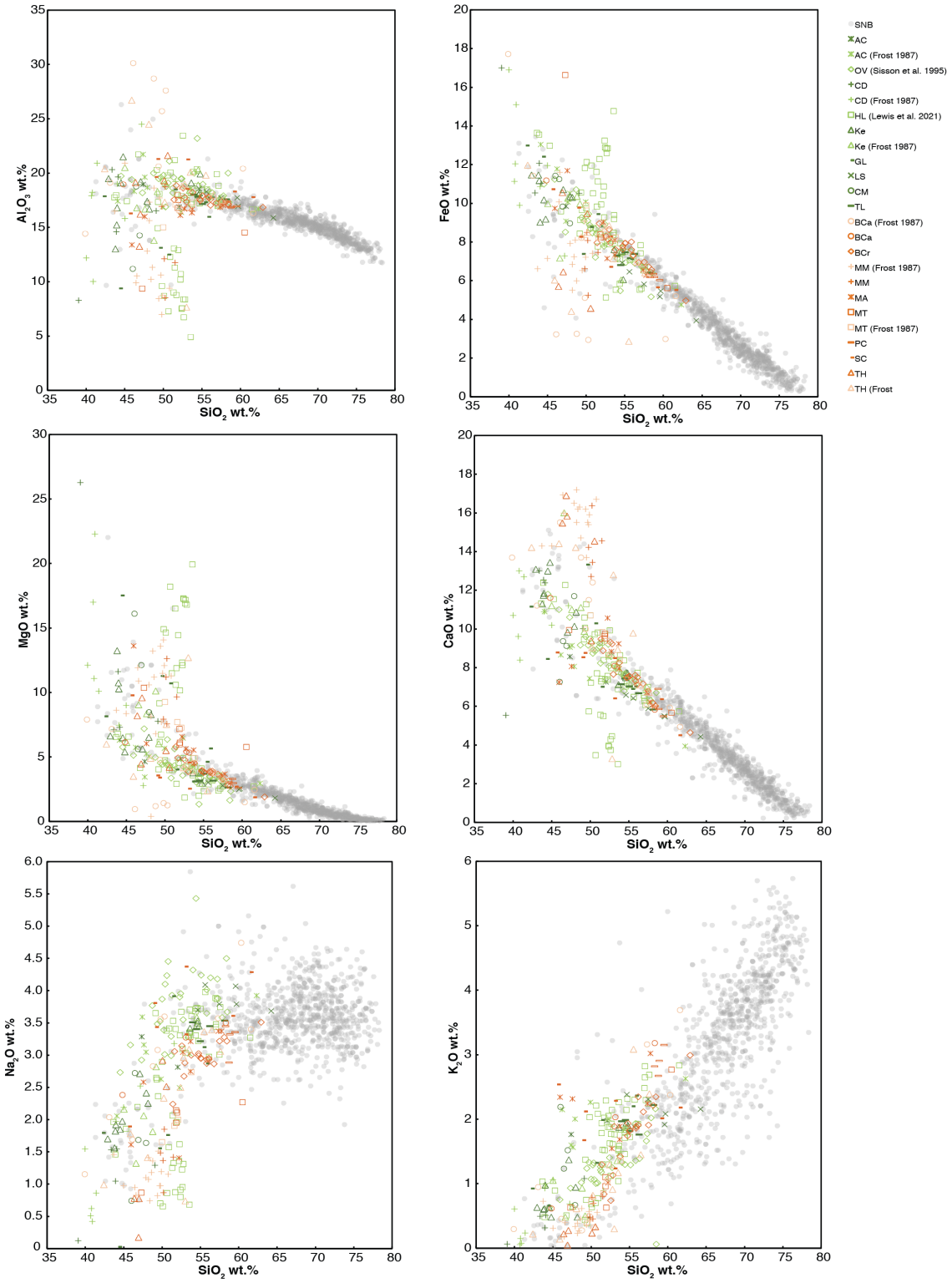

Figure A2 SiO_2 vs oxide plots for all mafic samples from the astern SNB, and granitoids from the SNB for comparison. All symbols are as in Figure 3. Orange symbols are Jurassic bodies, and green symbols are Cretaceous intrusions. Darker colored symbols are new to this study, and lighter symbols have been previously published.

Appendix Figure A3

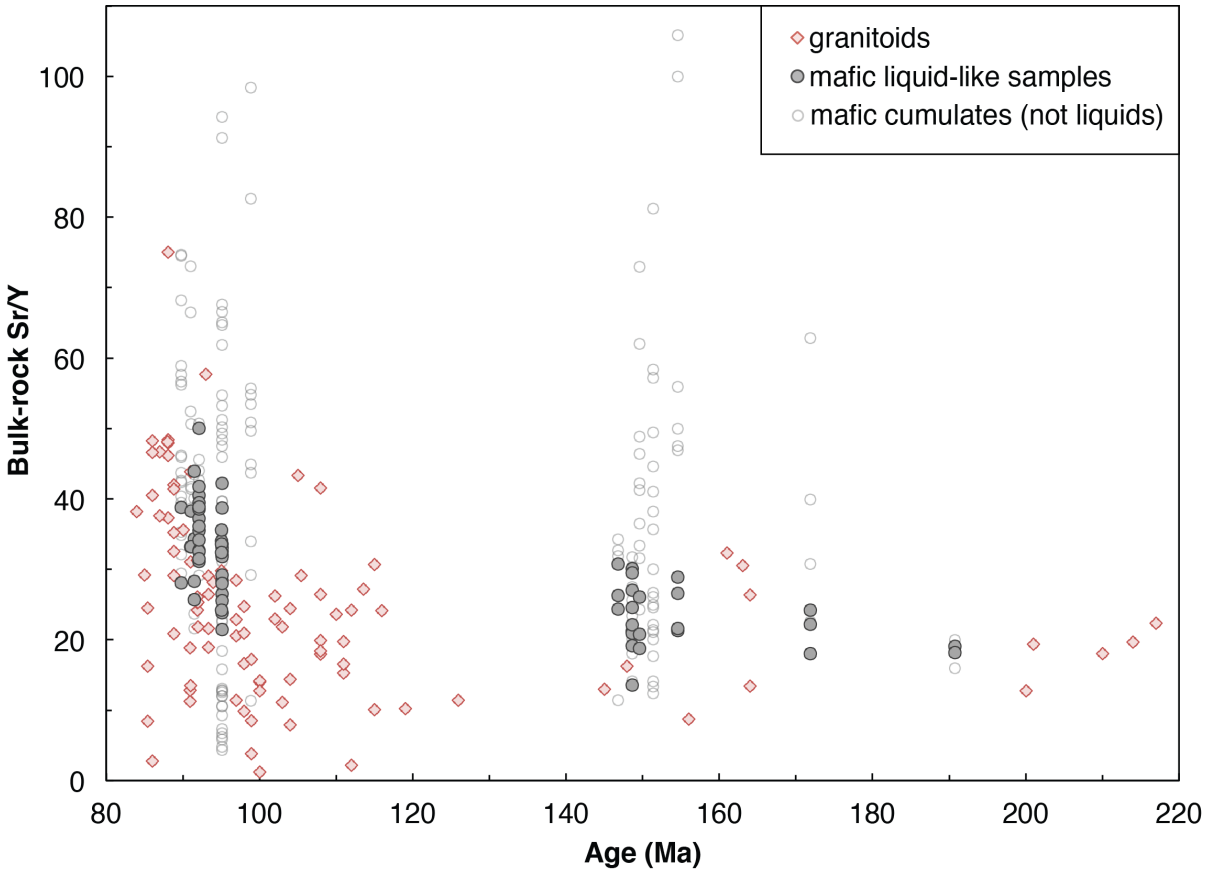

Figure A3 Sr/Y ratios for all individual samples in this study (not averages), including new mafic samples, mafic compositions reported by Frost (1987), and granitoid samples from Lackey et al. (2008).

Appendix Figure A4

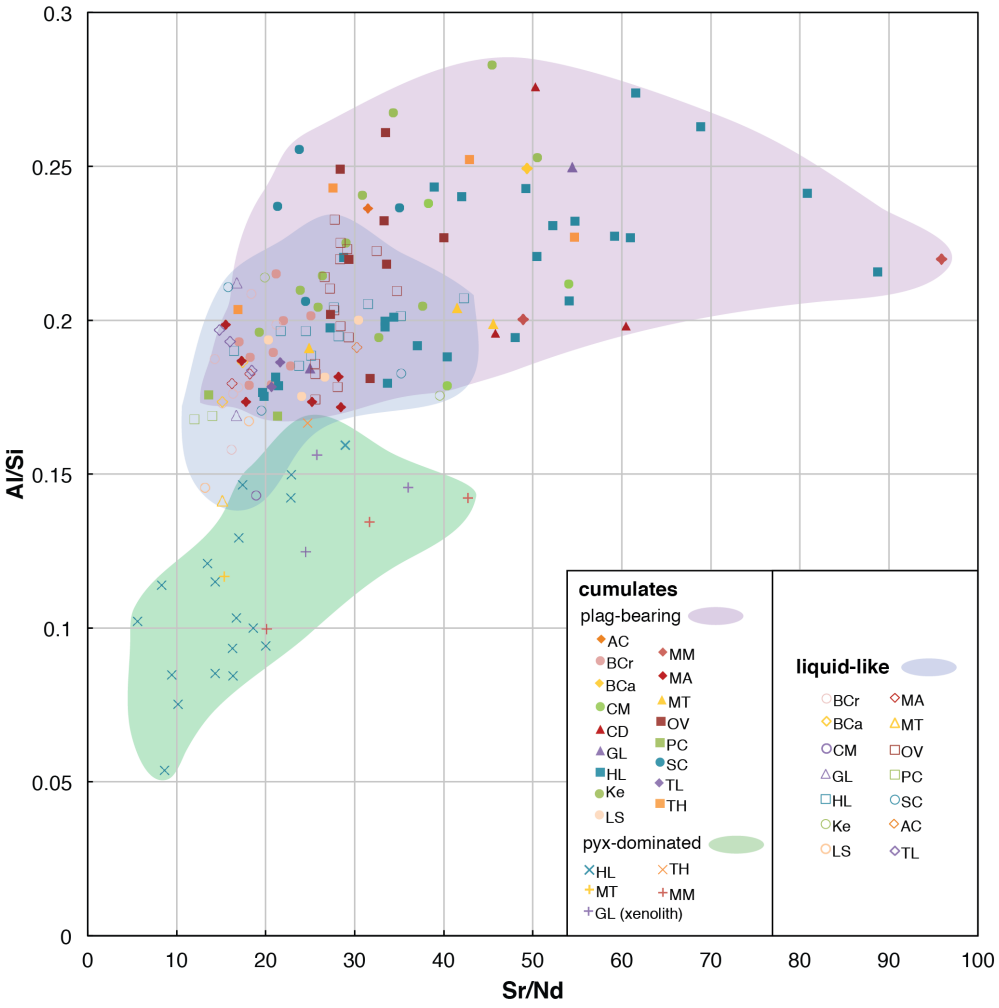

Figure A4 Bulk-rock Sr/Nd vs Al/Si ratios for mafic samples in this study and in Lewis et al. (2021). Shaded fields outline the areas where cumulate and liquid-like samples are found. As the parental melt compositions are likely variable between each mafic body, there is considerable overlap between the liquid-like and plagioclase-bearing cumulate fields. However, within each body, liquid-like samples have lower Al/Si and Sr/Nd ratios than samples of cumulative origin. We also take textural evidence (dike, pillow, or fine-grained rocks) into account to classify a sample as liquid-like. Both elemental ratios are proxies for accumulation of plagioclase, so pyroxene dominated cumulates (norite, clinopyroxene-rich gabbro, peridotite, and a clinopyroxenite xenolith), though they may contain interstitial plagioclase, have low Sr/Nd and Al/Si despite their cumulate textures.

Appendix Figure A5

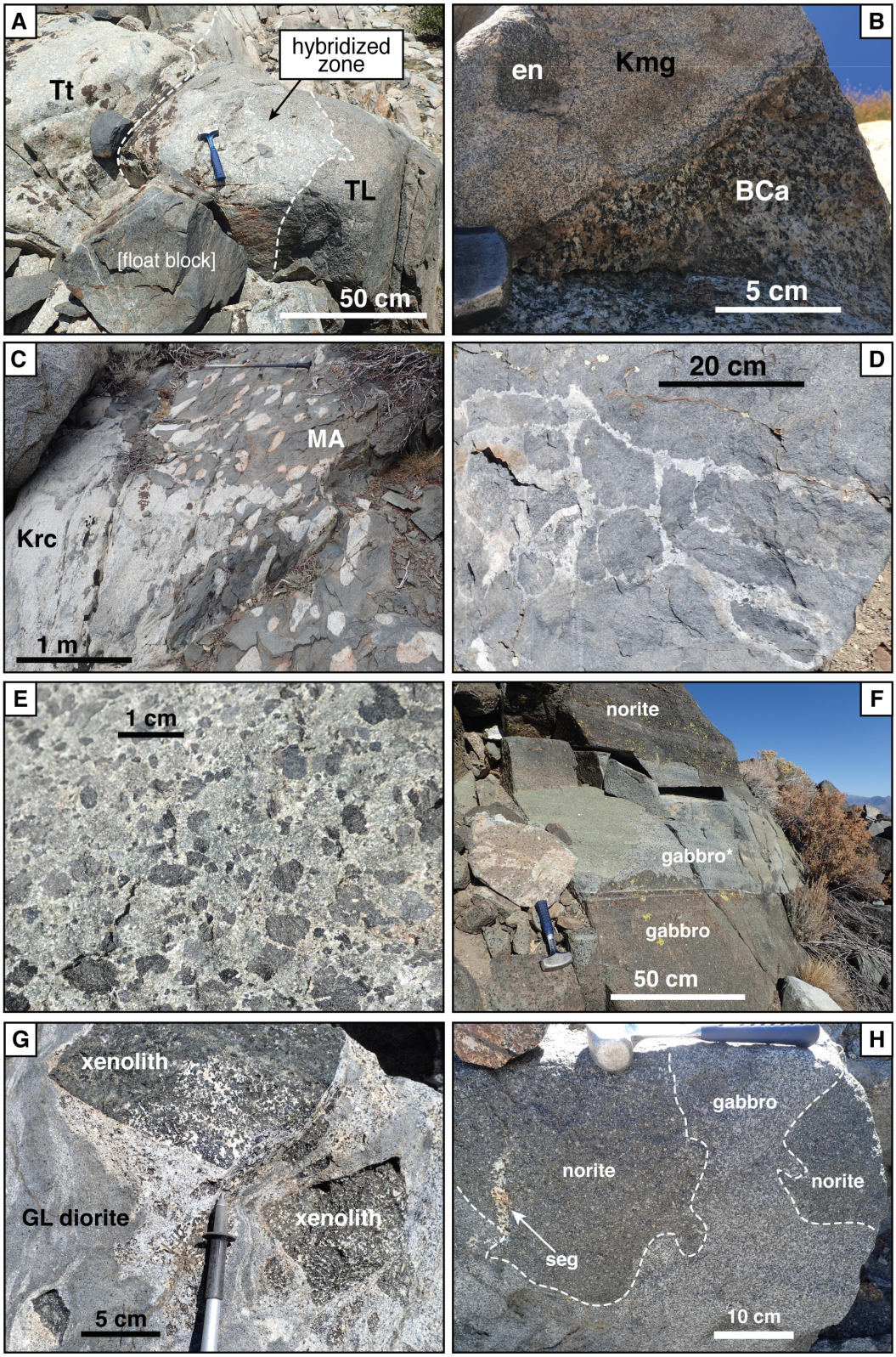

Figure A5 A selection of field photos from the eastern SNB mafic complexes. **a** Gradational contact with a hybridized zone between the Tungsten Hills quartz monzonite (Tt) and younger amphibole gabbro-diorite of Tamarack Lakes (TL). **b** Sharp contact where the McGann pluton (Kmg) intrudes the weakly-foliated biotite-diorite of Black Canyon (BCa). Here, the McGann pluton contains a mafic enclave (en) that is unrelated to the Jurassic mafic complex. **c** Pipes of the leucogranite of Rawson Creek (Krc) where it intrudes the fine-grained gabbros of Mount Alice (MA). **d** Pillowed fine-grained diorite with felsic septa (lighter colored) in the Green Lakes mafic complex. This diorite is an example of a texture that we consider liquid-like, however this composition is more evolved than the compositions that we use for crustal thickness calculations. **e** Porphyritic amphibole gabbro of McMurray Meadows. Black crystals are amphibole, and the fine-grained matrix is plagioclase and clinopyroxene. **f** Cumulate layering of norite (top) and gabbro (bottom) at McMurray Meadows. Note that the lightest colored area (labeled gabbro*) is part of the gabbroic layer, but is light colored mainly due to recent exposure of the surface rather than a lithologic difference. **g** Clinopyroxene-rich gabbro xenoliths in the Green Lake diorite (GL), which is locally mingled with felsic septa. **h** Pods of cumulate norite surrounded by gabbro at Mount Tom. A plagioclase+ amphibole segregation (seg) extends from the norite into the gabbro, which we interpret as an example of late-stage melt extraction from the cumulates.

3.15 Appendix Tables

Appendix Table 1: Geochronology Summary

Mafic Body	Sample # or [reference]	latitude	longitude	Age (Ma)	2σ	n (good grains)	MSWD
Keough	SNB-18-53	37.25729	-118.38608	89.8	0.7	18	36.5
Cargyle Meadows	SNB-19-14	37.57189	-119.15573	91.0	0.9	11	27.1
Lake Sabrina*	[Coleman et al. (1995)]			91.1	0.2		
Armstrong Canyon*	[Coleman et al. (1995)]			91.5	0.2		
Onion Valley*	[Coleman et al. (1995)]			92.1	0.3		
Tamarack Lakes	SNB-18-13	37.41301	-118.71196	95.1	0.8	36	41.7
Hidden Lakes*	[CH1]			95-96.5			
Green Lake	SNB-19-43	37.17112	-118.52915	95.1	0.9	23	255
Casa Diablo	SNB-19-8	37.55014	-118.70701	98.9	1.1	24	143
Mount Tom	SNB-19-16	37.34702	-118.63694	146.8	2.4	20	7.45
Mount Alice	SNB-18-CB4	37.12515	-118.44491	147.8	2.2	34	23.2
Bishop Creek	SNB-18-23	37.24170	-118.55610	148.6	2.0	41	18.3
Tungsten Hills	SNB-19-34	37.35391	-118.52570	149.6	2.0	30	47.5
McMurray Meadows	SNB-19-64	37.06480	-118.37350	151.4	2.1	35	69.8
Black Canyon	SNB-19-23	36.87073	-118.30384	154.6	2.4	32	71.8
Shannon Canyon	SNB-19-52	37.20338	-118.39962	171.9	2.4	34	18.2
Pine Creek	SNB-19-60	37.35350	-118.72951	190.8	3.9	20	15.2
Mule Lake pluton (at Armstrong Canyon)	SNB-17-4	36.95081	-118.34650	158.7	3.1	32	8.74
Tungsten Hills qzm (at Bishop Creek)	SNB-18-45	37.23537	-118.56112	167.8	3.3	28	6.69
Leucogranite of Rawson Creek (at Keough)	SNB-18-52	37.25538	-118.39072	96.5	0.8	28	76.6
Tungsten Hills qzm (at Mt Tom)	SNB-19-21	37.34917	-118.62954	200.0	4.6	17	20
Tungsten Hills qzm (at Shannon Canyon)	SNB-19-54	37.20490	-118.39680	171.5	2.7	21	24.5
Spook pluton (at Black Canyon)	SNB-19-24	36.87163	-118.30086	106.6	1.1	26	64.3
Grd of MacMurray Meadows	SNB-19-63	37.06490	-118.37382	145.7	2.5	5	1.42
Kca (at Shannon Canyon)	SNB-19-56	37.21500	-118.38915	146.1	3.0	40	19

***** The Lake Sabrina, Armstrong Canyon, and Onion Valley complexes have been dated by Coleman et al. (1995), and geochronology data from the Hidden Lakes complex is included in Lewis et al. (2021)

CHAPTER 4

Anomalous Pacific-Antarctic Ridge Volcanism Precedes Glacial Termination 2: Insights from Glass Shard Geochemistry

4.1 ABSTRACT

A 20 cm interval in sediment core OC170-26-159, taken from off-axis of the Pacific-Antarctic ridge (PAR), contains abundant basaltic glass shards that are the products of unusually energetic submarine eruptions. Oxygen isotope stratigraphy places the peak in basalt content between 128 and 148 kyr BP, overlapping with glacial Termination 2. The glasses are similar to MORB composition with remarkable homogeneity between shards, but are more evolved (5.8-6.5 wt.% MgO) than effusively erupted basalts from the PAR axis. H_2O and incompatible trace element contents are also elevated compared to typical MORB. Volatile saturation pressures are consistent with eruption from water depths at the PAR axis rather than a deeper, off-axis vent. We calculate a fractional crystallization liquid line of descent from a primitive axial basalt through the glass shard compositions, which strongly implies that the shards erupted from the PAR axis. At the time of ash deposition, the core location was 7 km from the PAR axis, though glasses from other mid-ocean ridges are not reported beyond 3 km from their eruption site. Therefore, dispersal of glasses to this distance requires a series of anomalously large eruptions. The interval of glass shard deposition lags a rapid drop in sea level, which is expected to enhance mantle melting, by ~50 kyr, consistent with estimates of magma migration timescales from melting depths to the ridge axis. We posit that the unusual compositions of the glass shards are also a result of sea level modulation of mantle melting, and may have played a role in influencing the explosive eruption style.

4.2 INTRODUCTION

Volcanism at mid-ocean ridges (MOR) constitutes roughly 70% of the global volcanic output, yet these eruptions are difficult to access and thus minimally studied in comparison to

subaerial volcanism. MORs are classically assumed to produce effusive eruptions at relatively steady, mantle- and tectonically-driven rates. However, a growing body of evidence from hydrothermal metal fluxes and seafloor bathymetry suggests that volcanic activity and melt flux to ridge axes can be perturbed by changes in sea level, and is thus tied to the global climate as water is transferred between Earth's oceans and ice sheets. This includes variability in the deposition of hydrothermal metals in pelagic sediments on Milankovitch timescales, with maximum hydrothermal fluxes coinciding with glacial terminations (Costa et al. 2017; Lund et al. 2016; Middleton et al. 2016). As seawater percolates through oceanic crust it is heated by proximity to shallow magma bodies, which promotes leaching of metals from the crust (Fe, Mn) and enables their release through hydrothermal vents. Therefore, elevated magma intrusion rates increase the hydrothermal metal flux into deep ocean sediments. Moreover, the spacing of abyssal hills is used as a proxy for crustal thickness, thereby also tracking temporal variation in magma supply. Higher melt flux will presumably produce thicker crust and high topography, while periods of low magmatic flux generate thinner crust resulting in valleys. Some studies find that abyssal hill periodicity is consistent with glacial-interglacial forcing (Boulahanis et al. 2020; Crowley et al. 2015; Tolstoy 2015), but the significance of these bathymetric features as records of crustal thickness, and therefore melt production, is debated (Carbotte et al. 2006; Goff 2015; Olive et al. 2015).

Decreases in sea level are expected to enhance melt production due to decompression melting, while sea level rise during glacial terminations should result in suppressed melting (Boulahanis et al. 2020; Lund and Asimow 2011). The rate of decompression due to sea level change during initiation or termination of glacial periods (~±10 mm/yr) generates pressure changes on the order of ±100 Pa/yr (Lund and Asimow 2011). This is a considerable change

compared to decompression rates caused by plate spreading (500-2000 Pa/yr, depending on spreading rate), resulting in alteration of the melting rate by 15 to 100% in response to rapid sea level change, relative to the MOR average (Lund and Asimow 2011). As melting of the mantle occurs primarily between 50 and 100 km depth at moderate- to fast-spreading ridges (Forsyth et al. 1998; Langmuir et al. 1992; Presnall et al. 1979; Shen and Forsyth 1995), melt migration rates estimated for typical MOR systems (1-10 m/yr; Kelemen et al. 1997; Lund and Asimow 2011; Lund et al. 2018) result in sea level-driven signals reaching the axial magmatic system 15 to 50 kyr after the sea level change (Boulahanis et al. 2020; Lund and Asimow 2011; Lund et al. 2016). Thus, enhanced hydrothermal flux observed during glacial terminations is not likely tied to the concomitant sea level rise, but rather is triggered by rapidly falling sea level during stages of ice sheet growth.

Another potential record of glacial-interglacial fluctuation in MOR magmatism is submarine pyroclastic volcanic deposits, which preserve fragments of MOR lavas within the stratigraphic column. Ash layers containing volcanic glass have been reported associated with both fast- and slow-spreading ridges (Clague et al. 2009; Portner et al. 2015; Sohn et al. 2008), indicating that mildly explosive eruptions MOR settings are more common than previously assumed. These deposits are beneficial for studying the timing of MOR eruptions because ash layers can be dated using oxygen isotope analyses of sediments from the same horizon as the volcanic glasses to construct a chronology of ash-producing eruptions.

We investigate basaltic glass shards from an ash layer in core OC170-26-159, retrieved from 13.5±1.5 km west of the Pacific-Antarctic ridge (PAR) axis at a water depth of 2754 m (Fig 1). Glass shards range from 36 to 1000 μm in size with most falling between 125 and 250 μm, and are vitreous and largely aphyric, with rare plagioclase and olivine microphenocrysts (Fig 2).

Shards are abundant in a layer between 128 and 148 cm depth, or from 120 to 200 kyr BP as determined by the oxygen isotope age model for the core, with the maximum glass content at 138 kyr BP (Fig 2) (Lund et al. 2018). The interval with most the abundant glass shards (128-145 kyr BP) is coincident with glacial Termination 2 (T2). We interpret these glass shards as the products of explosive (Strombolian) submarine eruptions.

During T2 and the interval of greatest glass shard accumulation, the core location was located approximately 7 km off-axis of the PAR, based on the estimated half spreading rate of 49 mm/yr (https://www.ldeo.columbia.edu/~menke/plates.html). Glasses from ridge segments of the East Pacific Rise, Juan de Fuca Ridge, and associated seamouts are reported only within 3 km of their respective sources (Clague et al. 2015; Sohn et al. 2008), and thus the T2 ash layer represents an anomalously energetic series of eruptions. Dispersal of shards to a distance of 7 km requires a buoyant plume of hot water and pyroclasts at least 2000 m high, filling most of the water column of approximately 2500 m during the sea level low-stand preceding T2 (Lund et al. 2018). Our compositional analyses of glass shards in core OC170-26-159 and fractionation modeling reveal details of the magmatic conditions prior to eruption, consistent with the effects of sea-level change on mantle melting beneath the PAR.

4.3 ANALYTICAL METHODS

4.3.1 Major and trace element analyses

Major elements (Si, Ti, Al, Fe, Mn, Mg, Ca, Na, K, and Cl) of 67 glass shards were analyzed using Caltech's JEOL JXA-8200 electron microprobe, operating at a 15 kV voltage and 10 nA current with a 10 μm diffuse electron beam. Counting times were 30 s on-peak and 10 s at each background location for all elements, with Na, K, and Cl in the first pass. Standards were

synthetic forsterite, fayalite, Mn-olivine, anorthite, TiO_2, and Cr_2O_3 as well as natural Amelia albite, Asbestos microcline, and sodalite. All elements measured in VG-2 basalt glass were within <2% relative of accepted concentrations. Data were reduced using the CITZAF matrix correction program (Armstrong 1995) to obtain weight percent oxide values. Five or more spots were measured on each glass shard, and points contaminated by olivine or plagioclase microphenocrysts were discarded. Reported concentrations and uncertainties are averages and 1σ of remaining analyses on single shards.

Trace elements in the basaltic glasses were measured by laser-ablation inductively coupled plasma mass spectrometry (LA-ICPMS) in the Resnick Water and Environment Laboratory at Caltech. With a New Wave Research UP 193 Solid State Laser System (193 nm wavelength, 3 ms pulse width) attached to an Agilent 8800 ICP-MS, we analyzed, in spectrum mode, ^{29}Si, ^{43}Ca, ^{44}Ca, ^{47}Ti, ^{85}Rb, ^{88}Sr, ^{89}Y, ^{90}Zr, ^{93}Nb, ^{133}Cs, ^{137}Ba, ^{138}Ba, ^{139}La, ^{140}Ce, ^{141}Pr, ^{146}Nd, ^{147}Sm, ^{151}Eu, ^{157}Gd, ^{159}Tb, ^{163}Dy, ^{165}Ho, ^{166}Er, ^{169}Tm, ^{172}Yb, ^{175}Lu, ^{178}Hf, ^{181}Ta, ^{208}Pb, ^{232}Th, and ^{238}U. One replicate with 90 sweeps and 0.0501s integration time for all masses except ^{44}Ca (0.1000 s) gave total acquisition time of 11 s per spot. Washout delay (7 s) and gas blank (10 s) ensured return to background signals between analyses. 100 μm spots were pre-ablated (1 s, 45% laser power, 10 Hz repetition rate) before each analytical ablation (10 s, 35 μm spot, 80% laser power). ICPMS parameters were 1550 W RF power, 1 L/min Ar carrier gas flow and 8 mL/min He option gas flow. Before and after unknowns, six spots were ablated on primary reference standard NIST612 glass. ^{29}Si content by electron microprobe was used as an internal standard. Three to six spots were analyzed on each shard depending on size, and reported uncertainties for each shard are 1σ of the calculated concentrations.

4.3.2 Volatile content analyses

Concentrations of H_2O and CO_2 were determined by transmission Fourier Transform Infrared Spectroscopy (FTIR) on shards doubly-polished to less than 100 μm thick (measured using a digital micrometer). We used a Thermo-Nicolet iS50 FTIR Spectrometer (KBr beam splitter; InGaAs detector) and Nicolet Continuum Infrared Microscope for the analyses. Spectra (1300-6000 cm^{-1}) were averaged over 200 to 300 scans. Two to four 25 to 40 μm spots were measured on each shard. Absorption intensities were determined for OH and H_2O peaks centered at 3500 and 1630 cm^{-1}, and carbonate peaks at 1515 cm^{-1}. To remove background from the low intensity CO_2 peaks, we subtracted the spectrum of a quantitatively degassed basalt glass (S.Newman, unpublished spectra). Volatile species concentrations were obtained from peak heights and the modified Beer-Lambert law: $C = \frac{\mu A}{\rho d \varepsilon}$; where C is concentration, μ is molecular weight of the relevant volatile species, A is the absorbance (i.e., peak height), ρ is the glass density, d is the sample thickness, and ε is the molar absorptivity for each peak. Absorptivity values uses are as follows: 63 L/mol·cm for the 3500 cm^{-1} peak, 25 L/mol·cm for the 1630 cm^{-1} peak (Dixon et al. 1995), and 375 L/mol·cm 1515 cm^{-1} peak (Fine and Stolper 1986). Density was estimated as 2.89 g/cm^3 using Glass Density Calc v3.2 (http://www.kaylaiacovino.com/tools-for-petrologists). Concentrations and uncertainties are reported as averages and 1σ of the 2 to 4 analyses on each shard.

4.4 RESULTS

4.4.1 Glass shard geochemistry

Major oxide concentrations for all of the basaltic glass shards (Fig 4, Table CH4-S1) form a single population (MgO = 5.8-6.5 wt.%; average 6.2±0.3 wt.%, 2σ) and do not appear to

vary in composition with depth in the core. This compositional span is comparable to that of individually mapped lava flows from MOR axes (Rubin et al. 2001), however the glasses are significantly more evolved than average MORB. The shards have MgO contents lower than those of basalts collected from the nearest segment of the modern PAR axis (6.8-7.9 wt.% MgO) (Fine and Stolper 1986; Hekinian et al. 1999). Compositional variability within the shard population forms linear trends on MgO variation diagrams (Fig 4), contiguous with trends through the axial compositions. MgO contents in Foundation Seamount glasses span 5.8 to 8.4 wt.% and they differ from the shards and axial samples in means, slopes, and degrees of scatter in oxide concentrations.

Incompatible trace elements (Fig 5) are enriched in the glass shards relative to modern axial basalts. Moreover, as with the major elements, the shard population falls along common linear trends with the axial basalts and they are much more homogeneous than the few scattered samples from the Foundation Seamounts. Sr is only slightly enriched in the glass shards relative to axial basalts, consistent with plagioclase fractionation.

4.4.2 Glass shard volatile content

Dissolved H_2O concentrations in the glass shards range from 0.3% to 0.65 wt.% (Fig 6, Table CH4-S1). This range is slightly higher than modern axial PAR glasses (0.15-0.4 wt.% H_2O; http://earthchem.org/petdb). H_2O (rather than OH) contents were negligible and indicate minimal hydration from seawater during eruption or post-deposition. CO_2 contents (120-400 ppm) are elevated compared to average MORB, but there are no published CO_2 data for axial PAR samples for comparison. Both H_2O and CO_2 are incompatible species during vapor-undersaturated magmatic fractionation, and therefore expected to increase with decreasing MgO

content. H_2O is typically only slightly affected by syn-eruptive degassing of seafloor basalts, whereas CO_2 in effusively erupted glasses is significantly degassed and reveals more information on eruption pressures and dynamics than on volatile contents before or during fractionation (Soule et al. 2012). The volatile contents observed are consistent with the glass shards representing evolved samples of the axial magmatic system. The data do not require anomalous volatile enrichments in the parental magma or in the axial magma chamber at the time of eruption. For ridge axis depths > 2 km, the slight elevation in volatile content would not be the main driving force for large explosive eruptions, although higher initial CO_2 cannot be excluded using partially degassed glass shards.

Using the dissolved H_2O and CO_2 data in combination, vapor saturation pressure can be calculated for each shard (Fig 6; Dixon et al. 1995; Newman and Lowenstern 2002). Typically, submarine glasses are saturated or oversaturated in volatiles at their eruption depths, because rapid ascent and quenching inhibits full degassing. Thus, volatile undersaturated samples are quite rare. In this case, volatiles in the shards define a degassing path from maximum 860 bars (interpreted as a lower bound on axial magma chamber pressure) to minimum 260 bars (interpreted as a maximum eruption depth). Lithostatic pressure of 860 bars corresponds to a minimum storage depth 2.2 km below the seafloor. The maximum potential eruption depth estimate, 260 bars, is larger than seafloor pressure at the ridge axis (228 bars) but lower than seafloor pressure at the present-day core site (278 bars).

4.4.3 Differentiation Modeling

To test whether the glass shards are chemically related to the axial magmatic system, we used the MELTS thermodynamic model (Ghiorso and Sack 1995) to calculate a fractional

crystallization liquid line of descent from an axial-like composition through the PAR glass shards. The starting composition was varied within the range of primitive (MgO ~7.7-7.9 wt.%) axial basalts from ridge segment N6 of the PAR to generate the best fit, and the starting composition is given in Table 1. We used a constant pressure of 900 bars, consistent with the minimum storage pressure determined from our volatile content analyses. Oxygen fugacity is set to two log units below the QFM buffer. These conditions were selected as they create the best match to MORB fractionation in MELTS (Asimow et al. 2004), yielding a trend through both the axial basalts and glass shard compositions (Fig 4 and 5). The fit of the model suggests the glass shards are related to the axial magmatic system by fractional crystallization and represent more evolved members of the same sequence. The modeled fractionation results in 36% crystallization by mass and cooling of the system from 1190 to 1150°C. This corresponds to a temperature and composition-dependent increase in magma viscosity from 23 Pa·s to 759 Pa·s (Giordano et al. 2008).

4.5 DISCUSSION

4.5.1 An axial magmatic source

The volatile content, major element, and trace element analyses of the T2 glasses all support an axial source. Major element and trace element results fall in a single population with linear trends consistent with derivation from a single magmatic system. The shards have MgO contents lower than basalts from the modern PAR axis and their compositions are consistent with derivation from the axial magmatic system by fractional crystallization (Fig 4 and 5). Both major and trace element results fall along a modeled liquid line of descent connecting modern axial basalt compositions with the glass shards. The agreement between model results and

observations suggests that fractionated axial magmas were the source of the glasses in OC170-26-159. The Foundation Seamount compositions demonstrate the highly variable major and trace element concentrations and more scattered fractionation trends of off-axis eruptions compared to the glass shard analyses (Fig 4 and 5). Although the range of major element variation among seafloor basalts can be small, the variability in trace elements is orders of magnitude larger than the analytical uncertainty. The match between the glass shards and the fractionation trend through the axial glasses in all analyzed trace elements is unlikely to be coincidental.

While we cannot completely rule out the possibility that the glass shards erupted from off-axis vents but happen to resemble fractionated products of axial eruptions, this is extremely unlikely. Fast-spreading mid-ocean ridge axes are characterized by persistent axial magma chambers (Detrick et al. 1987; Macdonald and Fox 1988) that facilitate mixing and homogenization of melts (Batiza and Niu 1992; Sinton and Detrick 1992). Off-axis eruptions typically bypass this axial mixing system and produce a broader range of compositions related to the variability of mantle melting conditions (Hall and Sinton 1996; Niu and Batiza 1997; Niu et al. 2002). The diversity among the Foundation Seamount samples is typical of such unmixed products. Further, axial magmatic systems are relatively stable in composition over time because mixing and storage act to smooth out fluctuations in successive batches of magma (Goss et al. 2010; Reynolds et al. 1992). Off-axis systems typically lack such temporal stability, with successive eruptions poorly correlated in composition (Fornari et al. 1988). The glass shards show consistent compositions through multiple eruptions over a period of several thousand years, based on intercalation with the well-preserved oxygen isotope stratigraphy. Hence, the mean compositions, variability of compositions within each layer, and homogeneity between layers are consistent with derivation from the axial magma system.

Concentrations of dissolved H_2O in the glasses are elevated relative to axial basalts, but only to the degree expected for the enrichment of incompatible components due to fractional crystallization of an axial liquid. The maximum calculated saturation pressures are consistent with the depth of typical axial magma chambers at fast-spreading ridges, and with the fractionation model used to reproduce the axial and glass-shard populations. Off-axis eruptions typically do not stall or fractionate under perpetual magma storage conditions at these depths, and this would be a coincidence if the glass shards had not fractionated in the axial magmatic system. Furthermore, volatile saturation pressures range down to a minimum consistent with eruption at the relatively shallow axial summit depth and lower than that at the core site. Had these samples erupted on the ridge flanks or a deeper off-axis source, they would have been vapor undersaturated upon eruption, which is rare in submarine glasses. The most likely explanation is that the glass shards erupted from a vent at a shallower water depth than the core site, most likely the PAR axis.

The PAR glasses are evolved not only relative to the PAR axial samples but also compared to limu o Pele (i.e. bubble wall fragments) from other mid-ocean ridge locations. At similar K_2O concentrations (0.18-0.26 wt.%), the PAR glasses have distinct MgO values (5.8-6.6 wt.% MgO) compared to the compilation of Clague et al. (2009) from several locations in the Pacific, which group primarily from 6.5 to 8.5 wt.% MgO. A small batch of samples from the Juan de Fuca Ridge (n=11) has MgO concentrations overlapping with the PAR data, but these are unusual in the broader population (n=960). Thus, the PAR glasses represent unusually fractionated magmas compared to other settings, which may have contributed to elevated magmatic viscosity and enhanced explosivity during T2.

Had the glass shards erupted from an off-axis source and had compositions resembling

the axial lavas only coincidentally, their dispersal to the core location would be unlikely. During the eruptions, the shards were deposited 7 km from the ridge axis, which is the closest known source based on available bathymetry data and is still the farthest reported glass transport distance during a MOR eruption. As dispersal was likely accomplished by a buoyant water plume, transport distances are limited to 10 km by the water depth (Lund et al. 2018). The closest known seamounts, part of the Foundation Seamount chain, are at least 25 km from the core site, far beyond the range of potential sources.

4.5.2 Melting, differentiation, and eruption style influenced by sea level

We put forward a mechanism for the observed unusual glass compositions and eruption style based on eruption timing and the results of our fractionation model, as illustrated in Figure 7. The MELTS fractional crystallization model predicts cooling of the axial magma chamber by 40°C prior to eruption, which can be explained by a period of low magmatic flux, and thus low heat flux to the ridge axis. We propose that rising sea level followed by high, fairly stagnant sea level during MIS 7 (Fig 3, ~220-200 kyr BP) caused a temporary decrease in melt production (i.e. Lund and Asimow 2011). Subsequently, rapid sea level drop at the beginning of MIS 6 (Fig 3, ~195-185 kyr BP) stimulates a pulse of enhanced melting in the mantle (Fig 7c).

We speculate that these signals reach the ridge axis approximately 35 to 50 kyr after the sea level forcing events, consistent with estimates from abyssal hill bathymetry of the East Pacific Rise (Boulahanis et al. 2020). As such, low magmatic flux to the axial magma chamber likely occurred between roughly 190 and 160 kyr BP, when both glass and titanium concentrations in the core are low (Fig 3), indicating low ash content and a lack of large explosive eruptions. During this period, the axial magma chamber cools and fractionates (Fig

7b). When the melt pulse generated by the MIS 6 sea level drop arrives at the level of the axial magma chamber (~150-130 kyr BP), the fractionated melt is remobilized, triggering a series of anomalously energetic eruptions that distribute glass shards across the sea floor (Fig 7d). This coincides with an increase in hydrothermal metal output, reflecting increased temperatures below the ridge axis. Explosivity of these eruptions is enhanced by the elevated volatile contents and viscosity of the fractionated melt compared to typical MORB. However, hydrostatic pressure at the eruption depth (~250 bars) limits the volumetric expansion of exsolved, superheated H_2O, thus limiting its potential to drive explosivity. The heat input associated with high magma flux rates during this period likely plays a greater role in generating the buoyant plume that is key to glass dispersal.

The enhanced volcanism caused by sea level drop may function as a climate feedback loop, providing heat and CO_2 to the oceans at the start of glacial terminations to further drive glacial melting (Burley and Katz 2015). Though MORs contribute upwards of 70% of the global volcanic output, these melts contribute a low overall CO_2 flux (1.2-6.0 x 10^{13} g C yr^{-1}; Dasgupta and Hirschmann 2010) compared to continental volcanism. In addition, removal of ice sheets from high latitudes during glacial terminations may promote continental eruptions that produce large amounts of CO_2 (Huybers and Langmuir 2009). However, this release of CO_2 will be offset several ka after the onset of ice loss and thus does not contribute to the initiation of glacial terminations. MORs are more likely to have an effect on atmospheric CO_2 by warming of the deep oceans by enhanced hydrothermal flow and greater magnitude and frequency of eruptions, thus contributing to the release of stored marine carbon (Hofmann and Maqueda 2009).

4.6 CONCLUSIONS

The basaltic glass shards in core OC170-26-159 are evolved compared to effusively erupted lavas from the modern PAR axis, yet are consistent with derivation from the axial magmatic system. The shards fall into a tightly constrained population with MgO contents ranging from 5.8 to 6.5 wt.%, in contrast to lavas from nearby seamounts, which are scattered in both major and trace element abundances. Calculated volatile saturation pressures indicate that the glass shards erupted from no deeper than 260 bars, and thus support an axial source. Our MELTS differentiation modeling further confirms an axial affinity, as the glass shards lie on a liquid line of descent consistent with fractional crystallization of an axial basalt at MOR conditions. This fractionation is accompanied by 40°C of cooling and a 30-fold increase in viscosity.

The ejection of the glass shards 7 km from their axial source over a >15 kyr interval requires a series of highly energetic eruptions that produced buoyant water plumes reaching nearly to the sea surface. The period of fractionation necessary to develop the shard compositions indicates low magmatic flux to the axial magma chamber, an affect of sea level rise during MIS 7. Rapid sea level drop at the start of MIS 6 produced a pulse of melting at depth, which explosively remobilized the fractionated magma. Sea level changes are offset from by 35 to 50 kyr from signals recognized at the PAR, reflecting the time required for melt to migrate from the melting depth to the shallow axial chamber. Modulation of the melting regime and shallow crustal conditions beneath the PAR by glacial-intergralcial cycles is recorded by the compositions and timing of anomalous MOR volcanism.

4.7 Acknowledgements

We thank Chi Ma for assistance with the EPMA, Nathan Dalleska for help with LA-ICPMS analyses, and George Rossman for use of the FTIR lab. EPMA work was carried out in the Caltech GPS Division analytical facility, supported in part by NSF Grants EAR- 0318518 and DMR-0080065. MJL and PDA were supported by NSF awards OCE-1558372 and EAR-1551433.

4.8 References Cited

Armstrong JT (1995) Citzaf-a package of correction programs for the quantitative Electron Microbeam X-Ray-Analysis of thick polished materials, thin-films, and particles. Microbeam Analysis 4(3):177-200

Asimow PD, Dixon JE, Langmuir C (2004) A hydrous melting and fractionation model for mid-ocean ridge basalts: Application to the Mid-Atlantic Ridge near the Azores. Geochemistry, Geophysics, Geosystems 5(1)

Asimow PD, Ghiorso MS (1998) Algorithmic modifications extending MELTS to calculate subsolidus phase relations. American Mineralogist 83(9-10):1127-1132

Batiza R, Niu Y (1992) Petrology and magma chamber processes at the East Pacific Rise~ 9° 30′ N. Journal of geophysical research: solid earth 97(B5):6779-6797

Boulahanis B, Carbotte SM, Huybers PJ, Nedimović MR, Aghaei O, Canales JP, Langmuir CH (2020) Do sea level variations influence mid-ocean ridge magma supply? A test using crustal thickness and bathymetry data from the East Pacific Rise. Earth and Planetary Science Letters 535:116121

Briais A, Ondreas H, Klingelhoefer F, Dosso L, Hamelin C, Guillou H (2009) Origin of volcanism on the flanks of the Pacific-Antarctic ridge between 41 30′ S and 52 S. Geochemistry, Geophysics, Geosystems 10(9)

Burley JM, Katz RF (2015) Variations in mid-ocean ridge CO2 emissions driven by glacial cycles. Earth and Planetary Science Letters 426: 246-258

Carbotte SM, Detrick RS, Harding A, Canales JP, Babcock J, Kent G, Van Ark E, Nedimovic M, Diebold J (2006) Rift topography linked to magmatism at the intermediate spreading Juan de Fuca Ridge. Geology 34(3):209-212

Clague DA, Paduan JB, Davis AS (2009) Widespread strombolian eruptions of mid-ocean ridge basalt. Journal of Volcanology and Geothermal Research 180(2-4):171-188

Costa KM, McManus JF, Middleton JL, Langmuir CH, Huybers PJ, Winckler G, Mukhopadhyay S (2017) Hydrothermal deposition on the Juan de Fuca Ridge over multiple glacial–interglacial cycles. Earth and Planetary Science Letters 479:120-132

Crowley JW, Katz RF, Huybers P, Langmuir CH, Park S-H (2015) Glacial cycles drive variations in the production of oceanic crust. Science 347(6227):1237-1240

Dasgupta R, Hirschmann MM (2010) The deep carbon cycle and melting in Earth's interior. Earth and Planetary Science Letters 298(1-2):1-13

Detrick R, Buhl P, Vera E, Mutter J, Orcutt J, Madsen J, Brocher T (1987) Multi-channel seismic imaging of a crustal magma chamber along the East Pacific Rise. Nature 326(6108):35-41

Dixon JE, Stolper EM, Holloway JR (1995) An experimental study of water and carbon dioxide solubilities in mid-ocean ridge basaltic liquids. Part I: calibration and solubility models. Journal of Petrology 36(6):1607-1631

Fine G, Stolper E (1986) Dissolved carbon dioxide in basaltic glasses: concentrations and speciation. Earth and Planetary Science Letters 76(3-4):263-278

Fornari DJ, Perfit MR, Allan JF, Batiza R, Haymon R, Barone A, Ryan WB, Smith T, Simkin T, Luckman MA (1988) Geochemical and structural studies of the Lamont seamounts: seamounts as indicators of mantle processes. Earth and Planetary Science Letters 89(1):63-83

Forsyth DW, Webb SC, Blackman BK, Detrick RS, Toomey DR, Sheehan AF, Solomon SC, Wilcock WSD (1998) Imaging the deep seismic structure beneath a mid-ocean ridge: The MELT experiment. Science 280(5367):1215-1218

Freund S, Beier C, Krumm S, Haase KM (2013) Oxygen isotope evidence for the formation of andesitic–dacitic magmas from the fast-spreading Pacific–Antarctic Rise by assimilation–fractional crystallisation. Chemical Geology (347):271-283

Ghiorso MS, Sack RO (1995) Chemical mass transfer in magmatic processes IV. A revised and internally consistent thermodynamic model for the interpolation and extrapolation of liquid-solid equilibria in magmatic systems at elevated temperatures and pressures. Contributions to Mineralogy and Petrology 119(2-3):197-212

Giordano D, Russell JK, Dingwell DB (2008) Viscosity of magmatic liquids: a model. Earth and Planetary Science Letters 271(1-4):123-134

Goff JA (2015) Comment on “Glacial cycles drive variations in the production of oceanic crust”. Science 349(6252):1065-1065

Goss A, Perfit M, Ridley W, Rubin K, Kamenov G, Soule S, Fundis A, Fornari D (2010) Geochemistry of lavas from the 2005–2006 eruption at the East Pacific Rise, 9 46' N–9 56' N: Implications for ridge crest plumbing and decadal changes in magma chamber compositions. Geochemistry, Geophysics, Geosystems 11(5)

Hall LS, Sinton JM (1996) Geochemical diversity of the large lava field on the flank of the East Pacific Rise at 8 17′ S. Earth and planetary science letters 142(1-2):241-251

Hekinian R, Stoffers P, Ackermand D, Révillon S, Maia M, Bohn M (1999) Ridge–hotspot interaction: the Pacific–Antarctic Ridge and the foundation seamounts. Marine Geology 160(3-4):199-223

Hekinian R, Stoffers P, Devey C, Ackerman D, Hémond C, O'Connor J, Binard N, Maia M (1997) Intraplate versus ridge volcanism on the Pacific-Antarctic Ridge near 37° S–111° W. Journal of Geophysical Research: Solid Earth 102(B6):12265-12286

Hofmann M, Morales Maqueda MA (2009) Geothermal heat flux and its influence on the oceanic abyssal circulation and radiocarbon distribution. Geophysical Research Letters 36(3)

Huybers P, Langmuir C (2009) Feedback between deglaciation, volcanism, and atmospheric CO2. Earth and Planetary Science Letters 286(3-4):479-491

Kelemen PB, Hirth G, Shimizu N, Spiegelman M, Dick HJ (1997) A review of melt migration processes in the adiabatically upwelling mantle beneath oceanic spreading ridges. Philosophical Transactions of the Royal Society of London. Series A: Mathematical, Physical and Engineering Sciences 355(1723):283-318

Klingelhoefer F, Ondréas H, Briais A, Hamelin C, Dosso L (2006) New structural and geochemical observations from the Pacific-Antarctic Ridge between 52° 45′ S and 41° 15′ S. Geophysical research letters 33(21)

Langmuir CH, Klein EM, Plank T (1992). Petrological systematics of mid-ocean ridge basalts: Constraints on melt generation beneath ocean ridges. Mantle flow and melt generation at mid-ocean ridges 71:183-280

Lund D, Asimow P, Farley K, Rooney T, Seeley E, Jackson E, Durham Z (2016) Enhanced East Pacific Rise hydrothermal activity during the last two glacial terminations. Science 351(6272):478-482

Lund DC, Asimow PD (2011) Does sea level influence mid-ocean ridge magmatism on Milankovitch timescales? Geochemistry, Geophysics, Geosystems 12(12)

Lund DC, Seeley EI, Asimow PD, Lewis MJ, McCart SE, Mudahy AA (2018) Anomalous Pacific-Antarctic Ridge Volcanism Precedes Glacial Termination 2. Geochemistry, Geophysics, Geosystems 19(8):2478-2491

Macdonald KC, Fox PJ (1988) The axial summit graben and cross-sectional shape of the East Pacific Rise as indicators of axial magma chambers and recent volcanic eruptions. Earth and Planetary Science Letters 88(1-2):119-131

Maclennan J, Jull M, McKenzie D, Slater L, Grönvold K (2002) The link between volcanism and deglaciation in Iceland. Geochemistry, Geophysics, Geosystems 3(11):1-25

Middleton JL, Langmuir CH, Mukhopadhyay S, McManus JF, Mitrovica JX (2016) Hydrothermal iron flux variability following rapid sea level changes. Geophysical Research Letters 43(8):3848-3856

Newman S, Lowenstern JB (2002) VolatileCalc: a silicate melt–H2O–CO2 solution model written in Visual Basic for excel. Computers & Geosciences 28(5):597-604

Niu Y, Batiza R (1997) Trace element evidence from seamounts for recycled oceanic crust in the Eastern Pacific mantle. Earth and Planetary Science Letters 148(3-4):471-483

Niu Y, Regelous M, Wendt IJ, Batiza R, O'Hara MJ (2002) Geochemistry of near-EPR seamounts: importance of source vs. process and the origin of enriched mantle component. Earth and Planetary Science Letters 199(3-4):327-345

Olive J-A, Behn M, Ito G, Buck W, Escartín J, Howell S (2015) Sensitivity of seafloor bathymetry to climate-driven fluctuations in mid-ocean ridge magma supply. Science 350(6258):310-313

Portner RA, Clague DA, Helo C, Dreyer BM, Paduan JB (2015) Contrasting styles of deep-marine pyroclastic eruptions revealed from Axial Seamount push core records. Earth and Planetary Science Letters 423:219-231

Presnall DC, Dixon JR, O'donnell TH, Dixons SA (1979) Generation of mid-ocean ridge tholeiites. Journal of Petrology 20(1):3-35

Reynolds JR, Langmuir CH, Bender JF, Kastens KA, Ryan WB (1992) Spatial and temporal variability in the geochemistry of basalts from the East Pacific Rise. Nature 359(6395):493-499

Rubin K, Smith M, Bergmanis E, Perfit M, Sinton J, Batiza R (2001) Geochemical heterogeneity within mid-ocean ridge lava flows: Insights into eruption, emplacement and global variations in magma generation. Earth and Planetary Science Letters 188(3-4):349-367

Ryan WB, Carbotte SM, Coplan JO, O'Hara S, Melkonian A, Arko R, Weissel RA, Ferrini V, Goodwillie A, Nitsche F, Bonczkowski J, Zemsky R (2009) Global multi-resolution topography synthesis. Geochemistry, Geophysics, Geosystems 10(3)

Shen Y, Forsyth DW (1995) Geochemical constraints on initial and final depths of melting beneath mid-ocean ridges. Journal of Geophysical Research: Solid Earth 100(B2):2211-2237

Sinton JM, Detrick RS (1992) Mid-ocean ridge magma chambers. Journal of Geophysical Research: Solid Earth 97(B1):197-216

Sohn RA, Willis C, Humphris S, Shank TM, Singh H, Edmonds HN, Kunz C, Hedman U, Helmke E, Jakuba M (2008) Explosive volcanism on the ultraslow-spreading Gakkel ridge, Arctic Ocean. Nature 453(7199):1236-1238

Soule SA, Nakata DS, Fornari DJ, Fundis AT, Perfit MR, Kurz MD (2012) CO2 variability in mid-ocean ridge basalts from syn-emplacement degassing: Constraints on eruption dynamics. *Earth and Planetary Science Letters* (*327*):39-49

Tolstoy M (2015) Mid-ocean ridge eruptions as a climate valve. Geophysical Research Letters 42(5):1346-1351

4.9 Figures and captions

Figure 1

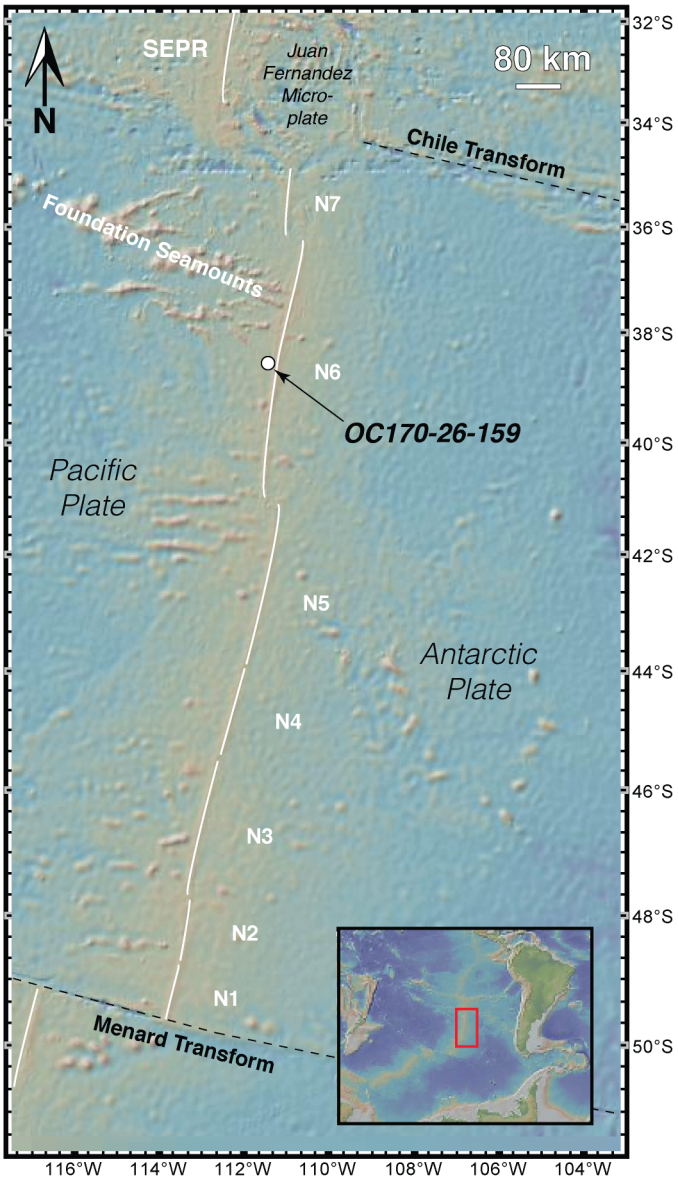

Figure 1 Map of the Pacific-Antarctic Ridge including the location of core OC170-26-159: 38.967°S, 111.350°W, 2754 m water depth. White lines indicate PAR axial segments N1 through N7 (Klingelhoefer et al. 2006; Briais et al. 2009), as well as the southern East Pacific Rise (SEPR). The core site is located 13.5±1.5 km west of the PAR axis. The available bathymetry data indicate the nearest seamount (part of the Foundation Seamounts) is located approximately 25 km west of the core site. Map generated using GeoMapApp (Ryan et al. 2009). Figure taken from Lund et al. (2018).

Figure 2

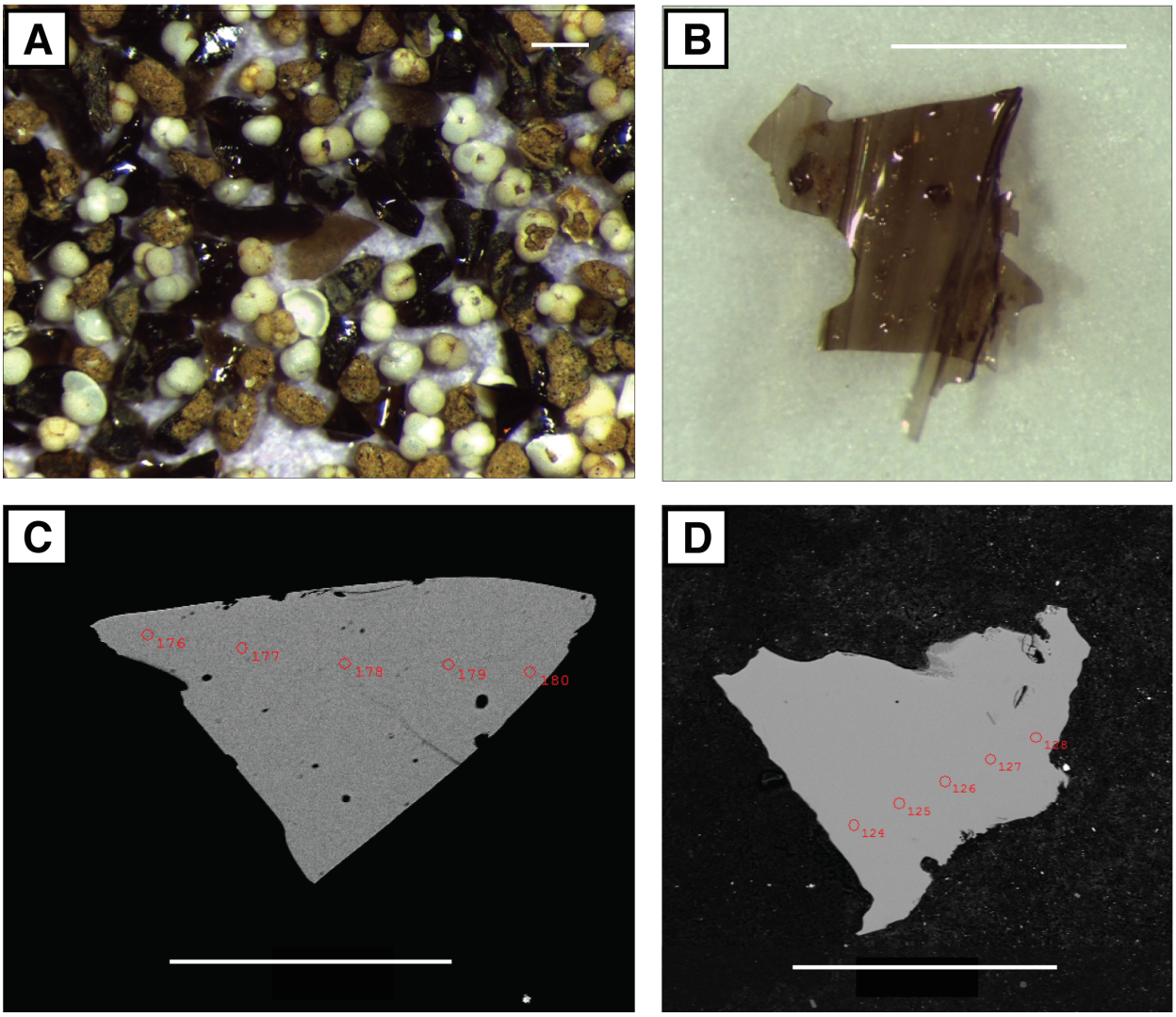

Figure 2 Images of the bulk sediment and individual glass shards from the T2 ash layer. **a** Bulk sediment, showing blocky glass shards (black), foraminifera (white), and pelagic muds (brown). **b** Single limu o Pele (bubble wall fragment) shard, containing small bubbles. **c** and **d** BSE images of representative shards, showing small vesicles in c, and a plagioclase microphenocryst in d, as well as the locations of EPMA spots (10 μm). Scale bars in all panels are 250 μm. Panels a and b from Lund et al. (2018).

Figure 3

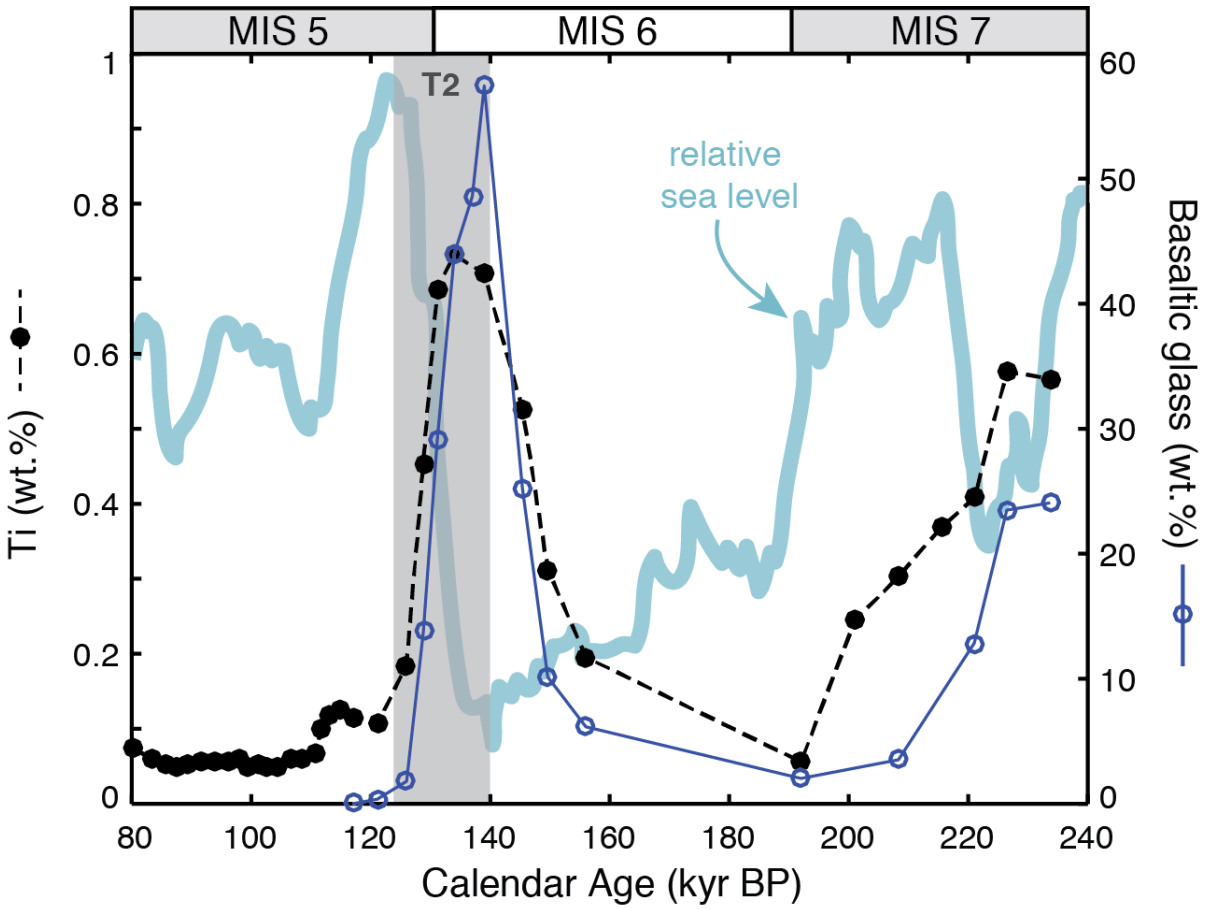

Figure 3 Basaltic glass (blue points) and titanium content (black points) in core OC170-26-159 through the 235 to 80 kyr time interval. The age model is based on oxygen isotope stratigraphy from benthic foraminifera in the core. Relative sea level is also shown (thick blue curve), but not quantified. Marine isotope stages (MIS) 5 (interglacial), 6 (glacial), and 7 (interglacial) are indicated. The vertical gray bar indicates the approximate timing of glacial Termination 2 (T2). At its peak (140 kya), basaltic glass composes nearly 60% of the bulk sediment weight. Ti and basalt levels increase concurrently and begin to rise prior to T2. Figure and data adapted from Lund et al. (2018).

Figure 4

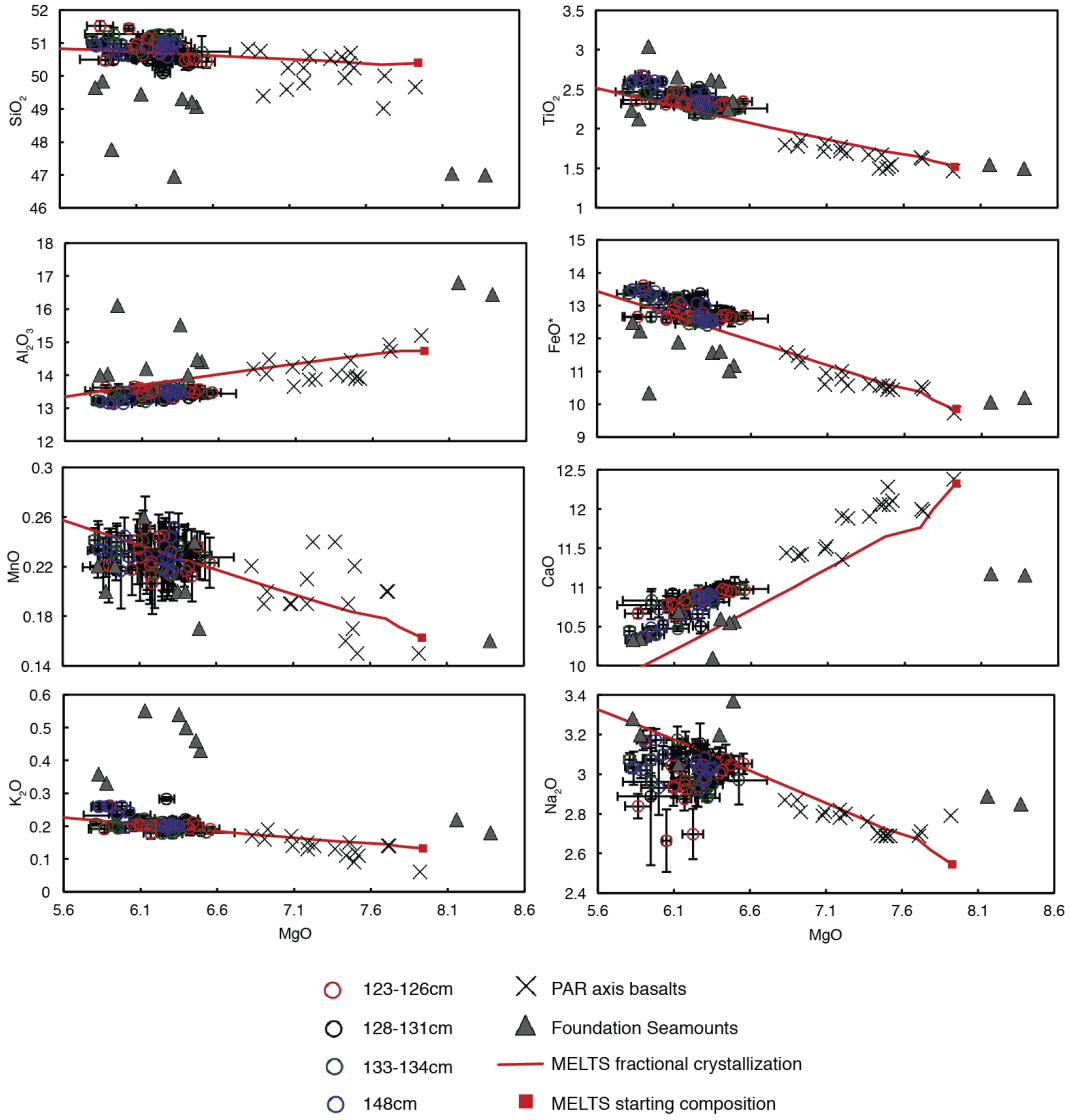

Figure 4 Major element oxide compositions for the basaltic glass shards in core OC170-26-159 at four different age intervals. The glass shards are consistently more evolved (lower MgO content) than basalts erupted from the current ridge axis (black X's)(compositions from Freund et al. 2013; Hekinian et al. 1999) and define a single population. The population lies along a liquid line of descent (red dashed line) determined using the MELTS thermodynamic model (Asimow and Ghiorso 1998; Ghiorso and Sack 1995) with a starting composition similar to basalts erupted from the ridge axis and pressure and fO_2 values consistent with mid-ocean ridge conditions. Compositions from the proximate Foundation Seamounts (gray triangles) (Hekinian et al. 1997) are included for comparison; the fractionation trend defined by the glass shards is not consistent with this neighboring magmatic system.

Figure 5

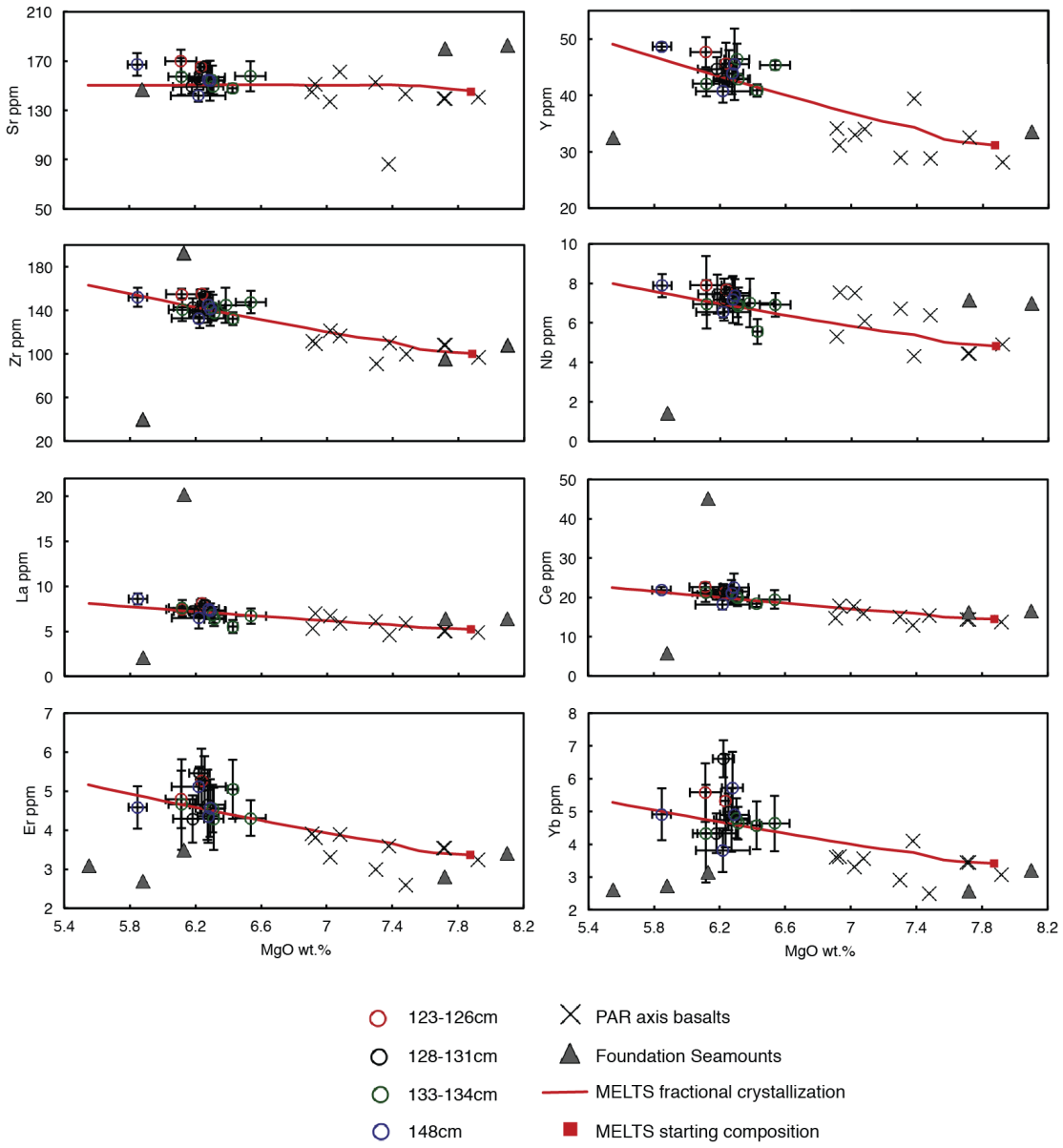

Figure 5 Selected trace element concentrations versus wt.% MgO for the basaltic glass shards in OC170-26-159 at four different depth intervals (open circles). Concentrations of incompatible elements are elevated relative to basalts erupted from the modern ridge axis (black X's) (axial compositions from Hekinian et al. 1997; Freund et al. 2013). The glass shard compositions fall along a liquid line of descent (red line) calculated using the same pressure, fO2, and major element composition input values for the MELTS model as in Figure 3. Consistent with the major element modeling, basalts from the Foundation Seamounts (Hekinian et al. 1997) do not fall on this fractionation trend.

Figure 6

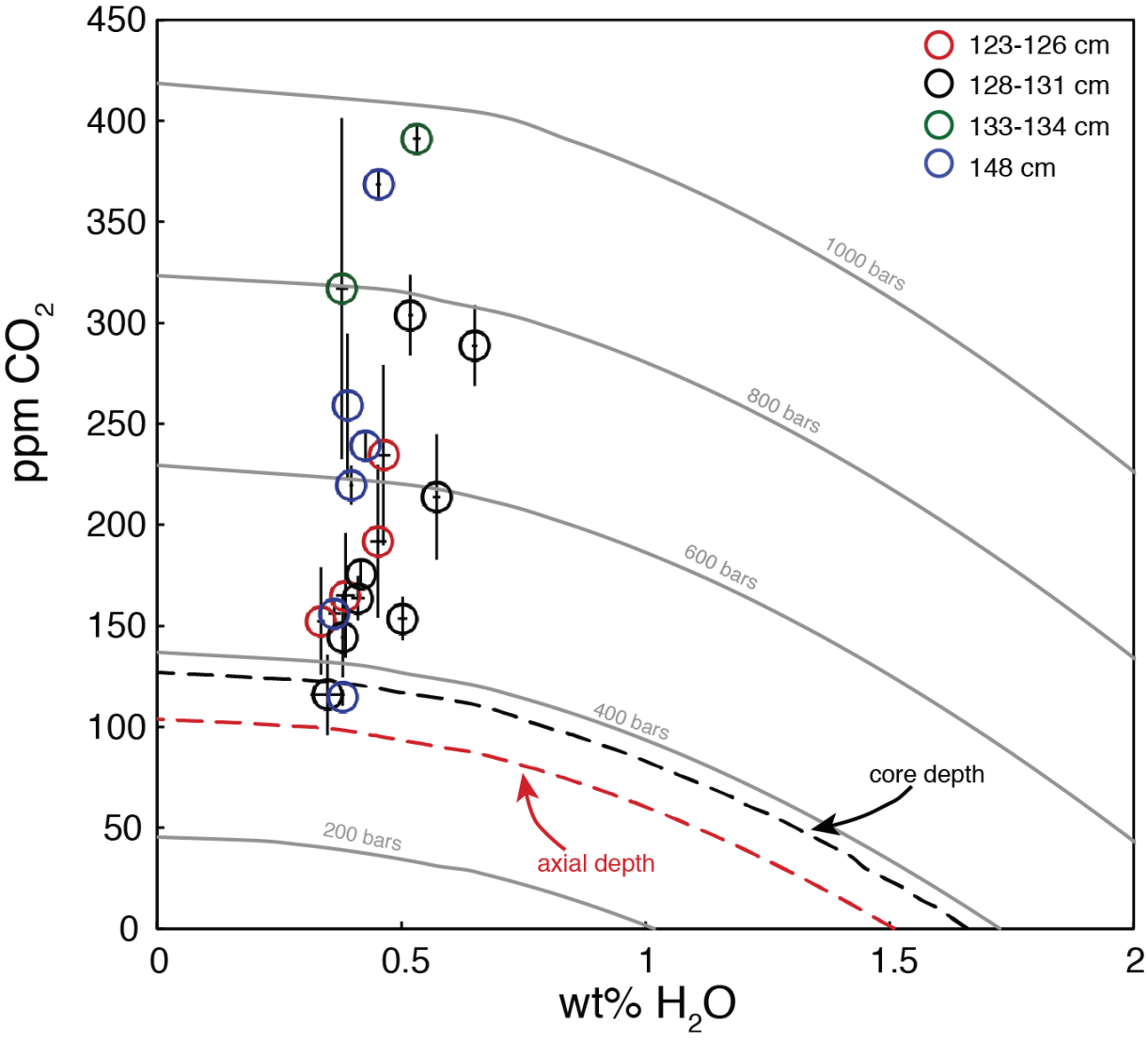

Figure 6 Volatile content for the basaltic glass shards measured using transmission FTIR spectroscopy. Saturation pressure contours were calculated using VolatileCalc 2.0 (Newman and Lowenstern 2002). Concentrations of both H2O and CO2 are slightly elevated from that of average MORB. Collectively the glasses record a degassing trend, in which the highest pressure sample records a saturation pressure of 860 bars, and the lowest pressure samples quenched at a maximum of 260 bars. Pressure at the ridge axis and core depth are represented by dashed contours in red and black, respectively. Samples that fall below the core depth contour equilibrated at a water depth shallower than where the core was retrieved at 2754 m.

Figure 7

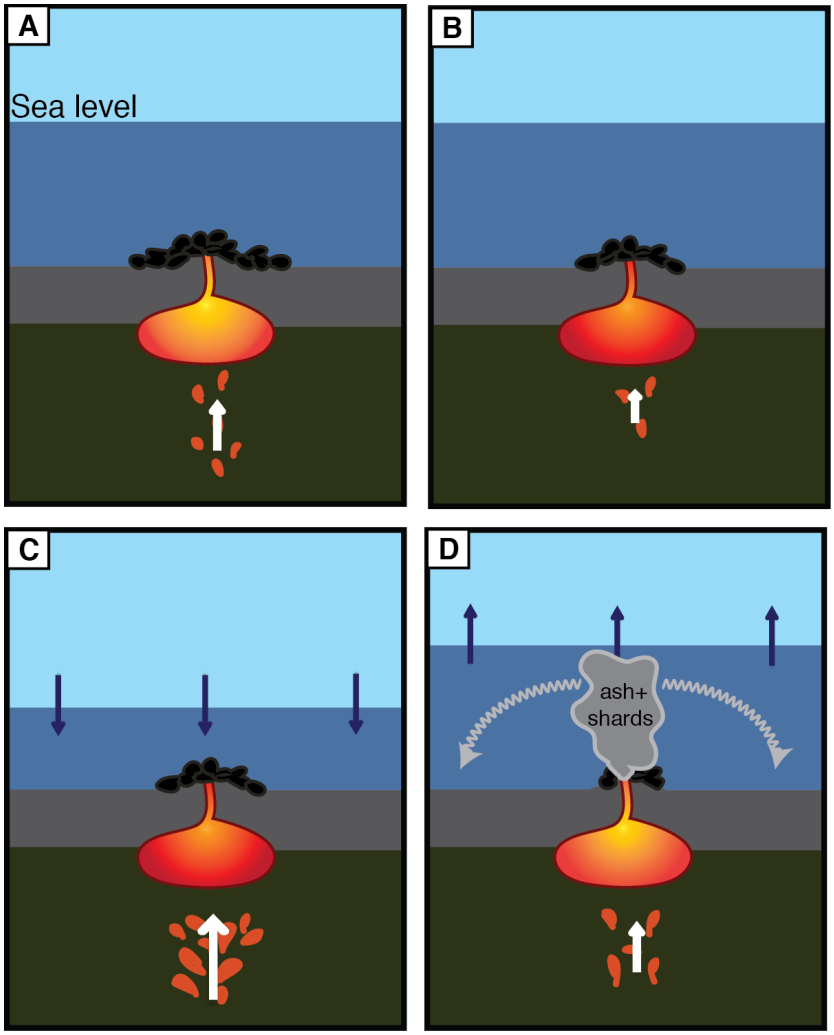

Figure 7 Schematic diagram showing the sequence of sea level changes and magmatic responses that lead to Strombolian eruptions at the PAR, in this case. **a** The PAR during a period of relatively stable sea level, with an un-modulated melt flux and magma chamber of normal MORB composition. **b** High, rising high sea level suppresses melting beneath the ridge axis, leading to a decreased melt flux into the axial magma chamber. With a less voluminous source of new melt, the axial chamber cools slightly and fractionates to create a more viscous, evolved melt. **c** Sea level decreases rapidly, stimulating a pulse of melting at depth. The melt must percolate upwards from the melting depth before it reaches the axial magma chamber, so it does not yet affect eruption style or composition. **d** The melt pulse reaches the axial magma chamber. Melt flux to the ridge axis is high, which remobilizes the viscous fractionated magma in a series of anomalously explosive eruptions that disperse evolved basaltic glass shards.

4.10 Tables

Table 1: Starting composition for MELTS modeling

Oxide	**wt.%**
SiO_2	50.2
TiO_2	1.5
Al_2O_3	14.7
FeO*	9.65
MgO	7.78
CaO	13.5
Na_2O	2.3
K_2O	0.13
Cr_2O_3	0.04
MnO	0.16
H_2O	0.3

Element	**ppm**
Rb	1.61
Sr	146
Y	31.3
Zr	101
Nb	4.83
Ba	22.1
La	5.23
Ce	14.5
Nd	10.9
Eu	1.51
Dy	4.92
Er	3.36
Yb	3.41
Th	0.35

CHAPTER 5

Multiple Sills Tapped by Explosive Eruptions from the East Pacific Rise: Ties to Sea Level Variation

5.1 ABSTRACT

Mid-ocean ridge magmatism is dominantly driven by lithospheric unloading due to plate spreading, which causes mantle melting at a relatively constant rate. However, hydrostatic pressure change is also capable of perturbing the melting regime, enhancing melting by up to 50% due to rapid sea level drops during the onset of glacial periods. Modulation of mantle melting by sea level change leads to variability in the melt flux to the ridge axis, which may in turn facilitate changes in eruption styles and erupted compositions. We investigate an ash layer in sediment core Y71-07-53, retrieved off axis from the southern East Pacific Rise, which contains basaltic glass shards deposited between 343 and 348 ka. The glass shards are interpreted as the products of submarine explosive eruptions and fall into three compositional groups based on major and trace element compositions. The shard compositions extend to the lowest MgO contents yet reported from submarine pyroclasts. We model crystallization of primitive axial basalts along two separate liquid lines of descent to produce the glass compositions, indicating physically isolated sills for storage of these melts beneath the ridge axis. This modeling, together with calculated vapor saturation pressures of the glasses, strongly support an axial source for the shard-producing eruptions. During this series of eruptions, the core site was 8 to 9 km from the ridge axis, indicating that these shards are the products of exceptionally energetic submarine eruptions. The timing of these large eruptions, slightly preceding glacial Termination 4 and lagging a rapid drop in sea level by approximately 50 kyr, supports a hypothesis of sea level-driven fluctuation in melt flux to the ridge axis.

5.2 INTRODUCTION

Mid-ocean ridge (MOR) magmatism is classically explained as a steady-state process of decompression melting in the mantle followed by relatively constant degrees of melt evolution leading to effusive eruptions restricted to a rather limited compositional range. Moreover, a long-lived shallow axial magma chamber is thought to exist beneath ridge axes, particularly at fast spreading ridges (Detrick et al. 1987; Hussenoeder et al. 1996; Sinton and Detrick 1992). This magma plumbing model facilities the homogenization of upwelling melts prior to eruption, thus dampening short-term signals of chemical variation associated with fractionation, assimilation, or variability in the melting regime. However, perturbations to the rate of melt generation, melt flux to the ridge axis, and differentiation processes may create uncommon compositions and result in atypically energetic eruption styles over thousands of years (Lund and Asimow 2011; Lund et al. 2018).

Melt supply to mid-ocean ridge systems is a function of mantle decompression due to plate spreading, and thus melting rates scale, to first order, in proportion to spreading rates. For example, unloading of ~200-500 Pa/yr occurs beneath the slow-spreading Mid-Atlantic ridge, compared to ~1500-2000 Pa/yr beneath the fast-spreading East Pacific Rise (Lund and Asimow 2011). More subtly, changes in hydrostatic pressure from the water column also affect the melting regime. A rate of sea level drop consistent with glacial terminations (~10 mm/yr) modifies the decompression rate by ~100 Pa/yr, equivalent to 5 to 50% of lithostatic unloading, expected to be a larger fractional perturbation at slower spreading ridges (Lund and Asimow 2011). These perturbations to the decompression rate occur with glacial-interglacial cycles on ~20 to 120 kyr timescales, with occasional rapid excursions lasting a few kyr, as water mass is transferred between the ocean and terrestrial ice sheets (Huybers and Wunsch 2005; Raymo

1997). This variation occurs on much shorter timescales than changes in plate spreading rate, which typically vary on tectonic timescales, > 1 to 10 Myr (Cogné and Humler 2004; Wilson 1996). Hence rapid sea level changes are likely a significant driver of variation in magma production from MORs over short periods. Once generated at depths of dominantly ~50 to 100 km (Gregg et al. 2012; Langmuir and Forsyth 2007; Langmuir et al. 1992; Presnall et al. 1979; Shen and Forsyth 1995), melts rise buoyantly towards the ridge axis at a finite rate, inducing a delay in the response of the axial system to a sea-level perturbation. Estimates of melt migration velocities range from 1 to 50 m/yr, but the rate for typical MORs is probably closer to 1 m/yr except in highly melt-rich regions such as Iceland (Boulahanis et al. 2020; Lund et al. 2018; Maclennan et al. 2002; Weatherley and Katz 2016). Thus, signals of changes to the melting regime are expected to arrive at the ridge axes tens of thousands of years after corresponding changes in the rate of sea level change (Boulahanis et al. 2020; Lund et al. 2018).

Multiple proxies support the prediction that MOR magmatism is coupled to Milankovitch cycles: hydrothermal metal fluxes, crustal thickness, and deposition of volcanic ash. The sub-ridge temperature at MORs is controlled by the magma flux to the ridge axis, and thus seawater circulating through fractured oceanic crust can be heated to greater extents when the magma flux to the ridge axis is high (Baker 2009; Baker and German 2004; Coumou, et al. 2008; Morton and Sleep 1985). Elevated hydrothermal temperatures lead to more efficient leaching of metals from the crust, particularly iron and manganese (Elderfield and Schultz 1996), which are then released into the deep ocean through hydrothermal vents. Metal-rich particles precipitate from hydrothermal fluids when they come in contact with cold deep ocean water, thereby depositing metals on the sea floor near ridge axes. Peaks in hydrothermal metal flux have been recognized coincident with glacial terminations at the East Pacific Rise (Lund et al. 2016; Lund et al. 2019),

Mid-Atlantic Ridge (Middleton et al. 2016), and Juan de Fuca Ridge (Costa et al. 2017), suggesting a link between sea level cyclicity and magma flux.

MORs are also expected to generate thicker crust during periods of enhanced magma flux and thinner crust during periods of relative quiescence. Crustal thickness has commonly been interrogated using the heights and wavelength of abyssal hills, which have been found to have periodicities consistent with glacial-interglacial timescales at the East Pacific Rise (Tolstoy 2015) and Australian-Antarctic Ridge (Crowley et al. 2015). However, the relationship between abyssal hill heights and crustal thickness is uncertain, as tectonic factors may also play a role in hill formation (Carbotte et al. 2006; Goff 2015; Olive et al. 2015). A recent study using multichannel seismic data to directly assess crustal thickness (as opposed to inferring it from bathymetry) along the East Pacific Rise finds variation in crustal thickness on 80 kyr timescales, consistent with sea level forcing (Boulahanis et al. 2020).

Studies of subaerial volcanism find a significant increase in volcanic output at high latitudes following ice sheet decay (Huybers and Langmuir 2009; Jellinek et al. 2004; Maclennan et al. 2002), however records of eruption ages in MOR settings of sufficient length and fidelity to test for a corresponding relationship are quite rare. While ash layers produced by Strombolian submarine eruptions have been recognized from the Juan de Fuca Ridge, Gorda Ridge, and East Pacific Rise (Clague et al. 2009; Ferguson et al. 2017), only a single previous study investigates whether Strombolian-like activity at mid-ocean ridges responds to glacial-interglacial forcing. Lund et al. (2018) find an ash layer off axis from the Pacific-Antarctic Ridge, deposited approximately 50 kyr after a rapid drop in sea level following Marine Isotope Stage (MIS) 7, consistent with predictions of signal lags from melting depths and melt migration rates. Here, we evaluate a second sediment core containing an off-axis ash deposit near the East Pacific Rise

(EPR). These cores are beneficial for studies of MOR volcanism as the ash layers are direct evidence of enhanced volcanism and can be dated by stratigraphic methods, allowing magmatic composition and eruption timing be tied to the sea level record.

5.3 BACKGROUND

5.3.1 Core Y71-03-53

In this study, we discuss the composition and deposition of basaltic glass shards from sediment core Y71-07-53, taken from 34 km west of the East Pacific Rise (EPR) at approximately 11°S and a water depth of 3180 m (Fig 1). This core records sedimentation from 20 to 360 ka, with a gap in the record from 186 to 228 ka, likely due to erosion by deep ocean currents. The age model, basalt abundance, and hydrothermal metal fluxes were constructed by McCart (2020) and are shown in Figure 2. This study focuses on basaltic glass shards from a 20 cm interval from 491 to 511 cm depth, corresponding to 343 to 348 ka. The ash-producing eruptions precede glacial Termination 4 (T4) by approximately 5 kyr. In addition, the fluxes of hydrothermal metals (Fe, Mn) sharply increase by a factor of five during T4.

The basaltic glass shards within the ash layer exhibit both blocky and sheet morphologies (Fig 3) (McCart 2020), consistent with quench shattering of basalt and with bubble wall fragments, respectively (Clague et al. 2009). Glasses are dispersed throughout the 20 cm ash interval and reach a maximum abundance of 8 wt.% basalt at the 503 cm depth (346 ka). Shard grain sizes vary from ~50 to 1000 μm, with most grains falling between 125 and 425 μm. The ash layer exhibits a coarsening upwards grain size distribution, with shards > 700 μm only found in layers 346 ka and younger (McCart 2020).

5.3.2 Glass shard distribution mechanism

Given the half spreading rate of 74 mm/yr on this segment of the EPR (www.ldeo.columbia.edu/~menke/plates.html), the core site has moved approximately 25 km west (relative to the ridge axis) from its location at 343 ka. Thus, the core site was located ~8 to 9 km from the ridge axis during the interval of ash and glass accumulation. The nearest mapped seamounts were located at least 50 km from the core site during the ash eruptions, suggesting that the glasses were sourced from the ridge axis or a more proximal unmapped seamount. Dispersal of shards by 8 km is beyond the maximum glass dispersal distance reported at Juan de Fuca and Gorda Ridges, or at other locations along the EPR (≤5 km) (Clague et al. 2009; Ferguson et al. 2017; Pegler and Ferguson 2020). On the other hand, it is comparable to the 7 km dispersal distance estimated for shards sourced from explosive eruptions of the Pacific-Antarctic Ridge during glacial Termination 2 (Lund et al. 2018). This dispersal distance suggests that the glass shards are the products of a series of unusually large or energetic eruptions from the EPR axis or a nearby unmapped vent. Models for distribution of submarine glasses to distances greater than 3 km invoke a buoyant, hot water-driven megaplume fed by heat from the combination of high lava effusion rate and elevated flux of high-temperature hydrothermal fluids (Lund et al. 2018; McCart 2020; Pegler and Ferguson 2020), in order to loft shards to sufficient height in the water column that spreading of the plume and ocean currents can carry them several km laterally before the shards settle from the plume. Such megaplumes can scatter glass shards nearly 10 km laterally from their source even without the aid of currents (Pegler and Ferguson 2020); their formation requires the anomalous heat input that would be associated with unusually energetic MOR eruptions.

5.4 ANALYTICAL METHODS

5.4.1 Major and trace element analyses

Glass shards were sampled from six depths in the core (491, 495, 499, 503, 507, and 511 cm), along with chips of the basaltic basement from the core cutter. Five to eleven shards in a representative range of sizes from each depth were mounted in epoxy and polished for analysis. Major element compositional analyses were collected for 12 major elements (Si, Ti, Al, Fe, Mn, Mg, Ca, Na, K, Cr, Cl, F) on the JEOL JXA-8200 electron probe microanalyzer (EPMA) at Caltech. Operating conditions were 15 kV and 10 nA, using a 10 μm diffuse beam. On-peak counting times were 30 s for each element. Na, K, Cl, and F were analyzed in the first pass to minimize diffusive loss from the glass. Standards were natural VG-2 basalt glass, Amelia albite, Asbestos microcline, and sodalite, as well as synthetic forsterite, fayalite, anorthite, Mn-olivine, TiO_2, Cr_2O_3, and fluorphlogopite. Data were reduced using the CITZAF matrix correction program (Armstrong 1995), and we use a mean atomic number (MAN) background correction that eliminates the need for background counting at each analytical spot with its associated additional beam damage. Nine to eighteen spots were analyzed on each shard, and reported compositions and errors are averages and 1σ of all analyses on a single shard. Where olivine and plagioclase phenocrysts were larger than the beam diameter (> 10 μm), their compositions were analyzed with the same procedure.

A suite of trace elements (^{29}Si, ^{43}Ca, ^{51}V, ^{52}Cr, ^{59}Co, ^{60}Ni, ^{63}Cu, ^{66}Zn, ^{85}Rb, ^{88}Sr, ^{89}Y, ^{90}Zr, ^{93}Nb, ^{137}Ba, ^{139}La, ^{140}Ce, ^{141}Pr, ^{146}Nd, ^{147}Sm, ^{151}Eu, ^{157}Gd, ^{159}Tb, ^{163}Dy, ^{165}Ho, ^{166}Er, ^{169}Tm, ^{172}Yb, ^{175}Lu, ^{206}Pb, ^{232}Th, ^{238}U) were measured in the glasses by laser ablation inductively coupled plasma mass spectrometry (LA-ICPMS) at Pomona College, using an Agilent 8900 triple quadrupole ICPMS and ESI NWR193 excimer laser. The laser was operated with a 4.7 J/cm^3

fluence and He carrier gas. Two pre-ablation laser shots (100 μm diameter) precede the analytical period of 30 s at 8 Hz laser pulse repeat frequency (80 μm diameter). 45 sweeps through all measured masses were performed, and a 15 s washout delay was included between each analysis. Monitoring of the background counts during the washout delay ensured a return to baseline prior to subsequent analyses. Data were reduced using the Iolite software (Paton, et al. 2011), with NIST612 as the primary reference standard and ^{29}Si (measured by EPMA) as the internal standard. MPI-DING glass references KL2-G (basalt) and GOR128-G (komatiite) were analyzed as unknowns, and results are within 5% of the accepted values (Jochum et al. 2006). At least 3 spots were analyzed on each shard, with up to 6 spots on larger shards. Microphenocrysts were avoided where possible, however given the large spot size, plagioclase was included in the analytical volume of some spots. As these crystals are very small (typically < 10 μm), they do not contribute significantly to the overall composition. Concentrations are reported as the average of all analyses on a single shard, and errors are 1σ of these analyses.

5.4.2 Volatile content

The concentrations of volatile species (H_2O and CO_2) in the EPR glasses were measured via transmission Fourier-transform infrared spectroscopy (FTIR) at Caltech. Shards were doubly polished to between 60 and 180 μm thickness (measured using a digital micrometer) and placed over a 50 μm aperture in a Nicolet Continuum Infrared Microscope. Using a Thermo Scientific Nicolet iS50 FT-IR spectrometer with KBr beam splitter, IR source, and InGaAs detector, we collected absorption spectra between 4000 and 650 cm^{-1}. Background spectra were collected between every 10 unknown analyses and subtracted from the subsequent spectra. Peak heights above baseline were measured at 3500 cm^{-1} to assess OH concentration (reported as wt.% H_2O).

As the carbonate peaks (1515 cm^{-1}) have very low intensities (absorbance 0.01-0.1), we subtracted the spectrum of an experimentally degassed basalt to remove the background intensity. Volatile concentrations were calculated using molar absorptivities of 63 L/mol·cm for H_2O at 3500 cm^{-1} (Dixon et al. 1995) and 375 L/mol·cm for CO_2 at 1515 cm^{-1} (Fine and Stolper 1986). Each shard was analyzed at 3 to 4 spots containing minimal microphenocrysts, with concentrations reported as the average of all spots on an individual shard.

5.5 RESULTS

Results of major element, trace element, and volatile content analyses are included in Table CH4-S1 of the Supplementary Data file.

5.5.1 Major Element Chemistry

To determine if the glasses are similar in composition to lavas from the ridge axis, we conducted major element composition analyses of glass shards from each sampled depth in the core (Fig 4). The shards cluster into two populations based solely on MgO content, with high-MgO (6.5-7 wt.% MgO) and low-MgO (5-5.7 wt.% MgO) populations. The higher MgO population is further divided into two groups based on Al_2O_3 content, which we refer to as the low-Al_2O_3 group (13.2-13.7 wt.% Al_2O_3; 6.5-6.8 wt.% MgO) and the high-MgO group (14.3-15 wt.% Al_2O_3; 6.6-6.9 wt.% MgO). These two higher MgO populations are also distinguishable by K_2O content, with lower K_2O in the low-Al_2O_3 group (0.14-0.16 wt.% K_2O) than in the high-MgO group (0.22-0.27 wt.% K_2O). The low-MgO group has higher concentrations of elements that are incompatible during gabbro fractionation (TiO_2, FeO, MnO, Cl, F) than the high-MgO and low-Al_2O_3 groups, and lower concentrations of CaO, Cr_2O_5, and Al_2O_3. K_2O contents of the

low-MgO shards (0.16-0.21 wt.% K_2O) are higher than in the low-Al_2O_3 shards, but lower than in the high-MgO shards. We also analyzed chips of basalt from the base of the core, which have the lowest MgO content of the analyzed glasses (4.9 wt.% MgO) and are most similar in composition to the low-MgO shards. Cl and F contents (0.03-0.1 wt.% Cl, 0.12-0.18 wt.% F) do not exceed typical fresh MORB contents, indicating that alteration by seawater has been minimal.

Out of a total of 52 shards selected for analysis, the high-MgO shards are the most common (n=35), followed by the low-MgO shards (n=12) and the low-Al_2O_3 shards (n=5). The glasses are not stratified by composition, as shards from both the low-MgO and high-MgO groups are found at nearly all sampled depths (Fig 5). Though the low-Al_2O_3 shards are found only at depths 499 and 507 cm, this may a coincidental result of sampling a small number of shards. Similarly, the lack of low-MgO shards at depth 499 cm does not preclude the presence of low-MgO shards at this depth within the core or in the broader lateral extent of the ash layer.

The glass shards fall along linear trends contiguous with samples from the modern EPR axis (Fig 4) (Bach,et al. 1994; Eissen 1982; Engel and Engel 1964; Funkhouser et al. 1968; Laschek 1985; Puchelt and Emmermann 1983; Scheidegger and Corliss 1981), except for a group of high-K_2O axial lavas (Fig 4g) (Batiza et al. 1982; Nielsen et al. 2014; Scheidegger and Corliss 1981) classified as E-MORB by Waters et al. (2011). Hereafter, our discussions of axial lavas refer only to the lower-K_2O, N-MORB group unless otherwise stated. The high-MgO and low-Al_2O_3 shards overlap in composition with the range of axial compositions (axial samples 6-8.3 wt.% MgO), but generally fall on the lower MgO end of this range. The low-MgO shards and core base chips have lower MgO contents than any samples from the closest segment of the EPR. Analyses from a chain of unnamed seamounts located 80 km northwest of the core site (Fig 1)

have greater MgO contents than any of the shards (7.4-8.6 wt.% MgO), but do overlap in compositions with the range of axial compositions (Eissen 1982; Puchelt and Emmermann 1983).

5.5.2 Trace Element Chemistry

Trace element concentrations corroborate the distinctions between the three compositional groups of glass shards. The low-Al_2O_3 and low-MgO shards have roughly parallel N-MORB-normalized incompatible element patterns (Fig 6), wherein the average trace element concentration of the low-MgO shards is approximately 1.5 times that of the low-Al_2O_3 shards. These patterns are relatively flat, except for a large negative Sr anomaly that is likely due to fractionation of plagioclase. The high-MgO shards have steeper negative slopes through the highly incompatible elements (Rb to Nb in Fig 6), as well as a positive K_2O anomaly and smaller negative Sr anomaly than the other two groups. The incompatible element pattern of the average core base chip is most similar to the low-MgO shards, though on the higher end of this range and extending above the range of low-MgO shards in the most incompatible elements.

When trace elements are plotted against MgO content (Fig 7), the three populations form distinct groups consistent with the clustering observed in major element compositions. In fact, the low-Al_2O_3 and high-MgO groups are more readily separated using trace elements and the low-Al_2O_3 shards have consistently lower concentrations of incompatible elements. Linear trends with MgO content are evident within the low-MgO group, particularly in moderately to strongly incompatible elements (Fig 7e-h). The core base chips tend to fall off of this trend, having slightly lower incompatible element concentrations for their MgO content than predicted by a linear trend through the low-MgO shards. Minimal axial data are available for comparison and

the scatter in the data make linear trends unclear, possibly due to method-limited accuracy in previous studies (instrumental neutron activation, atomic absorption spectroscopy) (Laschek 1985; Puchelt and Emmermann 1983; Scheidegger and Corliss 1981). Despite this, some axial samples tend to overlap in composition with the glass shards at similar MgO contents, and generally extend to lower incompatible element concentrations with increasing MgO contents.

5.5.3 Volatile Content

Measured concentrations of dissolved H_2O and CO_2 in the shards represent the post-degassing volatile content of the rapidly quenched glasses, and concentrations for each analyzed shard are shown in Figure 8. H_2O contents are the lowest in the low-Al_2O_3 group, ranging from 0.12 to 0.18 wt.%, and modestly but distinctly higher in the low-MgO group (0.23-0.33 wt.% H_2O) and high-MgO group (0.34-0.57 wt.% H_2O). This is generally within the range of axial samples for this segment of the EPR (0.17-0.98 wt.% H_2O) (Bach et al. 1994; Eissen 1982; Funkhouser et al. 1968; Laschek 1985; Puchelt and Emmermann 1983), though data from axial samples are limited. The range of CO_2 contents in each compositional group essentially overlap, with 125 to 400 μg/g in the low-Al_2O_3 group, 120 to 400 μg/g in the low-MgO group, and 120 to 350 μg/g in the high MgO group. The core base chips have the lowest CO_2 contents of the sample suite (~100 μg/g) and some of the highest H_2O contents (0.45 wt.%). CO_2 content does not vary systematically with MgO, indicating that the variation in CO_2 is dominantly controlled by degassing processes and that most shards were not fully degassed prior to quenching. While degassing likely plays a role in modifying the H_2O contents of the glasses, the distinction in H_2O content between the three groups appears to be controlled by the pre-eruptive melt hydration.

Volatile Saturation Pressures

The combination of H_2O and CO_2 measurements can be used to calculate the vapor saturation pressures for individual glass shards using the VolatileCalc 2.0 model (Fig 8; Newman and Lowenstern 2002). At low H_2O contents (< ~1 wt.% H_2O), calculated equilibrium pressures are dominantly controlled by CO_2 content. Saturation pressures are calculated assuming a melt temperature of 1150°C, consistent with the average liquidus temperature of the shard compositions at ~1.8 km depth. We act under the assumption that all shards are saturated or oversaturated in volatiles at the time of eruption, as eruption of undersaturated basalts requires rare melts with exceptionally depleted primary volatile contents (Michael and Graham 2015; Saal et al. 2002). Thus, the minimum calculated pressure for the shards of 280 bars, or 2800 m water depth, is taken as the eruption pressure. Greater calculated pressures represent incompletely degassed glasses, which are common due to rapid ascent from magma storage depths (Sarda and Graham 1990; Soule et al. 2012). The maximum vapor pressure of 850 bars, which is nearly identical for the low-MgO and low-Al_2O_3 shards, indicates a minimum magma storage depth of 1.9 km below the seafloor. The high-MgO shards have a slightly lower maximum pressure of 760 bar, or minimum storage depth of 1.6 km.

Minimum saturation pressures from several shards representing all three compositional groups are within error of the hydrostatic pressure at the ridge axis (280 bars), and several would be undersaturated in volatiles at the core retrieval depth (320 bars). Therefore, the shards must have erupted from a vent shallower than the depth of the core, indicating an axial vent based on available bathymetry. The core base chips record an exceptionally low eruption pressure (220±50 bars) that suggests quenching between 1970 and 2700 m depth.

5.5.4 Mineral Chemistry

Out of 52 analyzed shards, 22 contain olivine or plagioclase phenocrysts large enough to analyze (> 10 μm). Plagioclase is more common, constituting 47 of the 65 analyzed crystals, while 18 olivine grains make up the remaining analyses. The high-MgO shards are the most likely to have suitable phenocrysts, as 20 of the 22 shards with mineral analyses are from this group. The remaining two shards are from the low-MgO population, whereas the low-Al_2O_3 shards are completely aphyric. Forsterite content (Fo=100*Mg/[Mg+Fe]) in olivine ranges from 79.5 to 82 in the high-MgO shards, and a single olivine grain in the low-MgO shards has a forsterite content of 68. Anorthite content (An=100*Ca/[Ca+Na+K]) in plagioclase ranges from 77 to 84 in the high-MgO shards and is ~77 in the low-MgO shards. Plagioclase phenocrysts are common in the core base chips with an average anorthite content of 72.5, and rare olivine grains have forsterite contents of approximately 69.

5.6 DISCUSSION

5.6.1 Crystallization from an Axial Source

Compositions and calculated volatile saturation pressures suggest that the all three populations of glass shards are evolved products of the axial magmatic system. Both the high-MgO and low-Al_2O_3 shards overlap in composition with the N-MORB axial lavas in all major element contents. Though the trace element data for the axial samples is sparse, the two higher-MgO shard populations also tend to fall within the range of axial compositions. The major element compositions of the low-MgO shards fall on roughly linear trends through the axial compositions, suggesting that these shards are related to the axial compositions by a liquid line of descent. Though the major element compositions of samples from the nearest mapped

seamounts are similar to the axial lavas and thus could appear to be related to the glass shards, the seamounts were located at least 50 km from the core site at the time of the glass shard deposition, making it extremely unlikely that the shards could have been sourced from these seamounts.

The glass shards record a degassing path from 1.6 to 1.9 km below the ridge axis to their approximate eruption pressure. The most degassed shards record an eruption pressure of 280 bars, consistent with eruption from the EPR axis (2800 m) but requiring the rare condition of volatile undersaturation if erupted from the seafloor near the core site (3180 m). This strongly points to an axial source, but we note that available bathymetry data are incomplete and we cannot rule out that the shards may have been sourced from an unmapped off-axis vent on an edifice that stands as much as 300 m above the core depth. Given typical axial magma chamber depths at the EPR of 1.5 to 3 km (Sinton and Detrick 1992), off-axis vents located greater than 3 km from the ridge axis yet still sourcing melts from the axial magmatic system would require significant horizontal transport of these melts within the crust through channels oblique to previously emplaced sheeted dikes. Eruption of the shards from an off-axis vent located several km from the ridge axis would still require transport of the shards a minimum of 5 km from their eruption site to the core site, with decreased local hydrothermal fluid output to drive shard dispersal, therefore still representing uncommonly large eruptions.

5.6.2 Crystallization Model

Based on linear trends in major element compositions between the glass shards and axial lavas, as well as volatile saturation pressures that indicate eruption from a source shallower than the off-axis sea floor, we posit that the glass shards are related to the axial magmatic system by

crystallization of a melt with an axial composition. To test this hypothesis, we construct crystallization models using MELTS (Asimow and Ghiorso 1998; Ghiorso and Sack 1995) to describe liquid lines of descent from primitive axial melt compositions through the glass shard compositions.

Evidence for multiple LLDs

Major and trace element contents of the three compositional groups indicate that multiple LLDs are required to describe the shard compositions; no single function of MgO can fit all the data within the stated measurement errors. Because the low-Al_2O_3 and high-MgO groups have nearly identical MgO contents but distinct Al_2O_3, K_2O, and strongly incompatible element contents, it is impossible to generate both groups using identical starting compositions and crystallization conditions. Reproducing the shard compositions therefore requires at least two LLDs. This compositional contrast in some elements, particularly Al_2O_3, Sr, and Ba, is consistent with enhanced plagioclase crystallization to generate the low-Al_2O_3 shards in comparison to the high-MgO shards, however differing starting compositions are required to explain the elevated nature of some elements (e.g. K_2O, Nb, Th) in the high-MgO shards. The nearly parallel incompatible element patterns between the low-Al_2O_3 and low-MgO shards are consistent with derivation by various degrees of differentiation from a common parental melt (Fig 6). Trace element vs. MgO trends through the low-MgO group intersect the low-Al_2O_3 group and corroborate this inference (Fig 7). Furthermore, the relation between these groups is supported by vapor saturation pressures, as the low-MgO and low-Al_2O_3 groups have indistinguishable maximum saturation pressures (~850 bars), while the high-MgO group is offset to a lower pressure (~760 bars). Though these maximum pressures represent only the minimum storage

depth for the melts and thus could be in agreement for all three groups, the consistency with our assertion of two LLDs is striking.

The necessity of at least two LLDs implies the existence of at least two physically separated magma bodies, as the similar viscosities and high temperatures of MORB melts promote rapid homogenization when introduced into the same magma chamber (Batiza and Niu 1992; Sinton and Detrick 1992). Crystallization within these magma bodies can then generate separate LLDs and compositionally stratified sills, allowing for the eruption of lavas from different degrees along the LLDs. These magma bodies likely have either different parental melt compositions or significantly different crystallization conditions. Because the range of crystallization conditions (e.g. pressure, temperature, fO_2) are relatively narrow within the MOR environment, much of the compositional difference between the two LLDs likely stems from different starting compositions, which can be generated in either the melting regime (e.g. percent melting and composition of the mantle source) or in the crust by differential assimilation or partial melting of altered wall rocks.

Model input parameters

Two isobaric LLDs were constructed to replicate both the glass shards and axial lavas by crystallization of a primitive axial-like composition: LLD1 fits the low-MgO and low-Al_2O_3 groups, and LLD2 fits the high-MgO group. The calculations are performed using MELTS at pressures of 850 bars for LLD1 and 800 bars for LLD2, consistent with the maximum vapor saturation pressures recorded by the glasses in the respective groups. Assuming that crystallization occurs during magma storage rather than ascent, these pressures equate to storage depths of 1.6 to 1.9 km below the sea floor, which is consistent with estimations of shallow axial

magma chamber depths at fast-spreading ridges based on observation of seismic low-velocity zones (Detrick et al. 1987; Sinton and Detrick 1992). Oxygen fugacity (fO_2) was estimated using Fe/Mg ratios of coexisting glass and olivine. This calculation relies on two assumptions: 1) all Fe in olivine is FeO, and 2) the olivine grains are in chemical equilibrium with surrounding glass. Using an Fe/Mg olivine-melt partition coefficient of 0.303 (Beattie 1993), we calculate the presumed FeO and Fe_2O_3 contents of the glass to determine an approximate magmatic fO_2. At an approximate liquidus temperature of 1150°C, eight shards from the high-MgO group return fO_2 values between 0.4 log units below and 0.7 log units above the fayalite-magnetite-quartz buffer, disregarding two additional outliers that returned values of approximately FMQ–3, for an average of 0.05±0.3 (1σ) log units away from the FMQ buffer. Only one olivine grain was large enough for analysis in the low-MgO shards and returns fO_2 value of FMQ–1.4. Because this is an approximation of fO_2 that relies on our unproven assumptions, the fO_2 values used in the LLD calculations were varied within the estimated range for LLD2 (FMQ -0.4 to +0.7), and ±0.5 log units of the LLD1 estimate. The best-fit conditions were FMQ–1.7 for LLD1 and FMQ for LLD2.

Starting compositions were varied such that the crystallization models reproduce both the glass shards and the axial compositions from a melt representative of a primitive MORB (~8.5 wt.% MgO); starting compositions that produced the best fits are included in Table 1. We ran MELTS in equilibrium crystallization mode, as this most accurately reproduces the glass shard compositions. In particular, the rate of enrichment of incompatible elements in the melt is beyond what can be achieved by fractional crystallization. Because the compositional differences between the high-MgO and low-Al_2O_3 groups are consistent with elevated plagioclase crystallization in the low-Al_2O_3 group, LLD1 is given a lower starting H_2O content of 0.06 wt.%,

whereas LLD2 begins with a H_2O content of 0.33 wt.%. These values lie near the lower and upper bounds, respectively, of the range of measured H_2O contents in primitive MORB glasses from the EPR (Fig 9) (PetDB, https://www.earthchem.org/petdb).

Model results

The best-fit LLDs resulting from our modeling are shown in Figures 4, 7 and 9. The starting compositions for both LLDs are given in Table 1. The success of this modeling in reproducing the glass shard compositions is compelling evidence for an axial source of the glass shard eruptions.

During crystallization of LLD1, 40°C of cooling occurs between the liquidus of the starting composition at 1210°C and eruption of the low-Al_2O_3 shards at 1170°C. An additional 40°C of cooling is required to produce the low-MgO shards, resulting in 78% crystallization by mass of the starting composition to produce the most evolved shards. LLD2 results in 35% crystallization with 35°C of cooling from 1190 to 1155°C to produce the high-MgO shards. This cooling and compositional evolution in both LLDs causes an increase in viscosity from 1.5 to 2.3 log Pa·s in LLD1 to generate low-MgO shard compositions, and 1.3 to 1.7 log Pa·s through LLD2 to produce the high-MgO shards (Fig 10, Giordano, et al. 2008). Volatile measurements from the axial samples on this section of the EPR are minimal, preventing accurate calculation of axial lava viscosities. Regardless, axial lava viscosities likely fall between the two LLDs for the MgO contents observed in axial lavas, as the H_2O content of the majority of samples from the full length of the EPR fall between LLD1 and LLD2 (Fig 9, 10). These modest increases in viscosity are unlikely to have been the main driver of the explosive eruption style needed to

disperse the shards to > 8 km from their source, in particular because magma viscosities of the high-MgO and low-Al_2O_3 groups overlap with the effusively erupted axial lavas.

Origin of compositional differences

The starting compositions for LLD1 and LLD2 differ most significantly in their H_2O contents (0.06 wt.% in LLD1; 0.33 wt.% in LLD2), resulting in the suppression of plagioclase crystallization to lower temperatures in LLD2. Comparatively elevated plagioclase crystallization in LLD1 produces melts with lower Al_2O_3 content at the same MgO content. In fact, LLD2 has a lower starting Al_2O_3 content than LLD1, which increases rapidly with olivine and clinopyroxene crystallization to generate the slightly elevated Al_2O_3 contents in the high-MgO shards. The starting composition for LLD2 has elevated K_2O and highly incompatible element contents (Rb, Ba, Th, U, Nb) compared to LLD1. In addition, LLD1 requires more reducing conditions (fO_2= FMQ–1.7), while LLD2 is comparatively oxidized (FMQ). The elements with elevated concentrations are typically enriched in E-MORB, but true E-MORB is much more enriched, with incompatible element concentrations over an order of magnitude greater than N-MORB (i.e. Fig 4g, Waters et al. 2011). As the shard compositions are most similar to N-MORB, yet E-MORB lavas are present on this section of the EPR (Batiza et al. 2014; Scheidegger and Corliss 1981; Waters et al. 2011), it is likely that an N-MORB melt assimilated a small proportion of E-MORB melt or crust to generate the LLD2 starting composition. As the H_2O content and fO_2 of LLD2 are also elevated, we posit that a primitive N-MORB melt assimilated hydrothermally altered E-MORB crust, which had been hydrated and oxidized by circulating seawater. This assimilation likely occurred when the parental melt to

LLD2 intruded to a shallow storage level where much of the surrounding wall rock had been hydrothermally altered (Gillis 1995).

As the three shard compositional populations were all erupted within 5 kyr and are present at the same depths in the core, magmas of these compositions must have been stored in the axial crust concurrently. Maintenance of different LLDs within a single storage chamber is unlikely, as MOR axial magma chambers facilitate rapid homogenization of intruding melts (Batiza and Niu 1992; Sinton and Detrick 1992). Thus, the existence of two LLDs implies the existence of multiple storage levels beneath the EPR that were sourced for eruptions during the same period of time. The bimodal composition of shards from LLD1 (low-MgO and low-Al_2O_3 groups) may indicate a third storage chamber created by extraction of liquid from the LLD1 sill and further fractionation or it may reflect one strongly zoned sill. Though stratified magma chambers are recorded in ophiolite exposures (Browning 1984; MacLeod and Yaouancq 2000), this geometry would be expected to produce a continuous range of MgO contents, rather than a bimodal population.

Vapor saturation pressures for the shards record identical minimum storage depths for both populations in LLD1 (1.9 km), and a slightly shallower depth for LLD2 (1.6 km). Though these are minimum constraints on storage depths, the fact that the best-fit MELTS models also utilize approximately these pressures suggests that the storage depths were in fact different for the two LLDs. This is in contrast to the classical interpretation of MOR magmatic systems as a single, shallow melt-rich lens beneath the ridge axis from which all eruptions are sourced. Rather, we prefer a model of a series of chemically and physically isolated melt lenses within a generally melt-rich horizon, though individual lenses are likely smaller than what is distinguishable by seismic studies (Morgan, et al. 1994; Sinton and Detrick 1992).

5.6.3 Atypical Eruptions

Unique Compositions

The low-MgO shards are the most evolved (lowest MgO) pyroclastic glasses yet recorded from a mid-ocean ridge explosive eruption (Fig 11). Glass shards from the Juan de Fuca Ridge and near-ridge seamounts, Gorda Ridge, Fiji Basin, and other samples from the northern and southern EPR most commonly have MgO contents greater than 7 wt.% (Clague et al. 2009). Glass shards from core OC170-26-159, retrieved near the Pacific-Antarctic ridge (PAR), range from 5.8 to 6.6 wt.% MgO (Lund et al. 2018). These PAR glasses extend to lower MgO values than typical MORB but are still not as extensively evolved as the low-MgO shard group from core Y71-07-53. Core AT2619-12PC, taken from ~20 km off axis of the Juan de Fuca Ridge (JdF), contains a bimodal distribution of glass shard compositions erupted over 65 kyr. However in contrast to the bimodal glass compositions in core Y71-07-53, MgO contents in the JdF core are temporally correlated becoming systematically more evolved as time progressed (Ferguson et al. 2017).

The Y71-07-53 glasses from the T4 interval studied here are the only recognized series of bimodal MOR pyroclast glass compositions erupting simultaneously within a short time interval (5 kyr). The eruption of multiple compositions (e.g. N-MORB and E-MORB) from individual ridge segments at essentially the same time (Waters et al. 2011) is widely recognized from study of effusive axial lavas, so it is unsurprising that MORs can sustain multiple shallow storage chambers simultaneously. In the case of the EPR segment near Y71-07-53, E-MORB lavas have only been sampled along a short section of the ridge axis approximately 100 km north of the core site, yet the LLD2 starting composition shows evidence for interaction with E-MORB melts below the surface. We infer that melts with E-MORB affinity may be more widely distributed in

the axial crustal section than has been recognized from the limited surface sampling. Given the way that sediment cores sample pyroclasts and the time resolution of core Y71-07-53 we cannot distinguish whether the different compositions erupted in the same events, or in different events within a closely-spaced eruption series. As the different shard compositions are distributed relatively evenly throughout the ash interval (Fig 5) and the oxygen isotope stratigraphy is well preserved, it is unlikely that reworking of the sediment has vertically redistributed the shards (McCart 2020). It is therefore probable that both magmatic storage levels were active over the same time period between 348 and 343 ka.

The basalt chips from the base of core Y71-07-53 also represent a very anomalous composition, as these are even more evolved than the T4 glass shards. The compositions of these chips appear possibly consistent with derivation from the axial magma chamber, as they lie near the low-MgO predictions for LLD1. However, there is not enough compositional variability among the chips themselves to discern a differentiation trend from these chips. The oceanic crust underlying the core site was built at roughly 460 ka, based on a spreading rate of 74 mm/yr and 34 km distance from the ridge. The chips presumably reflect an exceptionally fractionated portion of the magmatic system at this time and their volatile saturation pressures indicate an unusual eruption style. The vapor saturation pressures of these chips, while variable, record quenching depths of 2200±500 m (220±50 bars), shallower than the ridge axis depth of ~2800 m. While sea level was at a low stand at the estimated eruption time of 460 kyr, the amplitude of glacial-interglacial sea level fluctuation is only on the order of 100 m and so does not account for the low pressure recorded in the core base chips. We posit that the core base chips represent a volcanic bomb that was lofted to 2700 m depth or shallower, possibly entrained in a hot water

plume like the later shards. The bomb must have been large enough to avoid immediate quenching at the eruption depth.

Eruption Scale

The T4 glass shards in core Y71-07-53 were deposited 8 to 9 km from the EPR axis at the time of the eruption series. Pyroclastic glasses from the Gorda Ridge, Juan de Fuca Ridge, and other sites along the EPR are dispersed only up to 5 km from their eruption sites (Clague et al. 2009; Ferguson et al. 2017). Eruptions similar to the T4 shards from core Y71-07-53 occurred from the PAR, expelling shards up to 7 km from the ridge axis (Lund et al. 2018). Thus, the shards in core Y71-07-53 apparently represent a series of exceptionally energetic eruptions. The shard dispersal distance is not explained simply by enhanced volatile contents in the magma, as the range of volatile contents measured is similar to axial MORB and the hydrostatic pressure at 2800 m depth inhibits significant expansion of bubbles.

The increase in viscosity from the LLD starting compositions to the most evolved erupted shards is nearly an order of magnitude, however the difference between evolved axial lavas (MgO ~6 wt.%) and the low-MgO shards is minor, and both groups of higher MgO shards have lower viscosities than the most evolved, yet still effusively erupted, axial lavas. Thus, the viscosity increase caused by differentiation of axial magmas may have played a minor role in increasing the overpressure buildup to prior to the explosive eruptions but was not the dominant driver of the anomalous eruption style.

Most likely, the extremely energetic eruption style was caused by an unusually high melt flux beneath the ridge axis, supplying heat to repeatedly mobilize the stored and evolved melts as well as to heat hydrothermal fluids which then drove a buoyant plume dispersal mechanism. We

envision an event similar to the megaplumes described in Pegler and Ferguson (2020) and Baker et al. (2012), which generate an umbrella of hot water and pyroclastic material that spreads laterally where the head of the plume reaches neutral buoyancy. Based on the models of Pegler and Ferguson (2020), the ~9 km dispersal distance of the glass shards is near the maximum possible distance that can be achieved by megaplumes of observed volumes (maximum ~100 km^3 of fluid; Baker, et al. 2012). Therefore, the eruptions that produced the glass shards in this study are of the scale of the most explosive observed MOR events.

The grain size distributions in core Y71-07-53 indicate multiple eruptive events of slightly different scales, but all eruptions must have been very large to have dispersed glasses to > 8 km. The ash layer is 20 cm thick, corresponding to a 5 kyr depositional period. The deeper strata are dominated by finer shards, while coarser shards (> 500 μm) are found almost exclusively in the upper 10 cm of the ash interval (McCart 2020). Had this deposit formed from a single eruption, we would expect the opposite sense of particle-size grading, in which larger grain sizes settle out first and finer grains are deposited in the upper layers. While it is possible that shards could have been moved vertically by bioturbation, it is unlikely that the grain size distribution would have been completely reversed. We prefer a multiple eruption scenario, specifically with at least one slightly smaller event to produce the deeper layers of shards, followed by larger events that were able to disperse larger grains to the same distance.

5.6.4 Timing of eruptions

The eruptive period spans the interval of 343 to 348 ka, approximately 5 kyr prior to glacial termination T4 and 53 kyr after a rapid drop in sea level at the boundary between Marine Isotope Substages 11b and 11c. This timing is very similar to the timing of glass shard deposition

off axis of the PAR during T2, 57 kyr after a rapid sea level drop at the onset of MIS 6 and also interpreted as the product of large explosive submarine eruptions (Fig 12) (Lund et al. 2018). We interpret this temporal offset as the time necessary for magmas to migrate from the melting depth (50-100 km) (Gregg et al. 2012; Langmuir and Forsyth 2007), rather than the relatively short period required for melting to occur. The timing of both deposits is consistent with the sea-level forcing hypothesis that predicts modulation of melt flux from the mantle due to rapid changes in sea level (Boulahanis et al. 2020; Huybers and Langmuir 2009; Lund et al. 2016; Lund and Asimow 2011) when accounting for magma migration time from the melting depth. According to this hypothesis, rapid drops in sea level will promote enhanced melt production beneath the ridge axis, while rising or constant sea level will cause melt production to decline (Lund and Asimow 2011). Signals of enhanced or suppressed melting are expected to reach the shallow magma storage system at the ridge axis ~50 kyr after the sea level forcing events (Boulahanis et al. 2020; Lund et al. 2018; Weatherley and Katz 2016), consistent with the 53 and 57 kyr offsets observed at the EPR and PAR. Enhanced hydrothermal flux at the EPR, Mid-Atlantic Ridge, and Juan de Fuca Ridge during or slightly preceding glacial terminations corroborate this hypothesis (Costa et al. 2017; Lund et al. 2016; Lund et al. 2019; McCart 2020; Middleton et al. 2016).

Thus, we propose the following series of events for the formation of the evolved compositions and leading up to the large explosive eruptions from the EPR between 343 and 348 ka. As sea level rose prior to ~410 ka, mantle melting was suppressed relative to the average MOR system production rate. At approximately 400 ka, sea level dropped rapidly as water was sequestered into ice sheets (Fig 12). This caused a pulse of melting to occur at depth, though these signals had not yet affected the axial magmatic system. As the rate of sea level drop decreased after 390 kyr BP, the effect of on melt production of depressurization from hydrostatic

unloading declined and the melt production returned to a more typical rate. The melt flux modulation generated by this sequence of low melt production, peak in melt production, and return to baseline melt production arrived at the ridge axis about 50 kyr later. Thus, a period of decreased melt flux to the ridge axis, driven by rising sea level prior to 410 ka, preceded the large eruptions. This decreased melt flux allowed for cooling of the crust, such that melts within the axial storage system underwent partial crystallization along LLDs 1 and 2. There may have been an associated period of relative eruptive and hydrothermal quiescence at the ridge axis. At approximately 350 ka, the melt pulse that was generated by sea level drop between ~405 to 400 ka reached the ridge axis and mobilized melts from at least two stored magma bodies. The influx of heat from this melt pulse accelerated the circulation of hydrothermal fluids, enabling the formation of megaplumes during the eruptions. The glass shards dispersed by these plumes are interpreted to represent stored magma, as opposed to melts generated during the period of enhanced melting, which might be expected to have higher MgO contents than average, inconsistent with the slightly evolved glass compositions found in the T4 ash layer. Both the period of rapid sea level drop and the interval of ash deposition are roughly 5 kyr long, further supporting a link between these events.

Unless a causative link can be found between increased mid-ocean ridge magmatism and triggering of a glacial termination, it seems that the large MOR eruptions and peaks in hydrothermal flux occur near the start of glacial terminations by coincidence. Certainly the causal relationship cannot be that a glacial termination causes a pulse of extra melting 50 kyr earlier. Rather it seems that the timescale of melt migration and the time interval between rapid sea level drops due to ice sheet growth and the subsequent glacial termination both happen to be 50 to 60 kyr. The driving force of the large explosive eruptions is exceptionally high magma flux

to the ridge axis generated by preceding rapid sea level fall, rather than the glacial termination itself or low absolute sea levels during glacial periods.

5.7 CONCLUSIONS

Glass shards in sediment core Y71-07-53 are remarkable in both their degree of differentiation compared to typical MORB and the scale of the eruptions that distributed them. The ash layer was expelled by a series of anomalously energetic eruptions from the EPR axis approximately 5 kyr prior to glacial termination T4. The glasses have compositions consistent with derivation from the axial magmatic system, overlapping with slightly evolved axial lava compositions and extending to even lower MgO contents. The glass shards are unique in following a bimodal compositional distribution presumably within single eruptions, and they are the lowest MgO glasses yet reported from submarine explosive eruptions. Crystallization modeling using MELTS shows that the glass shard compositions can be generated by fractionation of two axial basalt compositions following two separate LLDs. Combined with evidence from volatile contents indicating eruption pressures at the depth of the ridge axis, this strongly implies that the glass shards were sourced from the axial magmatic system. The starting compositions differ most notably in their K_2O and H_2O contents and best-fit fO_2 values, which can be explained by assimilation of hydrothermally altered E-MORB. As E-MORB has erupted from the modern EPR along the ridge segment most proximal to the core, this assimilation hypothesis is reasonable.

The glass shards were deposited > 8 km from their source at the EPR axis, farther than reported for any other submarine eruptions. This distribution requires a series of anomalously large eruptions that both generate ash and expel large volumes of hot hydrothermal fluid to form

a buoyant megaplume. Glasses can then be carried 8 to 9 km from their source by a laterally spreading umbrella at the top of the plume, with additional scattering aided by ocean currents during shard settling. The timing of these exceptionally energetic eruptions is consistent with models of sea level modulation of MOR magma flux, with enhanced melting generated by rapid sea level drop. This magma pulse then reaches the ridge axis roughly 50 kyr after the decompression trigger, causing fractionated melts to be explosively mobilized in a series of unusually large eruptions.

5.8 Acknowledgements

We thank Chi Ma for help with EPMA analyses, George Rossman for use of the FTIR lab, and Jade Star Lackey and Kyle McCarty for use of the Pomona College LA-ICPMS lab and assistance with analyses. This work would not have been possible without the expert preservation and curation of marine sediment cores by the Oregon State Core Repository. We are grateful to C. Langmuir for providing basalt chips from the base of core Y71-07-53. This work was supported by NSF award EAR-1558372.

5.9 References Cited

Armstrong JT (1995) Citzaf-a package of correction programs for the quantitative Electron Microbeam X-Ray-Analysis of thick polished materials, thin-films, and particles. Microbeam Analysis 4(3):177-200

Asimow PD, Ghiorso MS (1998) Algorithmic modifications extending MELTS to calculate subsolidus phase relations. American Mineralogist 83(9-10):1127-1132

Bach W, Hegner E, Erzinger J, Satir M (1994) Chemical and isotopic variations along the superfast spreading East Pacific Rise from 6 to 30 S. Contributions to Mineralogy and Petrology 116(4):365-380

Baker ET (2009) Relationships between hydrothermal activity and axial magma chamber distribution, depth, and melt content. Geochemistry, Geophysics, Geosystems 10(6)

Baker ET, Chadwick Jr WW, Cowen JP, Dziak RP, Rubin KH, Fornari DJ (2012) Hydrothermal discharge during submarine eruptions: The importance of detection, response, and new technology. Oceanography 25(1):128-141

Baker ET, German CR (2004) On the global distribution of hydrothermal vent fields. Mid-Ocean Ridges: Hydrothermal Interactions Between the Lithosphere and Oceans, Geophys Monogr Ser 148:245-266

Batiza R, Niu Y (1992) Petrology and magma chamber processes at the East Pacific Rise~ 9° 30′ N. Journal of geophysical research: solid earth 97(B5):6779-6797

Batiza R, Oestrike R, Futa K (1982) Chemical and isotopic diversity in basalts dredged from the East Pacific Rise at 10 S, the fossil Galapagos Rise and the Nazca Plate. Marine Geology 49(1-2):115-132

Beattie P (1993) Olivine-melt and orthopyroxene-melt equilibria. Contributions to Mineralogy and Petrology 115(1):103-111

Boulahanis B, Carbotte SM, Huybers PJ, Nedimović MR, Aghaei O, Canales JP, Langmuir CH (2020) Do sea level variations influence mid-ocean ridge magma supply? A test using crustal thickness and bathymetry data from the East Pacific Rise. Earth and Planetary Science Letters 535:116121

Browning P (1984) Cryptic variation within the cumulate sequence of the Oman ophiolite: magma chamber depth and petrological implications. Geological Society, London, Special Publications 13(1):71-82

Carbotte SM, Detrick RS, Harding A, Canales JP, Babcock J, Kent G, Van Ark E, Nedimovic M, Diebold J (2006) Rift topography linked to magmatism at the intermediate spreading Juan de Fuca Ridge. Geology 34(3):209-212

Clague DA, Paduan JB, Davis AS (2009) Widespread strombolian eruptions of mid-ocean ridge basalt. Journal of Volcanology and Geothermal Research 180(2-4):171-188

Cogné J-P, Humler E (2004) Temporal variation of oceanic spreading and crustal production rates during the last 180 My. Earth and Planetary Science Letters 227(3-4):427-439

Costa KM, McManus JF, Middleton JL, Langmuir CH, Huybers PJ, Winckler G, Mukhopadhyay S (2017) Hydrothermal deposition on the Juan de Fuca Ridge over multiple glacial–interglacial cycles. Earth and Planetary Science Letters 479:120-132

Coumou D, Driesner T, Heinrich CA (2008) The structure and dynamics of mid-ocean ridge hydrothermal systems. Science 321(5897):1825-1828

Crowley JW, Katz RF, Huybers P, Langmuir CH, Park S-H (2015) Glacial cycles drive variations in the production of oceanic crust. Science 347(6227):1237-1240

Detrick R, Buhl P, Vera E, Mutter J, Orcutt J, Madsen J, Brocher T (1987) Multi-channel seismic imaging of a crustal magma chamber along the East Pacific Rise. Nature 326(6108):35-41

Dixon JE, Stolper EM, Holloway JR (1995) An experimental study of water and carbon dioxide solubilities in mid-ocean ridge basaltic liquids. Part I: calibration and solubility models. Journal of Petrology 36(6):1607-1631

Eissen J (1982) Petrologie comparee de basaltes de differents segments de zones d'accretion oceanique ë taux d'accretion varies (Mer Rouge, Atlantique, Pacifique). Thesis Or Dissertation, Doctoral, Univ Strasbourg

Elderfield H, Schultz A (1996) Mid-ocean ridge hydrothermal fluxes and the chemical composition of the ocean. Annual Review of Earth and Planetary Sciences 24(1):191-224

Engel A, Engel CG (1964) Igneous Rocks of the East Pacific Rise: The alkali volcanic suite appear to be differentiated from a tholeiitic basalt extruded from the mantle. Science 146(3643):477-485

Ferguson DJ, Li Y, Langmuir CH, Costa KM, McManus JF, Huybers P, Carbotte SM (2017) A 65 ky time series from sediment-hosted glasses reveals rapid transitions in ocean ridge magmas. Geology 45(6):491-494

Fine G, Stolper E (1986) Dissolved carbon dioxide in basaltic glasses: concentrations and speciation. Earth and Planetary Science Letters 76(3-4):263-278

Funkhouser JG, Fisher DE, Bonatti E (1968) Excess argon in deep-sea rocks. Earth and Planetary Science Letters 5:95-100

Ghiorso MS, Sack RO (1995) Chemical mass transfer in magmatic processes IV. A revised and internally consistent thermodynamic model for the interpolation and extrapolation of liquid-solid

equilibria in magmatic systems at elevated temperatures and pressures. Contributions to Mineralogy and Petrology 119(2-3):197-212

Gillis KM (1995) Controls on hydrothermal alteration in a section of fast-spreading oceanic crust. Earth and Planetary Science Letters 134(3-4):473-489

Giordano D, Russell JK, Dingwell DB (2008) Viscosity of magmatic liquids: a model. Earth and Planetary Science Letters 271(1-4):123-134

Goff JA (2015) Comment on "Glacial cycles drive variations in the production of oceanic crust". Science 349(6252):1065-1065

Gregg PM, Hebert LB, Montesi LG, Katz RF (2012) Geodynamic models of melt generation and extraction at mid-ocean ridges. Oceanography 25(1):78-88

Hussenoeder SA, Collins JA, Kent GM, Detrick RS (1996) Seismic analysis of the axial magma chamber reflector along the southern East Pacific Rise from conventional reflection profiling. Journal of Geophysical Research: Solid Earth 101(B10):22087-22105

Huybers P, Langmuir C (2009) Feedback between deglaciation, volcanism, and atmospheric CO2. Earth and Planetary Science Letters 286(3-4):479-491

Huybers P, Wunsch C (2005) Obliquity pacing of the late Pleistocene glacial terminations. Nature 434(7032):491-494

Jellinek AM, Manga M, Saar MO (2004) Did melting glaciers cause volcanic eruptions in eastern California? Probing the mechanics of dike formation. Journal of Geophysical Research: Solid Earth 109(B9)

Jochum KP, Stoll B, Herwig K, Willbold M, Hofmann AW, Amini M, Aarburg S, Abouchami W, Hellebrand E, Mocek B (2006) MPI-DING reference glasses for in situ microanalysis: New reference values for element concentrations and isotope ratios. Geochemistry, Geophysics, Geosystems 7(2)

Langmuir CH, Forsyth DW (2007) Mantle melting beneath mid-ocean ridges. Oceanography 20(1):78-89

Langmuir CH, Klein EM, Plank T (1992) Petrological systematics of mid-ocean ridge basalts: Constraints on melt generation beneath ocean ridges. Mantle flow and melt generation at mid-ocean ridges 71:183-280

Laschek D (1985) Geochemische Untersucungen an Basalten vom Galapagos Spreading Center und vom East Pacific Rise. PhD Thesis Universität (TH) Fredericiana

Lisiecki LE, Raymo ME (2005) A Pliocene-Pleistocene stack of 57 globally distributed benthic δ18O records. Paleoceanography 20(1)

Lonsdale P (1989) The rise flank trails left by migrating offsets of the equatorial East Pacific Rise axis. Journal of Geophysical Research: Solid Earth 94(B1):713-743

Lund D, Asimow P, Farley K, Rooney T, Seeley E, Jackson E, Durham Z (2016) Enhanced East Pacific Rise hydrothermal activity during the last two glacial terminations. Science 351(6272):478-482

Lund DC, Asimow PD (2011) Does sea level influence mid-ocean ridge magmatism on Milankovitch timescales? Geochemistry, Geophysics, Geosystems 12(12)

Lund DC, Pavia FJ, Seeley EI, McCart SE, Rafter PA, Farley KA, Asimow PD, Anderson RF (2019) Hydrothermal scavenging of 230Th on the Southern East Pacific Rise during the last deglaciation. Earth and Planetary Science Letters 510:64-72

Lund DC, Seeley EI, Asimow PD, Lewis MJ, McCart SE, Mudahy AA (2018) Anomalous Pacific-Antarctic Ridge Volcanism Precedes Glacial Termination 2. Geochemistry, Geophysics, Geosystems 19(8):2478-2491

Maclennan J, Jull M, McKenzie D, Slater L, Grönvold K (2002) The link between volcanism and deglaciation in Iceland. Geochemistry, Geophysics, Geosystems 3(11):1-25

MacLeod CJ, Yaouancq G (2000) A fossil melt lens in the Oman ophiolite: Implications for magma chamber processes at fast spreading ridges. Earth and Planetary Science Letters 176(3-4):357-373

McCart SE (2020) Assessing the Sea Level Hypothesis with Hydrothermal and Volcanic Ash Records from the East Pacific Rise and Pacific-Antarctic Ridge. Master's Thesis, University of Connecticut

Michael PJ, Graham DW (2015) The behavior and concentration of CO2 in the suboceanic mantle: Inferences from undegassed ocean ridge and ocean island basalts. Lithos 236:338-351

Middleton JL, Langmuir CH, Mukhopadhyay S, McManus JF, Mitrovica JX (2016) Hydrothermal iron flux variability following rapid sea level changes. Geophysical Research Letters 43(8):3848-3856

Morgan JP, Harding A, Orcutt J, Kent G, Chen Y (1994) An observational and theoretical synthesis of magma chamber geometry and crustal genesis along a mid-ocean ridge spreading center. International Geophysics 57:139-178

Morton JL, Sleep NH (1985) A mid-ocean ridge thermal model: Constraints on the volume of axial hydrothermal heat flux. Journal of Geophysical Research: Solid Earth 90(B13):11345-11353

Newman S, Lowenstern JB (2002) VolatileCalc: a silicate melt–H2O–CO2 solution model written in Visual Basic for excel. Computers & Geosciences 28(5):597-604

Nielsen SG, Shimizu N, Lee CTA, Behn MD (2014) Chalcophile behavior of thallium during MORB melting and implications for the sulfur content of the mantle. Geochemistry, Geophysics, Geosystems 15(12):4905-4919

Olive J-A, Behn M, Ito G, Buck W, Escartín J, Howell S (2015) Sensitivity of seafloor bathymetry to climate-driven fluctuations in mid-ocean ridge magma supply. Science 350(6258):310-313

Paton C, Hellstrom J, Paul B, Woodhead J, Hergt J (2011) Iolite: Freeware for the visualisation and processing of mass spectrometric data. Journal of Analytical Atomic Spectrometry 26(12):2508-2518

Pegler S, Ferguson D (2020) Rapid heat discharge during deep-sea eruptions generates megaplumes and disperses tephra. Nature Communications: pre-print.

Presnall D, Dixon J, O'donnell T, Dixons S (1979) Generation of mid-ocean ridge tholeiites. Journal of Petrology 20(1):3-35

Puchelt H, Emmermann R (1983) Petrogenetic implications of tholeiitic basalt glasses from the East Pacific Rise and the Galapagos spreading center. Chemical Geology 38(1-2):39-56

Raymo M (1997) The timing of major climate terminations. Paleoceanography 12(4):577-585

Saal AE, Hauri EH, Langmuir CH, Perfit MR (2002) Vapour undersaturation in primitive mid-ocean-ridge basalt and the volatile content of Earth's upper mantle. Nature 419(6906):451-455

Sarda P, Graham D (1990) Mid-ocean ridge popping rocks: implications for degassing at ridge crests. Earth and Planetary Science Letters 97(3-4):268-289

Scheidegger K, Corliss J (1981) Petrogenesis and secondary alteration of upper layer 2 basalts of the Nazca plate. Mem Geol Soc Am 154:77-107

Shen Y, Forsyth DW (1995) Geochemical constraints on initial and final depths of melting beneath mid-ocean ridges. Journal of Geophysical Research: Solid Earth 100(B2):2211-2237

Sinton JM, Detrick RS (1992) Mid-ocean ridge magma chambers. Journal of Geophysical Research: Solid Earth 97(B1):197-216

Soule S, Nakata D, Fornari D, Fundis A, Perfit M, Kurz M (2012) CO2 variability in mid-ocean ridge basalts from syn-emplacement degassing: Constraints on eruption dynamics. Earth and Planetary Science Letters 327:39-49

Sun S-S, McDonough WF (1989) Chemical and isotopic systematics of oceanic basalts: implications for mantle composition and processes. Geological Society, London, Special Publications 42(1):313-345

Tolstoy M (2015) Mid-ocean ridge eruptions as a climate valve. Geophysical Research Letters 42(5):1346-1351

Waters CL, Sims KW, Perfit MR, Blichert-Toft J, Blusztajn J (2011) Perspective on the genesis of E-MORB from chemical and isotopic heterogeneity at 9–10 N East Pacific Rise. Journal of Petrology 52(3):565-602

Weatherley SM, Katz RF (2016) Melt transport rates in heterogeneous mantle beneath mid-ocean ridges. Geochimica et Cosmochimica Acta 172:39-54

Wilson DS (1996) Fastest known spreading on the Miocene Cocos-Pacific plate boundary. Geophysical Research Letters 23(21):3003-3006

5.10 Figures and captions

Figure 1

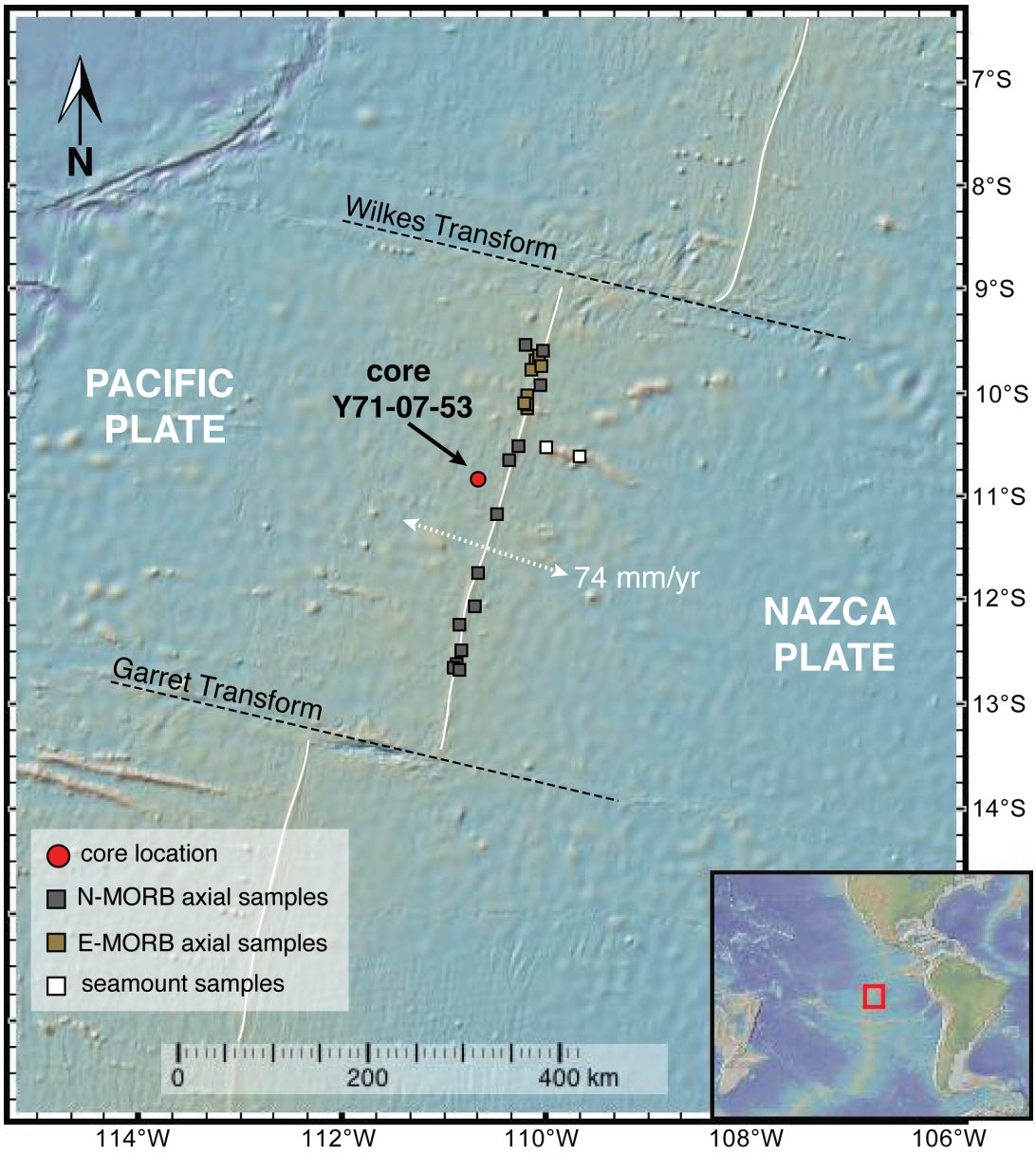

Figure 1 Map of the southern East Pacific Rise, showing the location of the ridge axis (white lines) and major transforms (black dashed lines), as in Lonsdale (1989). The location of core Y71-07-53 (-10.88°N, 110.73°W, 3180 m water depth) is shown as a red circle, and the locations of axial and seamount samples used as geochemical comparisons are shown as squares (locations from PetDB, https://www.earthchem.org/petdb). Map generated using GeoMapApp (http://www.geomapapp.org).

Figure 2

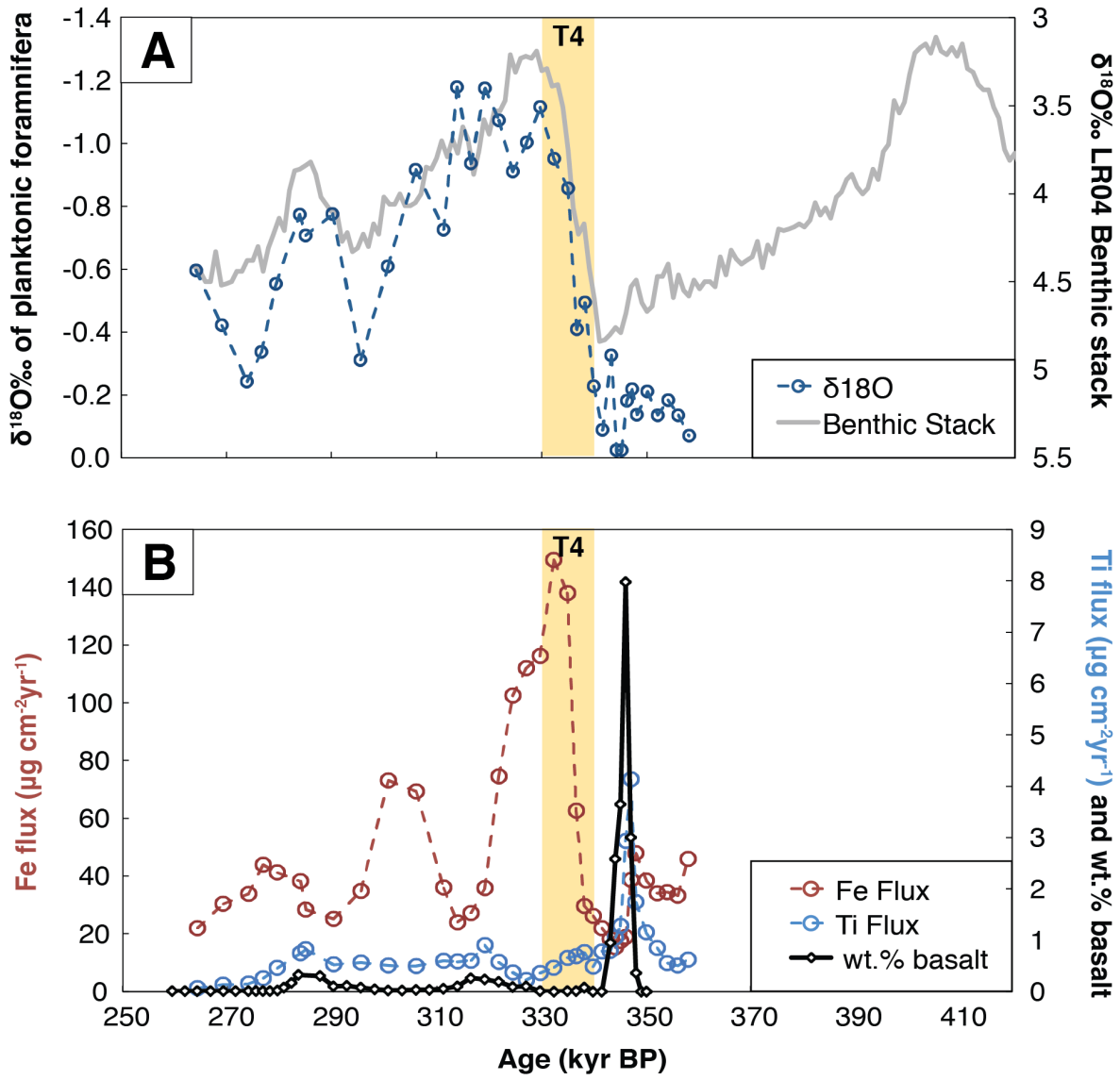

Figure 2 Age model, hydrothermal fluxes, and basalt abundance in core Y71-07-53. **a** Oxygen isotope values ($\delta^{18}O‰$) measured at different depths in the core (blue line) correlated with the benthic stack (sea level proxy) of Lisiecki and Raymo (2005) (gray line) to create the depth vs age model for the core. **b** Flux of hydrothermal Fe, flux of Ti (a proxy for volcanic ash), and abundance of basaltic glass plotted against age. The peak in hydrothermal flux is coeval with T4 (highlighted in yellow) whereas the peaks in Ti and basalt precede the start of glacial termination by approximately 5 kyr. All data and age model are from (McCart 2020).

Figure 3

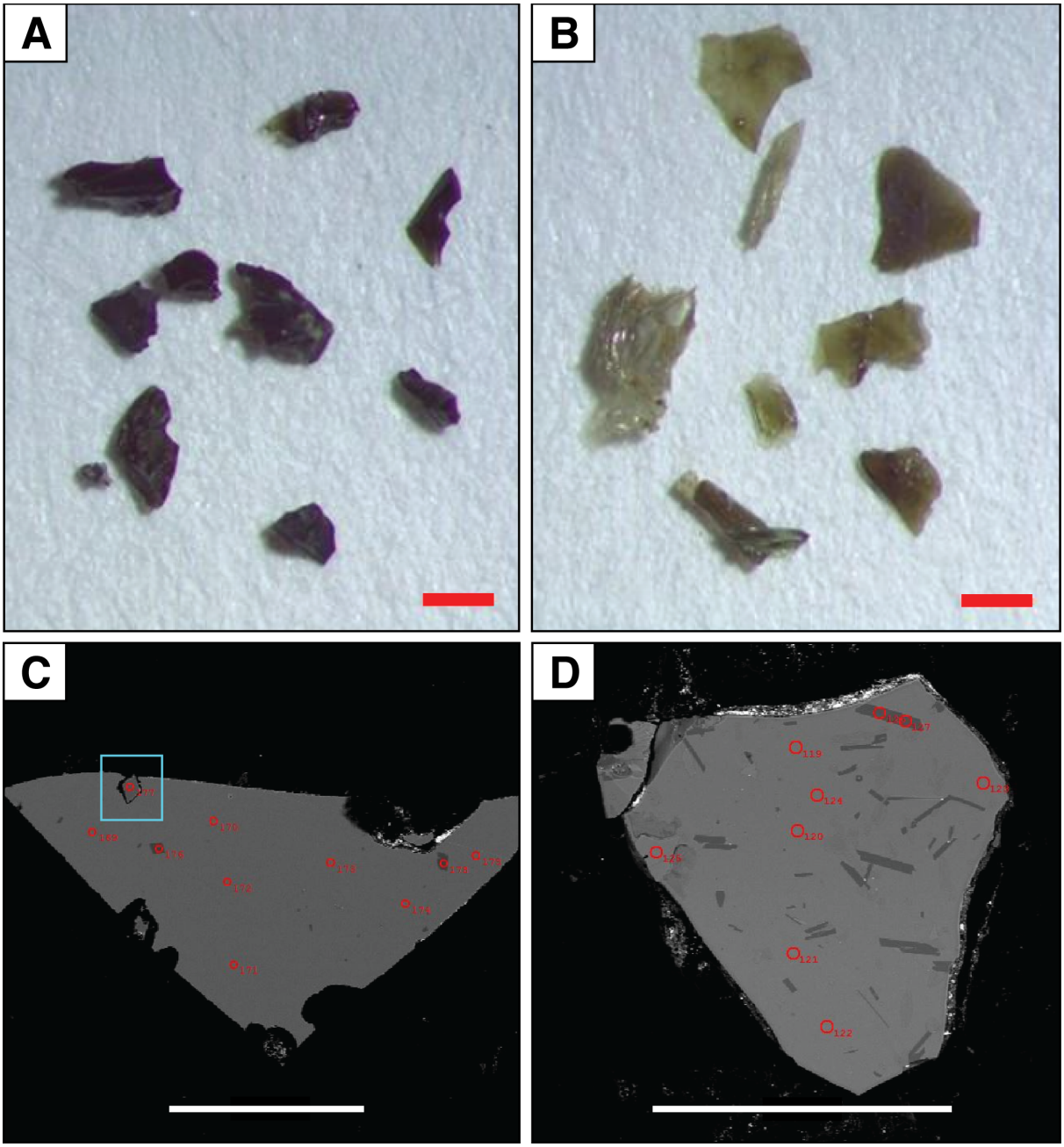

Figure 3 Images of glass shards separated from core Y71-07-53. **a** blocky shards and **b** sheet-like shards. **c** and **d** backscattered electron (BSE) image of a polished shards showing the location of analyses (red circles). Analytical spots are 10 μm. **c** shows a nearly aphyric shard with broken vesicles around its surface, few small plagioclase phenocrysts (dark gray), a single olivine phenocryst (inside the blue square). **d** is a typical plagioclase-rich shard (dark gray laths). Scale bars in all panels are 250 μm. Images in **a** and **b** are taken from (McCart 2020).

Figure 4

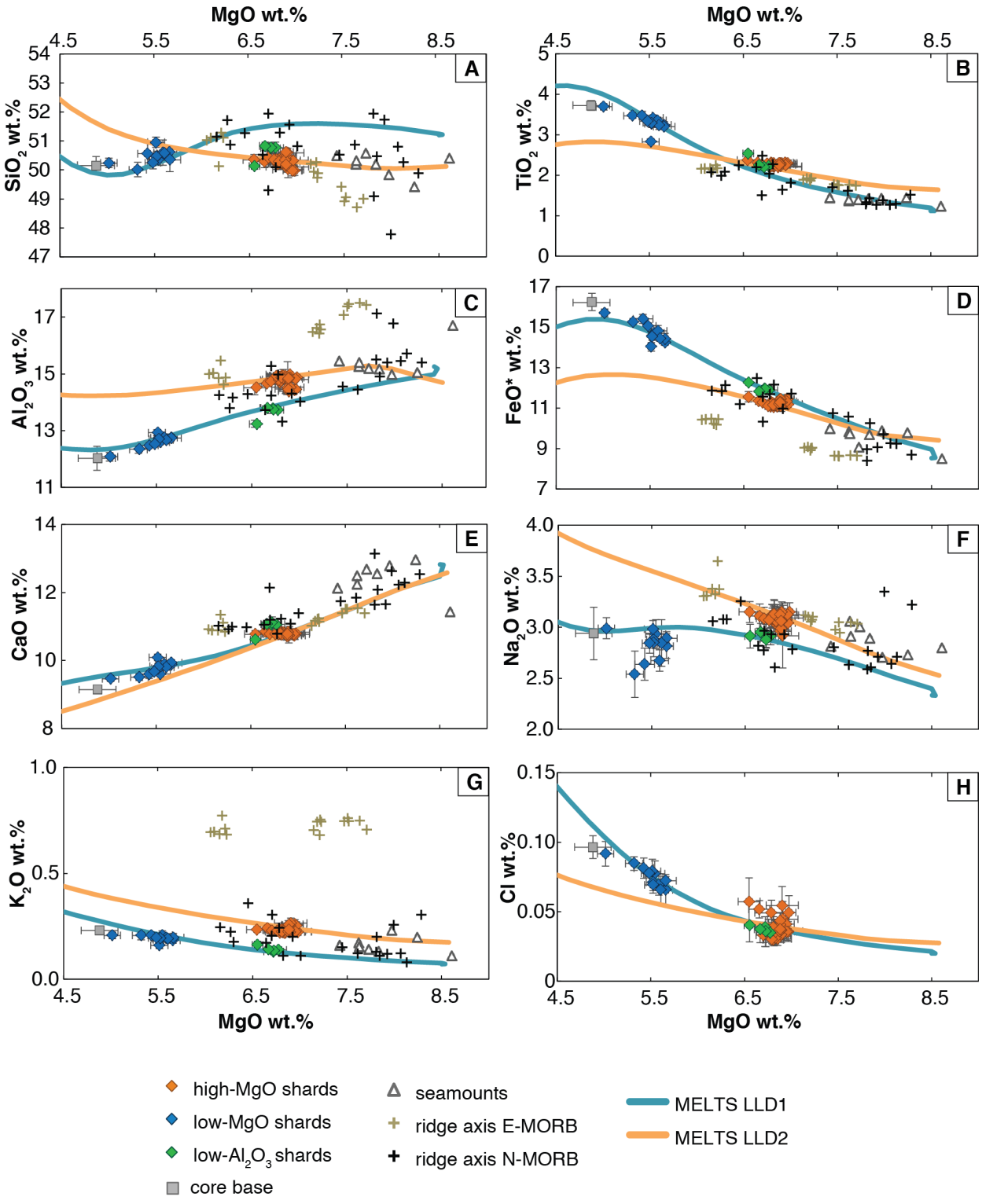
MgO wt.%
A
B
C
D
E
F
G
H
SiO2 wt.%
TiO2 wt.%
Al2O3 wt.%
FeO* wt.%
CaO wt.%
Na2O wt.%
K2O wt.%
Cl wt.%
high-MgO shards
low-MgO shards
low-Al2O3 shards
core base
seamounts
ridge axis E-MORB
ridge axis N-MORB
MELTS LLD1
MELTS LLD2

Figure 4 Selected major oxide compositions of glass shards in the core, all plotted as variation diagrams against MgO (wt. %) as a measure of differentiation progress: **a** SiO_2, **b** TiO_2, **c** Al_2O_3, **d** FeO* (total Fe reported as FeO), **e** CaO, **f** Na_2O, **g** K_2O, **h** Cl. Shards are divided into three groups based on major element compositions: low-MgO (blue), high-MgO (orange), and low-Al_2O_3 (green). Each point represents a single shard, with plotted compositions representing the average composition of all analyses on that shard. The low-Al_2O_3 shards have MgO contents comparable to the high-MgO group, but are distinct in other oxide contents, particularly Al_2O_3 and K_2O. Compositions from proximal seamounts and lavas from the modern ridge axis are shown for comparison. Two liquid lines of descent (LLDs) calculated using MELTS are shown, indicating conditions that produce the shard compositions by crystallization of the axial compositions. Axial and seamount compositions are from Bach et al. (1994), Eissen (1982), Scheidegger and Corliss (1981), Laschek (1985), Puchelt and Emmermann (1983), Funkhouser et al. (1968), Engel and Engel (1964), Batiza et al. (1982), and Nielsen et al. (2014).

Figure 5

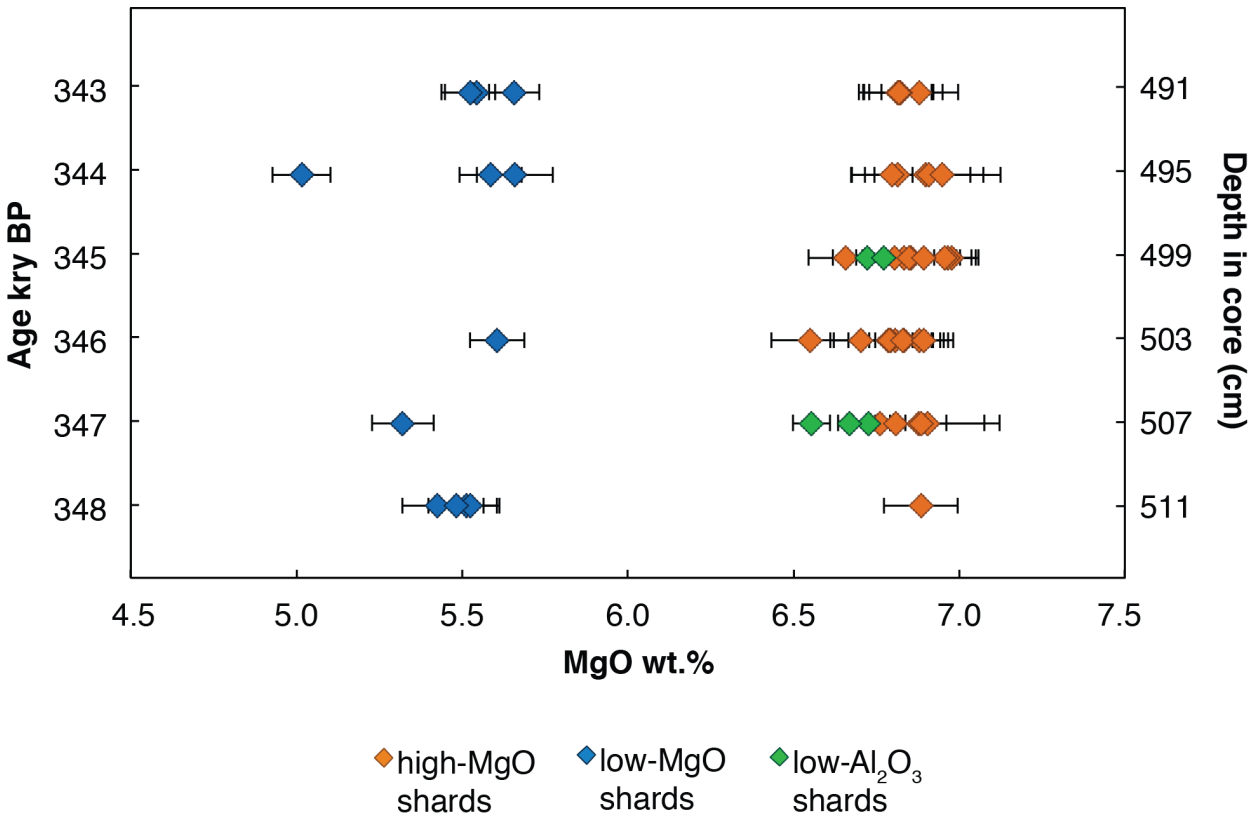

Figure 5 MgO content (wt.%) compared to depth in the core and depositional age. Both the high-MgO and low-MgO groups are represented at most depths. The low Al_2O_3 shards are less common overall and were analyzed only at depths 499 and 507 cm (345 and 347 ka). Absence of shards from this group at other depths and the lack of low-MgO shards at depth 499 cm may be results of insufficient sampling, as only 5 to 11 shards were analyzed from each depth.

Figure 6

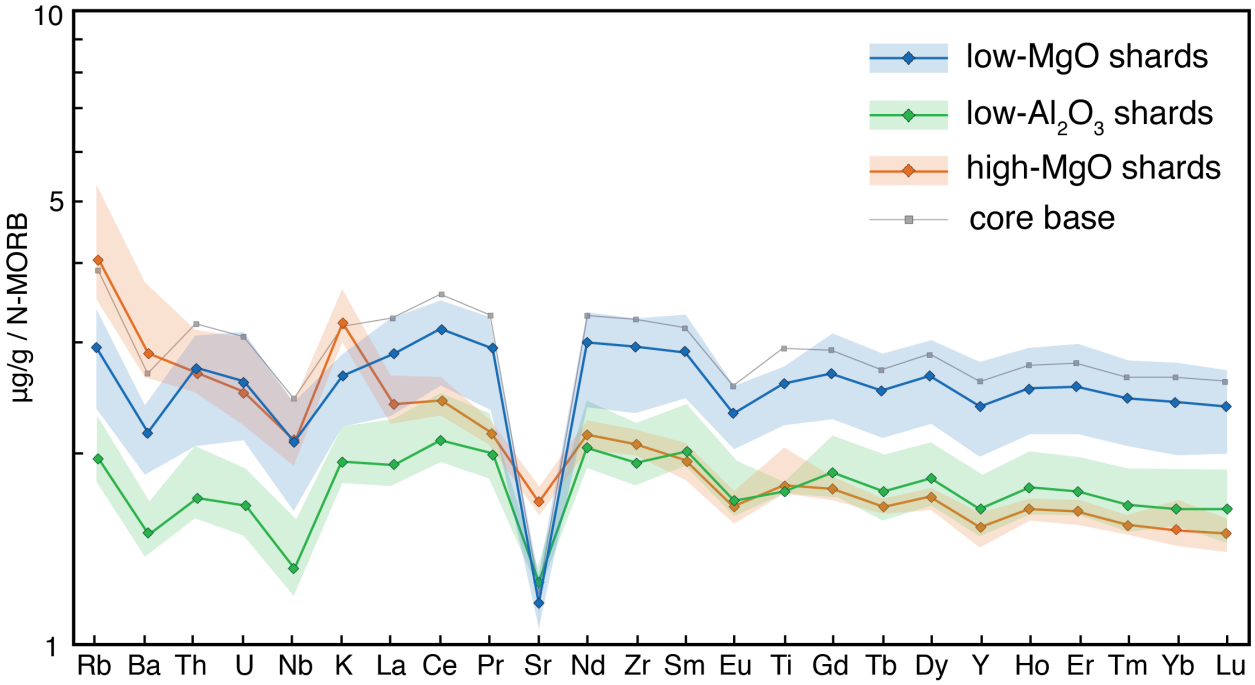

Figure 6 Summary of trace element abundances, normalized to N-MORB (Sun and McDonough 1989). Elements are ordered based on relative incompatibility during peridotite melting, with the most incompatible elements on the left. The large negative Sr anomaly is a result of plagioclase fractionation. Lines are the average of all shards in each compositional group, and shaded areas represent the full range of trace element abundances in all shards from each group. Trace element patterns for the low-MgO and low-Al_2O_3 groups are offset but roughly parallel, suggesting that these groups are likely related by closed-system differentiation, whereas the high-MgO group, which has a steeper slope through the most incompatible elements, represents a different evolution series.

Figure 7

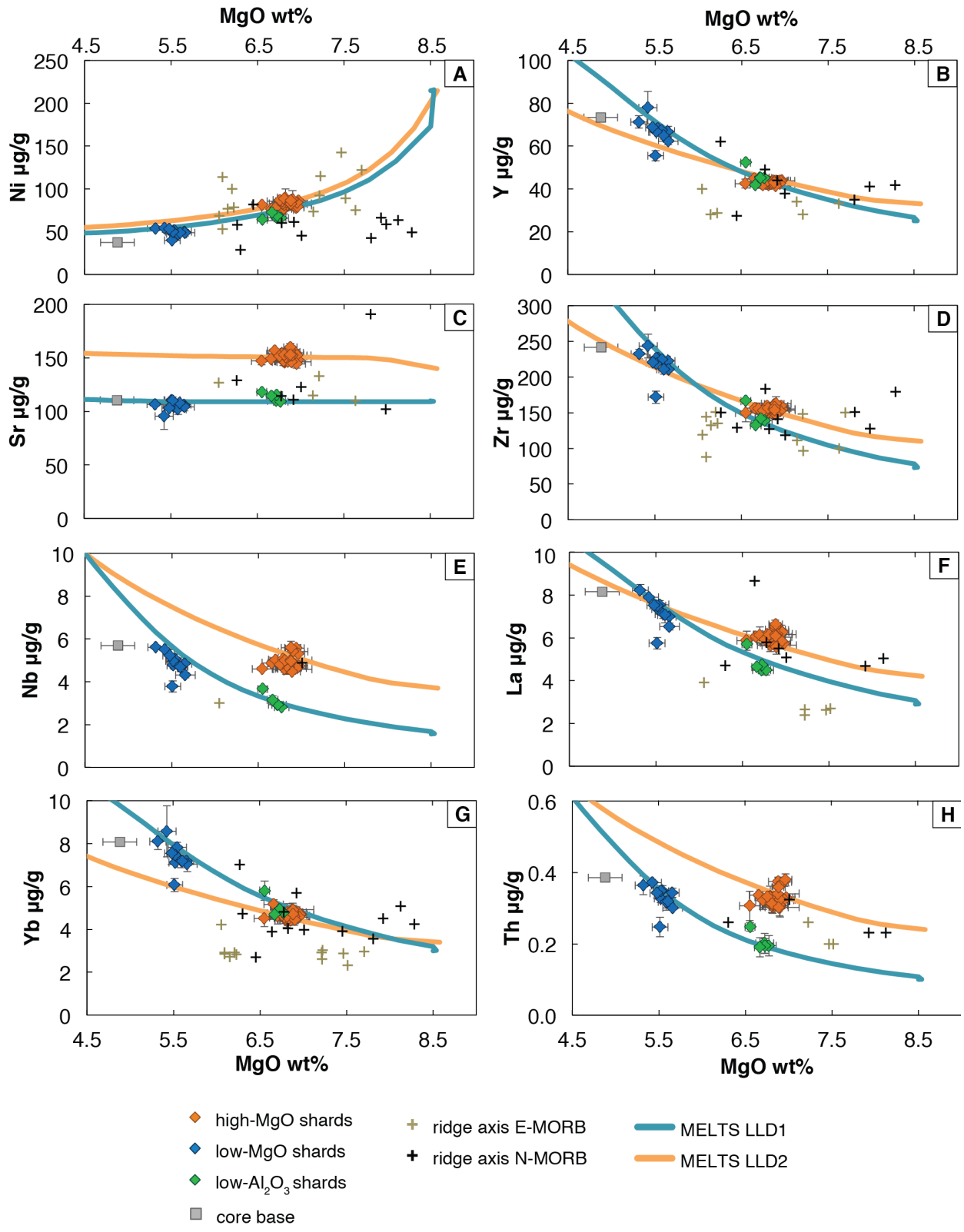
MgO wt%
A
Ni µg/g
B
Y µg/g
C
Sr µg/g
D
Zr µg/g
E
Nb µg/g
F
La µg/g
G
Yb µg/g
H
Th µg/g
high-MgO shards
low-MgO shards
low-Al2O3 shards
core base
ridge axis E-MORB
ridge axis N-MORB
MELTS LLD1
MELTS LLD2

Figure 7 Selected trace element contents relative to wt.% MgO: **a** Ni, **b** Y, **c** Sr, **d** Zr, **e** Nb, **f** La, **g** Yb, **h** Th. The three compositional groups (high-MgO, low-MgO, and low-Al_2O_3) are distinct in most trace element vs. MgO spaces. Data from axial samples are limited, but are included where available. Trace element data were not available for the seamount samples. Blue and orange curves are LLDs calculated using MELTS.

Figure 8

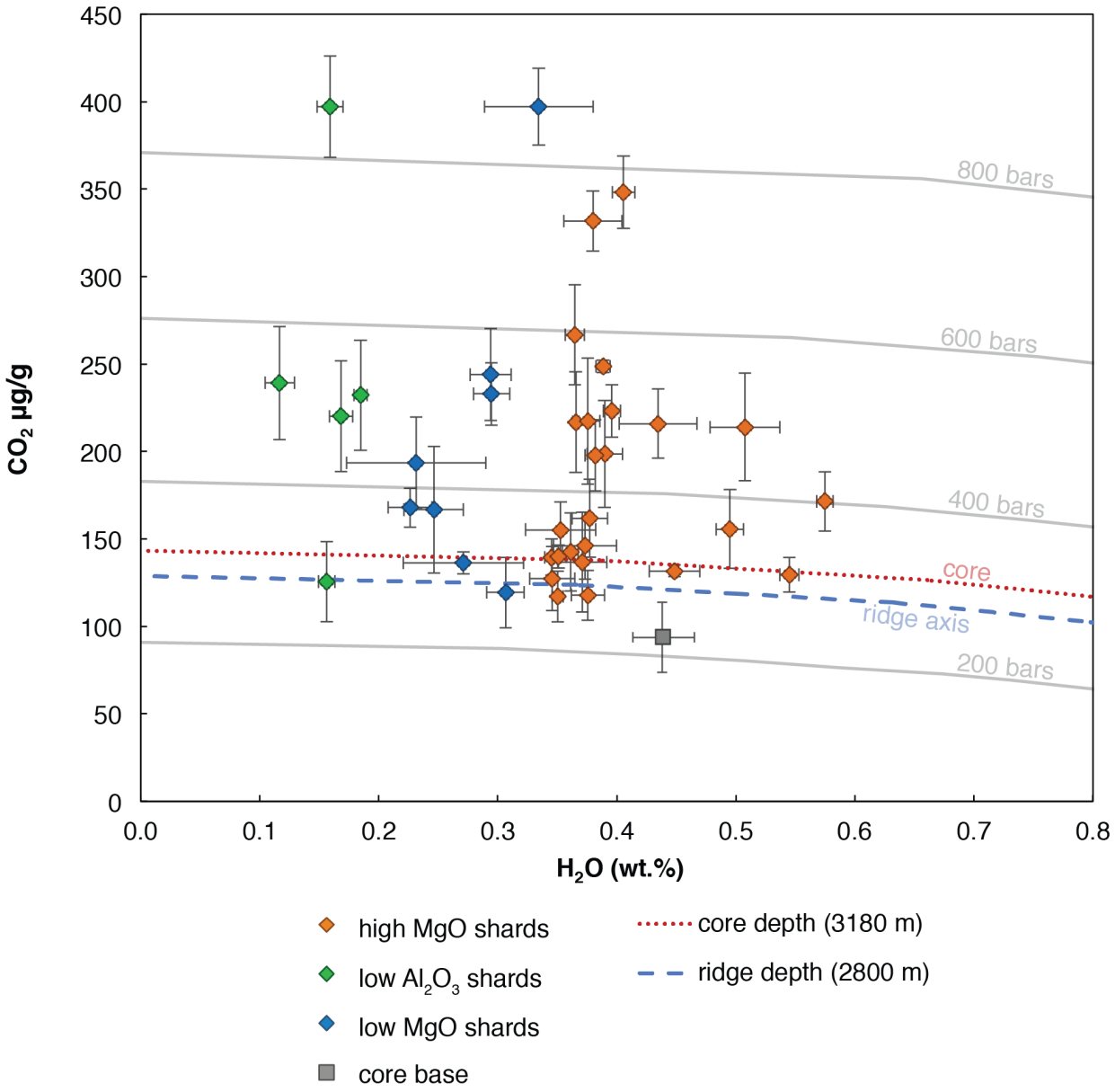

Figure 8 Concentrations of H_2O and CO_2 in the glass shards, as well as volatile saturation curves for a range of pressures. Glasses are undersaturated in volatiles at a specific pressure if they plot below the volatile saturation curve for that pressure. As such, some shards would be undersaturated at the water depth where the core was retrieved (3180 m), but are within error of saturation at the water depth of the ridge axis (~2800 m). Each point represents the average of all analyses on a single shard, with 1σ error bars. Volatile saturation curves were calculated for a melt temperature of 1150°C using VolatileCalc 2.0 (Newman and Lowenstern 2002).

Figure 9

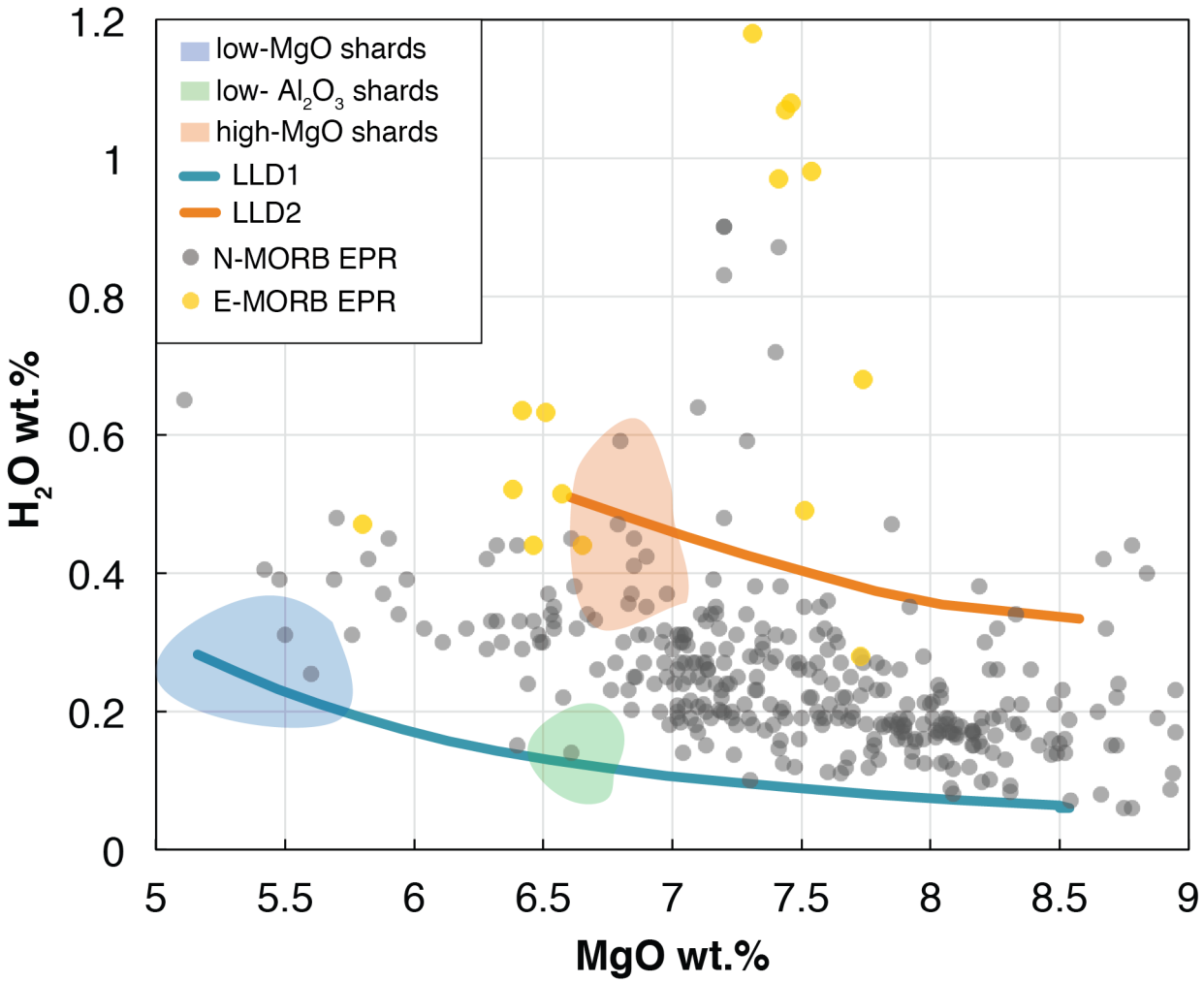

Figure 9 H_2O vs MgO of the shards and LLDs, compared to axial lavas. Because few H_2O measurements are available for the segment nearest to core Y71-07-53, axial lavas from the full length of the EPR are included (http://earthchem.org/petdb). H_2O contents for LLD1 and LLD2 are on the lower and higher ends of the EPR range, respectively, but are within the scope of existing lavas. The glass shards are not anomalously hydrated.

Figure 10

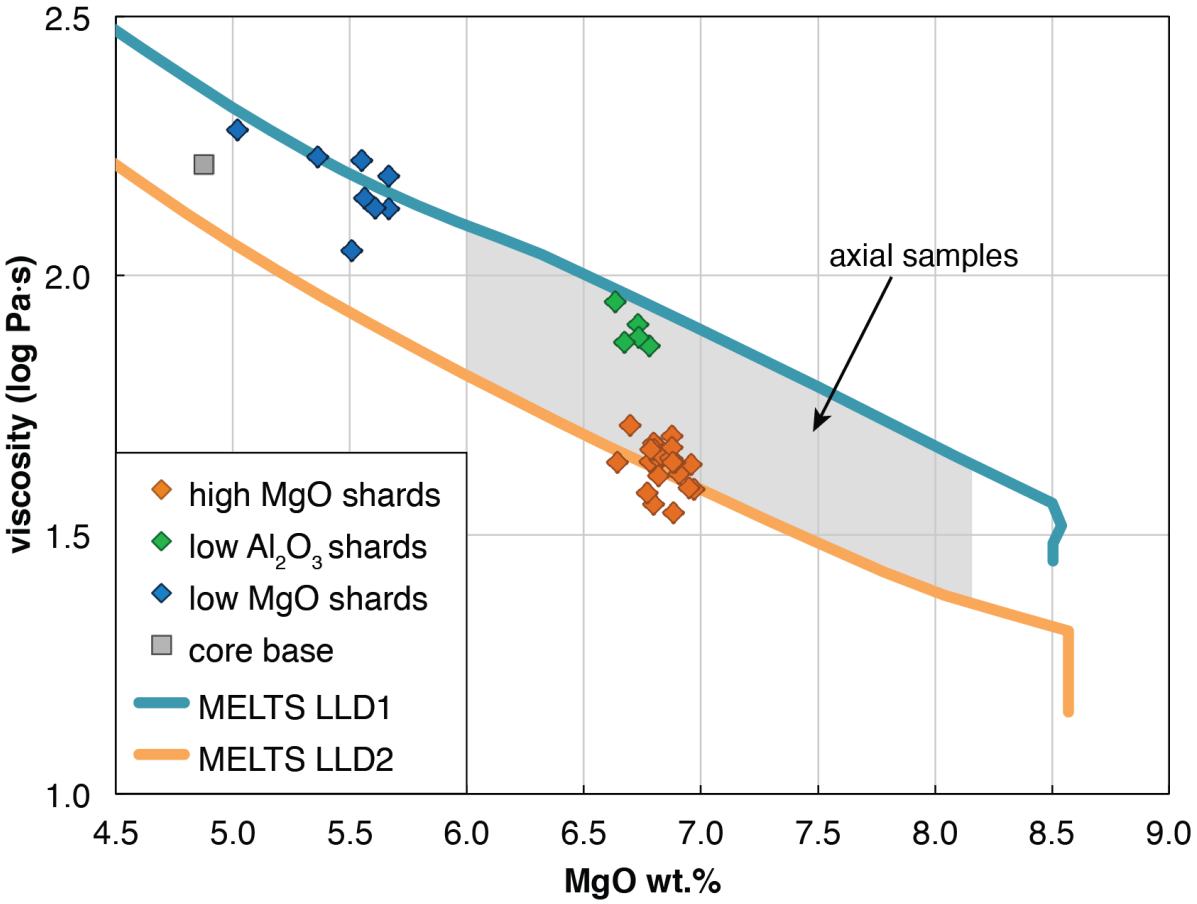

Figure 10 Viscosity increase along the MELTS LLD curves, and estimated viscosities of each glass shard immediately prior to eruption. The gray area shows the MgO range of the EPR axial samples. Axial samples, represented by the gray shaded area, will likely have similar viscosities to the LLDs at the same MgO contents, though the lack of H_2O data from axial samples prohibits accurate calculation of axial viscosities. Shard viscosities are calculated using the liquidus temperature for each individual shard composition (calculated using MELTS) and the Giordano, Russell and Dingwell (2008) viscosity model. This model does not include the effects of bubbles and crystals, however both crystals and vesicles are rare within the shards. As some shard morphologies represent bubble wall fragments, the bulk viscosity of the erupting melt may have been greater than estimated.

Figure 11

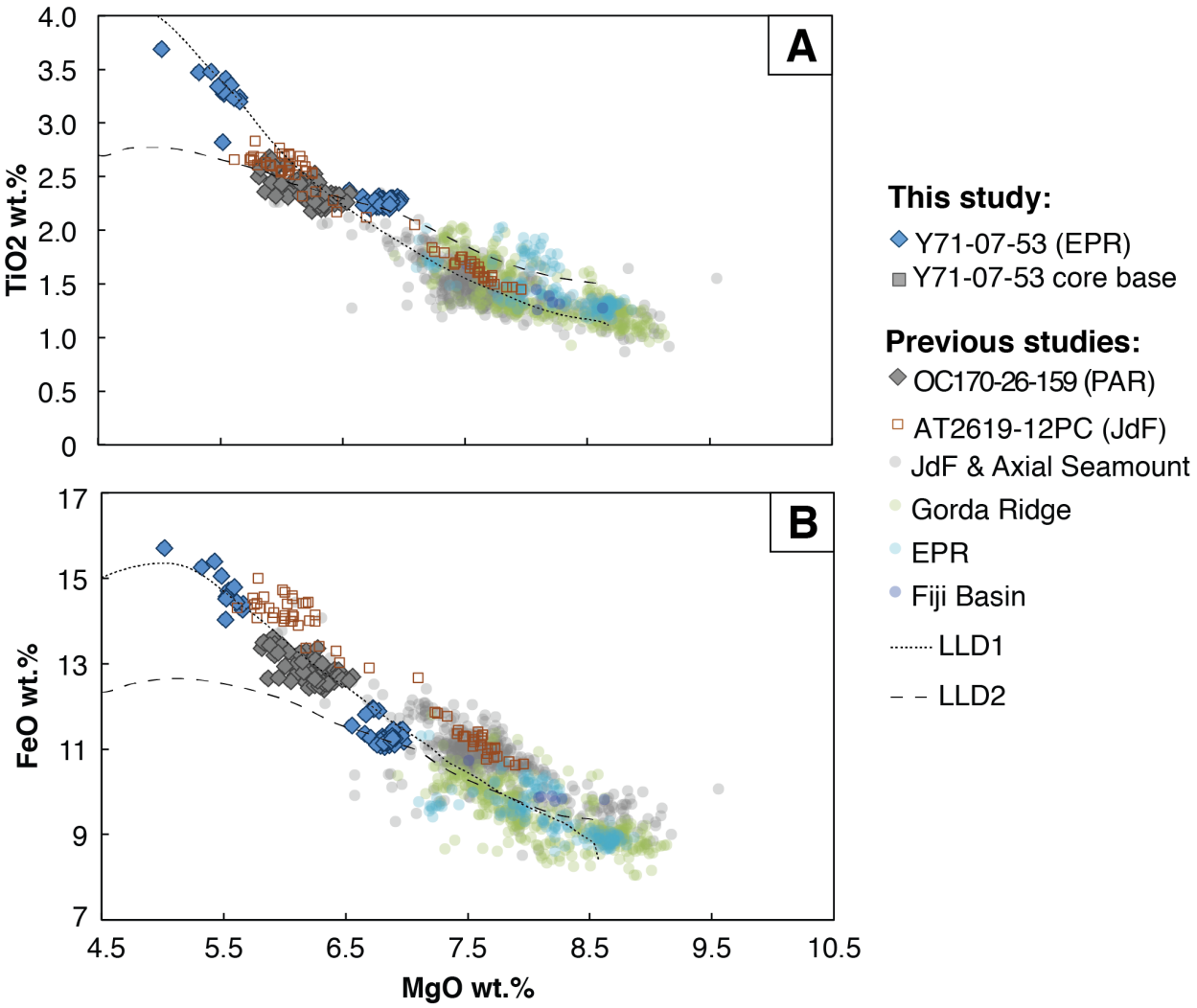

Figure 11 Comparison of the Y71-07-53 shard (East Pacific Rise, EPR) compositions to other basaltic glass shards found in sediment cores, showing **a** TiO_2 and **b** FeO* vs MgO (wt.%). For simplicity, the Y71-07-53 shards are not colored by their compositional groups in these plots. Core OC170-26-159 was taken near the Pacific-Antarctic ridge (PAR), and contains glass shards distributed during glacial Termination 2 (Lund et al. 2018). Core AT2619-12PC was taken from 20 km west of the Juan de Fuca ridge (JdF) and contains glasses from 545 to 610 ka (Ferguson et al. 2017). Additional glass compositions from sediment cores near the JdF (including Axial Seamount), EPR, Gorda Ridge, and Fiji Basin were taken from (Clague et al. 2009). MgO contents from Clague et al. (2009) are multiplied by 1.05 to adjust analyses for updated standard compositions (D. Clague, personal communication).

Figure 12

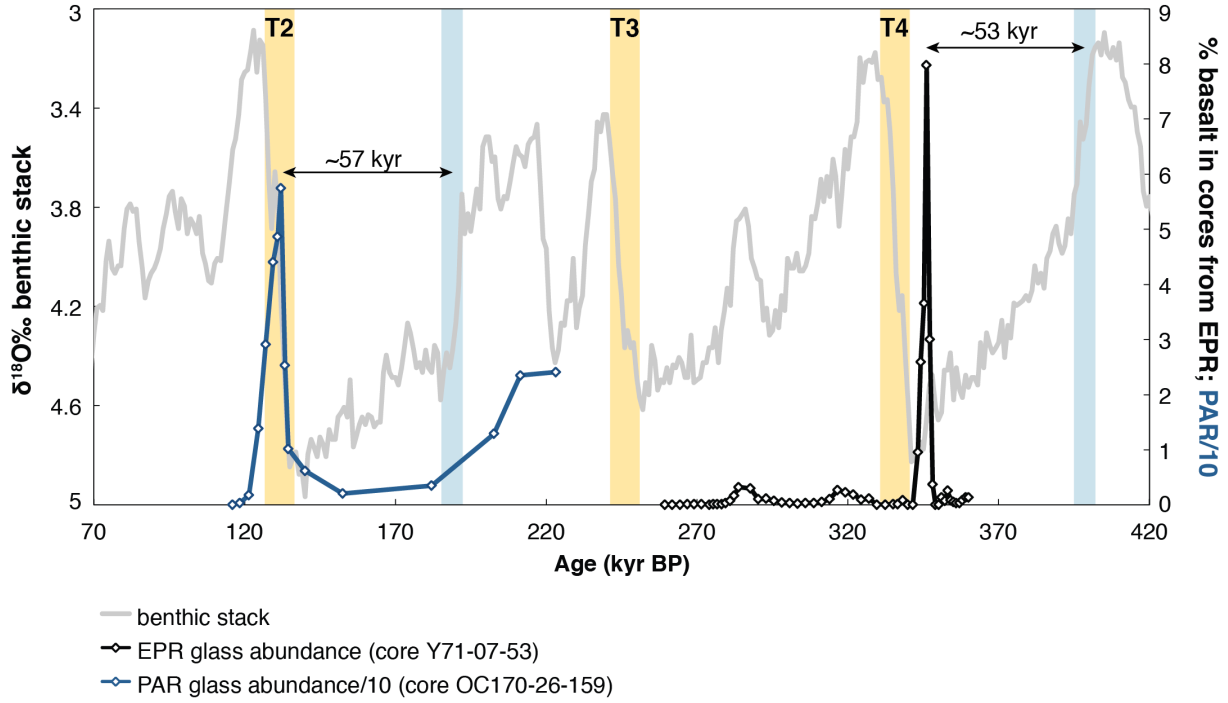

Figure 12 The timing of the EPR eruptions (black peak) preceding T4 compared to eruptions from the PAR (blue peak) during the early stages of T2 (Lund et al. 2018). Glacial terminations are highlighted in yellow, and selected periods of rapidly falling sea level are shaded in blue. Note that the abundance of basalt in the PAR core is shown as wt.% basalt/10, such that both cores can be plotted on the same axis. The timing of these eruptions, ~50-60 kyr after sea level drops, and the compositional similarity of the glasses (i.e. more evolved than axial samples) suggests similar eruption and fractionation processes for these two ash deposits. Benthic stack sea level proxy curve from Lisiecki and Raymo (2005) and EPR glass abundance and age model from McCart (2020). Neither core suitably records sedimentation during T3.

5.11 Tables

Table 1: LLD Starting Compositions

	LLD1	LLD2
P (bars)	850	800
fO_2 (ΔFMQ)	-1.7	0
wt.%		
SiO_2	51.13	49.87
TiO_2	1.11	1.63
Al_2O_3	15.24	14.46
FeO*	8.50	9.36
MgO	8.49	8.53
MnO	0.09	0.17
CaO	12.81	12.52
K_2O	0.07	2.51
Na_2O	2.33	0.17
Cr_2O_5	0.03	0.03
H_2O	0.06	0.33
CO_2	0.01	0.01
µg/g		
Cl	200	275
F	500	900
V	395	355
Co	42.8	42.8
Ni	215	215
Rb	0.5	1.5
Sr	110	140
Y	25	33
Zr	73	110
Nb	1.56	3.7
Ba	5.45	14.5
La	2.9	4.2
Ce	9.3	13.5
Pr	1.49	2.15
Nd	8.25	11.9
Sm	3.05	4.1
Eu	1.5	1.38
Gd	3.9	5
Tb	0.7	0.85
Dy	4.8	6
Ho	1	1.3
Er	2.9	3.4
Tm	0.45	0.53
Yb	3	3.4
Lu	0.4	0.5
Pb	0.45	0.75
Th	0.1	0.24
U	0.04	0.085

CHAPTER 6

Hosting of REE in Accessory Minerals in the Wadi Karim BIF: Implications for the Preservation of Bulk-Rock Trace Element Signatures in Iron Formation

6.1 ABSTRACT

The abundances of rare earth elements (REEs) in iron formation (IF) samples are commonly used to quantify the relative contributions of Fe and Si from different sources, as well as to understand the redox conditions of ancient seawater. This relies on the assumption that the measured REE abundances reflect the chemical signatures of their sources at the time of deposition. However, REEs are highly incompatible in many iron-bearing minerals and chert, and the mineral hosts of REEs in IFs and their petrogenesis are uncertain. We determined the principal mineral hosts of REEs in the Wadi Karim BIF (WKB) of the Eastern Desert, Egypt, through investigation of microtextures and *in-situ* analyses of REEs in major and accessory minerals. The Neoproterozoic-age (~750 Ma) WKB is a dominantly oxide facies IF, with alternating, cm-scale oxide and chert or carbonate bands interbedded with metavolcanic layers. We observed that though Fe-oxides comprise 61 to 82 percent of the BIF based on calculated mineralogy, they contain low ΣREE, averaging 28 μg/g compared to an average of 73 μg/g in the bulk-rock, thereby hosting only 12 to 60% of the total REE budget. We identified apatite as a major REE host, present at 1.6 to 3.3% abundance but containing up to 3300 μg/g ΣREE and so hosting an average of 61% of the total REEs. In samples containing carbonate bands, calcite (4% calculated abundance) is another accessory host of REEs, containing up to 14% of the corresponding bulk-rock REEs. Using calculated proportions of Fe-oxides and apatite ± calcite calculated from bulk-rock compositions, we reproduced the bulk rock values, indicating that REEs are dominantly hosted in accessory minerals. Apatite is most common in the carbonate-rich bands and present in the oxide bands, but absent from chert bands, suggesting a common source for Fe, REEs, and P. Multiple generations of veins containing apatite and calcite indicate that these phases were mobile post deposition. The hosting of REEs dominantly in accessory

phases introduces the possibility that these signatures could have been modified during diagenesis and metamorphism, particularly in IFs with high phosphate content or that have experienced high degrees of metamorphism or post-depositional alteration.

6.2 INTRODUCTION

6.2.1 Iron Formation and REEs

Sedimentary iron formations (IFs) are Fe-rich deposits formed by precipitation of Fe-bearing minerals, quartz (as chert), and carbonates in Precambrian marine basins. The thinly bedded formations with greater than 15 wt.% Fe (Beukes 1973; James 1983; Trendall 2002) result from episodic precipitation of iron-bearing mineral phases in both shallow and deep marine environments. Oxygen levels in these basins were much lower than in the modern day, particularly prior to the 2.3-2.4 Ga Great Oxidation Event (Gumsley et al. 2017; Holland 2002; Kasting 2001), so as to allow for the transport and concentration of reduced iron in seawater. IFs have a limited areal extent in Precambrian continental crust and occur in the geologic record between 3.5 and 2.5 Ga, with a period of reappearance from 0.8 to 0.6 Ga associated with the Neoproterozoic glacial intervals (Hoffman et al. 1992; Kirschvink 1992), suggesting that the specific conditions and processes necessary for IF deposition are no longer widely present in modern oceans (James 1983; Klein 2005; Trendall 2002). It is widely accepted that IF deposition required generally anoxic, yet episodic, redox conditions (Gaucher et al. 2015; Klein 2005) to form layering that is occasionally interpreted as annual cycles (Trendall 2002). Multiple models have been offered to explain the deposition of IFs in different tectonic settings and time periods, including precipitation of silica-gel and Fe-oxyhydroxides from hydrothermal fluids associated with nearby volcanism (Algoma-type, e.g., Gourcerol et al. 2016; Rasmussen et al. 2019;

Rasmussen et al. 2021a; Sial et al. 2015) and oxidation of upwelling Fe-rich waters from the anoxic deep ocean by mixing with oxygenated surface waters (Superior-type, e.g., Frei et al. 2013; Gaucher et al. 2004). IFs associated with glaciomarine deposits (Rapitan-type) are exclusive to late Neoproterozoic time, forming during the retreat of global glaciations and exposure of anoxic water to atmospheric oxygen after millions of years trapped beneath extensive ice cover (e.g., Baldwin et al. 2012; Hoffman and Schrag 2002).

In each of these IF-forming mechanisms, the Fe, Si, and other components are derived from a mixture of seawater, hydrothermal fluids, and detrital inputs in different proportions. The relative contribution of Fe and Si from each potential source is commonly determined based on shale-normalized patterns of rare earth elements and yttrium (REEs) in the IF bulk-rock samples (e.g., Abd El-Rahman et al. 2020; Basta et al. 2011; Frei and Polat 2007; Jacobsen and Pimentel-Klose 1988; Khan and Naqvi 1996; Klein 2005). As different sources have distinct features in REE patterns, the volumetric contributions from each source can hypothetically be quantified. For example, positive Eu anomalies on shale-normalized REE diagrams are taken to reflect incorporation of hydrothermal fluid, whereas light-REE (LREE) element depletion relative to heavy-REE (HREE) is a seawater signature. Thus, REEs are used as a tool for distinguishing the different IF depositional processes. Algoma-type IFs tend to have pronounced hydrothermal signatures, whereas Superior- and Raptian-type IFs display a seawater affinity. REEs in IFs have long been used as a proxy for IF sources and the trace element composition of Precambrian seawater (Abd El-Rahman et al. 2020; Bolhar et al. 2004; Derry and Jacobsen 1990; Lan et al. 2019; Viehmann et al. 2015), and are taken to record the redox conditions of IF depositional settings (Danielson et al. 1992; Paul et al. 2020).

As IFs are Neoproterozoic or older in age (>600 Ma) and preserved on ancient cratons, nearly all occurrences of IF have been metamorphosed to some degree. Nevertheless, the IF bulk-rock REE contents have been presumed to be relatively resistant to alteration. However, REEs are highly incompatible in Fe-oxides and chert (Monecke et al. 2002; Nadoll and Koenig 2011; Nielsen et al. 1992), the major IF-forming minerals that together comprise 60-95% of IF volumes (Klein 2005). Thus, it is not clear which minerals in IFs host the majority of REEs and how these elements are incorporated into the sediments. As REEs are fluid mobile during upper greenschist facies metamorphism or higher (Ague 2017; Gruau et al. 1992) and the original depositional phases of IFs are thought to be hydrous and very fine-grained or amorphous, mobilization of elements during metamorphic recrystallization is likely. As such, the questions stand as to where REEs are hosted in IFs, and whether bulk-rock REE concentrations in IFs represent the primary depositional composition or whether the composition is altered by diagenesis and metamorphism. A few studies have begun to consider these effects (Bonnand, et al. 2020), suggesting mobility of REEs in IFs and calling REE patterns as records of primary depositional signatures into question. Here, we report a case study of the Wadi Karim banded IF (WKB) in the Eastern Desert, Egypt, aimed at determining the mineral hosts of REEs and investigating the potential for mobility of REEs in these deposits.

6.2.2 Geologic Background

The Wadi Karim banded IF (WKB) is one of a series of IFs in the Eastern Desert of Egypt, located on the 0.9 to 0.62 Ga Arabian-Nubian Shield (Avigad et al. 2007), as shown in Figure 1a. The IFs of the Eastern Desert represent a marine basin that covered an area of approximately 20,000 km^2. Though many of the largest Neoproterozoic IFs are thought to be

glaciomarine in origin based on their association with diamictites (Gaucher et al. 2015; Ilyin 2009), the IFs of the Eastern Desert are interbedded with metavolcanic and volcaniclastic deposits, suggesting an oceanic arc source (i.e. Algoma-type) for much of the Fe and Si (Abd El-Rahman et al. 2020; Basta et al. 2011, El-Habaak 2021; Stern et al. 2013).

The WKB deposit is located approximately 30 km southwest of the city of Quseer, Egypt, with IF outcrops interbedded with mafic to intermediate metavolcanic units over an area of 1.6 km^2 (Fig 1b). Ridge-forming lenses of oxide facies IF containing chert and carbonate range from <1 to 12 m in thickness (Basta et al. 2011). The surrounding metavolcanic rocks were deposited at approximately ~750 Ma and were metamorphosed to greenschist facies and lower grades (Ali et al. 2010; Basta et al. 2011; Stern et al. 2013). Based on major and trace element concentrations (including REE), the WKB is interpreted to contain between 25 and 65% hydrothermal components and between 35 and 75% seawater components, with very little detrital input (Basta et al. 2011). Bulk-rock concentrations of selected oxides and REE are shown in Figure 2. Of note are the very high iron contents (40-83 wt.% Fe_2O_3) and fairly low silica contents (14-49 wt.% SiO_2) compared to other IFs throughout Earth history (Klein 2005). REE contents are roughly correlated with wt.% P_2O_5 and do not correlate with other major oxide components (Fig 2)—a pattern that suggests significant amounts of REEs within these rocks may be hosted in a phosphorus-bearing phase.

6.3 ANALYTICAL METHODS

6.3.1 Mineral Identification and Element Maps

To conduct preliminary compositional point analyses and identify mineral phases, scanning electron microscopy (SEM) and energy dispersive X-ray spectroscopy (EDS) were

used to create high-resolution elemental concentration maps of the polished and carbon-coated samples. The ZEISS 1550 VP Field Emission Scanning Electron Microscope in the Geological and Planetary Sciences Division Analytical Facility at the California Institute of Technology (Caltech) was operated at a 15 kV accelerating voltage, 5 nA beam current, and ~7.5 mm working distance for both mapping and point analyses. Full section montaged EDS maps were created for the abundant elements of interest: Si, Fe, Ca, and P (Fig 3). In high-magnification mapped areas, EDS maps were generated by averaging at least three full scans of the area. No elements were excluded from the scans, such that the maps in Figure 4 show all elements (except O and C) present at concentrations above detection limits in the sample areas.

6.3.2 In-Situ Mineral Chemistry

Major element compositions of Fe-oxides and apatite were collected using Caltech's JEOL JXA-8200 electron probe micro-analyzer (EPMA). These phases were targeted as potential REE hosts and for internal standardization of trace element analyses conducted on the same grains. Instrument operating conditions were a 15 kV accelerating voltage and focused beam current of 25 nA. Concentrations of SiO_2, TiO_2, Al_2O_3, Fe_2O_3, MnO, MgO, CaO, Na_2O, P_2O_5, Cr_2O_5 were collected in all phases, plus Cl and F in apatite. Standards used were natural Amelia albite, sodalite, Minas Gerais magnetite, F-phlogopite, and Durango apatite, as well as synthetic anorthite, spinel, TiO_2, Cr_2O_3, and Mn-olivine. Counting times for each element were 30 s on peak, with Na, Cl, and F in the first pass. Data were reduced using mean atomic number (MAN) background corrections and the CITZAF matrix correction program (Armstrong 1995).

Concentrations of all REEs including Y, plus Si and Ca were measured *in situ* in apatite by laser-ablation inductively coupled mass spectrometry (LA-ICPMS) using the New Wave

Research UP 193 Solid State Laser System and Agilent 8800 triple quadrupole ICPMS in the Resnick Water and Environment Laboratory at Caltech. Laser spots 35 μm in diameter were targeted based on careful inspection of SEM-EDS element maps to avoid Fe-oxide and chert inclusions in the analyzed area. The majority of apatite grains in the WKB samples were <35 μm and contained abundant inclusions, so only the largest grains were suitable for analysis by this technique. The laser was operated at 45% power for a 1 s pre-ablation period and 80% power during analytical ablation (20 s, 200 total shots), both periods with a 10 Hz frequency and 3.5 J/cm^2 fluence. The analytical period was followed by a 20 s washout delay between analyses to ensure a return to background count levels. An Ar carrier gas and He option gas were used to carry the ablated material to the ICPMS. Masses measured were ^{29}Si, ^{43}Ca, ^{56}Fe, ^{89}Y, ^{139}La, ^{140}Ce, ^{141}Pr, ^{146}Nd, ^{147}Sm, ^{151}Eu, ^{157}Gd, ^{159}Tb, ^{163}Dy, ^{165}Ho, ^{166}Er, ^{169}Tm, ^{172}Yb, and ^{175}Lu. The primary reference standard was NIST610 glass, analyzed after every 6 unknown spots, and Ca content (collected by EPMA) was used as an internal standard. Data were reduced using the TERMITE script (Mischel et al. 2017) and analytical uncertainties are reported as 2σ of results from ~40 sweeps within each analytical ablation period. Analyses of a Durango apatite standard at the beginning and end of unknown runs were within error of accepted trace element values (Chew et al. 2016; Pang et al. 2017).

This same suite of elements was analyzed in calcite bands and veins in samples K74 and K76 by LA-ICPMS at Pomona College using the ESI NWR193 excimer laser and Agilent 8900 triple quad ICPMS. Laser spots were 50 μm in diameter and the laser was operated with 4.7 J/cm^2 fluence, 8 Hz shot frequency, and 0.24 mJ laser energy. Two 70 μm laser shots were used for pre-ablation of the sample surface. Analytical ablation time for each spot was 30 s, with a washout delay (10 s) and a gas blank measurement (15 s) between each analysis. NIST612 glass

and the calcium carbonate reference material MACS-3 were analyzed between each six sample analyses. NIST612 was used as the primary calibration standard and MACS-3 was processed as a sample and returned measured elemental concentrations within 10% of the accepted values (Jochum et al. 2019). Data were reduced using Iolite software (Paton et al. 2011) and reported uncertainties are 2σ of concentrations calculated from 45 sweeps through the analyzed masses.

Compositional analyses of bulk Fe-oxide separates from samples K37 and K76 were previously included in Maurice (2006). For samples lacking bulk Fe-oxide measurements (K18 and K74), the concentrations of REEs in Fe-oxides were too low for reliable detection via LA-ICPMS, so we collected measurements of 14 REEs plus Ca and Fe from euhedral Fe-oxide grains by secondary ion mass spectrometry (SIMS). Furthermore, we supplemented the LA-ICPMS measurement of relatively rare large, inclusion free apatite grains with additional SIMS analyses of the same suite of elements (minus Fe) in apatite. Au-coated samples were analyzed using the Cameca IMS 7f-GEO ion microprobe in the Caltech Microanalysis Center. An O^- primary beam was accelerated to 13 keV, with a beam current of ~15 nA, resulting in spot sizes of approximately 10 μm on both apatite and Fe-oxide targets. Glass standards NIST610 and NIST612 were used for primary standardization of apatite and Fe-oxide analyses. Compositional analyses of Ca (in apatite) and Fe (in Fe-oxides) collected using EPMA were used for internal standardization.

6.4 RESULTS

6.4.1 Mineralogy and Textural Descriptions

We completed detailed textural observation and mineral identification of four oxide facies samples from the WKB, consisting of alternating chert and oxide bands (K18 and K37) or

carbonate and oxide bands (K74 and K76). Calculated mineralogy of each sample, based on identified mineral phases and bulk-rock geochemistry (Basta et al. 2011; Herrmann and Berry 2002) is given in Table 1, and resulting bulk-rock compositions are given in Table 2. Fe-oxides are the most abundant minerals in the WKB, constituting 61 to 82% of the samples, followed by quartz (mainly as chert), which makes up 13 to 30%. Calcite (2-4.4%), Fe-rich chlorite (0.4-6.4%), and apatite (1.6-3.3%) are the most common accessory minerals.

At macroscopic scales the samples display a mesobanded texture and grain sizes are generally very fine (single grains <50 μm). Descriptions of mineral associations and textures are given below, and SEM-EDS element maps of the full samples and selected detailed areas are included in Figures 3 and 4, respectively. Common minerals in all samples are magnetite, hematite, quartz, calcite, and apatite, and mineral compositions determined by EPMA point analyses are included in Supplementary Table 1. Because hematite is commonly pseudomorphic after magnetite in these samples and magnetite and hematite can be difficult to distinguish in element maps, we refer to these two phases together as Fe-oxides.

Chert-oxide samples

Samples K18 and K37 were characterized by alternating bands of dark gray oxide and red chert, 0.6 to 2.5 mm and 1.2 to >15 mm thick, respectively (Fig 3a,b). Oxide mesobands contain euhedral magnetite grains with rims oxidized to hematite, typically 10 to 40 μm in size. Fine-grained, elongate hematite with abundant chert inclusions is present between euhedral oxides, and chert was also observed as an interstitial phase (Fig 4a-f). Within the oxide bands (>60% Fe-oxides), microbanding is distinguishable by variability in the chert content (~5-40% chert) on the 1 to 2 mm scale, roughly parallel to the mesobands. Chert mesobands do not display internal

layering and are comprised of nearly pure very fine-grained (micro)quartz, with few small blebs of Fe-oxide (<15 μm) and calcite (<30 μm) (Fig 4a). Quartz veins 25 to 100 μm wide are distinct in K18 (Fig 3a), forming two nearly perpendicular vein sets.

Calcite is present along many fracture and dislocation features in the chert bands, and coats the oxide band-chert band boundaries in K37. K18 contains very little calcite outside of the chert bands, while calcite in K37 is associated with the chert bands and found in two sets of veins (25-350 μm thick) that cross-cut the microbanding (Fig 3b). In K37, veins oriented nearly perpendicular to banding contain almost pure calcite with minor quartz, while veins oriented oblique to banding (~20° from horizontal) contain calcite along with albite and apatite (Fig 4d,e). Because the calcite in these samples does not form distinct bands but rather exists as features that cross cut the mesobands or are associated with deformation features, the calcite in these textures is not a primary depositional phase. Thus, the carbonates are secondary and we classified K37 in the chert-oxide group, despite the presence of carbonate minerals.

Apatite is a common accessory mineral dispersed through oxide bands and essentially absent from chert bands. Apatite is concentrated in relict veins and sinuous apatite-rich patches (Fig 3a,b; Fig 4a,b,c), while the remaining area of the oxide bands is comparatively void of apatite. Individual grains range from blocky to string-like in shape and are 5 to 45 μm in diameter. Inclusions of both Fe-oxides and chert are common within the apatite grains, suggesting that apatite grew around these phases after deposition.

Other accessory minerals include Fe-rich chlorite (chamosite; present only in the Fe-oxide bands as irregularly shaped flakes between Fe-oxide grains) and albite (present within some calcite veins). Rare barite was present in chert bands and xenotime (one occurrence, ~5 μm) was also observed in an oxide band. Gypsum was observed in cracks that have not been

completely filled, suggesting that it is a relatively recent precipitate—perhaps related to incipient weathering and sulfide and disulfide phases elsewhere within the strata.

Carbonate-oxide samples

Samples K74 and K76 were distinguished from the chert-bearing samples by the presence of distinct carbonate mesobands and absence of nearly-pure chert bands (Fig 3c,d). However, chert is present in significant proportions (up to 70%) in oxide-bearing bands. Oxide mesobands in these samples were ≥9 mm thick and display internal microbanding defined by varying proportions of Fe-oxides and chert. Within oxide bands, Fe-oxide proportions vary from 20 to 80%. Euhedral Fe-oxide grains (10-70 μm) are common and fine-grained hematite exhibits a mesh-like texture with abundant chert inclusions (Fig 4g). Chert was found interstitial to Fe-oxides grains or supporting them in a suspension (Fig 4i,k,l), depending on the Fe-oxide abundance. Apatite grains are rare in these microbands outside of veins, and calcite blebs (5-10 μm) are somewhat common (Fig 4 k,l). In contrast, blocky-textured microbands 0.6 to 1.2 μm thick contain blocks (<1 mm) of Fe-oxide without distinguishable euhedral grains, separated by elongate, ~100 μm, quartz-dominated patches oriented perpendicular or oblique to the banding (Fig 3c). Apatite and carbonates are generally absent from these microbands.

Carbonate bands are 0.5 to 2.1 mm thick and can vary in thickness by up to 50% across the length of our samples (20 mm). These bands consist of approximately 50 to 85% calcite that surrounds abundant (5-40%) irregularly shaped grains of apatite (<120 μm), as well as abundant blebs of chert (<60 μm) and Fe-oxides (<80 μm) (Fig 4g,h,j). The apatite itself also contains Fe-oxide and quartz inclusions. In K74, apatite is most concentrated near the boundaries of the carbonate bands, within 200 μm of the oxide bands, but in K76 apatite is distributed throughout

the carbonate band. Chert-dominated swaths (~130 μm thick) within the carbonate bands are oriented perpendicular to the banding, but do not appear to extend as veins through the adjacent oxide bands (Fig 4j).

Veins of varying mineralogy and degree of preservation are pervasive throughout the samples. Relict apatite veins 10 to 20 μm thick commonly cut through oxide mesobands, but are absent or indistinguishable from other apatite grains in carbonate bands. These features appear as disconnected chains of apatite "beads" that typically weave between Fe-oxide grains (Fig 4i,k). Thicker (200-300 μm), sinuous quartz+apatite veins in K76 with uneven, rounded edges (Fig 4l) cross-cut the relict apatite veins. Also in K76, a composite quartz vein with a calcite core is associated with offsets in the banding and in apatite veins that it cross-cuts (Fig 3d).

In addition to the major minerals discussed above, the carbonate-oxide samples also contain rare xenotime (4 grains observed, <5 μm), halite (<10 μm), and Fe-rich chlorite (10-20 μm). Halite and chlorite were present only in oxide bands, while xenotime was found in both oxide and carbonate bands.

6.4.2 Mineral Compositions

Average REE compositions of apatite, Fe-oxides, calcite, and reconstructed bulk-rock compositions for each sample are given in Table 3. Concentrations of major elements and REEs from individual mineral analyses are included in the Supplementary Table 2.

Fe-oxides

Based on textural features and reflected light petrography, the Fe-oxides present are dominantly magnetite and hematite, with possible additional oxy-hydroxides. Compositional

analyses were performed on the abundant euhedral grains, most of which comprise both magnetite and pseudomorphic hematite. These grains provide an optimal analytical surface and typically do not contain inclusions, which are abundant in the fine-grained, mesh-textured hematite (e.g., Fig 4c). EPMA analyses of Fe-oxides in all samples are essentially identical, with >92 wt.% Fe_2O_3 (unnormalized, total Fe reported as Fe_2O_3), and minor amounts of SiO_2 (average 1.0 wt.%, maximum 3.9 wt.%), TiO_2 (<0.20 wt.%), Al_2O_3 (<0.33 wt.%), and CaO (<0.44 wt.%).

Average total REE (ΣREE) concentrations in Fe-oxide phases in each sample, measured by SIMS (K18 and K74; this study) or by solution ICPMS of bulk Fe-oxide separates (K37 and K76; Maurice 2006), range from 18 to 46 μg/g, and ΣREE of individual grains range from 9 to 64 μg/g. In contrast, bulk-rock ΣREE contents are between 56 and 101 μg/g (Basta et al. 2011). In sample K18, most of the REEs are contained in Fe-oxide grains, as the ΣREE concentration in Fe-oxides is 52% of the bulk-rock ΣREE content. In the remaining samples, Fe-oxide ΣREE ranges from only 12 to 24% of the bulk-rock ΣREE content. Similarly, Y concentrations in Fe-oxide range from 7.2 to 15.7 μg/g (2.7-25 μg/g for individual grains), or 13 to 44% of the bulk-rock concentration.

Quartz

SEM-EDS spot analyses showed that chert bands and interstitial quartz in oxide bands range from relatively pure SiO_2 (Fe content below EDS detection) to 15.7% Fe_2O_3. This iron content likely reflects micro-inclusions of Fe-oxides that lead to the red coloring of chert bands. Quartz was assumed to have a negligible contribution to the bulk rock REE budget due to very low compatibility of REEs in fluid-precipitated quartz (Monecke et l. 2002).

Carbonates

Carbonates occur in carbonate bands, in veins, and as replacement minerals in chert bands. In all occurrences, the carbonate is classified as calcite with minor Fe. The maximum Fe content is 4.4 wt.% as measured by SEM-EDS (6.3 wt.% Fe_2O_3); six of thirty spots do not have detectable levels of Fe. Calcite in carbonate bands does not contain detectable levels of Mn, while most chert-replacing calcite contains small amounts of Mn (≤0.51 wt.%) and vein calcite contains similar amounts of Mn (≤0.57 wt.%).

REE concentrations were analyzed in calcite from carbonate bands and from veins in samples K74 and K76. Within carbonate bands, K74 and K76 have significantly different calcite trace element values: 180 μg/g ΣREE with 74 μg/g Y in K74, versus 500 μg/g ΣREE with 225 μg/g Y in K76. ΣREE (including Y) of the bulk-rock for these samples mimics this difference, resulting in calcite ΣREE concentrations that are three to six times the bulk-rock values. Calcite in veins has very low REE contents, which were not included in the REE budget calculations because concentrations are not reliably above detection limit for all REEs. The maximum ΣREE in these veins is found in a single point with 6.7 μg/g and 1.6 μg/g Y, while all other analyses contain <3 μg/g ΣREE and <1.5 μg/g Y.

Apatite

Apatite is the most common phosphate-bearing phase in the WKB, while rare xenotime grains (5 grains observed, all <5 μm) likely also contain REEs but were not analyzed or included in the REE budget calculations due to their rarity and very small size. As with the Fe-oxides, apatite major element contents are not significantly different between samples. Of note are Cl contents ≤0.027 wt.% and F contents between 1.2 and 2.4 wt.%. SiO_2 and Fe_2O_3 contents ranged

from 0 to 4.33 wt.% and 0.27 to 6.67 wt.%, respectively, likely indicating that small chert and Fe-oxide inclusions contributed to the analyzed volumes despite the use of a focused (<1 μm) beam.

REEs are far more concentrated in apatite than in the more common WKB minerals. ΣREE in individual grains range from 750 to 3270 μg/g and average concentrations for each sample range from 1450 to 3050 μg/g, or 23 to 30 times the bulk-rock concentration. Y content was similarly high, ranging from 310 to 1390 in single grains and 590 to 820 μg/g for sample averages, extending from 20 to 26 times that of the bulk rock.

6.4.3 REE Budget of the WKB

Despite its low abundance in the WKB (1.6-3.2 %), apatite hosts 36 to 75% of the bulk-rock REE content. Where present, calcite in carbonate bands is also a significant host of these elements, containing 10 to 13% of the bulk-rock REE content while constituting just 2 to 4% of the carbonate+oxide samples. Though the REE content of Fe-oxides is low, their abundance (61-82%) means they host 12 to 52% of the total REE budget of the WKB samples.

We reconstructed the bulk-rock REE patterns and concentrations of the WKB to ensure that the analyzed phases host an overwhelming majority of the REE budget. Mineralogy estimates (Table 1) were calculated based on bulk-rock major-element compositions from Basta et al. (2011). We used this method rather than estimating modal mineral abundances based on point counting in the polished section surfaces because the bulk-rock REE contents are taken from the same aliquots as the major element data, and the sample section surfaces may not be representative of the mesoband distribution and mineral abundances in the bulk rock. The mineralogy calculations assumed that all P_2O_5 is held in apatite, as this is the most abundant

observed phosphate mineral and xenotime grains are extremely rare and very small (<5 μm). All excess calcium (CaO) that is not held in apatite is presumed to be incorporated into calcite. Because CO_2 or C contents are not known for these samples, CO_2 was added to the calculation to balance all of the CaO contained in calcite. Fe-chlorite (chamosite) is assumed to contain all of the Al_2O_3 in all samples except K37, which also contains an amount of albite corresponding to the bulk-rock Na_2O content. Albite was not included in the calculation for the other three samples because it was not observed. All remaining Fe_2O_3 and SiO_2 are assigned to Fe-oxide and quartz, respectively.

The reconstructed REE budget was calculated using the calculated abundances and measured REE concentrations for each mineral. Calcite is included in the calculation for oxide+carbonate samples, but excluded for oxide+chert samples because, as noted above, vein and replacement calcite contain negligible concentrations of REEs. The results of this calculation are given in Table 3, and shale-normalized (PAAS: Post-Archean Australian Shale; McLennan 2018) REE patterns of average mineral compositions, the bulk rock, and REE budget calculations are shown in Figure 5.

The bulk-rock REE contents were reproduced within uncertainty for each sample and nearly all elements. Y contents in the carbonate+oxide samples (K74 and K76; Fig 5c,d) could not be replicated by a combination of Fe-oxides, calcite, and apatite in the estimated proportions. The bulk-rock REE patterns of carbonate+oxide samples exhibit positive Y anomalies that are greater than those in the chert+oxide samples, while the REE patterns of apatite and Fe-oxides from both sample groups are similar. Calcite also displays a positive Y anomaly, however, the abundance of calcite is not great enough to match the bulk-rock Y values. Xenotime, which generally hosts high REE content and considerably more Y than other REEs, was observed more

often in the carbonate+oxide samples than in the chert+oxide samples, and is a potential host of the missing Y in the budget for these samples.

6.5 DISCUSSION

6.5.1 Evidence of Recrystallization and Fluid Flow

Mineral textures and association

Textural observations indicated that the WKB has undergone metamorphism and post-depositional interactions with fluids. Peak metamorphic grade was no higher than greenschist facies, based on the presence of chlorite and albite and the absence of amphibole or pyroxenes, which would be characteristic of higher metamorphic grades (Klein 2005). As is common for IFs, the current mineral assemblage likely does not represent the original depositional phases (Bekker et al. 2010; Beukes 1983; Bontognali et al. 2013; Fischer and Knoll 2009; Rasmussen et al. 2014; Rasmussen et al. 2013). The WKB may have been deposited as very fine-grained precipitates of Fe-oxyhydroxides and carbonates, intermixed with amorphous silica. Dehydration of the Fe-oxyhydroxides and reduction of iron(III) to form the observed euhedral magnetite crystals occurred either during diagenesis or during a subsequent metamorphic event. Presently, partial replacement of magnetite by hematite is ubiquitous on euhedral Fe-oxide grains. This martitization process creates pseudomorphic hematite rims and hematite planes parallel to the magnetite crystal faces. This indicates that the WKB was permeated by and reacted with oxidizing fluids (Mücke and Cabral 2005) after crystallization of the euhedral magnetite.

Apatite grains generally have very irregular, anhedral forms, suggesting that they are not detrital but rather grew in place. Where apatite grains are in contact with euhedral Fe-oxide crystals outside of veins, apatite appears to grow around the Fe-oxide grains, suggesting that the

Fe-oxides were present in their euhedral forms before the crystallization of this apatite (Fig 4b,c). In addition, apatite crystals commonly engulf chert and Fe-oxide inclusions, indicating that small grains of Fe-oxide and chert were present as the apatite formed. Apatite is most common in carbonate bands, suggesting that apatite crystalized from a Ca-limited reaction with a phosphate-bearing fluid, or that the two minerals (or their precursor depositional phases) precipitated from a common fluid.

Veins

At least three suites of veins were observed with varying degrees of preservation, indicating multiple stages of fluid flow and alteration through the WKB. The earliest preserved set of veins consists of narrow (10-20 μm) relict apatite veins, common in both the chert+oxide and carbonate+oxide samples. The originally near-planar walls of these veins have been recrystallized by metamorphism, resulting in anhedral apatite grains configured like a string of beads and containing few to no inclusions (Fig 4i,j,k). Rarely, apatite is also scattered through thicker (200-300 μm) sinuous quartz veins, which appear to have experienced ductile deformation associated with metamorphism (Fig 4l). Because cross cutting relationships between these thicker quartz+apatite veins and the thin apatite veins were not observed, their relative timing of emplacement could not be determined, but due to the deformation and recrystallization of both vein sets, we assume that these were some of the first veins to form in the WKB. There is a second generation of quartz-only veins (Fig 3a,d; Si maps) that cross-cut the apatite veins and traverse the oxide and carbonate bands. Finally there is a third generation of thin calcite-bearing veins, many of which also contain apatite and albite (Fig 4d,e) and cross-cut the quartz veins, but tend not to extend through chert and carbonate bands. Development of thicker calcite veins (as in

K76, Fig 3d) and replacement of chert bands (K37, Fig 3b) may have also occurred at this stage, or at an additional later stage.

This abundance of veins indicates movement of mineral-saturated fluids through the WKB and the redistribution of fluid-mobile elements. The apatite, quartz+apatite, and small carbonate veins are not seen intruding through either the chert or carbonate bands, and thus may only reflect local transport and remobilization within individual mesobands. However, some apatite veins terminate against the carbonate bands (Fig 3d; P map), suggesting that they once extended into the carbonate bands but that vein apatite recrystallized onto rims of preexisting apatite within the carbonate bands. Thus, the nearly-pure chert mesobands may act as barriers to fluid infiltration when fractures are minimal, while oxide and possibly carbonate bands may have been sufficiently more permeable as to allow fluid transport.

Compositional Evidence

Curiously, the WKB samples with carbonate bands do not display significantly greater CaO contents or calcite abundances than the oxide facies samples, yet the REEs hosted in calcite in the carbonate-banded samples are necessary to satisfy the REE budget. This finding could be explained by late stage crystallization of low-REE calcite in veins and as chert replacement in the oxide+chert samples (Fig 3b,d). As the vein-filling calcite in K76 (Fig 3d) has very low REE concentrations, we posited that the late stage carbonates in veins do not contribute significantly to the overall REE budget of the WKB. Rather, carbonates present in calcite-dominated bands contain much higher concentrations of REEs and thus are important for reconstructing the bulk-rock REE patterns.

The WKB extends to anomalously high iron contents (62.1-82.3 wt% Fe_2O_3 for samples in this study, Basta et al. 2011) compared to Algoma-type IFs on other cratons (~28-47 wt.% Fe_2O_3, Klein 2005), as well as other Neoproterozic IFs (~45-52 wt% Fe_2O_3, Klein 2005). This may suggest an exceptionally high depositional flux of iron in the WKB marine basin, comparatively low rates of silica precipitation, or loss of silica or carbonate from the WKB after deposition. Because quartz veins are common and the chert bands in sample K37 show evidence of replacement by calcite (Fig 3b), we posit that silica was mobile in periods after the diagenesis of the IFs, and thus could be subject to removal. Leaching of silica and resulting iron enrichment has been described in the Archean IF deposits in Western Australia (Angerer et al. 2013; Duuring and Hagemann 2013; Lascelles 2006), where this process can be important for upgrading the economic quality of the deposit.

6.5.2 Origin of Significant REE hosts in the WKB

Our trace element budget reconstruction shows that a significant fraction (41-84%) of the REE content of the WKB is held in accessory phases, dominantly apatite and subordinately calcite. The origin of these phases — be they primary, diagenetic, or metamorphic — and whether or not their components originated internally or externally to the WKB are important issues for the accurate interpretation of bulk-rock REE patterns.

Apatite

Apatite in both veins and in carbonate bands in the WKB is unlikely to have originated as a detrital phase. The paleoenvironmental setting is remote from detrital inputs, consistent with the abundance of authigenic phases in the IF. This is consistent with apatite morphologies that

are very irregular and contain inclusions of Fe-oxides and chert. Additionally, Basta et al. (2011) estimated a very low fraction of detrital input to the WKB based on Al_2O_3 and Zr contents. Formation of authigenic apatite in the WKB requires a source of phosphate, though the original depositional form of the phosphorus-bearing material need not necessarily be apatite. Scavenging of dissolved phosphate by precipitating Fe-oxyhydroxides has been observed at the Juan de Fuca ridge and has been hypothesized for IFs (Feely et al. 1990; Jones et al. 2015). This process results in seawater depleted in dissolved phosphate above hydrothermal vents, and complementary deposition of phosphate-enriched particulates (Feeley et al. 1996). Thus, near-vent hydrothermal solutions can have lower phosphorus concentrations (0.09-0.31 μg/g) than modern seawater below the mixed layer (~3 μg/g) (Massoth, et al. 1989) due to scavenging on iron oxides produced within the hydrothermal system (Berner 1973). In addition, the presence of apatite nanoparticles in Archean IFs of South Africa and Western Australia indicate direct precipitation of a phosphate-bearing phase from a seawater-hydrothermal fluid mixture (Rasmussen et al. 2021b). Both adsorption and precipitation are potential mechanisms for the incorporation of phosphorus into the WKB, as the dominant iron source is interpreted to be Fe-rich hydrothermal fluids (Basta et al. 2011). This explains the incorporation of phosphorus and later apatite crystallization within oxide bands and the absence of apatite in chert bands, as chert bands represent periods with little hydrothermal flux. The original phosphate distribution is expected to be relatively homogenous throughout the oxide bands rather than concentrated in phosphate-rich patches (Fig 4a,b,c), suggesting that phosphate was mobilized within the oxide bands to create the current occurrences of apatite in patches and veins. The apatite patches and veins did not appear to have permeated the chert bands in the chert+oxide samples, suggesting that this apatite has not migrated more than a few centimeters up- or down-section from its

depositional site within the WKB. We cannot, however, rule out long-distance lateral transport within individual oxide mesobands. The apatite patches likely formed at low temperatures prior to full lithification of the WKB, as higher metamorphic grades tend to produce larger, idioblastic apatites. Also, the patches follow sinuous, sheared patterns that are not evident in the rest of the banding, perhaps tracing permeable paths or indicating soft-sediment deformation (Fig 4a).

The phosphate needed to produce significant amounts of apatite in carbonate bands in samples K74 and K76 may have been incorporated by the mechanisms above, as Fe-oxides are present within the carbonate bands, but may also have originated from co-precipitation of carbonate minerals and apatite. Such co-precipitation occurs in modern seawater upon increases in temperature, pH, or salinity, or due to addition of Ca and P (Gulbrandsen 1969). Though it is difficult to determine the specific deep marine conditions for the WKB basin in the Neoproterozoic, the high abundance of apatite in these bands suggests another mechanism in addition to scavenging by adsorption and co-precipitation on Fe-oxyhydroxides, which generates lower apatite abundances in the oxide+chert samples. Because the carbonate+oxide samples lack the apatite-rich patches found in oxide bands in the chert+oxide samples, it is likely that any phosphorus mobilized into the fluid phase encountered Ca in the carbonate bands and precipitated locally as apatite. This explains why the highest concentrations of apatite are found near the borders of carbonate bands, where phosphate originating outside the carbonate band would be sequestered.

At least two stages of apatite-bearing veins are evident in the sample suite, comprising relict apatite and quartz+apatite veins, and later calcite+apatite veins. These veins are only observed within the oxide bands in both the chert+oxide and carbonate+oxide samples, although in the carbonate+oxide samples some veins terminate against the carbonate bands. This may

show that a phosphorus-bearing fluid was released into the carbonate band from the vein fracture to form apatite, or that any apatite from veins that once cut through the carbonate bands has since been dissolved and redistributed throughout the carbonate band. The apatite distribution in chert+oxide samples suggests only local mobilization of apatite within individual oxide mesobands, while more significant redistribution of apatite and REE is possible in the carbonate+oxide samples.

Calcite

The only carbonate phase we identified in the WKB samples was calcite, though many BIFs contain Fe-carbonates such as ankerite and siderite (Fischer et al. 2009; Hagemann et al. 2016; Kaufman et al. 1990). The WKB calcites have REE contents one to two orders of magnitude greater than that of average limestones (Fig 6), indicating that this calcite did not originate from common seawater. As the bulk of the REE and Fe in the WKB likely had a common hydrothermal source (Basta et al. 2011), it is unlikely that carbonate precipitation from this fluid would incorporate only REE and exclude Fe and Mn. While calcite could be a primary precipitate, if so it likely would have formed during periods of low Fe supply and thus low REE supply, similar to the periods of chert deposition. Alternatively, we prefer a mechanism in which the carbonate bands originally precipitated from a hydrothermal Fe- and REE-bearing solution as Fe-carbonates. During a later metamorphic event, the carbonates were recrystallized to calcite as Fe was extracted to form magnetite in the oxide bands, while the REEs remained in the calcite.

In contrast, calcite in veins of the WKB, and presumably other late-stage calcite, has very low REE contents, lower than average limestone and almost three orders of magnitude lower than in the calcite in WKB carbonate bands (Fig 6). This shows that the vein calcite did not

originate from hydrothermal solutions or directly from seawater, but rather was likely transported in veins from a source outside of the WKB. Because this vein-forming calcite has very low trace element contents, it does not significantly contribute to the REE budget and does not noticeably alter the REE patterns of the WKB.

6.5.3 Incorporation of REEs into the WKB

The REE patterns of apatite, magnetite, and calcite, and consequently the bulk rock, are roughly parallel, with the exception of positive Y anomalies in calcite and the bulk rock. This suggests that the REEs in all minerals were derived from the same source, likely a hydrothermal solution, as recognized by Basta et al. (2011). The association of apatite with oxide bands in the chert-banded samples also indicates a common hydrothermal source for Fe, P, and REE.

Studies indicate that REEs readily adsorb onto the surface of precipitating Fe-oxyhydroxide particles in seawater (Bau 1999; Ohta and Kawabe 2001; Quinn et al. 2004; Schijf et al. 2015), a similar mechanism to the incorporation of phosphorus into oxide bands. In addition, V may be scavenged by precipitating Fe-oxyhydroxide particles (Trefty and Metz 1989) and bulk-rock V concentration in the WKB (30-70 μg/g) is positively correlated with Fe_2O_3 content (Basta et al. 2011). This further supports an adsorption origin for incorporation of REEs and thus a common source for Fe and REEs. Thus REE ions are deposited together with the chemical sediment but not initially contained within a crystal structure. If a fraction of the apatite in carbonate bands was directly precipitated, it is probable that this occurred as co-precipitation of an iron-bearing carbonate and apatite from a hydrothermal solution, with the same REE source as the adsorbed REEs.

Experimental studies of adsorption processes indicate that Fe-oxyhydroxides have a lower affinity for LREE and Y than for MREE and HREE (Bau 1999; Quinn et al. 2004), and thus the patterns of REE abundance that are deposited into BIFs should not be expected to record the composition of seawater in the same proportion for each element. This could explain the slight enrichment of HREE over LREE in the WKB and should be accounted for in reconstructions of the IF sources, as the adsorption process will bias conclusions toward greater proportions of seawater.

6.5.4 Implications for bulk-rock REE patterns

In the WKB samples, 52 to 75% of the REE budget is hosted in apatite and calcite, though these minerals combined make up less than 8% of the rock. Because REEs are fluid mobile and the samples show evidence of apatite and calcite mobility in veins, this raises the question of whether bulk-rock REE patterns in the WKB (and IFs at large) record the original depositional REE contents and patterns. In the WKB, it is likely that chert+oxide samples largely retain their original REE patterns because apatite appears to remain within the original oxide bands, whereas both phosphorus and REEs were deposited along with precipitating Fe-oxyhydroxides. However, there is the potential for loss or introduction of REE-bearing fluids through fractures in the chert bands or locations where these bands pinch out laterally. The reliability of REE patterns in the carbonate+oxide samples is less certain, because apatite appears to have been introduced, at least in part, to the carbonate bands, showing that these bands are permeable to fluids during metamorphism. Though the bulk-rock REE contents in the carbonate+oxide samples are higher than in samples with chert bands, their general features (Eu and Ce anomalies, LREE/HREE) are similar, suggesting that the mobilization of apatite, calcite,

and REE has not significantly altered the bulk-rock REE patterns. Additionally, the REE patterns of apatite and Fe-oxides are roughly parallel, indicating that they record deposition from approximately the same source. Had metamorphism significantly affected the REE patterns of apatite, a discrepancy between the more mobile apatite and relatively refractory Fe-oxides would be expected.

Our study highlights that REEs are strongly enriched in easily mobilized accessory phases compared to common IF-forming minerals, which could be problematic for interpretations based on REE patterns. The Neoproterozoic WKB is part of the youngest global IF-forming episode and has experienced comparatively mild metamorphic conditions, whereas many older or more intensely metamorphosed IFs may have greater degrees of REE redistribution, loss, or gain. In addition, the Neoproterozoic Rapitan-type IFs tend to have high phosphate contents (up to 3 wt.%; Klein 2005) compared to the WKB (0.2-1.3 wt.%; Basta et al. 2011), both of which have greater phosphate concentrations than do Paleoproterozoic and Archean IFs (typically <0.5 wt.%; Klein 2005). High-phosphate IFs with common apatite may have a greater potential for REE reconfiguration at the same metamorphic grade compared to low-phosphate IFs. Moreover, carbonate facies IF —dominated by Fe-carbonates rather than Fe-oxides and not observed in the WKB— may have greater potential for REE redistribution than oxide facies IF. Common Fe-carbonates (e.g. ankerite and siderite) are more readily mobilized than Fe-oxides during metamorphism (Hu et al. 2020), and are potential hosts of significant REEs (Bolhar et al. 2005; Rong et al. 2020).

The effect of metamorphism on the REE patterns of IFs is not easily predictable. The fluid mobility of REE and the differential mobility of LREE and HREE are both dependent on the specific composition, temperature, and pH of the metamorphic fluid. Thus, both leaching and

enrichment of REEs are possible (Hetherington et al. 2010). Apatite is a likely host of REEs in many IFs, as phosphate and fluoride are both effective ligands for maintaining REEs in solution (Giere 1990). LREEs are slightly more compatible in apatite crystallized during metasomatic alteration than are HREEs (Ayers and Watson 1993; Exley 1980) so the removal of apatite will result in a depletion of LREEs in the BIF bulk-rock, or an increase in LREEs if apatite is added to the IF in veins.

The potential for redistribution of REEs in IFs through a few low abundance mineral phases indicates that detailed investigation of mineral associations are essential prior to the use of bulk-rock REE patterns for source interpretation. Careful consideration of the dominant REE mineral hosts and their origins, indicated by microtextures and chemistry, is valuable before drawing accurate inferences of the proportions of Fe and Si from different sources or of marine oxidation states. Source or redox interpretations made without consideration of host phases should be treated with caution.

6.6 CONCLUSIONS

Samples from the Wadi Karim BIF contain accessory phases—apatite and calcite—that host high concentrations of REEs. A combination of REE concentrations in Fe-oxides, apatite, and calcite in their estimated abundances largely reproduces the REE patterns of the bulk rock. However, apatite and calcite are also commonly found in veins or with textures and compositions that suggest they have been mobilized and/or recrystallized after deposition. Because interpretations based on REE patterns rely on the preservation of the original depositional REE pattern of the IF, this process can complicate interpretation of the recorded chemical signatures. Within the WKB, apatite does not appear to easily move through chert

mesobands, indicating that the original REE signatures in chert+oxide samples may have been maintained, whereas carbonate+oxide samples would have had a greater potential for alteration of REE patterns due to apatite and carbonate mobilization and recrystallization. As REEs are likely hosted in apatite, calcite, and possibly additional accessory phases in other IFs, the potential for REE pattern alteration in these unique and enigmatic lithotypes is widespread, particularly for high-phosphate or strongly metamorphosed deposits. Thus a detailed understanding of microtextures and mineral compositions will be valuable for making more accurate paleoenvironmental interpretations based on bulk-rock REE patterns in IFs.

6.7 Acknowledgements

We thank Nathan Dalleska, Jade Star Lackey, and Kyle McCarty for assistance with LA-ICPMS work, Yunbin Guan for operating the SIMS, and Chi Ma for help with the EPMA and SEM.

6.8 References Cited

Abd El-Rahman Y, Gutzmer J, Li X-H, Seifert T, Li C-F, Ling X-X, Li J (2020) Not all Neoproterozoic iron formations are glaciogenic: Sturtian-aged non-Rapitan exhalative iron formations from the Arabian–Nubian Shield. Mineralium Deposita 55(3):577-596

Ague JJ (2017) Element mobility during regional metamorphism in crustal and subduction zone environments with a focus on the rare earth elements (REE). American Mineralogist 102(9):1796-1821

Ali KA, Stern RJ, Manton WI, Johnson PR, Mukherjee SK (2010) Neoproterozoic diamictite in the Eastern Desert of Egypt and Northern Saudi Arabia: evidence of~ 750 Ma glaciation in the Arabian–Nubian Shield? International Journal of Earth Sciences 99(4):705-726

Angerer T, Hagemann SG, Danyushevsky L (2013) High-grade iron ore at Windarling, Yilgarn Craton: a product of syn-orogenic deformation, hypogene hydrothermal alteration and supergene modification in an Archean BIF-basalt lithostratigraphy. Mineralium Deposita 48(6):697-728

Armstrong JT (1995) Citzaf-a package of correction programs for the quantitative Electron Microbeam X-Ray-Analysis of thick polished materials, thin-films, and particles. Microbeam Analysis 4(3):177-200

Avigad D, Stern R, Beyth M, Miller N, McWilliams M (2007) Detrital zircon U–Pb geochronology of Cryogenian diamictites and Lower Paleozoic sandstone in Ethiopia (Tigrai): age constraints on Neoproterozoic glaciation and crustal evolution of the southern Arabian–Nubian Shield. Precambrian Research 154(1-2):88-106

Ayers JC, Watson EB (1993) Apatite/fluid partitioning of rare-earth elements and strontium: Experimental results at 1.0 GPa and 1000 C and application to models of fluid-rock interaction. Chemical Geology 110(1-3):299-314

Baldwin GJ, Turner EC, Kamber BS (2012) A new depositional model for glaciogenic Neoproterozoic iron formation: insights from the chemostratigraphy and basin configuration of the Rapitan iron formation. Canadian Journal of Earth Sciences 49(2):455-476

Basta FF, Maurice AE, Fontboté L, Favarger P-Y (2011) Petrology and geochemistry of the banded iron formation (BIF) of Wadi Karim and Um Anab, Eastern Desert, Egypt: implications for the origin of Neoproterozoic BIF. Precambrian Research 187(3-4):277-292

Bau M (1999) Scavenging of dissolved yttrium and rare earths by precipitating iron oxyhydroxide: experimental evidence for Ce oxidation, Y-Ho fractionation, and lanthanide tetrad effect. Geochimica et Cosmochimica Acta 63(1):67-77

Bau M, Dulski P, Moeller P (1995) Yttrium and holmium in South Pacific seawater: vertical distribution and possible fractionation mechanisms. Chem Erde 55(1):1

Bekker A, Slack JF, Planavsky N, Krapez B, Hofmann A, Konhauser KO, Rouxel OJ (2010) Iron formation: the sedimentary product of a complex interplay among mantle, tectonic, oceanic, and biospheric processes. Economic Geology 105(3):467-508

Berner RA (1973) Phosphate removal from sea water by adsorption on volcanogenic ferric oxides. Earth and Planetary Science Letters 18(1):77-86

Beukes N (1973) Precambrian iron-formations of southern Africa. Economic Geology 68(7):960-1004

Beukes N (1983) Palaeoenvironmental setting of iron-formations in the depositional basin of the Transvaal Supergroup, South Africa. In: Developments in Precambrian Geology, vol 6. Elsevier, pp 131-198

Bolhar R, Kamber BS, Moorbath S, Fedo CM, Whitehouse MJ (2004) Characterisation of early Archaean chemical sediments by trace element signatures. Earth and Planetary Science Letters 222(1):43-60 doi:https://doi.org/10.1016/j.epsl.2004.02.016

Bolhar R, Van Kranendonk MJ, Kamber BS (2005) A trace element study of siderite–jasper banded iron formation in the 3.45 Ga Warrawoona Group, Pilbara Craton—formation from hydrothermal fluids and shallow seawater. Precambrian Research 137(1-2):93-114

Bonnand P, Lalonde S, Boyet M, Heubeck C, Homann M, Nonnotte P, Foster I, Konhauser K, Köhler I (2020) Post-depositional REE mobility in a Paleoarchean banded iron formation revealed by La-Ce geochronology: A cautionary tale for signals of ancient oxygenation. Earth and Planetary Science Letters 547:116452

Bontognali TR, Fischer WW, Föllmi KB (2013) Siliciclastic associated banded iron formation from the 3.2 Ga Moodies group, Barberton greenstone belt, South Africa. Precambrian Research 226:116-124

Chew DM, Babechuk MG, Cogné N, Mark C, O'Sullivan GJ, Henrichs IA, Doepke D, McKenna CA (2016) (LA,Q)-ICPMS trace-element analyses of Durango and McClure Mountain apatite and implications for making natural LA-ICPMS mineral standards. Chemical Geology 435:35-48 doi:https://doi.org/10.1016/j.chemgeo.2016.03.028

Danielson A, Möller P, Dulski P (1992) The europium anomalies in banded iron formations and the thermal history of the oceanic crust. Chemical Geology 97(1-2):89-100

Derry LA, Jacobsen SB (1990) The chemical evolution of Precambrian seawater: evidence from REEs in banded iron formations. Geochimica et Cosmochimica Acta 54(11):2965-2977

Douville E, Bienvenu P, Charlou JL, Donval JP, Fouquet Y, Appriou P, Gamo T (1999) Yttrium and rare earth elements in fluids from various deep-sea hydrothermal systems. Geochimica et Cosmochimica Acta 63(5):627-643

Duuring P, Hagemann S (2013) Leaching of silica bands and concentration of magnetite in Archean BIF by hypogene fluids: Beebyn Fe ore deposit, Yilgarn Craton, Western Australia. Mineralium Deposita 48(3):341-370

El-Habaak GH (2021) Banded Iron Formation in the Egyptian Nubian Shield. In: The Geology of the Egyptian Nubian Shield, vol. Springer, pp 425-486

Exley R (1980) Microprobe studies of REE-rich accessory minerals: implications for Skye granite petrogenesis and REE mobility in hydrothermal systems. Earth and Planetary Science Letters 48(1):97-110

Feely R, Baker E, Marumo K, Urabe T, Ishibashi J, Gendron J, Lebon G, Okamura K (1996) Hydrothermal plume particles and dissolved phosphate over the superfast-spreading southern East Pacific Rise. Geochimica et Cosmochimica Acta 60(13):2297-2323

Feely RA, Massoth GJ, Baker ET, Cowen JP, Lamb MF, Krogslund KA (1990) The effect of hydrothermal processes on midwater phosphorus distributions in the northeast Pacific. Earth and Planetary Science Letters 96(3-4):305-318

Fischer WW, Knoll AH (2009) An iron shuttle for deepwater silica in Late Archean and early Paleoproterozoic iron formation. Geological Society of America Bulletin 121(1-2):222-235

Fischer WW, Schroeder S, Lacassie JP, Beukes NJ, Goldberg T, Strauss H, Horstmann UE, Schrag DP, Knoll A (2009) Isotopic constraints on the Late Archean carbon cycle from the Transvaal Supergroup along the western margin of the Kaapvaal Craton, South Africa. Precambrian Research 169(1-4):15-27

Frei R, Gaucher C, Stolper D, Canfield DE (2013) Fluctuations in late Neoproterozoic atmospheric oxidation—Cr isotope chemostratigraphy and iron speciation of the late Ediacaran lower Arroyo del Soldado Group (Uruguay). Gondwana Research 23(2):797-811

Frei R, Polat A (2007) Source heterogeneity for the major components of~ 3.7 Ga Banded Iron Formations (Isua Greenstone Belt, Western Greenland): tracing the nature of interacting water masses in BIF formation. Earth and Planetary Science Letters 253(1-2):266-281

Gaucher C, Sial AN, Blanco G, Sprechmann P (2004) Chemostratigraphy of the lower Arroyo del Soldado Group (Vendian, Uruguay) and palaeoclimatic implications. Gondwana Research 7(3):715-730

Gaucher C, Sial AN, Frei R (2015) Chemostratigraphy of Neoproterozoic banded iron formation (BIF): types, age and origin. In: Chemostratigraphy, vol. Elsevier, pp 433-449

Giere R (1990) Hydrothermal mobility of Ti, Zr and REE: examples from the Bergell and Adamello contact aureoles (Italy). Terra nova 2(1):60-67

Gourcerol B, Thurston P, Kontak D, Côté-Mantha O, Biczok J (2016) Depositional setting of Algoma-type banded iron formation. Precambrian Research 281:47-79

Gruau G, Tourpin S, Fourcade S, Blais S (1992) Loss of isotopic (Nd, O) and chemical (REE) memory during metamorphism of komatiites: new evidence from eastern Finland. Contributions to Mineralogy and Petrology 112(1):66-82

Gulbrandsen R (1969) Physical and chemical factors in the formation of marine apatite. Economic Geology 64(4):365-382

Gumsley AP, Chamberlain KR, Bleeker W, Söderlund U, de Kock MO, Larsson ER, Bekker A (2017) Timing and tempo of the Great Oxidation Event. Proceedings of the National Academy of Sciences 114(8):1811-1816

Hagemann S, Angerer T, Duuring P, Rosière C, e Silva RF, Lobato L, Hensler A, Walde D (2016) BIF-hosted iron mineral system: a review. Ore Geology Reviews 76:317-359

Haskin LA, Wildeman TR, Frey FA, Collins KA, Keedy CR, Haskin MA (1966) Rare earths in sediments. Journal of Geophysical Research 71(24):6091-6105

Hetherington CJ, Harlov DE, Budzyń B (2010) Experimental metasomatism of monazite and xenotime: mineral stability, REE mobility and fluid composition. Mineralogy and Petrology 99(3):165-184

Hoffman PF, Kaufman AJ, Halverson GP, Schrag DP (1998) A Neoproterozoic snowball earth. Science 281(5381):1342-1346

Hoffman PF, Schrag DP (2002) The snowball Earth hypothesis: testing the limits of global change. Terra nova 14(3):129-155

Holland HD (2002) Volcanic gases, black smokers, and the Great Oxidation Event. Geochimica et Cosmochimica acta 66(21):3811-3826

Hu J, Wang H, Tan J (2020) Fe and C isotopes constrain the pathways of hematite and Fe–rich carbonates formation in the Late Neoproterozoic Dahongliutan BIF, NW China. Ore Geology Reviews 121:103485

Ilyin A (2009) Neoproterozoic banded iron formations. Lithology and Mineral Resources 44(1):78-86

Jacobsen SB, Pimentel-Klose MR (1988) A Nd isotopic study of the Hamersley and Michipicoten banded iron formations: the source of REE and Fe in Archean oceans. Earth and Planetary Science Letters 87(1-2):29-44

James HL (1983) Distribution of banded iron-formation in space and time. In: Developments in Precambrian geology, vol 6. Elsevier, pp 471-490

Jochum KP, Garbe-Schönberg D, Veter M, Stoll B, Weis U, Weber M, Lugli F, Jentzen A, Schiebel R, Wassenburg JA (2019) Nano-powdered calcium carbonate reference materials: Significant progress for microanalysis? Geostandards and Geoanalytical Research 43(4):595-609

Kasting JF (2001) The rise of atmospheric oxygen. Science 293(5531):819-820

Kaufman AJ, Hayes JM, Klein C (1990) Primary and diagenetic controls of isotopic compositions of iron-formation carbonates. Geochimica et Cosmochimica Acta 54(12):3461-3473

Khan R, Naqvi S (1996) Geology, geochemistry and genesis of BIF of Kushtagi schist belt, Archaean Dharwar Craton, India. Mineralium Deposita 31(1-2):123-133

Kirschvink JL (1992) Late Proterozoic low-latitude global glaciation: the snowball Earth.

Klein C (2005) Some Precambrian banded iron-formations (BIFs) from around the world: Their age, geologic setting, mineralogy, metamorphism, geochemistry, and origins. American Mineralogist 90(10):1473-1499

Klinkhammer G, Elderfield H, Hudson A (1983) Rare earth elements in seawater near hydrothermal vents. Nature 305(5931):185-188

Lan C, Yang AY, Wang C, Zhao T (2019) Geochemistry, U-Pb zircon geochronology and Sm-Nd isotopes of the Xincai banded iron formation in the southern margin of the North China Craton: implications on Neoarchean seawater compositions and solute sources. Precambrian Research 326:240-257

Lascelles DF (2006) The Mount Gibson banded iron formation-hosted magnetite deposit: two distinct processes for the origin of high-grade iron ore. Economic Geology 101(3):651-666

Massoth G, Butterfield D, Lupton J, McDuff R, Lilley M, Jonasson I (1989) Submarine venting of phase-separated hydrothermal fluids at Axial Volcano, Juan de Fuca Ridge. Nature 340(6236):702-705

Maurice A (2006) Petrology and geochemistry of the banded iron-formation of some localities in the Eastern and Western Deserts of Egypt. Unpubl PhD thesis, Cairo University, Egypt

McLennan SM (2018) Rare earth elements in sedimentary rocks: influence of provenance and sedimentary processes. Geochemistry and mineralogy of rare earth elements:169-200

Michard A, Michard G, Stüben D, Stoffers P, Cheminée J-L, Binard N (1993) Submarine thermal springs associated with young volcanoes: The Teahitia vents, Society Islands, Pacific Ocean. Geochimica et Cosmochimica Acta 57(21-22):4977-4986

Mischel SA, Mertz-Kraus R, Jochum KP, Scholz D (2017) TERMITE: An R script for fast reduction of laser ablation inductively coupled plasma mass spectrometry data and its application to trace element measurements. Rapid Communications in Mass Spectrometry 31(13):1079-1087

Monecke T, Kempe U, Götze J (2002) Genetic significance of the trace element content in metamorphic and hydrothermal quartz: a reconnaissance study. Earth and Planetary Science Letters 202(3-4):709-724

Mücke A, Cabral AR (2005) Redox and nonredox reactions of magnetite and hematite in rocks. Geochemistry 65(3):271-278

Nadoll P, Koenig AE (2011) LA-ICP-MS of magnetite: methods and reference materials. Journal of Analytical Atomic Spectrometry 26(9):1872-1877

Nielsen RL, Gallahan WE, Newberger F (1992) Experimentally determined mineral-melt partition coefficients for Sc, Y and REE for olivine, orthopyroxene, pigeonite, magnetite and ilmenite. Contributions to Mineralogy and Petrology 110(4):488-499

Ohta A, Kawabe I (2001) REE (III) adsorption onto Mn dioxide (δ-MnO2) and Fe oxyhydroxide: Ce (III) oxidation by δ-MnO2. Geochimica et Cosmochimica Acta 65(5):695-703

Pang J, Zheng D, Ma Y, Wang Y, Wu Y, Wan J, Yu J, Li Y, Wang Y (2017) Combined apatite fission-track dating, chlorine and REE content analysis by LA-ICPMS. Science Bulletin 62(22):1497-1500

Paton C, Hellstrom J, Paul B, Woodhead J, Hergt J (2011) Iolite: Freeware for the visualisation and processing of mass spectrometric data. Journal of Analytical Atomic Spectrometry 26(12):2508-2518

Paul PP, Chakraborty PP, Shiraishi F, Das K, Kamei A, Bhattacharya S (2020) Clue on ocean redox condition from trace element and rare earth element (REE) composition of iron formation and carbonate rocks from the late Paleoproterozoic Morar Formation, Gwalior Group, central India. Journal of Mineralogical and Petrological Sciences 115(2):175-191

Quinn KA, Byrne RH, Schijf J (2004) Comparative scavenging of yttrium and the rare earth elements in seawater: competitive influences of solution and surface chemistry. Aquatic Geochemistry 10(1):59-80

Rasmussen B, Krapež B, Meier DB (2014) Replacement origin for hematite in 2.5 Ga banded iron formation: Evidence for postdepositional oxidation of iron-bearing minerals. Bulletin 126(3-4):438-446

Rasmussen B, Meier DB, Krapež B, Muhling JR (2013) Iron silicate microgranules as precursor sediments to 2.5-billion-year-old banded iron formations. Geology 41(4):435-438

Rasmussen B, Muhling JR, Fischer WW (2019) Evidence from laminated chert in banded iron formations for deposition by gravitational settling of iron-silicate muds. Geology 47(2):167-170

Rasmussen B, Muhling J, Krapež B (2021a) Greenalite and its role in the genesis of early Precambrian iron formations–A review. Earth-Science Reviews:103613

Rasmussen B, Muhling JR, Suvorova A, Fischer WW (2021b) Apatite nanoparticles in 3.46–2.46 Ga iron formations: Evidence for phosphorus-rich hydrothermal plumes on early Earth. Geology

Rohstoffe FK (1963) Iron ore project, Kosseir (Upper Egypt): Main survey, first phase. Unpublished report. Geological Survey of Egypt

Rong H, Jiao Y, Liu X, Wu L, Jia J, Cao M (2020) Effects of basic intrusions on REE mobility of sandstones and their geological significance: A case study from the Qianjiadian sandstone-hosted uranium deposit in the Songliao Basin. Applied Geochemistry 120:104665

Schijf J, Christenson EA, Byrne RH (2015) YREE scavenging in seawater: A new look at an old model. Marine Chemistry 177:460-471

Sial AN, Campos MS, Gaucher C, Frei R, Ferreira VP, Nascimento RC, Pimentel MM, Pereira NS, Rodler A (2015) Algoma-type Neoproterozoic BIFs and related marbles in the Seridó Belt (NE Brazil): REE, C, O, Cr and Sr isotope evidence. Journal of South American Earth Sciences 61:33-52

Stern RJ, Hedge CE (1985) Geochronologic and isotopic constraints on late Precambrian crustal evolution in the Eastern Desert of Egypt. American Journal of Science 285(2):97-127

Stern RJ, Mukherjee SK, Miller NR, Ali K, Johnson PR (2013) ~ 750 Ma banded iron formation from the Arabian-Nubian Shield—Implications for understanding neoproterozoic tectonics, volcanism, and climate change. Precambrian Research 239:79-94

Tanaka K, Kawabe I (2006) REE abundances in ancient seawater inferred from marine limestone and experimental REE partition coefficients between calcite and aqueous solution. Geochemical Journal 40(5):425-435

Trefry JH, Metz S (1989) Role of hydrothermal precipitates in the geochemical cycling of vanadium. Nature 342(6249):531-533

Trendall A (2002) The significance of iron-formation in the Precambrian stratigraphic record. Precambrian sedimentary environments: A modern approach to ancient depositional systems:33-66

Viehmann S, Bau M, Hoffmann JE, Münker C (2015) Geochemistry of the Krivoy Rog Banded Iron Formation, Ukraine, and the impact of peak episodes of increased global magmatic activity on the trace element composition of Precambrian seawater. Precambrian Research 270:165-180

6.9 Figures and captions

Figure 1

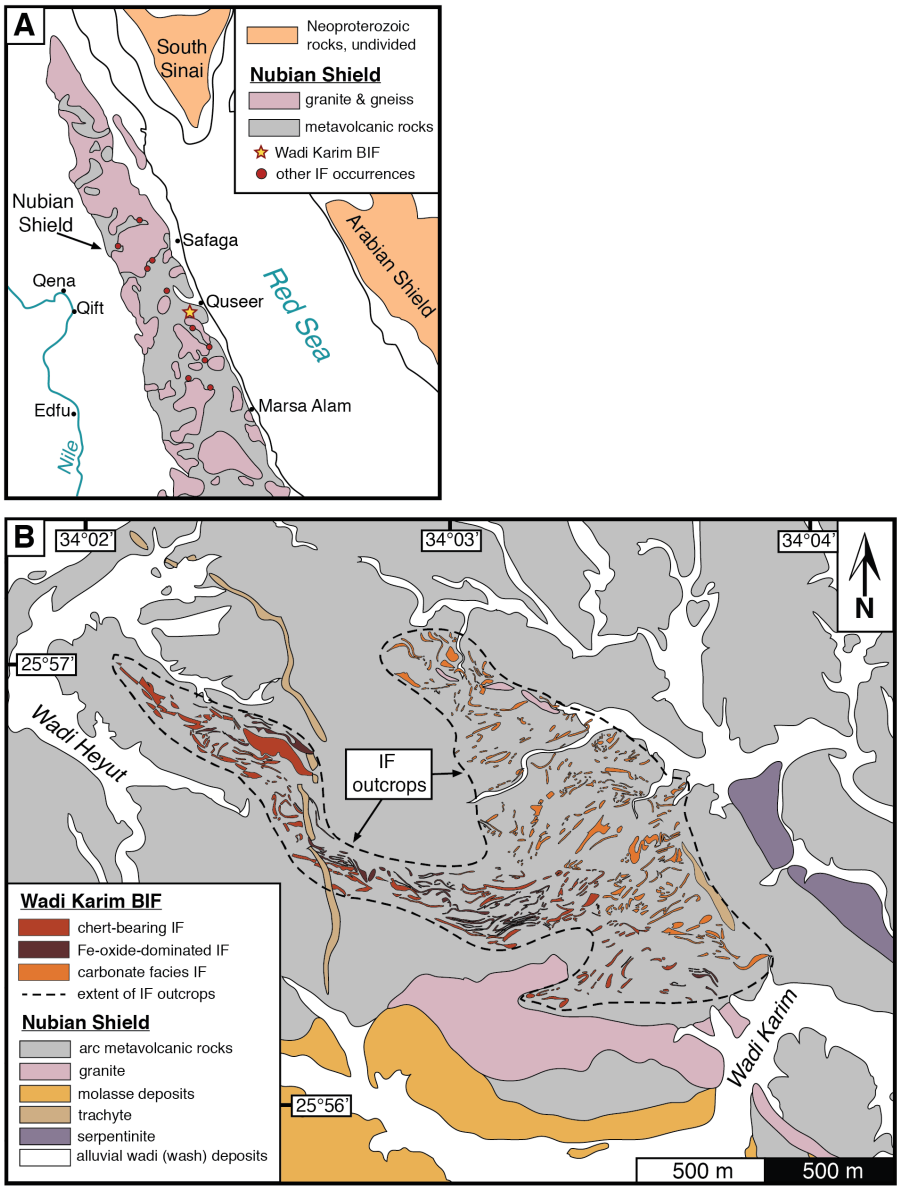

Figure 1 Map of the Wadi Karim BIF and surrounding areas. **a** Overview map showing the location of the WKB within the Arabian-Nubian Shield, as well as the locations of other IFs in the Eastern Desert, Egypt. **b** Map of exposures within the WKB, including interbedded arc metavolcanic lithologies. Samples in this study are from the chert-bearing and carbonate-bearing IF units. Maps are modified from Maurice (2006), Basta et al. (2011), Stern and Hedge (1985), and Rohstoffe (1963).

Figure 2

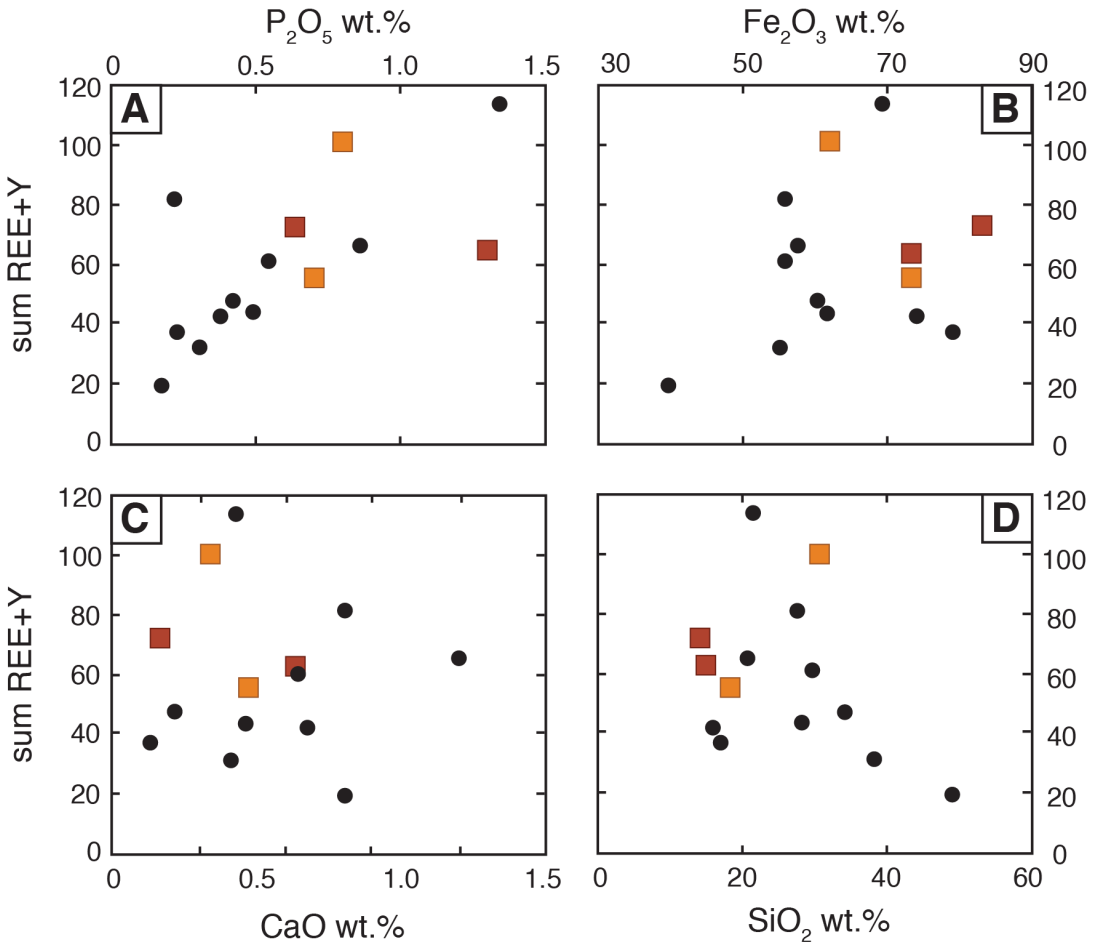

Figure 2 Selected major oxide compositions and REE contents of bulk-rock WKB samples. Red squares denote oxide+chert samples (K18, K37) and orange squares are the oxide+carbonate samples (K74, K76). Black points represent other samples from the WKB that are not included in this study. Plots of REE versus **a** P_2O_5, **b** Fe_2O_3, **c** CaO, and **d** SiO_2. Panels **b**, **c**, and **d** do not show a correlation between the oxide and REE. The rough positive correlation in panel **a** between P_2O_5 and REE suggest that these elements are present in the same minerals, bands, or other correlated areas within the samples. Compositional data are from Basta et al. (2011).

Figure 3

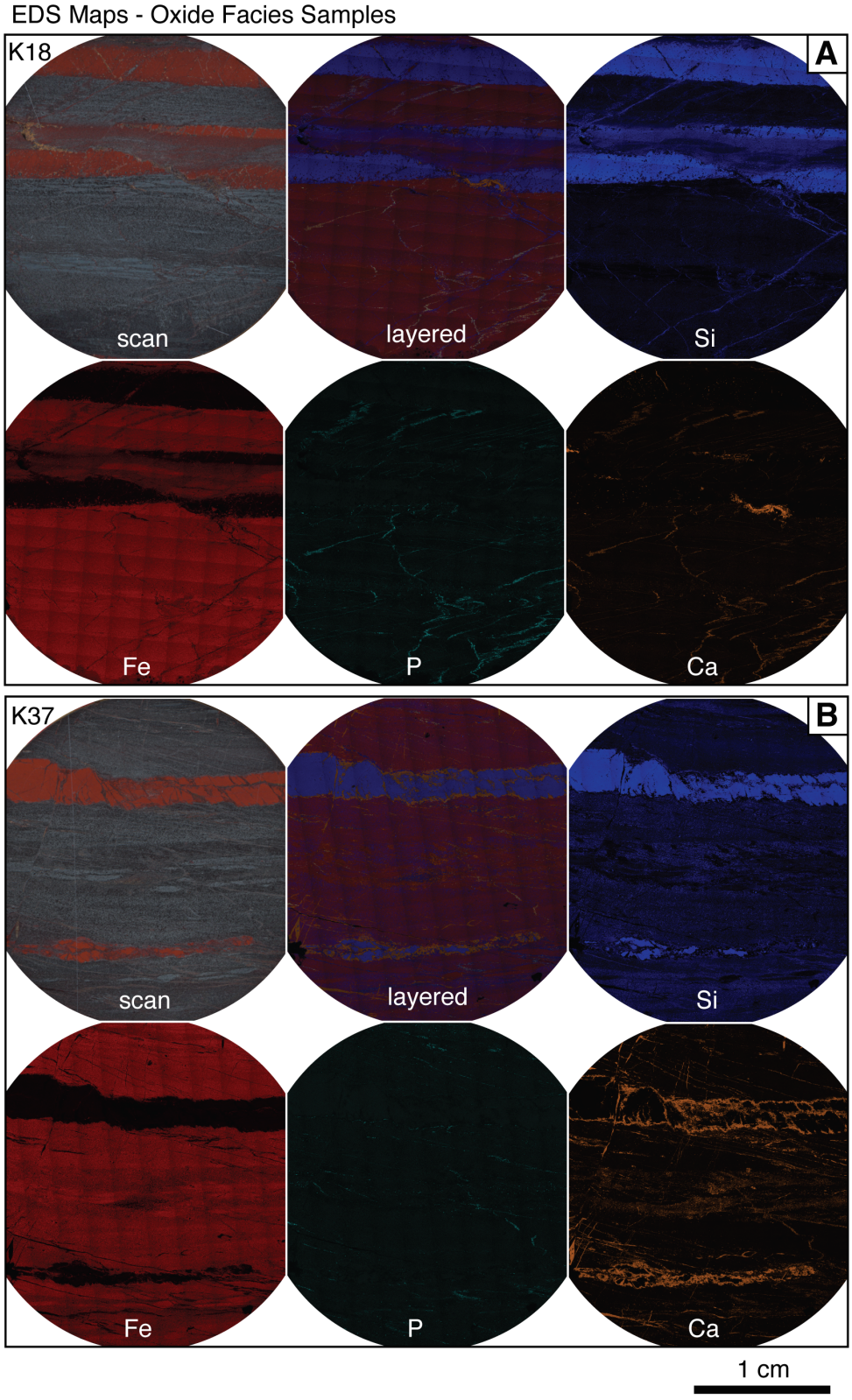
EDS Maps - Oxide Facies Samples
K18
A
scan
layered
Si
Fe
P
Ca
K37
B
scan
layered
Si
Fe
P
Ca
1 cm

Figure 3 (cont.)

EDS Maps - Carbonate Facies Samples

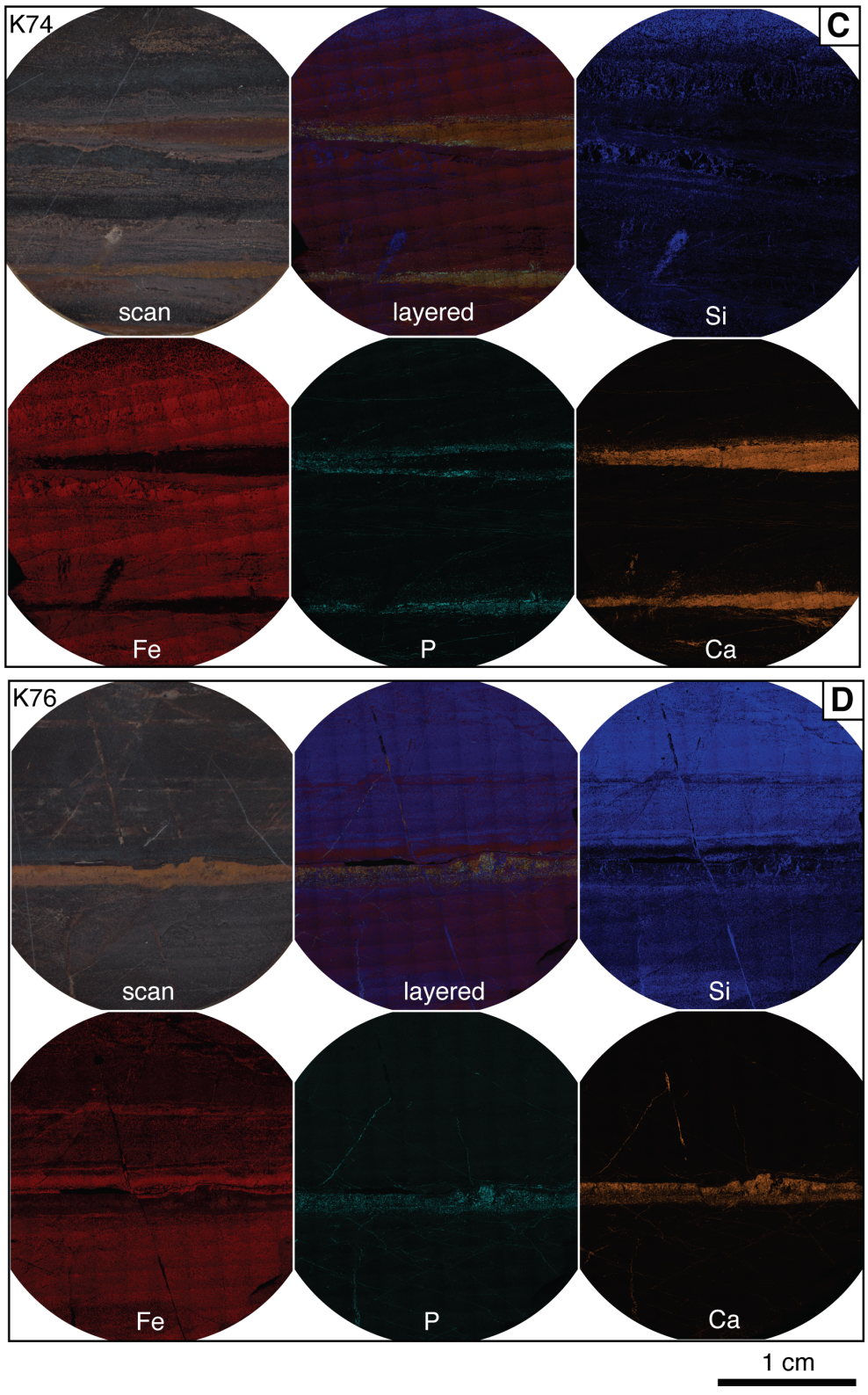

Figure 3 SEM-EDS element maps of 1 inch round sections of each sample. **a** K18 and **b** K37 contain both oxide and chert bands. Though K37 contains a significant amount of calcite that has crystallized in veins or infiltrated along the edges of the chert bands, distinct bands of carbonates that represent depositional bedding are absent. **c** K74 and **d** K76 contain both carbonate (calcite-dominated) bands and oxide bands with interstitial chert. Apatite is most apparent in the P panels, while calcite is recognized by bright locations in the Ca maps with an absence of P.

Figure 4

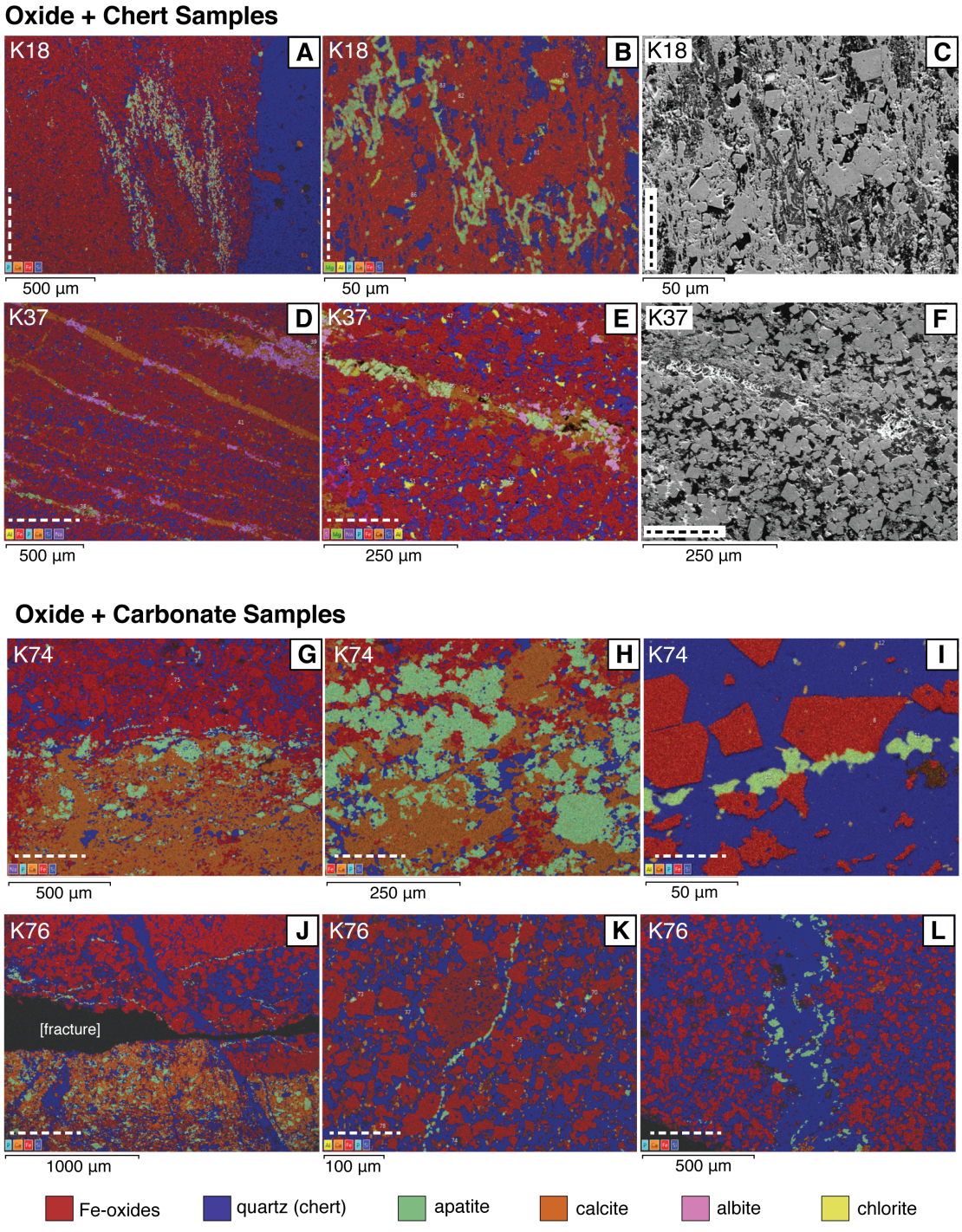
Oxide + Chert Samples
K18
A
500 µm
K18
B
50 µm
K18
C
50 µm
K37
D
500 µm
K37
E
250 µm
K37
F
250 µm
Oxide + Carbonate Samples
K74
G
500 µm
K74
H
250 µm
K74
I
50 µm
K76
J
[fracture]
1000 µm
K76
K
100 µm
K76
L
500 µm
Fe-oxides
quartz (chert)
apatite
calcite
albite
chlorite

Figure 4 High magnification SEM-EDS element maps (a,b,d,e,g-l) and SE images (c,f) of selected detailed areas. Note that the dashed white lines in each panel indicate the orientation of banding, and different scale bars are indicated for each panel. **a** Apatite-rich patch in an oxide band in K18, near the boundary between a chert band and oxide band. **b** Apatite-rich patch in oxide band in K18, showing both euhedral and mesh-textured Fe-oxides. **c** SE image of the same area as in b, showing the contrast between the euhedral and mesh-textured Fe-oxides. **d** Calcite, apatite, and albite veins through an oxide band in K37. **e** Detail of one of the composite veins in K37, and chert and Fe-oxide textures within the oxide band. **f** SE image of the same area as in e, highlighting euhedral Fe-oxides with interstitial chert. **g** Boundary between oxide and carbonate band in K74, showing the abundance of apatite within the carbonate near the boundary with the oxide band. **h** Apatite and carbonate morphologies within a carbonate band in K74. **i** Relict apatite vein through an oxide band in K74 showing the "string of beads" texture that is common to apatite veins in the WKB. **j** Boundary between oxide and carbonate bands in K76, separated by void space caused by a fracture (black area). A blocky textured oxide microband is visible at the very top of the image. Apatite veins are common in the oxide band but absent from the carbonate band, and a quartz vein cuts through both mesobands. **k** Relict apatite vein in an oxide band of K76 that is deflected around a large Fe-oxide grain with abundant quartz inclusions. **l** Sinuous quartz and apatite vein through a chert-dominated section of an oxide band in K76.

Figure 5

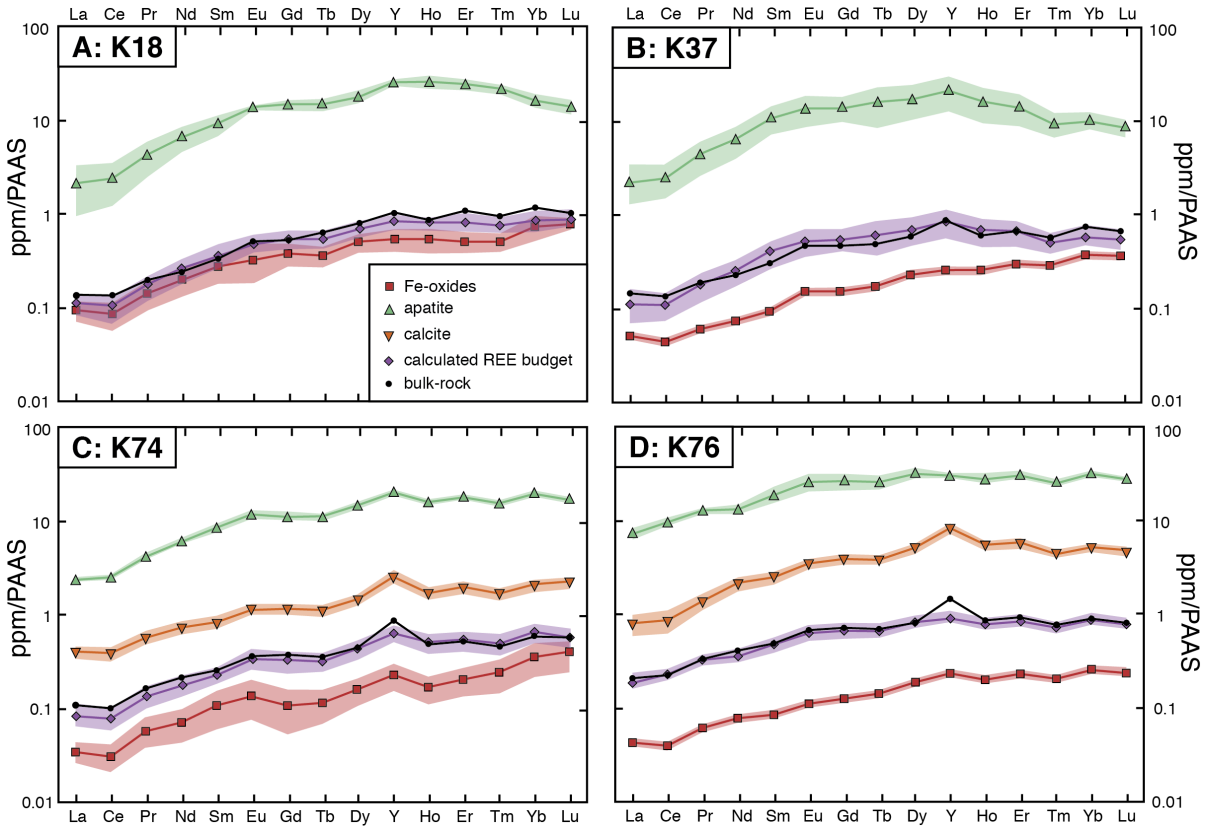

Figure 5 PAAS-normalized (McLennan 2018) REE pattern budget reconstructions of the WKB samples **a** chert+oxide sample K18, **b** chert+oxide sample K37, **c** carbonate+oxide sample K74, and **d** carbonate+oxide sample K76. Apatite in all panels, Fe-oxides in panels a and c, and calcite in panels c and d are averages of all analyses within each sample (n=4-13, Table 3), and error envelopes are 2SE. Fe-oxide compositions in panels b and d are measurements of Fe-oxide separates from Maurice (2006), and bulk-rock analyses are from Basta et al. (2011). Plots showing all individual point analyses from this study are included in Supplementary Figure 1.

Figure 6

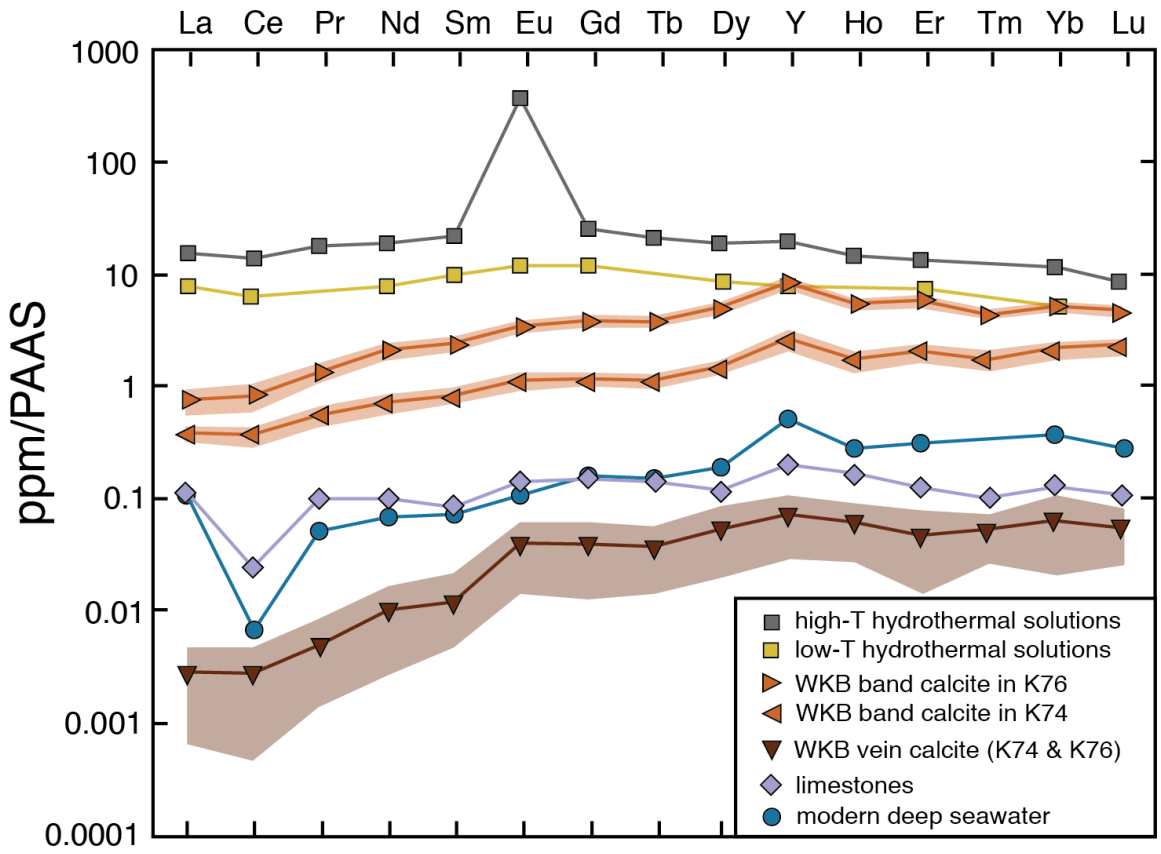

Figure 6 Comparison of average REE in calcite bands and veins from the WKB, as well as average seawater (Bau et al. 1995; Douville et al. 1999; Klinkhammer et al. 1983), average post-Proterozoic limestones (Haskin et al.1966; Tanaka and Kawabe 2006), high-temperature hydrothermal solutions (Douville et al. 1999), and low-temperature hydrothermal solutions (Michard et al. 1993). Error envelopes are 2SE for the WKB calcites. Note that the vein calcites have lower REE contents than seawater or limestones (formed in modern seawater), while the band calcites have REE concentrations between those of hydrothermal solutions and seawater.

6.10 Tables

Table 1: Calculated Mineralogy

	oxide+chert		oxide+carbonate	
Sample:	**K18**	**K37**	**K74**	**K76**
Fe-oxides[a]	82.0	71.9	73.7	60.7
quartz (chert)	13.6	11.2	18.1	29.9
calcite	0.4	4.4	4.0	2.0
apatite	1.6	3.2	1.9	2.0
(Fe-)chlorite	2.4	6.4	2.4	5.2
albite[b]	-	1.7	-	-
RSS[c]	0.12	0.34	0.020	0.022

a Calculated as hematite
b Apatite was only observed in K37. Additional minor mineral species (including xenotime, gypsum, and barite) are present in negligible percents and not explicitly calculated.
c Residual sum of squares, as compared to bulk-rock chemistry

Table 2: Calculated Bulk-Rock Compositions, from Calculated Mineralogy

	K18			K37			K74			K76		
wt.%	measured[a]	calc.	residual[b]	measured	calc.	residual	measured	calc.	residual	measured	calc.	residual
SiO_2	14.11	14.11	0.00	14.82	14.82	0.00	18.31	18.31	0.00	30.58	30.58	0.00
TiO_2	0.09	0.00	0.09	0.16	0.01	0.14	0.07	0.00	0.06	0.10	0.01	0.09
Al_2O_3	0.45	0.46	-0.01	1.94	2.03	-0.10	0.44	0.46	-0.02	1.01	1.03	-0.02
Fe_2O_3	82.93	82.93	0.00	73.13	73.13	0.00	73.29	73.29	0.00	62.08	62.08	0.00
MnO	0.01	0.03	-0.02	0.02	0.09	-0.07	0.07	0.03	0.04	0.05	0.06	-0.01
MgO	0.16	0.09	0.07	0.81	0.29	0.52	0.18	0.08	0.10	0.29	0.20	0.09
CaO	1.07	1.06	0.01	4.25	4.23	0.02	3.13	3.12	0.01	2.25	2.22	0.03
Na_2O	0.00	0.00	0.00	0.48	0.42	0.16	0.07	0.03	0.04	0.04	0.01	0.03
K_2O	0.01	0.00	0.01	0.06	0.00	0.06	0.01	0.00	0.01	0.01	0.00	0.01
P_2O_5	0.64	0.65	-0.01	1.31	1.34	-0.03	0.71	0.72	-0.01	0.80	0.83	-0.03
CO_2		0.16			1.93			1.71			0.88	
sum	99.47	99.50	0.13	96.97	98.29	0.71	96.27	97.75	0.23	97.21	97.90	0.19

a Measured bulk-rock compositions are from Basta et al. (2011)
b measured – calculated compositions

Table 3: Mineral, bulk-rock, and calculated bulk-rock REE contents

	oxide+chert samples												
	K18							K37					
	Fe-oxides		apatite		bulk-rock	calculated		Fe-oxides	apatite		bulk-rock	calculated	
method:	SIMS		LA-ICPMS, SIMS		ICPMS[a]			ICPMS separate[b]	LA-ICPMS		ICPMS[a]		
	n=6		n=5						n=8				
	ppm	±	ppm	±	ppm	ppm	±	ppm	ppm	±	ppm	ppm	±
Y	15.7	3.5	748	2	29	24.6	2.9	7.2	593	11	25	24.3	0.88
La	3.8	0.8	86	21	5.2	4.5	1.0	2.0	90	17	5.6	4.3	0.70
Ce	7.2	2.1	206	38	11.0	9.1	2.3	3.5	199	31	10.9	9.0	1.26
Pr	1.3	0.4	40.7	4	1.8	1.7	0.3	0.5	39.2	3.6	1.7	1.7	0.16
Nd	6.8	2.1	229	10	8.0	9.2	1.9	2.4	206	12	7.4	8.4	0.55
Sm	1.61	0.5	55	1	1.87	2.18	0.4	0.53	60.6	2	1.71	2.33	0.10
Eu	0.37	0.1	16.0	0.1	0.56	0.56	0.1	0.17	15.3	0.4	0.51	0.61	0.03
Gd	1.91	0.5	74	0.6	2.54	2.72	0.4	0.72	65.7	1	2.20	2.64	0.10
Tb	0.29	0.1	12.3	0.1	0.50	0.43	0.1	0.13	12.1	0.4	0.37	0.48	0.02
Dy	2.30	0.4	85	1	3.64	3.21	0.4	1.02	75.4	2	2.56	3.17	0.13
Ho	0.56	0.1	28.0	0.1	0.87	0.90	0.1	0.26	15.9	0.4	0.62	0.70	0.03
Er	1.57	0.3	76.6	0.3	3.10	2.49	0.3	0.88	41.1	1.1	1.99	1.96	0.10
Tm	0.27	0.1	11.5	0.0	0.48	0.40	0.0	0.15	4.8	0.1	0.29	0.26	0.02
Yb	2.16	0.6	48.7	0.5	3.22	2.54	0.5	1.05	29.2	0.6	2.09	1.70	0.09
Lu	0.41	0.0	7.4	0.1	0.53	0.45	0.0	0.18	4.4	0.1	0.34	0.27	0.02
ΣREE-Y	30.5	6.6	976	15	43.3	40.3	5.7	13.5	858	29	38.3	37.4	3.81
ΣREE	46.2	8.6	1723	17	72.3	64.9	14.7	20.7	1451	34	63.3	61.7	5.19

Table 3: Mineral, bulk-rock, and calculated bulk-rock REE contents (cont.)

oxide+carbonate samples

	K74									K76							
	Fe-oxides		apatite		calcite		bulk-rock	calculated		Fe-oxides	apatite		calcite		bulk-rock	calculated	
method:	SIMS		LA-ICPMS, SIMS		LA-ICPMS		ICPMS[a]			ICPMS separate[b]	LA-ICPMS		LA-ICPMS		ICPMS[a]		
	n=4		n=13		n=11						n=5		n=6				
	ppm	±	ppm	±	ppm	±	ppm	ppm	±	ppm	ppm	±	ppm	±	ppm	ppm	±
Y	7.8	3.2	606	4	74	8.9	25	20.3	2.76	8.8	824	4	225	12	41	24.9	1.1
La	1.4	0.5	97	6	15.0	2.7	4.2	3.5	0.56	1.6	269	3	29.5	7.5	7.9	7.0	0.4
Ce	2.2	1.1	213	12	29.7	7.5	8.3	6.8	1.31	3.1	773	8	68	9.5	18.1	18.7	0.6
Pr	0.5	0.2	40.1	1.3	5.0	1.1	1.5	1.3	0.25	0.5	113	1	12.0	2.2	3.0	2.8	0.1
Nd	2.1	1.2	211	5	23.1	5.0	7.0	6.4	1.16	2.4	427	10	66	11	13.2	11.3	0.7
Sm	0.38	0.08	51.6	1.1	4.63	0.93	1.45	1.44	0.12	0.47	105	5	13.6	1.95	2.69	2.66	0.2
Eu	0.15	0.07	13.6	0.2	1.27	0.22	0.39	0.42	0.04	0.12	28.0	1.4	3.71	0.39	0.74	0.71	0.05
Gd	0.59	0.36	56	0.7	5.42	1.14	1.72	1.72	0.32	0.59	122	6	17.7	2.19	3.37	3.16	0.2
Tb	0.10	0.05	9.0	0.1	0.87	0.19	0.28	0.28	0.04	0.11	19.4	0.8	2.84	0.29	0.54	0.51	0.0
Dy	0.77	0.39	68	0.5	6.56	1.17	1.94	2.12	0.34	0.82	138	4	21.1	2.16	3.64	3.68	0.2
Ho	0.23	0.11	16.8	0.1	1.76	0.32	0.50	0.56	0.10	0.20	28.1	0.7	5.29	0.50	0.86	0.79	0.05
Er	0.60	0.27	55	0.4	5.85	0.88	1.54	1.72	0.24	0.66	89.2	2	16.2	1.92	2.62	2.50	0.1
Tm	0.12	0.05	8.1	0.1	0.86	0.15	0.23	0.28	0.05	0.10	12.7	0.2	2.18	0.21	0.38	0.36	0.02
Yb	0.91	0.30	58	0.4	6.02	0.85	1.66	2.01	0.26	0.71	89.2	1	14.0	1.18	2.51	2.49	0.1
Lu	0.14	0.03	8.9	0.1	1.15	0.15	0.29	0.32	0.03	0.12	13.8	0.2	2.27	0.25	0.40	0.39	0.0
ΣREE-Y	10.1	1.9	905	19	107	22.3	30.9	28.9	2.6	11.6	2229	27	274	24	60	57	5.0
ΣREE	17.9	3.2	1511	22	181	41.5	55.9	49.2	4.3	20.5	3053	53	500	26	101	82	9.0

a Data and methods from Basta et al. (2011)
b Data and methods from Maurice (2006)

6.11 Supplementary Figures

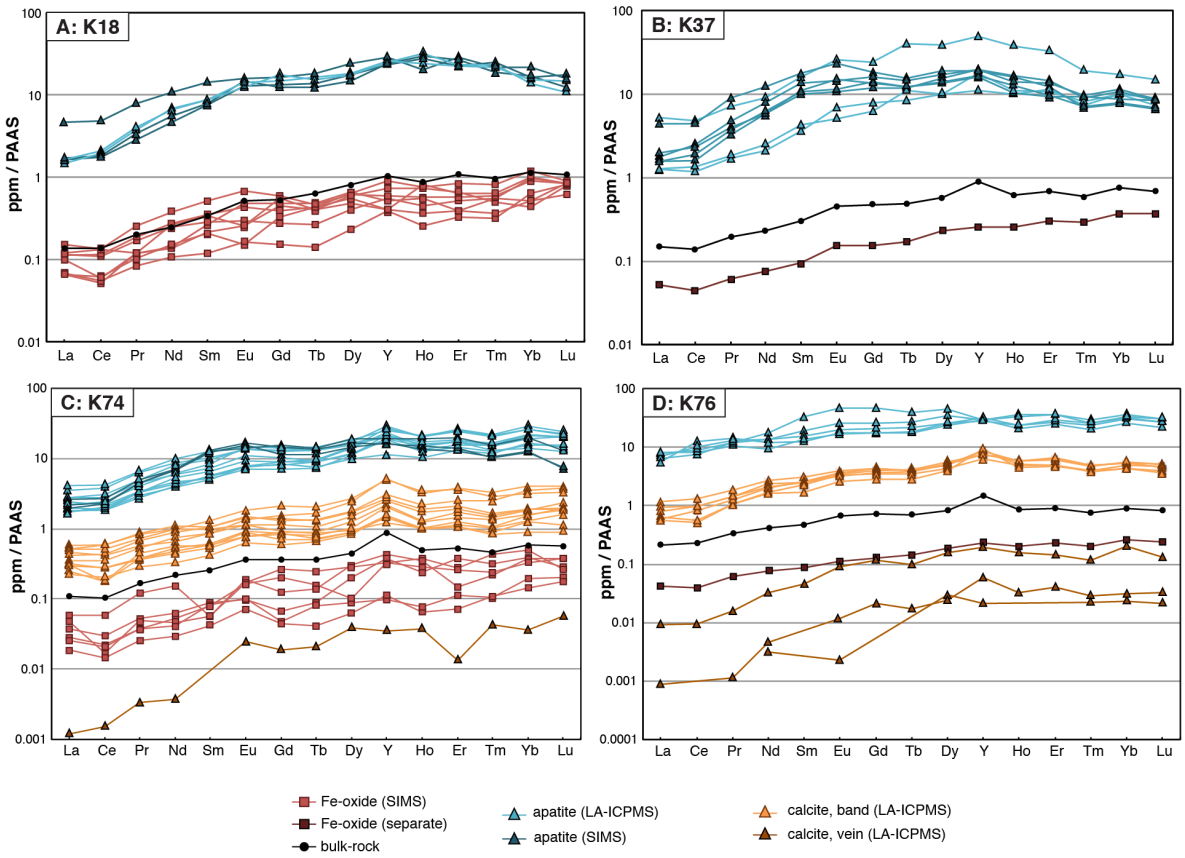

Supplementary Figure 1 PAAS-normalized (McLennan 2018) REE patterns of all individual mineral analyses and bulk-rock from the WKB for samples **a** K18, **b** K37, **c** K74, and **d** K76. Bulk-rock from Basta et al. (2011), and Fe-oxide separates (via ICPMS) from Maurice (2006).